ANGLE RESOLVED PHOTOEMISSION SPECTROSCOPY OF DELAFOSSITE METALS

Veronika Sunko

A Thesis Submitted for the Degree of PhD
at the
University of St Andrews

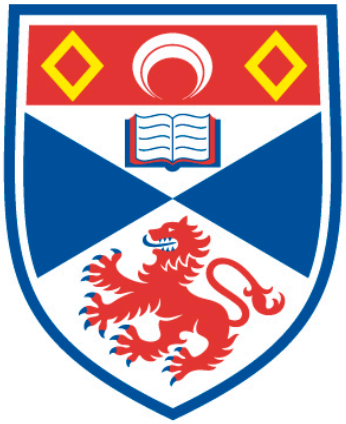

2019

Angle resolved photoemission spectroscopy of delafossite metals

Veronika Sunko

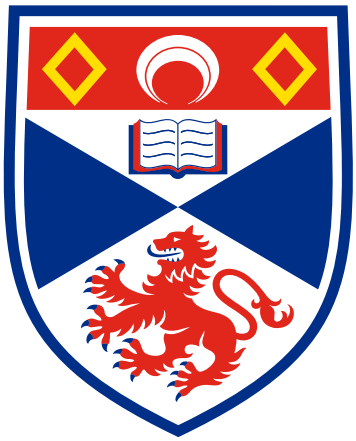

University of
St Andrews

This thesis is submitted in partial fulfilment for the degree of Doctor of Philosophy (PhD) at the University of St Andrews

April 2019

Declarations

Candidate's declaration

I, Veronika Sunko, do hereby certify that this thesis, submitted for the degree of PhD, which is approximately 57,000 words in length, has been written by me, and that it is the record of work carried out by me, or principally by myself in collaboration with others as acknowledged, and that it has not been submitted in any previous application for any degree.

I was admitted as a research student at the University of St Andrews in August 2015.

I received funding from an organisation or institution and have acknowledged the funder(s) in the full text of my thesis.

Date: 28.05.2019. Signature of candidate

Supervisor's declaration

I hereby certify that the candidate has fulfilled the conditions of the Resolution and Regulations appropriate for the degree of PhD in the University of St Andrews and that the candidate is qualified to submit this thesis in application for that degree.

Date: 28.05.2019. Signature of supervisor

Permission for publication

In submitting this thesis to the University of St Andrews we understand that we are giving permission for it to be made available for use in accordance with the regulations of the University Library for the time being in force, subject to any copyright vested in the work not being affected thereby. We also understand, unless exempt by an award of an embargo as requested below, that the title and the abstract will be published, and that a copy of the work may be made and supplied to any bona fide library or research worker, that this thesis will be electronically accessible for personal or research use and that the library has the right to migrate this thesis into new electronic forms as required to ensure continued access to the thesis.

I, Veronika Sunko, have obtained, or am in the process of obtaining, third-party copyright permissions that are required or have requested the appropriate embargo below.

The following is an agreed request by candidate and supervisor regarding the publication of this thesis:

Printed copy

Embargo on all of print copy for a period of 2 years on the following ground(s):

- Publication would preclude future publication

Supporting statement for embargo request:
Some data in the thesis have not yet been published.

Electronic copy

Embargo on all of electronic copy for a period of 2 years on the following ground(s):

- Publication would preclude future publication

Supporting statement for embargo request:
Some data in the thesis have not yet been published.

Title and Abstract

- I agree to the title and abstract being published.

Date: 28.05.2019. Signature of candidate

Date: 28.05.2019. Signature of supervisor

Underpinning Research Data or Digital Outputs

Candidate's declaration

I, Veronika Sunko, understand that by declaring that I have original research data or digital outputs, I should make every effort in meeting the University's and research funders' requirements on the deposit and sharing of research data or research digital outputs.

Date: 28.05.2019. Signature of candidate

Permission for publication of underpinning research data or digital outputs

We understand that for any original research data or digital outputs which are deposited, we are giving permission for them to be made available for use in accordance with the requirements of the University and research funders, for the time being in force.

We also understand that the title and the description will be published, and that the underpinning research data or digital outputs will be electronically accessible for

use in accordance with the license specified at the point of deposit, unless exempt by award of an embargo as requested below.

The following is an agreed request by candidate and supervisor regarding the publication of underpinning research data or digital outputs:

Embargo on all of electronic files for a period of 2 years on the following ground(s):

- Publication would preclude future publication

Supporting statement for embargo request:
Some data in the thesis have not yet been published.

Date: 28.05.2019. Signature of candidate

Date: 28.05.2019. Signature of supervisor

Publication list

1. H.Usui, M.Ochi, S.Kitamura, T.Oka, D.Ogura, H.Rosner, M.W.Haverkort, V. Sunko, P. D. C. King, A. P. Mackenzie, and K. Kuroki. Hidden kagome - lattice picture and origin of high conductivity in delafossite $PtCoO_2$. *Physical Review Materials*, **3**(4):045002, (2019)

2. M. D. Watson, O. J. Clark, F. Mazzola, I. Marković, V. Sunko, T. K. Kim, K. Rossnagel, and P. D. C. King. Orbital- and k_z - Selective Hybridization of Se $4p$ and Ti $3d$ States in the Charge Density Wave Phase of $TiSe_2$. *Physical Review Letter*s, **122**(7):076404, (2019)

3. O. J. Clark, F. Mazzola, J. Feng, V. Sunko, I. Marković, L. Bawden, T. K. Kim, P. D. C. King, and M. S. Bahramy. Dual quantum confinement and anisotropic spin splitting in the multivalley semimetal $PtSe_2$. *Physical Review B*, **99**(4):045438, (2019)

4. V. Sunko, E. Abarca Morales, I. Marković, M. E. Barber, D. Milosavljević, F. Mazzola, D. A. Sokolov, N. Kikugawa, C. Cacho, P. Dudin, H. Rosner, C. W. Hicks, P. D. C. King, and A. P. Mackenzie. Direct Observation of a Uniaxial Stress-driven Lifshitz Transition in Sr_2RuO_4. *arXiv:1903.09581*, (2019)

5. M. S. Bahramy, O. J. Clark, B.-J. Yang, J. Feng, L. Bawden, J. M. Riley, I. Marković, F. Mazzola, V. Sunko, D. Biswas, S. P. Cooil, M. Jorge, J. W. Wells, M. Leandersson, T. Balasubramanian, J. Fujii, I. Vobornik, J. E. Rault, T. K. Kim, M. Hoesch, K. Okawa, M. Asakawa, T. Sasagawa, T. Eknapakul, W. Meevasana, and P. D. C. King. Ubiquitous formation of bulk Dirac cones and topological surface states from a single orbital manifold in transition-metal dichalcogenides. *Nature Materials*, **17**(1):21–28, (2018)

6. V. Sunko, F. Mazzola, S. Kitamura, S. Khim, P. Kushwaha, O. J. Clark, M. Watson, I. Marković, D. Biswas, L. Pourovskii, T. K. Kim, T.-L. Lee, P. K.

Thakur, H. Rosner, A. Georges, R. Moessner, T. Oka, A. P. Mackenzie, and P. D. C. King. Probing spin correlations using angle resolved photoemission in a coupled metallic/Mott insulator system. *arXiv:1809.08972*, (2018)

7. O. J. Clark, M. J. Neat, K. Okawa, L. Bawden, I. Markovic, F. Mazzola, J. Feng, V. Sunko, J. M. Riley, W. Meevasana, J. Fujii, I. Vobornik, T. K. Kim, M. Hoesch, T. Sasagawa, P. Wahl, M. S. Bahramy, and P. D. C. King. Fermiology and Superconductivity of Topological Surface States in $PdTe_2$. *Physical Review Letters*, **120**(15):156401, (2018)

8. S. Kitamura, H. Usui, R.-J. Slager, A. Bouhon, V. Sunko, H. Rosner, P. D. C. King, J. Orenstein, R. Moessner, A. P. Mackenzie, K. Kuroki, and T. Oka. Spin Hall effect in 2d metallic delafossite $PtCoO_2$ and vicinity topology. *arXiv:1811.03105*, (2018)

9. F. Mazzola, V. Sunko, S. Khim, H. Rosner, P. Kushwaha, O. J. Clark, L. Bawden, I. Marković, T. K. Kim, M. Hoesch, A. P. Mackenzie, and P. D. C. King. Itiner- ant ferromagnetism of the Pd-terminated polar surface of $PdCoO_2$. *Proceedings of the National Academy of Sciences*, **115**(51):12956–12960, (2018)

10. N. Nandi, T. Scaffidi, P. Kushwaha, S. Khim, M. E. Barber, V. Sunko, F. Mazzola, P. D. C. King, H. Rosner, P. J. W. Moll, M. König, J. E. Moore, S. Hartnoll, and A. P. Mackenzie. Unconventional magneto-transport in ultrapure $PdCoO_2$ and $PtCoO_2$. *npj Quantum Materials*, **3**(1):66, (2018)

11. F. Arnold, M. Naumann, S. Khim, H. Rosner, V. Sunko, F. Mazzola, P. D. C. King, A. P. Mackenzie, and E. Hassinger. Quasi-two-dimensional Fermi surface topography of the delafossite $PdRhO_2$. *Physical Review B*, **96**(7):075163, (2017)

12. P. Kushwaha, H. Borrmann, S. Khim, H. Rosner, P. J. W. Moll, D. A. Sokolov, V. Sunko, Yu. Grin, and A. P. Mackenzie. Single Crystal Growth, Structure, and Electronic Properties of Metallic Delafossite $PdRhO_2$. *Crystal Growth & Design*, **17**(8):4144–4150, (2017)

13. V. Sunko, H. Rosner, P. Kushwaha, S. Khim, F. Mazzola, L. Bawden, O. J. Clark, J. M. Riley, D. Kasinathan, M. W. Haverkort, T. K. Kim, M. Hoesch, J.

Fujii, I. Vobornik, A. P. Mackenzie, and P. D. C. King. Maximal Rashba-like spin splitting via kinetic-energy-coupled inversion-symmetry breaking. *Nature*, **549**(7673):492–496, (2017)

14. L. Bawden, S. P. Cooil, F. Mazzola, J. M. Riley, L. J. Collins-McIntyre, V. Sunko, K. W. B. Hunvik, M. Leandersson, C. M. Polley, T. Balasubramanian, T. K. Kim, M. Hoesch, J. W. Wells, G. Balakrishnan, M. S. Bahramy, and P. D. C. King. Spin - valley locking in the normal state of a transition-metal dichalcogenide superconductor. *Nature Communications*, **7**:11711, (2016)

15. P. Kushwaha, V. Sunko, P. J. W. Moll, L. Bawden, J. M. Riley, N. Nandi, H. Rosner, M. P. Schmidt, F. Arnold, E. Hassinger, T. K. Kim, M. Hoesch, A. P. Mackenzie, and P. D. C. King. Nearly free electrons in a $5d$ delafossite oxide metal. *Science Advances*, **1**(9):e1500692, (2015)

Abstract

This thesis describes the results of angle resolved photoemission spectroscopy (ARPES) experiments on delafossite oxide metals, and theoretical work explaining the observations. The main results of the thesis are reported in three chapters, each of which is dedicated to a different physical observation, as I describe below.

The delafossite metals exhibit extraordinarily high conductivity, motivating a study of bulk electronic structure. I report measurements of the bulk electronic structure of the non-magnetic delafossites $PdCoO_2$ and $PtCoO_2$. In each, a single fast band crosses the Fermi level, resulting in a highly two-dimensional Fermi surface of nearly hexagonal cross-section. The detailed differences between the materials are described, and so are the possible many-body renormalisations.

Extension of the measurements to the electronic structure of the antiferromagnetic delafossite metal $PdCrO_2$ reveals a signal which I realised cannot be explained in terms of standard pictures of electron behaviour in a periodic potential. Using a combination of experiment and theory, partly in collaboration with external groups, we were able to identify its origin as the Kondo-like coupling of itinerant Pd - and localised Cr - electrons. In doing so we are able to show that that ARPES can be sensitive to spin-spin correlations.

Furthermore, I report measurements and analysis of the surface states arising from the transition metal terminated surfaces of $PtCoO_2$, $PdCoO_2$ and $PdRhO_2$. The states support a large Rashba-like spin-splitting, the energy scale of which is comparable to the atomic spin-orbit coupling of the relevant transition metal ion. I show how this arises as a consequence of the large energy scale of inversion symmetry breaking at the surface, and that this is in turn a consequence of the unusual structure of the transition metal oxide layer.

Acknowledgements

The work presented in this thesis was done over the course of four years, both at the University of St Andrews and at the Max Planck Institute for Chemical Physics of Solids in Dresden. I lived in St Andrews for a year, and in Dresden for three. As a student of the Scottish Centre for Doctoral Training in Condensed Matter Physics, I took a number of graduate courses, and participated in teaching and outreach activities. Over the four years in the two locations I have benefited from the help, insight and friendship of numerous people, to all of whom I am grateful. I mention many of them in these Acknowledgements, making the section unusually long. I ask the reader to bear with me through the following few pages; if you ever meet anyone I mention say hi, it will be worth it!

Firstly I want to thank my two supervisors, Phil King and Andy Mackenzie. As well as teaching me a great deal, each of them in his own way showed me that the highest scientific standards can be combined with an atmosphere of enthusiasm, curiosity and friendship. They have given me the freedom and the time to pursue my own ideas, while always being happy to discuss them. Indeed, the physics conversations with Andy and/or Phil, be it while drinking coffee in comfy chairs, walking around a synchrotron, Skyping or hiking, are among my favourite memories of the last four years.

None of the work in the thesis would be possible without the high-quality samples grown initially by Pallavi Kushwaha, and mostly by Seunghyun Khim. I also want to thank Seunghyun for our conversations about delafossites, and in particular for the enthusiasm with which he always responded to ideas about new collaborations, and hypothetical materials.

Our beamtimes were always characterised by good teamwork and collaborative spirit, due to Phil's guidance, as well as the good humour and hard work of all the group members. For that I thank everyone who participated in them: Edgar Abarca Morales, Lewis Bawden, Deep Biswas, Oliver Clark, Phil King, Igor Marković, Fe-

derico Mazzola, Jon Riley and Matt Watson. I am especially grateful to Lewis and Federico, with both of whom I have shared numerous night shifts. The ones with Lewis were at the beginning of my PhD, when he patiently introduced me to experimental tricks, and gave me a practical tutorial in recognising and enjoying deadpan humour. The shifts with Federico were always energetic and fun, made more so by good music and loud discussions we enjoyed having. Many of those discussions were about delafossites, both on the projects I led and those he led, and for that I am particularly grateful.

In parallel to our measurements on the bulk electronic structure of delafossites, Frank Arnold and Elena Hassinger performed quantum oscillation experiments on $PtCoO_2$ and $PdRhO_2$. The conversations I had with them and Andy about those experiments made me appreciate the relative advantages and disadvantages of angle resolved photoemission and quantum oscillations as methods.

Our experiments inspired theoretical work, leading to a number of enjoyable collaborations with theory colleagues. I am grateful for discussions I had with all of them, listed here: Antoine Georges, Maurits Haverkort, Deepa Kasinathan, Sota Kitamura, Roderich Moessner, Takashi Oka, Leonid Pourovskii and Helge Rosner. Helge performed all the density functional theory calculations presented in the thesis, and was happy to share their output with me. Sota and Takashi developed the theory describing $PdCrO_2$ outlined in Chapter 5, which we discussed and dissected in the course of numerous warm afternoons. Roderich participated in many of these conversations, and always made me appreciate some new aspect of the physics. I learned from Maurits that plotting orbitals is a often a good idea, and he showed me how to do it.

I thank Chufo Borzi, Chris Hooley and Andreas Rost for the discussions about $PdCrO_2$. They all helped me turn the feeling that 'there is something strange going on' into a series of specific questions, eventually leading to the discussion given in Chapter 5.

I am grateful to Christoph Geibel for his careful reading of Chapter 6 of this thesis. His perceptive comments helped clarify my thinking on several points, and improved the discussion of those. I very much enjoyed our conversations.

I was able to have the conversations about theory in part due to the excellent graduate courses I took during my time in St Andrews. In particular, I want to mention the Quantum Field Theory course taught by Jonathan Keeling, the Mag-

netism course by Jonathan Keeling and Bernd Braunecker, and the course on Response Functions by Chris Hooley and Brendon Lovett. As well as teaching us the subject matter, those courses encouraged collaboration and teamwork among the students. I remember fondly a week spent discussing a Magnetism problem with Rhea Stewart and Scott Taylor; we got more joy from that solution than we knew homework could bring.

The time in St Andrews, both while living there and later when visiting, was made very enjoyable by a group of fun and friendly PhD students and post docs; in particular I am grateful for the time I shared with Maja Bachmann, Rhea Stewart, Scott Taylor, Matt Neat, JPh Reid, Igor Marković, Stephanie Matern, Philippa McGuinness, Natalie Mica, Oliver Clark, Lewis Bawden, Federico Mazzola, Eliott Levi, Ian Van Beek, Artem Strashko and Mike Lynch-White.

The move to Dresden, as well as numerous visits to St Andrews I made later, were greatly facilitated by the help of Julie Massey, Wendy Clark, Christine Edwards and Debra Thompson in St Andrews, as well as Claudia Strohbach and Uta Prautzsch in Dresden.

In addition to the work presented in the thesis, in Dresden I worked on several other experiments. Planning and executing measurements on electron-irradiated delafossites with Philippa McGuinness was a pleasure, as were the uncountable physics arguments we had in the process. For the later measurements we were joined by Elina Zhakina, making a dynamic and efficient team. At the moment I greatly enjoy watching Philippa and Elina take that project further, building on the work we started together. I worked with with Edgar Abarca Morales on the last experiments prior to writing this thesis, and found his enthusiasm and energy both helpful and inspiring.

I want to thank Clifford Hicks for our many conversations on a range of topics, especially the ones about new data and possible interpretations of it, as well as his inventiveness and creativity.

I thank Burkhard Schmidt for a number of discussions which increased my understanding of both physics and mathematics, as well as the superconductivity reading course we did at the beginning of my PhD. I also appreciate his help with all the IT issues I have encountered. More than that, I am grateful for every time he spontaneously asked me how was I doing.

All the experimental work done in Dresden was greatly facilitated by a number

of people ensuring the smooth running of the Institute as a whole, an excellent mechanical workshop, but especially my group members. They were all happy to help when needed, as well as to share ideas, problems, code and equipment. In particular I want to thank Mark Barber, with whom I shared an office for the whole duration of my stay in Dresden, and who could, and happily would, answer every lab- related question. Dan Brodsky, with whom I overlapped for a few months at the beginning of my PhD, taught me the basics of transport measurements, and the importance of keeping good lab books. I also acknowledge the help of Maja Bachmann, Jack Bartlett, Markus König, Nabhanila Nandi, Sebastian Seifert, Dmitry Sokolov, Alexander Steppke and Po-Ya Yang.

In general, the fantastic group atmosphere in Dresden has been established and maintained throughout the years by a number of people. I especially want to mention the lunch and general fun crowd, sorted according to office location and the alphabet: Markus König, Andy Mackenzie, Mark Barber, Dan Brodsky, Po-Ya Yang, Fabian Jerzembeck, You-Sheng Li, Nabhanila Nandi, Hilary Noad, Lishan Zhao, Elena Hassinger, Clifford Hicks, Elina Zhakina, Jack Bartlett, Philippa McGuinness, Alexander Steppke, Belén Zúñiga, Burkhard Schmidt, Alex Stern, Edgar Abarca Morales, Ekta Singh, Kim Modic, Kent Shirer, Maja Bachmann, Philip Moll, Daniel Hafner, Zuzana Medvecká, Seita Onishi, Manuel Brando, and Lucas Pili and Chufo Borzi during their long visits...

Maja and Nabhanila deserve a separate paragraph. The three of us were repeatedly and reliably 'having fun again,' increasing the level of high-frequency noise in the Institute and the surrounding areas. I am lucky to have been with Maja both in St Andrews and in Dresden, experiencing it all together. We have also been writing our theses simultaneously, sharing the joys and frustrations of the process, as well as more chocolate than we care to remember.

Many friends, some already mentioned, made me enjoy a variety of extra-curricular activities, which include, but are not limited to, pre- and post- conference exploration, spontaneous weekend trips and meticulously planned road trips, brunches and lunches, dinners whose duration defied all reason, and walks of a similar kind, in cities, on beaches, in forests and in the mountains, sneaky morning 'phone coffees', Taste coffees at any and every time of the day, cappuccino instructions, exploding an apple once and bottles quite a few times, constructing a giraffe, a snowlady and a scrapbook, making jam, nitrogen ice cream and more than one cake, game nights

and girls' nights, strangers' house parties, friends' couches and floors, parties for international holidays, and an occasional murder mystery, visits to various museums and one Swedish furniture store, the opera and comedy clubs, concerts and (seminar room) cinemas, pizza Tuesdays, pub Fridays, gym Saturdays... - to all of my physics and non-physics, Dresden, St Andrews and Zagreb friends, thank you! You know who you are, and I am looking forward to seeing you again.

I am very aware that my interest in physics started and initially developed long before the beginning of the PhD, but also that naming people who helped along the way would test the endurance of even the most patient reader. I do, however, want to mention Marija Vučković, with whom I have messed around in our high-school labs since we were 15 years old, studied at the University of Zagreb, and still share joys and annoyances, small and large, on a daily basis.

In the end I want to thank my family. I thank my brother Andrija for his insuppressible curiosity, enthusiasm when sharing all that interests him, as well as his perceptive questions, some of which were on my mind while writing sections of the thesis ('But wait, *how* do you know that?'). I thank my parents, Branka and Denis, for the kind of love that yields confidence, and the bits of wisdom I acquired through diffusion, and sometimes repetition; 'The job requires as much work as it does,' 'Just try - if it works it works, if not say you were just joking' and 'Always lock the pantry' come to mind[1]. More than anything, I thank them for giving me examples of happy lives, to which work and play, friends and family all contribute.

Lastly, I would like to acknowledge financial support from the Engineering and Physical Sciences Research Council via the Scottish Condensed Matter Centre for Doctoral Training under grant no. EP/L015110/1, and from the Max Planck Society.

Research data underpinning this thesis are available at:
https://doi.org/10.17630/0b976971-8f36-48d1-a662-e13f4629400d.

[1]Translations do not do justice here. The original versions are 'Posao traži koliko traži,' 'Probaj, ako radi radi, ako ne samo sam se šalila' and 'Uvijek zapatavaj konobu.'

Contents

1. Introduction

Understanding how observable properties of materials arise as a consequence of their structure and constituent elements is of deep fundamental interest, as it is a window onto the underlying quantum many-body problem. The multitude of complementary experimental probes and tuning parameters which can be used to study solids allows us to ask a variety of specific questions, and test predictions of the theories aiming to explain the resulting data. While there is no general recipe for the study of new materials, most often the first step is an observation which the experimentalists recognise as unusual. More experiments are done to gather information about the phenomenon, and theories are developed to explain it. In the most favourable cases, the theories motivate further experiments, sometimes inspiring new technological development, or perhaps the design of novel materials. Along the way new effects, which may or may not be related to the original one, are encountered, in turn motivating different new experiments and theories.

My aim in this thesis is to convey one such story of research motivated by an experimental observation, and leading to serendipitous discovery of new phenomena which I believe are interesting in their own right. The starting experimental observation was the extremely high conductivity in the non-magnetic delafossite metals $PtCoO_2$ and $PdCoO_2$. While the high conductivity was noticed as soon as they were first synthesised in 1971 [1–3], its underlying cause was not understood. In fact, it took more than thirty years for a more extensive experimental and theoretical investigation of these materials to start (Ref. [4], and references therein). As a part of the effort to understand the high conductivity, we decided to investigate the electronic states underlying it. The experimental technique I have used to do this is angle resolved photoemission spectroscopy (ARPES), which enables the imaging of quasiparticle dispersions, as described in detail in Chapter 2. While not giving a direct solution to the puzzle of high conductivity, our measurements of the delafossite bulk electronic structure [5], discussed in Chapter 4, did yield very sharp

quasiparticle spectra, which could be analysed over a much wider binding energy range than is usual for metallic oxides. They also motivated theoretical work which helped to understand how the properties of the delafossite Fermi surface lead to suppressed scattering [6].

While investigating the non-magnetic delafossite metals, we also decided to measure the antiferromagnetic metal $PdCrO_2$. We observed a signal which had been seen previously [7], and interpreted in terms of standard models of the behaviour of electrons in a periodic, in this case antiferromagnetic, potential. However, as described in Chapter 5, a careful investigation of our data and the predictions of such standard models led us to understand that the signal we observed had a different origin. This motivated our theory collaborators Sota Kitamura and Takashi Oka to perform a many-body calculation, which in turn motivated further experiments, eventually allowing us to understand our observation as a previously unidentified type of spectroscopic signal, arising as a consequence of coupling between itinerant and strongly correlated subsystems [8].

The study of effects arising from the bulk electronic structure, like the ones described above, is often complicated by the fact ARPES can typically probe only a $\sim 5\,\text{Å}$ thick layer near the crystal surface. The surface sensitivity can also be an advantage, as it offers an opportunity to investigate the electronic states which are affected by the reduced symmetry and the altered bonding environment at the surface. Specifically, both the Pd- terminated and the CoO_2 - terminated surfaces of delafossites host electronic states very different to those of the bulk [9]. They are compared, and their characteristic signatures are described briefly in Section 1.2. We were able to observe and study both types of surfaces states [10, 11]. While I discuss the states originating from the Pd - terminated surface only briefly in Appendix B, the investigation of the states localised on the CoO_2 - terminated surfaces of $PdCoO_2$ and $PtCoO_2$ forms a large part of this thesis (Chapter 6). They had been observed and identified prior to the work presented here [12]. That experiment was done, however, as a part of a study of the bulk electronic states, and the properties of the surface states were not investigated further. In the course of performing a more in-depth study, we noticed that they support an unusually large spin-splitting. Using a combination of experiment and theory we have been able to understand how the large spin-splitting arises as a consequence of the structure of the surface layer, as described in detail in Chapter 6. The conclusions we were able to draw are not

specific to delafossite oxides, and are applicable to a wide range of systems.

Overall, this thesis is an overview of the effects we have observed and studied by angle resolved photoemission spectroscopy of delafossite oxide metals. Those experimental observations motivated me to develop several minimal tight-binding models, with the aim of differentiating between features which can and cannot be explained in such a single-particle framework, and to understand the origin of the ones which can. The thesis contains the descriptions and results of these models, as well as the results of more advanced theory motivated by the experiments and the minimal models, and done by our collaborators. The physics underlying these theories is also discussed, along with implications for future experiments.

1.1. Delafossite oxides

1.1.1. Real and reciprocal lattice structure

The general formula of delafossite oxides is ABO_2. The term 'delafossite structure' is used for two different polymorphs, referred to as the $3R$ and $2H$ polymorph, which belong to the rhombohedral space group $R\overline{3}m$ (166) and the hexagonal space group $P6_3/mmc$ (194), respectively. The two polymorphs contain the same structural units, stacked differently. The most famous example of the $2H$ delafossites is Na_xCoO_2, which becomes superconducting when intercalated with water. All of the delafossites I have studied belong to the $3R$ polymorph, so the following description and the literature review refer to the materials of this structure. The structure of the $3R$ delafossite polymorph is shown in Figures 1.1(a, b). Each of the four ions in the formula unit, the A and B - type cations and the two oxygen anions, span a triangular lattice of the same lattice constant a. As evident in the top view shown in Figure 1.1b, the same-species atoms in neighbouring layers are staggered; the in-plane positions of atoms are the same only in every third layer of a given type. This is the structural difference between the two polymorphs: in the $2H$ structure the in-plane positions are the same in every other layer. The out-of-plane lattice parameter of the conventional hexagonal unit cell of a $3R$ delafossite is therefore equal to three separations between the neighbouring A (or B) planes (c in Figure 1.1a). The volume of the conventional unit cell, spanned by the out-of-plane lattice vector c and the in-plane lattice vector a (marked in Figure 1.1b), is therefore three

times larger than the volume of the rhombohedral unit cell.

The layered nature of the delafossite structure results in the intralayer coupling being considerably stronger than the coupling between the A and the BO_2 layers. When thinking of the properties of a specific delafossite, a good starting point is therefore to separately consider the properties of the individual layers, which are governed by the elements occupying the A and B sites, and the local environment of those sites. The A-type cations are linearly coordinated with two oxygen ions (Figure 1.1c), while each of the B-type cations is in the centre of an oxygen octahedron (Figure 1.1d). This octahedron is a common structural unit in transition metal oxides, creating an octahedral crystal field on the B site. However, the octahedra in the delafossite structure are edge sharing, in contrast to the more common corner sharing octahedra found in perovskites.

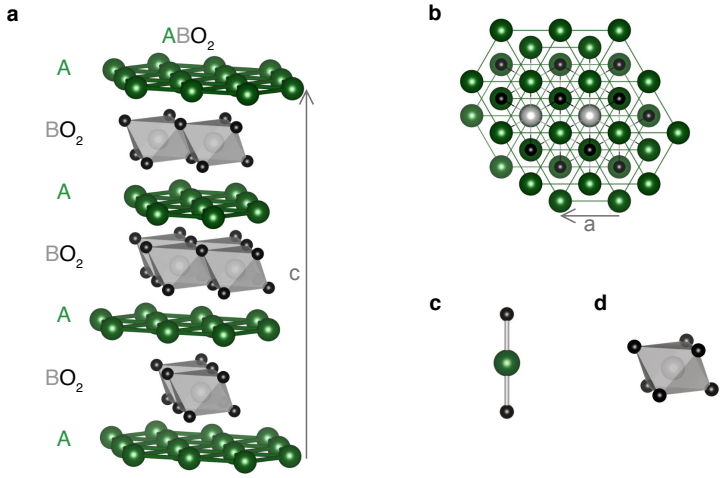

Figure 1.1.: The crystal structure of the $3R$ delafossite polymorph, (**a**) viewed from the side and (**b**) from the top. (**c**) Each A-type ion is linearly coordinated with two oxygen ions. (**d**) Each B-type ion is in the centre of an oxygen octahedron.

Because ARPES is a momentum-space probe, it is important to understand the reciprocal, as well as the real-space, unit cell of delafossites. The three-dimensional Brillouin zone of the $3R$ polymorph is shown in Figure 1.2a. The staggering of the neighbouring triangular layers in the real space structure leads to the faceting of the Brillouin zone, whose two-dimensional projection is shown in Figure 1.2b. As I will show in Section 4.1 below, from the point of view of photoemission it is justified to neglect the small out-of-plane dispersion of the Fermi surface, and consider the two

dimensional version of the Brillouin zone instead, shown by the green line in Figure 1.2c. This is the Brillouin zone of a two-dimensional triangular lattice of lattice spacing a; it is hexagonal, with the side of the hexagon given by $a_{BZ} = 4\pi/(3a)$. The high symmetry points of the zone are the $\overline{\Gamma}$, $\overline{K}$ and $\overline{M}$ points, as indicated in Figure 1.2c. In Table 1.1 I list the real space lattice parameters, as well as the parameters of the 2D Brillouin zone, of all the delafossites studied in this thesis.

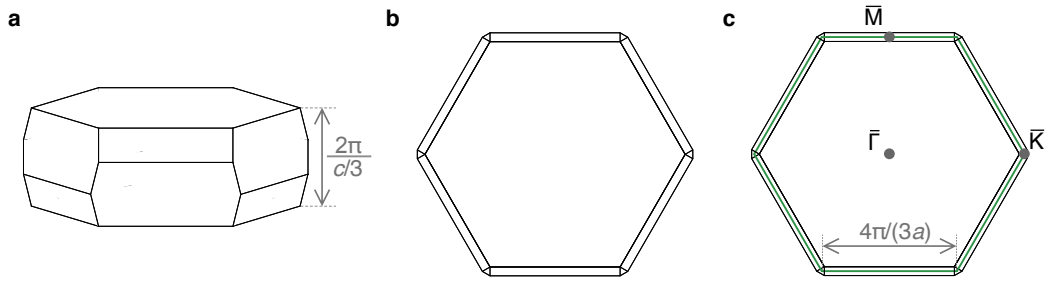

Figure 1.2.: (**a**) The three-dimensional Brillouin zone of the $3R$ delafossites. (**b**) The projection of the 3D zone onto a 2D plane. (**c**) The 2D Brillouin zone (green), compared to the projection of the 3D zone (black).

	a/Å	c/Å	$\left(\overline{\Gamma}-\overline{K}\right)$/Å^{-1}	$\left(\overline{\Gamma}-\overline{M}\right)$/Å^{-1}	A_{BZ}/Å^{-2}
$PtCoO_2$	2.82	17.808	1.485	1.286	5.73
$PdCoO_2$	2.83	17.743	1.479	1.281	5.69
$PdCrO_2$	2.93	18.087	1.429	1.237	5.30
$PdRhO_2$	3.02	18.083	1.386	1.201	4.99

Table 1.1.: Real space lattice constants a and c, as well as the distance between the high-symmetry points in the Brillouin zone and the 2D Brillouin zone volume of all the delafossites studied in this thesis. The side of the hexagonal Brillouin zone is equal to the $\overline{\Gamma}-\overline{K}$ distance (Figure 1.2c). The lattice constants are taken from Ref. [4], where the source references are listed.

1.1.2. Variety of delafossites

The delafossite structure is very accommodating, and can host a variety of elements on the A and B sites, leading to a wide range of properties across the structural series. This is illustrated by the periodic table shown in Figure 1.3, in which I mark all the elements which occupy the A or the B site in a known $3R$ delafossite oxide by green and grey, respectively. What is more, not only oxides can assume the delafossite structure. In Table 1.2 I note all the combinations of A and B site elements occurring in $3R$ delafossite oxides, sulphides, selenides and tellurides listed in the Inorganic Crystal Structure Database (ICSD, [13]), marked with the corresponding elemental symbols (O, S, Se and Te, respectively). In addition to these, there are also examples of delafossites whose oxygen site is occupied by elements which are not in the oxygen family (group 16 of the periodic table), such as Ca, Sr or N. Although not a comprehensive overview of all the delafossites synthesised to date, the table illustrates the range of compounds across the structural series, and is useful as a reference. I have studied its small subset, namely the four known delafossite oxides based on Pt or Pd.

Several general observations about the delafossite oxides can be made based on the considerations of the constituent elements in a local ionic picture. While a degree of covalent bonding between different ionic species means that this is never exact, it is a good approximation and a useful foundation on which to build a more detailed understanding. The periodic table in Figure 1.3 therefore contains the information on the most common oxidation states of every element in the top right corner of the corresponding field. There are two oxygens in the delafossite formula unit, each in the $2-$ oxidation state. To preserve charge neutrality the oxidation states of the A and B cations have to add up to $+4$. In the vast majority of delafossite oxides this occurs by the A and B site cations taking the oxidation states of $1+$ and $3+$, respectively. The only currently known exceptions are the mercury based delafossites, $HgCaO_2$, $HgSrO_2$ and $HgBaO_2$, in which both cations take the $2+$ oxidation state. This can be deduced by inspecting the 'grey' elements in the periodic table: the most common oxidation state of Ca, Sr and Ba is $2+$, as losing two electrons makes all of their electron shells closed. On the other hand, $3+$ is one of the most common oxidation states of all the other elements which occupy the B site in a known delafossite oxide. Even more informative is the analysis of

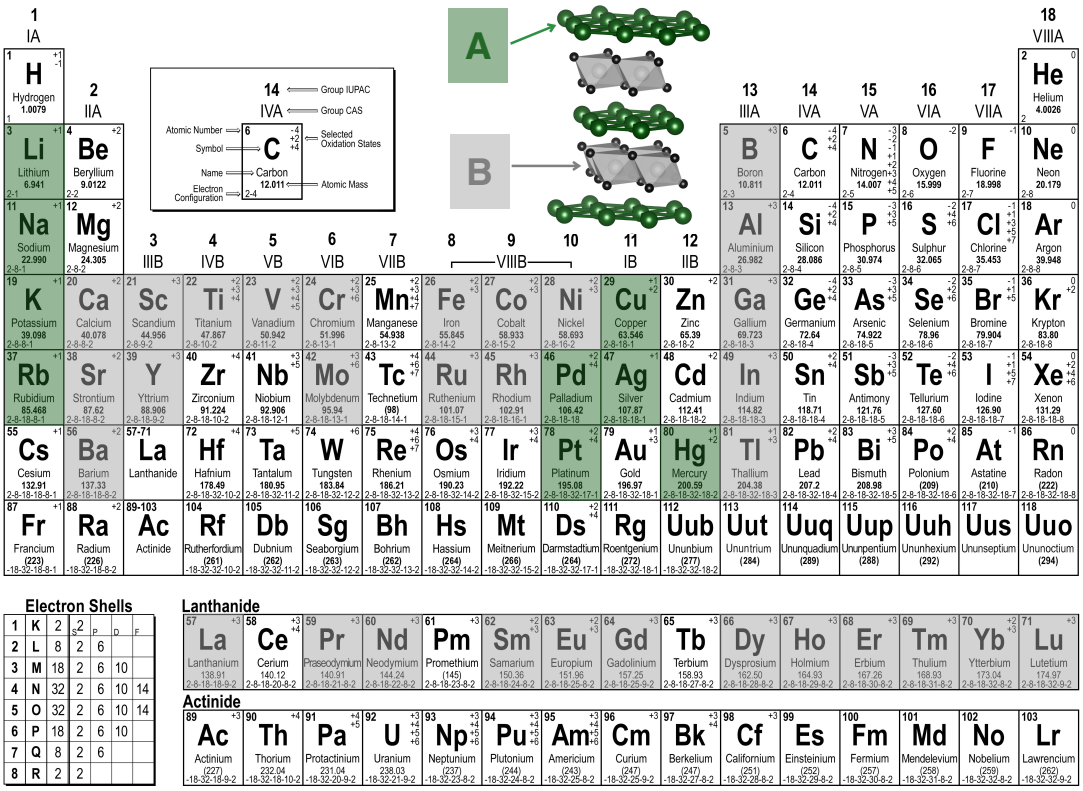

Figure 1.3.: The periodic table of elements, with the elements which occupy the A site and the B site in at least one known $3R$ delafossite oxide marked green and grey, respectively.

the elements found on the A-site. In the 1+ state the alkali metals (Li, Na, K, Rb) reach the noble gas electronic configurations, while copper and silver reach a closed d shell: $3d$ and $4d$ shell, respectively. This is why 1+ is one of their most common oxidation states, as is 2+ for mercury. The outliers to this general trend are Pd and Pt; in the delafossite structure they take the 1+ oxidation state, although this is very rare for them. The unusual oxidation state was pointed out when the Pd- and Pt- based delafossites were first synthesised in 1971. Pd and Pt in the delafossite structure assume the $4d^9$ and $5d^9$ electronic configurations, respectively, leaving one hole in the relevant d shell, and therefore making the Pd and Pt layers metallic. Consequently all of the Pd and Pt based delafossites are metals, and I study all of them in this thesis. The only known metallic delafossite oxide that contains

neither Pd nor Pt is $AgNiO_2$. It is, however, fundamentally different from the other metallic delafossites, as the metallic states are derived from the B-site element, i.e. Ni in the $3d^7$ configuration. I will not discuss it further, but will concentrate on $PtCoO_2$, $PdCoO_2$, $PdRhO_2$ and $PdCrO_2$ instead. The first three among these are non-magnetic, while $PdCrO_2$ exhibits local moment antiferromagnetism, and will therefore be discussed separately. My aim in this introduction is not to offer a comprehensive chronological review of the research done on delafossite oxide metals, because this was done in a recent review article [4]. Rather, I will summarise the results and conclusions necessary to understand and contextualise the research done as part of this thesis.

A / B	Li	Na	K	Rb	Cs	Pd	Pt	Cu	Ag	Hg	Tl
Ca										O	
Sr										O	
Ba										O	
Sc	S	O, S	O, S	O, S				O	O		Se, Te
Y	S, Se	O, S, Se	O, S, Te	O, S				O			S, Se, Te
Ti	S	O, S									
Zr			S								
V	O	O, S, Se									
Cr	O	O, S, Se	O, S			**O**		O	O, Se		
Mo	O	O									
Fe	O	O						O	O		
Ru		O									
Co	O	O				**O**	**O**	O			
Rh	O	O				**O**		O	O		
Ni	O								O		
Al	O	O						O			
Ga	O	S		Se				O			
In	Se	O, S, Se	O					O	O, S, Se		S
Tl		O									S
As									Se		
Sb									Te		Te
Bi				S					Se, Te		S, Se, Te
La		Se	O, S, Te	O, S, Se	S			O			
Ce		Se	S	S, Se, Te	S						
Pr		Se	O, S, Te	S, Se	S			O			Se, Te
Nd		S, Se	S, Te	O, S, Se, Te	S, Te			O			S, Se, Te
Sm		S, Se, Te	S, Se, Te	O, S, Se, Te	S			O			S, Se, Te
Eu		S	S	O, S	S			O			S
Gd	Se	S, Se	S, Te	O, S	S						S, Se, Te
Tb	Se	S, Se	S	S, Se	S						S, Se, Te
Dy	S, Se	S, Se	S	O, S	S						S, Se, Te
Ho	S, Se	O, S, Se	S	O, S, Se	S						Se, Te
Er	S, Se	O, S, Se	O, S, Te	O, S, Se	S						S, Se, Te
Tm		S	S	O, S	S						S, Se, Te
Yb	S	O, S, Se	S, Se	O, S	S				O		S, Se
Lu		S	S	O, S, Se	S				O		S, Se, Te

Table 1.2.: Combinations of A and B site elements that exist in the $3R$ delafossite structure. Oxides, sulphides, selenides and tellurides are marked with the corresponding elemental symbols, O, S, Se and Te, respectively.

1.1.3. Non-magnetic delafossite metals

By far the most studied among the metallic delafossites is $PdCoO_2$. As already mentioned, Pd ion in $PdCoO_2$ is in the 1+ valence state and thus has nine electrons in the $4d$ shell, making the Pd layer metallic. A simplified crystal field diagram shown in Figure 1.4a would suggest that the one carrier is of the $d_{3z^2-r^2}$ character, however the relevant bandwidth is larger than the crystal field splitting, mixing all the $4d$ orbitals, as allowed by symmetry. What is more, mixing of the $5s$ orbital with the $4d$ orbitals is also allowed, and has been proposed to significantly contribute to the high conductivity. A similar picture is valid for Pt in $PtCoO_2$, but the relevant orbital manifolds are $5d$ and $6s$, instead of $4d$ and $5s$. The crystal field on the Co site is octahedral, splitting the $3d$ orbital manifold into the lower energy t_{2g} and the higher energy e_g subspaces. In the real structure the octahedra are in fact trigonally distorted, leading to an additional small crystal field splitting of the t_{2g} manifold. The electronic configuration of Co^{3+} is $3d^6$, allowing the t_{2g} states to be fully occupied and the e_g states to remain empty (Figure 1.4b). Equivalently, in $PtCoO_2$ and $PdRhO_2$ the t_{2g} states of the $3d$ orbital manifold of Co, and those of the $4d$ orbital manifold of Rh, are fully occupied, while the corresponding e_g orbitals remain empty. The transition metal layers can therefore in the first approximation be thought of as simple insulators, separating the conductive layers of A cations.

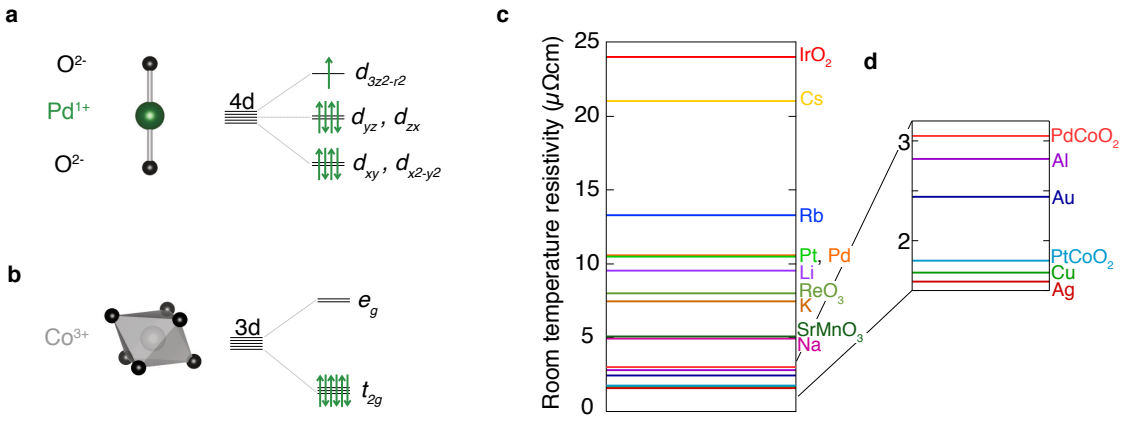

Figure 1.4.: The crystal field diagrams on the (**a**) A and (**b**) B site of $PdCoO_2$. (**c**) The room temperature resistivity of highly conductive metals, (**d**) with a zoom-in onto the most conductive room temperature metals. For $PtCoO_2$ and $PdCoO_2$ the in-plane resistivities are quoted.

As already mentioned, the high room temperature conductivity of $PtCoO_2$ and $PdCoO_2$ was noticed as soon as they were synthesised. To illustrate what is meant by 'unusually high conductivity', in Figure 1.4c I plot the resistivity at room temperature of a range of very conductive elemental metals, such as the alkali metals, bulk platinum and palladium, but also of a few examples of highly conductive oxides, such as IrO_2 , ReO_3 and $SrMnO_3$. At the bottom of the plot there is a cluster of most highly conductive room temperature metals, expanded in Figure 1.4d. As expected, elemental silver, copper, gold and aluminium are among them, but so are $PtCoO_2$ and $PdCoO_2$. The in-plane conductivity of these layered oxides is therefore comparable to that of silver and copper. This is even more striking when the conductivity per carrier of all of these metals is compared; because of the insulating CoO_2 layers, the carrier density in $PtCoO_2$ and $PdCoO_2$ is approximately one third of that of the elemental metals. In other words, the room temperature conductivity per carrier of $PtCoO_2$ is approximately three times higher than that of copper! The residual resistivity of delafossites is also very low, complicating its precise measurement. Values as low as 8 nΩcm in $PdCoO_2$ and 20 nΩcm in $PtCoO_2$ have been reported in samples of carefully defined geometries [14], corresponding to mean free paths of $\sim 20\,\mu m$ and $\sim 10\,\mu m$, respectively. This points to an unprecedentedly low level of disorder in an as-grown complex oxide, the underlying reason for which is still a topic of active investigation. Regardless of their origin, the long mean free paths have very interesting consequences, and have enabled the study of unconventional hydrodynamic and ballistic transport [15, 16].

The electronic structure of $PdCoO_2$ has, prior to the measurements done as a part of this thesis, been studied both by angle resolved photoemission [12] and quantum oscillations [17]. Those two techniques offer complementary information on the Fermi surface properties, making it highly desirable to perform both experiments on the same material. This is not always possible, as the two techniques have different material requirements and limitations. ARPES is sensitive to the in-plane electronic structure, while the out-of-plane dispersion broadens the signal, making it most suitable for the study of two dimensional electronic structures. Additionally, the surface sensitivity of the technique means that high quality data are typically obtained by cleaving in ultra high vacuum conditions. The material therefore has to be cleavable, typically requiring a layered crystal structure. On the other hand, the amplitude of quantum oscillations is exponentially sensitive to impurity scattering,

therefore requiring a high level of crystalline perfection. ARPES can yield information on the in-plane Fermi surface anisotropy inaccessible to quantum oscillations, while quantum oscillations are very sensitive to the degree and symmetry of the out-of-plane Fermi surface warping, and offer the most precise information on the Fermi surface volume. The ability to perform both types of experiments on $PdCoO_2$ led to a comprehensive experimental picture of its Fermi surface topography. It was found by ARPES that the Fermi surface has a hexagonal cross-section, as shown in Figure 1.5a. The quantum oscillation experiment found a very small degree of out-of-plane warping, consistent with the picture of $PdCoO_2$ as an alternating stack of two dimensional metallic layers separated by insulating spacer layers. The three dimensional Fermi surface plot, informed by both ARPES and quantum oscillations, is shown in Figure 1.5b. Quantum oscillations also revealed a small average effective mass of $\sim 1.5m_e$, consistent with the Fermi velocity measured by ARPES.

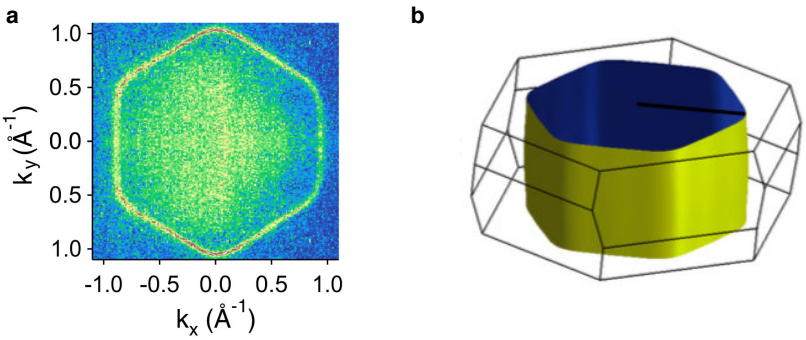

Figure 1.5.: (**a**) The in-plane bulk Fermi surface of $PdCoO_2$measured by angle resolved photoemission, reproduced with permission from Ref. [12]. (**b**) The 3D Fermi surface of $PdCoO_2$. The in-plane hexagonal shape is reproduced from the photoemission measurements shown in (a), while the out-of-plane warping is deduced based on the measurements of the de Haas van Alphen effect (Ref. [17]). Reproduced with permission from Ref. [17].

Interestingly, density functional theory calculations predict a larger degree of out-of-plane warping than is experimentally observed. This is a consequence of the hybridisation between the Pd and Co states, demonstrating that the simple ionic picture, in which palladium has a hard valence of 1+ and cobalt of 3+, does not capture the detailed physics. However, once the on-site Coulomb repulsion on the Co sites is included in the calculation, the hybridisation between the layers is suppressed,

the Co states are removed from the Fermi level, and the experimental Fermi surface is retrieved [17]. It is therefore still useful to think of the CoO_2 layers as insulating and the Pd layers as metallic in the first approximation, but the full justification of this picture is more subtle than that suggested by simple ionic arguments.

There were no published measurements on the electronic structure of $PtCoO_2$ prior to the ones done as a part of this thesis, because available single crystals were too small. Our photoemission measurements were done simultaneously with the quantum oscillation measurements performed by Frank Arnold and Elena Hassinger [5], so I will compare them in Chapter 4. The basic phenomenology is, however, similar in the two compounds, with the larger orbital overlap of the Pt $5d$ orbitals compared to the Pd $4d$ leading to lighter electron masses and more warped Fermi surfaces. Very similar fermiology is also found in $PdRhO_2$ [18, 19].

1.1.4. The antiferromagnetic metal $PdCrO_2$

The basic ionic picture of $PdCrO_2$ is similar to that of $PdCoO_2$: Pd is in the 1+ valence state, making the Pd layers metallic (Figure 1.6a), while the valence of Cr is 3+. The electronic configuration of Cr^{3+} is $3d^3$, leaving the three t_{2g} orbitals half-filled. A simple charge counting argument would therefore suggest that the Cr layer is also metallic, as seen in the DFT calculations of Ref. [20]. This is, however, not the case in reality because the on-site Coulomb repulsion introduces a large energetic cost for double occupancy of the individual orbitals, favouring electron localisation. If the three Cr electrons in the three t_{2g} orbitals all assume the same spin state, as sketched in Figure 1.6b, double occupancy is prevented by the Pauli principle. Because of this, the Cr layer becomes a correlated insulator, i.e. a Mott insulator, with a localised spin of $S = 3/2$ per Cr site. Those localised spins order antiferromagnetically below $T_N = 37.5\,\mathrm{K}$, as indicated by the measurements of magnetisation and heat capacity [21–23]. A more direct confirmation of the magnetic ordering is obtained through neutron scattering [24, 25], clearly showing magnetic Bragg peaks whose intensity increases below T_N (Figure 1.6c). The wavevectors of the magnetic Bragg peaks show that the in-plane magnetic order corresponds to a 120° antiferromagnetic spin structure, increasing the real space unit cell three times, as sketched in Figure 1.6d. Each localised spin assumes one of three directions, labelled 1, 2 and 3 in Figure 1.6d, with a 120° angle between each pair of spins. The direction of the spins with

respect to the crystalline axes, and in particular its variation between different Pd layers, has not been uniquely determined to date. In Reference [25] two models consistent with the neutron scattering data are proposed, both suggesting that the three spins lie in a plane containing the crystalline c axis, but the details of the layer-to-layer variation of the spin direction are model-dependent.

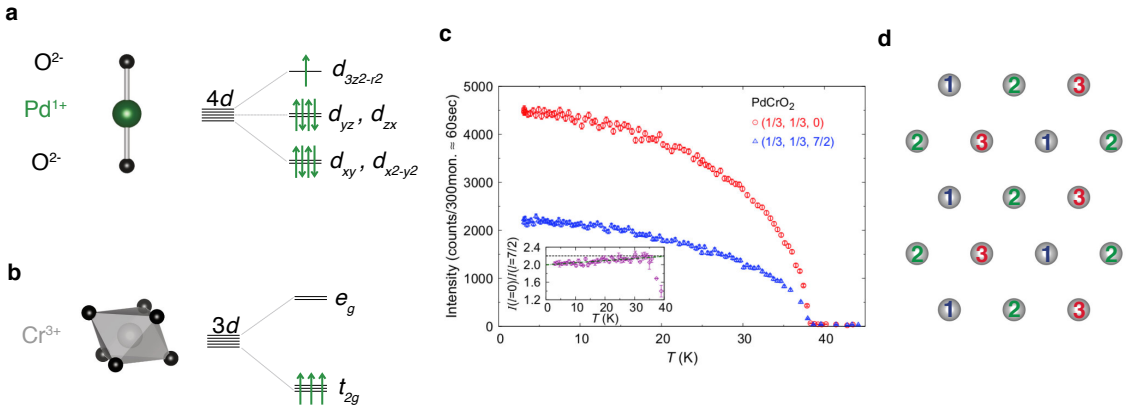

Figure 1.6.: The crystal field diagrams on the (**a**) A and (**b**) B site of $PdCrO_2$. The strong on-site correlations lead to the formation of localised spins S=3/2 on the Cr sites. (**c**) The localised spins order antiferromagnetically, with $T_N = 37\,\mathrm{K}$, as shown by the temperature dependence of the intensity of the corresponding magnetic Bragg peak. Reproduced with permission from Ref. [25]. (**d**) The Cr plane. The three directions the localised Cr spins can take are labelled 1, 2 and 3. The directions of the spins with respect to the crystalline axis cannot be unambiguously determined from the available data [25].

Irrespective of the details of the magnetic structure, it is clear that $PdCrO_2$ consists of alternating metallic and antiferromagnetic Mott insulating layers, both on a triangular lattice. The close proximity of such different electronic systems naturally leads to questions about their interaction. If the layers were entirely decoupled, the behaviour of the metallic layers would not be affected by the transition to the antiferromagnetic sate. This is not the case, as can easily be seen in the resistivity measurements, which show an unambiguous discontinuity at the Néel temperature (Figure 1.7a), most evident in the first derivative (bottom panel of Figure 1.7a). While proving the existence of some coupling between the magnetism and the metallic states, this observation does not offer direct insight into its nature.

The Fermi surface of $PdCrO_2$ was probed by quantum oscillations by Ok et al.

and Hicks et al. [26, 27]. Their results were consistent, and could be explained by the hypothesis that the Fermi surface of $PdCrO_2$ in the absence of the antiferromagnetic order is very similar to that of $PdCoO_2$. In the antiferromagnetic phase this $PdCoO_2$ - like Fermi surface reconstructs across the boundary of the magnetic Brillouin zone, as shown schematically in Figure 1.7a, leading to the observed quantum oscillation frequencies. This is precisely what would be expected if $PdCoO_2$ was placed in a weak periodic potential, whose periodicity corresponds to that of the Cr-site antiferromagnetism.

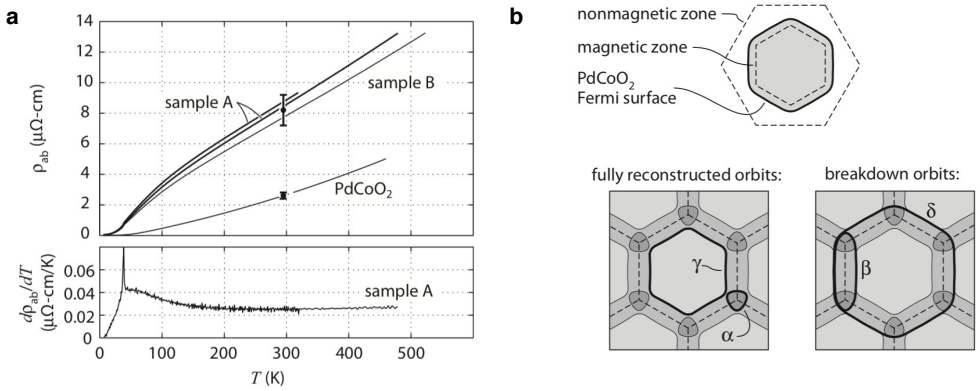

Figure 1.7.: (**a**) 2D model of the Fermi surface reconstruction. (**b**) The temperature dependent resistivity of $PdCrO_2$ (top panel), along with its derivative (bottom panel). The figures are reproduced with permission from Ref. [27].

Quantum oscillation measurements are, however, not sensitive to the in-plane shape of the Fermi surface, and are in practice limited to temperatures below the antiferromagnetic transition in $PdCrO_2$. Angle resolved photoemission measurements by Sobota et al. [28] confirmed that the $PdCrO_2$ Fermi surface is of hexagonal shape, very similar to that of $PdCoO_2$ (Figure 1.8a), both below and above the antiferromagnetic transition. However, they observed no reconstruction due to the antiferromagnetic order, and they speculated that the discrepancy with the quantum oscillations could be a consequence of the inherent surface sensitivity of ARPES. In contrast, a later measurement by Noh et al. [7] did show the electronic structure reconstruction consistent with the quantum oscillations (Figure 1.8b). What is more, at a temperature of 100 K, considerably higher than the Néel temperature of 37.5 K, the reconstructed bands were not visible anymore, and the Fermi surface resembled

the one of $PdCoO_2$. Noh et al. performed their measurements at a different photon energy to the one used by Sobota et al., and assumed that this was the reason for the inconsistency between the two ARPES experiments. We were also able to observe the apparent reconstruction of the electronic structure, but have shown how it is in fact not a consequence of the periodic potential caused by the Cr spins, but rather a more subtle consequence of the coupling between itinerant and Mott insulating states [8]. This will be described in detail in Chapter 5.

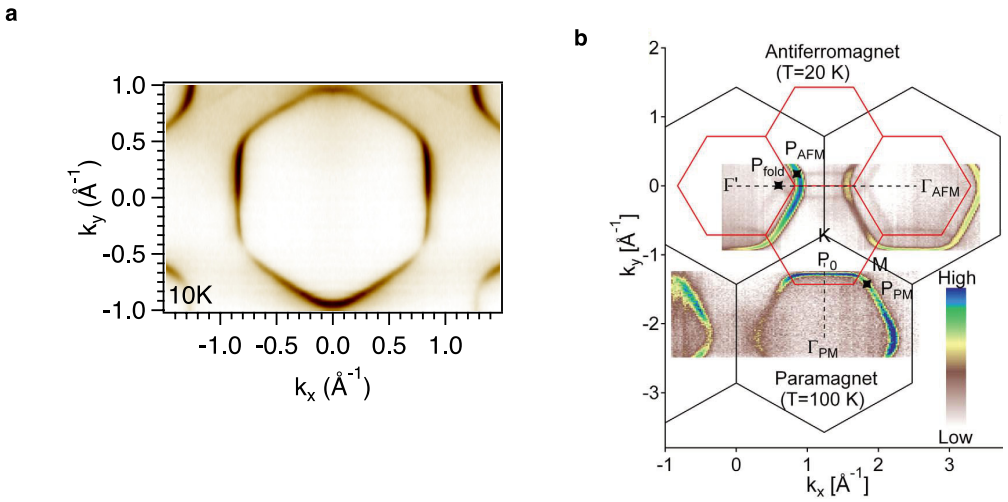

Figure 1.8.: The in-plane bulk Fermi surface of $PdCrO_2$measured by angles resolved photoemission, measured by (**a**) Sobota et al. [28], and (**b**) Noh et al. [7]. Figures reproduced with permission from the corresponding references.

1.2. Surface states

As already mentioned, ARPES can typically probe only a depth of $\sim 5\,\text{Å}$ below the surface of a crystal. If we are interested in the study of the bulk electronic structure, the surface sensitivity poses an immediate problem. The basic concepts used to describe the electronic structure of periodic solids, such as the Brillouin zone, band structure or the Fermi surface, rely on the underlying periodicity. However, at the surface of a crystal the periodicity in the direction perpendicular to the surface is necessarily broken. Since the experiment is not sensitive to a depth significantly larger than the interatomic spacing, it is not justified to assume a priori that a qua-

siparticle spectrum measured by ARPES is a bulk property of the material. There are, however, several ways to check the origin of the measured spectra. For instance, if the photoemission measurements are consistent with the bulk-sensitive quantum oscillation measurements, or the calculations of the bulk electronic structure, we can be confident that they are sensitive to the bulk. This is the case with the $PdCoO_2$ and $PdCrO_2$ Fermi surfaces discussed above, and is in fact common, especially in layered materials. Conversely, if the measured spectra are very sensitive to surface purity, they are likely to originate from the surface. The states localised in the vicinity of a surface are often interesting in their own right; the surface sensitivity of ARPES makes it an ideal technique to study their properties.

Topological surface states are a prominent example of such states, arising on the surfaces of materials which have a topological invariant different to that of vacuum. As they arise as a consequence of the bulk property of the solid, they appear regardless of the details of the surface structure. In contrast, there are other types of surface states which arise precisely because of the specific structure and composition of a surface. This is similar to how the bulk electronic structure is governed by the bulk crystal structure, and the composition of a material. Consequently, the surface states can exhibit a range of properties as wide as that of the bulk electronic states of three-dimensional crystals. The single feature all surface states have in common is their high degree of anisotropy; while they are delocalised Bloch states in the plane parallel to the surface, their wavefunctions exponentially decay perpendicular to it. The degree of the localisation depends on the system, and varies between a single atomic layer and tens of them. An introduction to the physics of surface states, as well as many prominent examples, are given in Reference [29]. I will not reproduce these general considerations here, but rather concentrate on the specific cases of the surface states found in delafossite oxides.

1.2.1. Surface states on delafossite oxides

Due to the layered nature of the delafossite structure, the crystals are most likely to cleave between the oxygen and the A- site ion, in principle yielding oxygen and A-site terminated surfaces with equal probability. Because of the strong bonding within the transition metal oxide layer, I will refer to the oxygen termination as the transition metal oxide termination. The schematic representations of the two ter-

minations expected in $PdCoO_2$ are shown in Figures 1.9(a, b). As discussed above, the bulk electronic structure of delafossites is highly anisotropic, and the properties of individual layers deduced from ionic arguments offer considerable insight into the behaviour of the material as a whole. Therefore, a reasonable first step towards understanding the electronic structure of the two surface terminations is to consider how the charge of individual layers is altered if they are found on a surface. In the bulk, the ionic charge of each ion is maintained by Pd 'donating' half an electron to the oxygen in the layer above it, and half an electron to the oxygen in the layer below it. This results in the total charge of $1+$ per formula unit in the Pd layers, and $1-$ in the CoO_2 layers. At the surface, however, such charge transfer cannot occur, as there is no layer above the surface layer. In the most simple picture this leads to an effective doping of the surface layers by half a carrier per unit cell, compared with their respective bulk charges. The CoO_2 layer is expected to be hole-doped, and the Pd layer electron-doped. Such self-doping at the polar surfaces necessarily leads to an electronic structure different to that of the bulk. It is important to note, however, that there is no a priori guarantee that the real surfaces can be appropriately described in this way. For instance, a surface structural reconstruction may significantly alter the electronic structure, or the excess charge may be shared across many layers. The true surface electronic structure therefore has to be determined experimentally, and compared to model predictions for 'slabs' including the surface in question.

Kim et al. [9] performed such density functional theory calculations for the two surface terminations of $PdCoO_2$, as well as for the bulk electronic structure. They allowed for the surface structure to relax, and they found surface states consistent with the above ionic picture. In Figures 1.9(c, d) I show their results for the bulk band structure and the Fermi surface of $PdCoO_2$. Consistent with the discussion of Section 1.1.3, they find a single electron-like band crossing the Fermi level, forming a two-dimensional Fermi surface of a hexagonal cross-section. At the CoO_2 - terminated surface (Figures 1.9(e, f)) in addition to this bulk band they find two more bands crossing the Fermi level, forming two Fermi surfaces, one of which is of hexagonal and the other one of circular cross-section. The bands are hole-like around the Γ - point of the zone. The authors comment that those two bands are split by spin-orbit coupling, i.e. in the absence of spin-orbit coupling there is only one surface band crossing the Fermi level. The appearance of metallic states in the

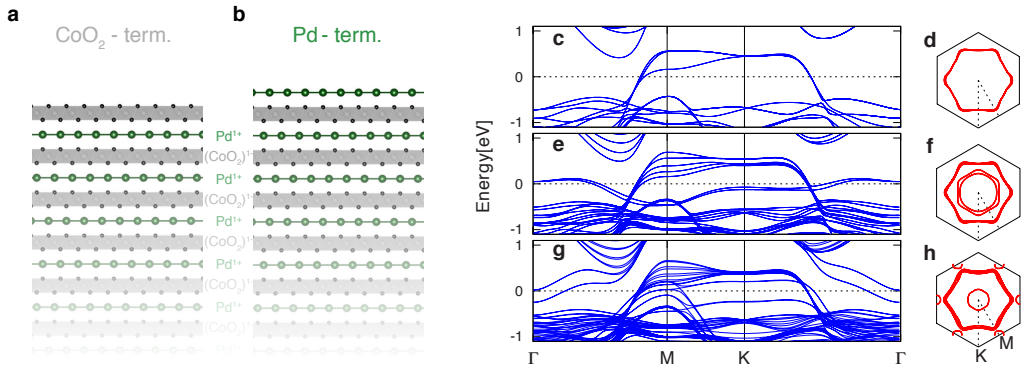

Figure 1.9.: Two surface terminations in $PdCoO_2$: (**a**) The CoO_2 - terminated surface, and the (**b**) Pd - terminated surface. Calculated (**c**, **g**, **e**) band structure and (**d**, **f**, **h**) Fermi surfaces of the (**c**, **d**) bulk $PdCoO_2$, (**e**, **f**) the CoO_2 and (**g**, **h**) the Pd - terminated surface of $PdCoO_2$. Panels c - h reproduced with permission from Ref. [9].

surface CoO_2 layer is consistent with the ionic picture: if the CoO_2 layer is hole-doped with respect to the bulk, the t_{2g} orbitals are not fully occupied, and the layer is metallic. An equivalent logic would suggest the electron-doped Pd-terminated surface should also host states different to those of the bulk, in order to accommodate the excess charge. This is indeed the case in the calculation (Figures 1.9(g, h)): in addition to the bulk band crossing the Fermi level, there is another band dispersing parallel to it. The Fermi surfaces formed by the bulk and the surface band are very similar, and are not easy to distinguish in Figure 1.9h. Additionally, the surface calculation shows a fully occupied flat band in the vicinity of the K point (Figure 1.9g). Those two bands, the fully occupied one and the dispersive one forming a hexagonal Fermi surface, are an exchange-split pair. Another exchange-split pair is found at the Γ point. One of the bands crosses the Fermi level, forming a circular Fermi surface pocket around it, while the other one remains unoccupied, just above the Fermi level. What is more, the calculation shows small Fermi surface pockets around the M point of the zone. Prior to the work done as a part of this thesis, surface states consistent with the above calculations were observed on the CoO_2 - terminated surface of $PdCoO_2$ [12]. The measurement (Figure 1.10a) clearly shows both the bulk Fermi surface and the two surface Fermi surfaces, consistent with the calculation shown in Figure 1.9f. No states reminiscent of the ones cal-

culated for the Pd - terminated surface were observed in $PdCoO_2$, although very similar states were observed in $PdCrO_2$ [28]. The measurements (Figure 1.10b) show two hexagonal Fermi surfaces very close to each other, and additional weight around the centre of the zone. This is consistent with the Fermi surface calculated for the Pd - terminated surface of $PdCoO_2$, although no Fermi surface pockets are observed around the M point. This suggests that the Pd - terminated surface of $PdCrO_2$ supports the same surface states as that of $PdCoO_2$.

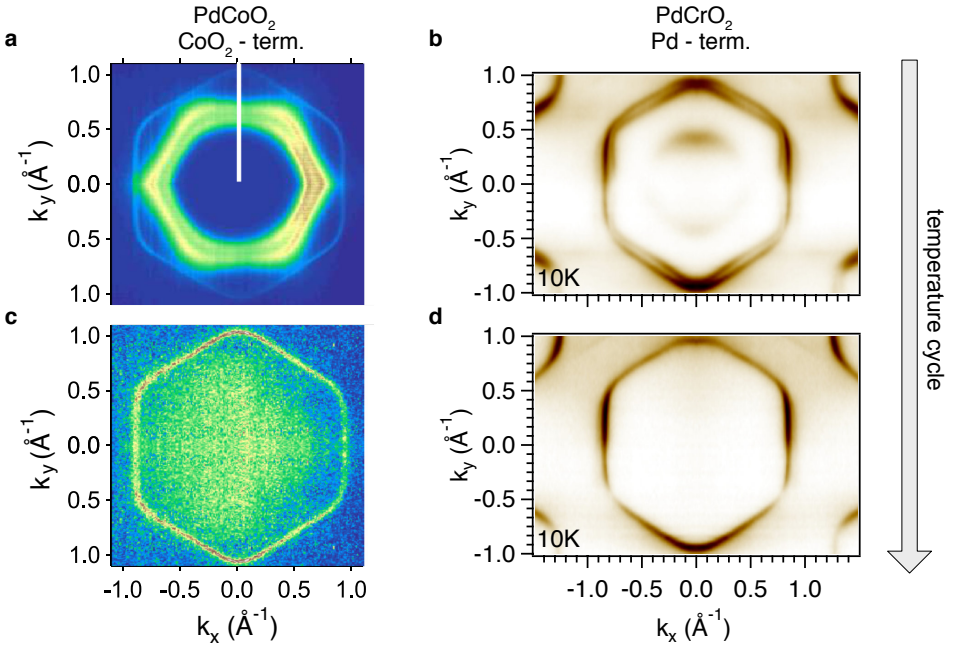

Figure 1.10.: A Fermi surface measured before thermal cycling (**a**) on $PdCoO_2$, showing the bulk Fermi surface and the states originating from the CoO_2surface and (**b**) $PdCrO_2$, showing the bulk Fermi surface and the states originating from the Pd surface. (**c, d**) After thermal cycling only the bulk states remain. Panels (a, c) and (b, d) are reproduced with permission from [12] and [28], respectively.

In both cases the surface derived nature of the states was confirmed by thermal cycling. This entails warming up the sample manipulator, leading to the desorption of the residual gases that have been absorbed on it. In particular, outgassing of hydrogen occurs at $\sim 17\,\mathrm{K}$, which can usually be noticed via an increase of the chamber pressure. As the manipulator is subsequently cooled down, the gases are re-adsorbed on the cold surfaces, including the sample surface. If the observed electronic states

are localised at the surface and are sensitive to its purity, this procedure can often passivate them. On the other hand, the bulk states originating from deeper layers in the sample are not expected to be significantly affected, although the data quality may be reduced due to surface scattering. In both reported cases of the surface states on delafossite oxide metals the surface states were removed by the thermal cycling [12, 28], leaving a well-defined hexagonal Fermi surface originating from the bulk electronic structure (Figure 1.10(c, d)).

1.3. Organisation of the thesis

In the remainder of the thesis, my goal is first to give the required theoretical and experimental background, and then describe the three main projects that comprise the results that I report. Chapter 2 is dedicated to a description of angle resolved photoemission spectroscopy, both from the theoretical and experimental point of view. In order to appreciate the range of information that can be accessed by ARPES experiments it is necessary to have a basic understanding of the phenomenology of many-body interactions. A simple introduction to Green's functions and self-energy formalism is therefore also given. The experimental section includes a general overview of synchrotron photoemission, with a special emphasis on the aspects relevant specifically for delafossites. Different surface terminations found on delafossites are also discussed.

Our photoemission measurements motivated both minimal tight-binding models and density functional theory calculations, the results of which I describe alongside the corresponding data throughout the thesis. The physics underlying those theoretical methods is given in Chapter 3.

Chapters 4 - 6 contain the main results of the thesis. In Chapter 4 I discuss our experimental results on the bulk electronic structure of $PtCoO_2$ and $PdCoO_2$. I compare them to de Haas van Alphen measurements, and analyse the dispersions for signatures of many-body interactions. In Chapter 5 I show our results on $PdCrO_2$, and tell the story of how careful thought about the physics behind an unusual spectroscopic signal led us to the understanding of its origin. This required a many - body calculation, performed by our theoretical collaborators Sota Kitamura and Takashi Oka, which I also outline. Chapter 6 is dedicated to the discussion of surface states originating from the transition metal oxide surfaces of delafossites, in which

we recognised an unusually large spin-splitting. In addition to the experimental results, first principles calculations and tight binding models were needed to reach a full understanding of the phenomenon, so I describe the results of these where appropriate. Our experimental results motivated me to revisit the basic physics behind spin-splitting in band structures, a description of which is also included in Chapter 6.

In addition to the surface states originating from the CoO_2 - terminated surfaces of $PdCoO_2$, we were also able to observe those originating from its Pd - terminated surface. Although I participated in the measurements and discussions of these states, the majority of the analysis was done by Federico Mazzola. I will therefore not describe this work at the same level of detail as that devoted to the other observed features, but I will summarise its main conclusions in Appendix B for completeness. Our findings are reported in Reference [10].

2. Angle resolved photoemission

Photoemission spectroscopies are experimental techniques based on the photoelectric effect, first observed by Heinrich Hertz in 1887 [30]. When light of sufficiently high frequency ν irradiates a metal, electrons with a maximum kinetic energy of $E_K^{max} = h\nu - W$, where W is the material work function, can be extracted. Einstein was awarded the Nobel prize for his explanation of the effect, which relies on the wave-particle duality of light. The same basic process is used in modern experiments to gain insight into the electronic structure of solids. The current of photoelectrons is related to the electronic density of states; the larger the number of electrons that leave a sample with a given kinetic energy, the larger is the density of states at the corresponding binding energy. Measuring the angular distribution of the outgoing electrons yields information on their crystal momentum. Combined with the binding energy measurement, this allows the determination of the quasiparticle spectrum, i.e. the non-interacting band structure and the relevant many-body renormalisations. This is crucial for understanding most properties of solids, making angle resolved photoemission spectroscopy (ARPES) an invaluable tool in the study of new materials.

In this chapter I will give an overview of the theoretical and experimental aspects of angle resolved photoemission spectroscopy. In addition to the basics relevant for every ARPES experiment, I will concentrate on those points which are needed to understand our experiments on delafossites. References [30–33] offer comprehensive reviews of photoemission as a technique, and I refer to them throughout the chapter.

2.1. Kinetics of photoemission

When light irradiates a surface, photoexcited electrons leave the material, as shown in Figure 2.1a. Their kinetic energy is determined by the photon energy $h\nu$, reduced by the sample work function W and the binding energy E_B that they had inside the solid,

$$E_K = h\nu - |E_B| - W. \tag{2.1}$$

The outgoing electrons are free, so their momentum $\vec{p}$ and kinetic energy E_k are related in the usual way, $|\vec{p}| = \sqrt{2m_e E_K}$. Their kinetic energy is measured using a hemispherical analyser, as will be described in more detail in Section 2.6.3. Crucially, the position of the detector in the outgoing cone specifies the direction of the measured electron momentum; only electrons traveling directly towards the detector can be analysed (Figure 2.1b), enabling the simultaneous measurement of the kinetic energy and vector momentum of the photoemitted electrons.

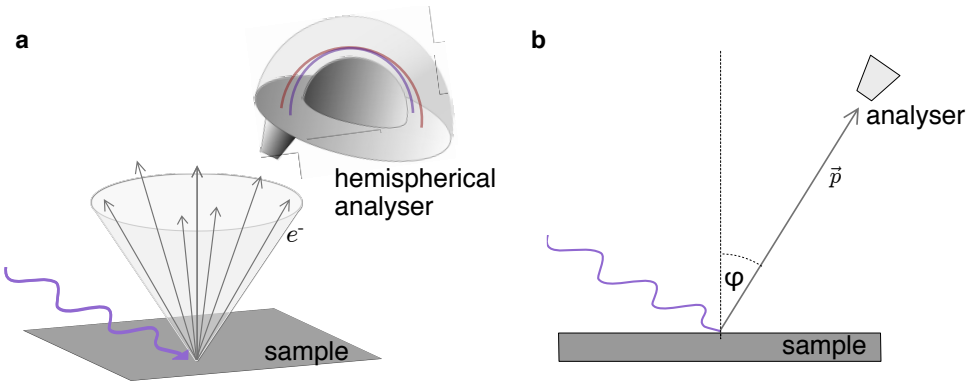

Figure 2.1.: Schematic of the ARPES experiment, (**a**) in 3D and (**b**) in the scattering plane.

Momentum parallel to the surface is conserved in the photoemission process up to a reciprocal lattice vector:

$$\vec{p}_{||} = \hbar\vec{k}_{||} + \vec{p}_{\nu||} + \vec{G}_{||}, \tag{2.2}$$

where $p_{||}$ and $\hbar k_{||}$ are momenta of the electron in vacuum and in the solid, respectively, $p_\nu = \frac{h\nu}{c}$ is the photon momentum, and $\vec{G}_{||}$ the reciprocal lattice vector. In the photon energy range used in standard photoemission (10-100eV) the photon

momentum is 0.5-5% of a typical Brillouin zone, and is usually neglected [32]. The crystal momentum parallel to the surface is therefore related to the measured kinetic energy E_K and the emission angle φ as:

$$\hbar k_{||} = \sqrt{2mE_K} \sin(\varphi), \tag{2.3}$$

with φ measured from the normal of the sample surface (Figure 2.1b). The momentum resolution depends on the kinetic energy as $\Delta k_{||} = \sqrt{2mE_K} \cos(\varphi) \Delta\varphi$; the best resolution is therefore obtained at low photon energies. Using relations 2.1 - 2.3 both the binding energy ($|E_B|$) and the in-plane momentum ($k_{||}$) can be directly related to the measurable quantities (E_K and φ), in principle allowing the determination of the dependence of $|E_B|$ on $k_{||}$, i.e. the in-plane quasiparticle spectrum.

In contrast, the out-of-plane momentum, k_z, cannot be determined directly from the measured quantities. The value of k_z that is probed in an experiment depends on the photon energy used; the reasons for this are outlined in Appendix A. Consequently, some conclusions about the out-of-plane spectrum can be drawn from photon energy dependent measurements. In particular, if the measured in-plane spectra show no photon-energy dependence, the out-of-plane dispersion is small, and the electronic structure two-dimensional within the experimental resolution. ARPES is, however, not the ideal technique to study the k_z dispersion for a few reasons. As already mentioned, k_z cannot be determined from measurable quantities alone, without additional assumptions (Appendix A). Furthermore, the out-of-plane momentum is not conserved as the electron leaves the material because of the potential step at the surface. However, probably the biggest issue is the surface sensitivity of photoemission. The electrons scatter on their way to the surface, with an inelastic mean free path of $l_{mfp} \sim 5\,\text{Å}$ at photon energies typically used for photoemission (Figure 2.2). Such a short effective depth means that the out-of-plane momentum is defined only within an uncertainty of $\Delta k_z \sim 1/l_{mfp} = 0.2\,\text{Å}^{-1}$, which is not negligible compared to the Brillouin zone size.

The finite probing depth also has consequences for the measurement of the in-plane quasiparticle spectra. As the out-of-plane momentum is defined only with the precision given by Δk_z , each measurement in fact probes a range of out-of-plane momenta of width Δk_z around the mean k_z, determined by the photon energy. Hence, if the binding energy of the observed state changes significantly within Δk_z,

the signal will be broadened. This effect, called k_z - broadening, is the fundamental reason ARPES is best suited for the study of two-dimensional band structures. As will become clear in the rest of the thesis, the conduction bands in delafossite oxides are two-dimensional within the experimental resolution, making them ideal systems for ARPES studies.

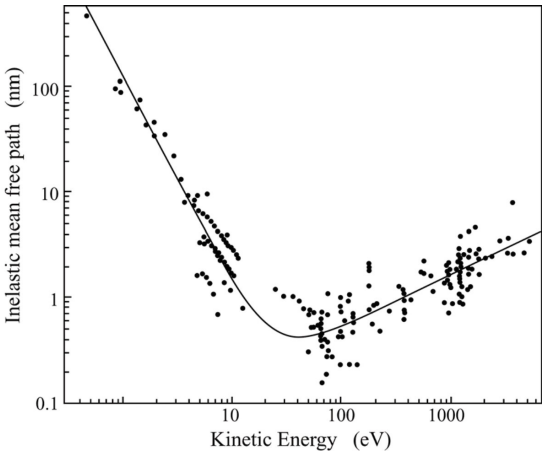

Figure 2.2.: Kinetic energy dependence of the 'universal' mean free path for excited electrons in solids. Reproduced with permission from Reference [33], after the data from Reference [34].

2.2. The three step model

While the simplified picture of photoemission used in the last section is sufficient to relate the measured quantities to the quasiparticle binding energy and the in-plane momentum, the full power of the technique can be understood only when it is treated as a quantum problem describing the transition between the initial and final state wavefunctions [30–33]. The initial state wave function Ψ_i^N is the ground state of the many-body Hamiltonian describing the semi-infinite crystal. The final state Ψ_f^N is an excited state of the same Hamiltonian, comprising an ionised crystal and a single electron state which is free-electron-like in vacuum, with a finite weight near the surface of the crystal. The transition between them is enabled by the interaction of the incident light with the material, described by the light-matter

interaction Hamiltonian, H_{int}. It is given by the minimal coupling, i.e. replacing the momentum operator $\vec{p}$ with $\vec{p} - \frac{e}{c}\vec{A}$, where $\vec{A}$ is the vector potential. Unless very high intensities are used it is sufficient to keep only terms linear in $\vec{A}$, giving the interaction Hamiltonian:

$$H_{int} = -\frac{e}{2mc}\left(\vec{p}\cdot\vec{A} + \vec{A}\cdot\vec{p}\right) = -\frac{e}{mc}\vec{p}\cdot\vec{A} + \frac{e}{2mc}\left[\vec{p},\vec{A}\right]. \tag{2.4}$$

The commutator $\left[\vec{p},\vec{A}\right]$ is proportional to $\nabla\vec{A}$, and can be neglected as long as the vector potential changes slowly at atomic length scales. The wavelength at the photoemission photon energies is in the $120 - 1200\,\text{Å}$ range, much larger than interatomic separations, so this so-called dipole approximation is valid. Using these wavefunctions and the interaction Hamiltonian, the photoemission probability can be calculated using Fermi's golden rule,

$$w_{if} = \frac{2\pi}{\hbar}\left|\left\langle \Psi_f^N \left| H_{int} \right| \Psi_i^N \right\rangle\right|^2 \delta\left(E_f^N - E_i^N - h\nu\right), \tag{2.5}$$

where E_i^N and E_f^N denote the initial and final state energies, respectively. This way of calculating the probability, called the one-step model, correctly treats photoemission as a single coherent quantum mechanical process, as illustrated in Figure 2.3a. The full one-step calculation has been successfully used in some cases, but it is often too complex to be useful to interpret experiments. A phenomenological model called the three-step model has been proven to be very successful, and is commonly used instead. The three steps of the model are described below, and illustrated in Figure 2.3b.

The first of the three steps is the optical excitation of an electron from an occupied Bloch state to a Bloch state which is unoccupied in equilibrium. The energy of the final state is determined by the photon energy; if it is high enough it is valid to think of it as a free-electron like state. This process is enabled by the light-matter interaction Hamiltonian, as is photoemission in the one-step model described above. In the second step the excited electron travels towards the surface. Its mean free path depends on its kinetic energy, as illustrated in Figure 2.2. The third step is the escape into vacuum, if the kinetic energy is high enough to overcome the work function. Once in vacuum, the electrons are truly free, so the classical kinetic arguments used to relate the measured kinetic energy to momentum (Section 2.1)

are always valid. The total photoemission probability is given by the product of the probabilities of the three individual steps, but the most relevant physical information is contained in the first step, the optical excitation, which I discuss in detail in the following section.

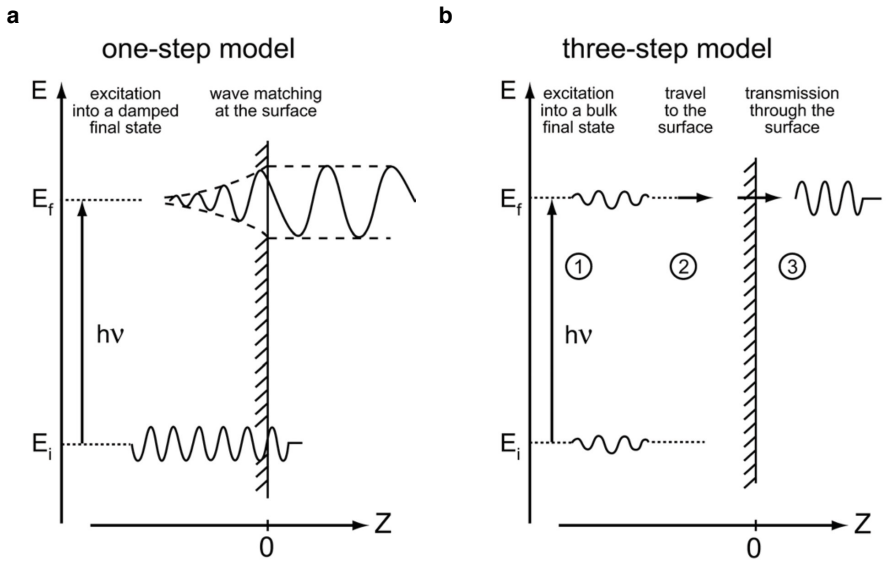

Figure 2.3.: Illustration of the (**a**) one-step model and (**b**) the three-step model of photoemission. Reproduced with permission from Reference [33], adapted from Ref. [30, 34].

2.3. ARPES in the sudden approximation

The probability of the optical excitation within the three step model is also given by Fermi's golden rule (equation 2.5), with the same initial state and the interaction Hamiltonian as in the one step model, but the final state $\Psi^N_{f,k}$ now consists of the $N-1$ bound electrons and one electron occupying a higher-energy Bloch state of the wave vector[1] $\vec{k}$. It is convenient to factorise this wave function into a part representing the leaving photoelectron, and a part representing the remaining system. Such a factorisation is justified only if it is reasonable to assume that the photoelectron does not interact with the system on its way to the surface, in the second step of

[1]In the following I will omit the vector symbol for simplicity, and write k instead of $\vec{k}$

the three step model. This assumption, called the sudden approximation, is never really valid in a semi-infinite crystal; as the scattering cross-section decreases the mean free path increases, leaving the number of scattering events approximately constant [35]. However, at high enough photon energies the inelastically scattered electrons contribute to the spectrum as a featureless background which can be subtracted. The physically significant features can then be interpreted assuming that the photoelectron leaves the sample suddenly, and does not interact with the remaining system. It has been shown that this approach is valid at energies as low as 20 eV in cuprates [32], and it is implicitly used in the interpretation of virtually all photoemission experiments.

Within the sudden approximation the final state wave function can be expressed as the product of the photoelectron Bloch state $|\varphi_{f,k}\rangle$ and the remaining $N-1$ body wave function,

$$\left|\Psi^N_{f,k}\right\rangle = \mathcal{A}\left|\varphi_{f,k}\right\rangle \left|\Psi^{N-1}_m\right\rangle, \tag{2.6}$$

where $\mathcal{A}$ is an antisymmetrisation operator ensuring that the N - electron wave function obeys the Pauli principle. The index m labels an eigenstate of the $N-1$ electron problem. In a general case the remaining system is left in a superposition of excited states, so the total excitation probability is given by a sum over all eigenstates m. In a similar fashion the initial state wave function $\left|\Psi^N_i\right\rangle$ can be formally factorised in the part corresponding to a single occupied Bloch state $|\varphi_{i,k}\rangle$ and the part corresponding to the N particle ground state from which one electron has been extracted:

$$\left|\Psi^N_i\right\rangle = c^\dagger_k c_k \left|\Psi^N_i\right\rangle = \mathcal{A}\left|\varphi_{i,k}\right\rangle \cdot c_k \left|\Psi^N_i\right\rangle. \tag{2.7}$$

Using the factorised forms of the wave functions the probability of the photoexcitation of an electron with momentum k can be expressed as:

$$W^{PE}(k) = \frac{2\pi}{\hbar}\sum_{i,f}\left|M^k_{if}\right|^2 \sum_m \left|\left\langle \Psi^{N-1}_{f,m}\left|c_k\right|\Psi^N_i\right\rangle\right|^2 \delta\left(E^N_i - E^{N-1}_m + h\nu - E_{f,k}\right), \tag{2.8}$$

with $M^k_{if} = \frac{e}{mc}\left\langle \varphi_{f,k}\left|\vec{A}\cdot\vec{p}\right|\varphi_{i,k}\right\rangle$. This expression determines the observable photoemission intensity, and is therefore important to understand in detail; its various factors are discussed separately below.

The matrix element

The one electron dipole matrix element, $M_{if}^{k} = \frac{e}{mc}\left\langle \varphi_{f,k} \left| \vec{A}\cdot\vec{p} \right| \varphi_{i,k} \right\rangle$, is a measure of the transition probability from the initially occupied single-particle state ($\varphi_{i,k}$) to the free-electron like final single-particle state ($\varphi_{f,k}$). The vector potential associated with monochromatic light is given by $\vec{A} = \exp\left(\imath\vec{k}\cdot\vec{r}\right)\hat{\varepsilon}$, where $\hat{\varepsilon}$ is the unit vector along the polarisation direction of the vector potential $\vec{A}$. The matrix element is therefore proportional to $M_{if}^{k} \sim \langle \varphi_{f,k} \left| \hat{\varepsilon}\cdot\vec{p} \right| \varphi_{i,k} \rangle$. It can also be expressed in terms of the position operator, using the position-momentum commutation relations. For momentum in the x direction:

$$\langle \varphi_{f,k} \left| p_x \right| \varphi_{i,k} \rangle = \imath\frac{m}{\hbar} \langle \varphi_{f,k} \left| [H,x] \right| \varphi_{i,k} \rangle = \imath\frac{m}{\hbar} \left(E_{f,k} - E_{i,k}\right) \langle \varphi_{f,k} \left| x \right| \varphi_{i,k} \rangle, \qquad (2.9)$$

where H is the Hamiltonian and $E_{i,k}$ and $E_{f,k}$ are the energies of the initial and final state, respectively. Similar expressions are of course valid for all directions in space, so the matrix element is proportional to $M_{if}^{k} \sim \langle \varphi_{f,k} \left| \hat{\varepsilon}\cdot\vec{r} \right| \varphi_{i,k} \rangle$, where $\vec{r}$ is the position operator. Both the momentum and position dependent forms of the matrix element are sometimes used in calculations. Regardless, the crucial point is that the matrix element introduces the photon energy, polarisation and geometry dependence of the measured intensity. Although these variations sometimes complicate the interpretation of photoemission experiments, they can also contain valuable information on the initial state wave function, as discussed in References [32, 36]. In particular, performing the same measurements with different light polarisations can reveal the symmetry of the initial one-electron state, $\varphi_{i,k}$. In Section 5.2 I will discuss, in the context of our measurements on $PdCrO_2$, how the matrix elements can be thought of as a Fourier transform of the initial state wave function. In practice, if we are not interested in explicitly studying the matrix element effects, we choose the photon energy, polarisation and geometry under which the matrix elements for photoemission from relevant states are most favourable at the beginning of a new measurement, and perform all subsequent measurements in those conditions.

The spectral function

The delta function in equation 2.8, $\delta\left(E_i^N - E_m^{N-1} + h\nu - E_{f,k}\right)$, ensures that the energy conservation is properly taken into account. $E_{f,k}$ is the kinetic energy of the excited photoelectron before leaving the solid; the measured kinetic energy is reduced by the work function, $E_K = E_{f,k} - W$. E_m^{N-1} and E_i^N are the energies of the m-th eigenstate of the $N-1$ particle problem, and of the N particle ground state, respectively. Introducing symbols $\omega = E_{f,k} - h\nu$ and $\omega_m^{N-1} = E_i^N - E_m^{N-1}$, corresponding, respectively, to the total energy the solid loses when an electron is extracted and the energy difference between the N particle ground state and the $N-1$ particle excited state, the delta function is reduced to $\delta\left(\omega - \omega_m^{N-1}\right)$. Using this notation, the second sum in equation 2.8 can be expressed as:

$$A^-(k,\omega) = \sum_m \left|\left\langle \Psi_{f,m}^{N-1} \left| c_k \right| \Psi_i^N \right\rangle\right|^2 \delta\left(\omega - \omega_m^{N-1}\right). \tag{2.10}$$

$A^-(k,\omega)$ is the so called one electron removal spectral function [32], proportional to the probability that an electron state with momentum k and binding energy ω is occupied in the initial many particle ground state Ψ_i^N. The total photoemission probability (equation 2.8) can be interpreted as the product of the probability that an electron with momentum k and energy ω exists in the original ground state ($A^-(k,\omega)$), and that, if it exists, is photoexcited and detected in the specified experimental conditions ($\left|M_{if}^k\right|^2$).

It should be mentioned for completeness that inverse photoemission, where an electron is added to the system, is also possible. The probability of adding an electron with momentum k and energy ω is given by the electron addition spectral function, $A^+(k,\omega)$, which can be calculated in direct analogy with $A^-(k,\omega)$:

$$A^+(k,\omega) = \sum_m \left|\left\langle \Psi_{f,m}^{N+1} \left| c_k^\dagger \right| \Psi_i^N \right\rangle\right|^2 \delta\left(\omega - \omega_m^{N+1}\right). \tag{2.11}$$

The total probability of adding or removing an electron is equal to the sum of the addition and removal spectral functions,

$$A(k,\omega) = A^-(k,\omega) + A^+(k,\omega). \tag{2.12}$$

In the ground state all negative energy states are occupied, and all positive energy

states are empty. Consequently, an added (removed) electron always has positive (negative) energy, i.e. $A^{+}(k,\omega)$ ($A^{-}(k,\omega)$) is non-zero only for positive (negative) ω. Thus, the $\omega > 0$ part of the spectral function describes electron addition, and the $\omega < 0$ part describes the hole addition. The full spectral function can be thought of as the density of one electron states.

2.4. Probe of band structure and many-body interactions

It is now clear how the photoemission signal can be related to the distribution of electrons in a solid as a function of their momentum and energy, i.e. the one electron removal spectral function. In this section I will discuss how the spectral function is directly related to the full interacting Green's function, enabling the extraction of many-body parameters from an ARPES experiment. After the general discussion presented here, I will in Section 2.5 give a few concrete examples to illustrate this point, by simulating the spectral function of a free electron gas, as well as that of Fermi liquids with electron-electron and electron-phonon interactions.

2.4.1. Green's functions

Green's functions can be defined in various ways appropriate for addressing different questions. The *causal* Green's function, which can most directly be related to photoemission experiments, is defined as

$$\widetilde{G}_0(r,t) = \begin{cases} -\imath \left\langle 0 \left| c(r,t)\, c^{\dagger}(0,0) \right| 0 \right\rangle & t > 0 \\ \imath \left\langle 0 \left| c^{\dagger}(0,0)\, c(r,t) \right| 0 \right\rangle & t < 0 \end{cases}, \tag{2.13}$$

where $c(r,t)$ and $c^{\dagger}(r,t)$ are the electron annihilation and creation operators, respectively [37]. The interpretation of equation 2.13 is straightforward: the first line corresponds to the probability amplitude that an electron created at time 0 at the origin is found at position r after a time t has passed, while the second line is the probability amplitude that a hole created at r at a time $-|t|$ is found at the origin a time t after creation. It is a compact way of describing the propagation of both electrons and holes in a single function, where negative times refer to hole creation and

positive to electron creation. The sign difference between the two lines in equation 2.13 is a consequence of the Fermi statistics.

As it is often more useful to consider the momentum and energy of an electron, rather than its position at a certain time, the Fourier transform of the Green's function, $G_0(k,\omega)$, should be found. However, if $\widetilde{G}_0(r,t)$ is calculated explicitly using the standard form of the time-dependent creation and annihilation operators, $c(r,t) \sim \sum_k c_k \exp(\imath(kr - \varepsilon(k)t))$, the Fourier transform integral diverges. This is a consequence of the unphysical assumption that the single electron levels are completely non-interacting. A particle placed in such a level stays in it forever, and can be extracted with unit probability at all later times, causing the divergence. As perfect decoupling is never possible, it is justified to add a small damping factor δ to the time dependence of the operators: $c(r,t) \sim \sum_k c_k \exp(\imath(kr - \varepsilon(k)t + \imath\delta))$. The integral is now well-behaved, and the Green's function in momentum space is given by

$$G_0(k,\omega) = \frac{1}{\omega - \varepsilon(k) + \operatorname{sign}\varepsilon(k)\,\imath\delta}. \tag{2.14}$$

The sign in front of the $\imath\delta$ term is different for electron ($\varepsilon(k) < 0$) and hole states ($\varepsilon(k) > 0$), reflecting the sign difference of the probability amplitude for electron and hole addition in equation 2.13. The poles of the Green's function correspond to the energies of particles $\varepsilon(k)$, i.e. they are given by the spectrum of the Hamiltonian describing the system. This remains true even in the interacting case, and is one of the reasons Green's functions are so useful. It can be shown that the real part of the pole describes the energy and the imaginary part the inverse lifetime of a (quasi)particle. In the noninteracting case $\delta \to 0$, so the lifetime is infinite, as it should be [37].

An interacting electron can be thought of as a free electron which can be found in a continuum of energy states, ω', with varying probabilities. As discussed in section 2.3, the probability of finding an electron, or a hole, of momentum k and energy ω' is equal to the spectral function $A(k,\omega')$ (equation 2.12). The Green's function of an electron in an interacting system can then be expressed as an integral of the non-interacting Green's function over all the energies an electron might have in the interacting case, weighted by the spectral function:

$$G(k,\omega) = \int_{-\infty}^{\infty} \frac{A(k,\omega')}{\omega - \omega' + \imath\omega'\delta} d\omega', \tag{2.15}$$

where ω' is multiplying the imaginary δ in order to keep the sign consistent with equation 2.14. This intuitively appealing expression for the interacting Green's function can be proven to be rigorously true, thus showing the relationship between the one electron spectral function measured in photoemission and the full interacting Green's function [37]. What is more, it is easy to show that the equation 2.15 is mathematically equivalent to stating that the spectral function is proportional to the imaginary part of the Green's function,

$$A(k,\omega) = -\frac{1}{\pi}\operatorname{sign}\omega \operatorname{Im} G(k,\omega). \tag{2.16}$$

In other words, if it is possible to calculate the interacting Green's function, it is trivial to obtain the spectral function, which is the quantity measured by photoemission.

2.4.2. Self-energy

The interacting Green's function is typically calculated using perturbation theory, with approximations appropriate for a specific case. In general, it takes the following form:

$$G(k,\omega) = \frac{1}{\omega - \varepsilon(k) - \Sigma'(k,\omega) - \imath\Sigma''(k,\omega)}, \tag{2.17}$$

where $\varepsilon(k)$ is the bare band dispersion of the non-interacting system, and $\Sigma(k,\omega) = \Sigma'(k,\omega) + \imath\Sigma''(k,\omega)$ the so-called self-energy. It is difficult to calculate for a specific material, but it is straightforward to interpret. The real part of the self-energy encodes information on the change of energy of single particle states due to interactions, while the imaginary part corresponds to the energy uncertainty of the state in the interacting case, i.e. the inverse quasiparticle lifetime.

Observable quasiparticle properties can be related to the self-energy. For example, the effective mass m^* is defined by the relation $m^* v_F = \hbar k_F$, where k_F stands for the Fermi vector, and v_F for the Fermi velocity, defined as the slope of the dispersion at the Fermi level, $v_F = \frac{1}{\hbar}\frac{d\varepsilon^*(k)}{dk}\Big|_{k_F}$. The renormalised band $\varepsilon^*(k)$ is given by the sum of the non-interacting bare band, and the real part of the self-energy, $\varepsilon^*(k) = \varepsilon(k) + \Sigma'(k,\omega)$. It is straightforward to show that the effective

mass is equal to

$$\frac{1}{m^*} = \frac{1}{m} + \frac{1}{\hbar^2 k_F} \left(\frac{d\Sigma'}{dk} + \left. \frac{d\Sigma'}{d\omega} \right|_{\omega=\varepsilon^*(k)} \frac{d\varepsilon^*(k)}{dk} \right) \Bigg|_{k_F}, \tag{2.18}$$

where m is the noninteracting band mass. The momentum variation of the self-energy is typically much smaller than the energy variation, so the first term in the brackets is neglected [37]. This assumption does not have to hold in a general case, and can in principle be checked by photoemission. However, if the momentum variation is negligible, it is straightforward to show that the effective mass equals

$$m^* = m(1+\lambda), \tag{2.19}$$

where λ is defined as the negative energy derivative of the self-energy at the Fermi level,

$$\lambda = -\left. \frac{d\Sigma'}{d\omega} \right|_{\omega=0}. \tag{2.20}$$

It can also be shown [37] that the quasiparticle weight, i.e. the overlap of the quasiparticle and the original electron, is related to the mass renormalisation λ by

$$Z = \frac{m}{m^*} = \frac{1}{(1+\lambda)}. \tag{2.21}$$

The quasiparticle weight is by definition smaller than one, so it immediately follows that $\lambda > 0$, i.e. the renormalised mass is larger than the band mass. Stronger interactions lead to a larger mass renormalisation and smaller quasiparticle weight.

For non-magnetic materials the electron-impurity, electron-electron and electron-phonon interactions are the main contributors to the total self energy. Their various contributions to the self-energy are additive to first order:

$$\Sigma(\omega) = \Sigma_{imp}(\omega) + \Sigma_{el}(\omega) + \Sigma_{ph}(\omega). \tag{2.22}$$

This statement is equivalent to Matthiessen's rule, stating that the various contributions to resistivity are additive. Each of the contributions to the total self-energy will be separately discussed in the following sections.

Electron-impurity scattering

Elastic scattering off impurities is local and causes no energy transfer. The impurity self-energy is therefore considered to be momentum and energy independent, and to be purely imaginary. It broadens the otherwise sharp features of the spectral function; the delta functions in the spectral function turn into Lorentzian peaks of finite width, Γ_{imp}, which can be related to the imaginary part of the self-energy as $\Sigma''_{imp}(\omega) = \frac{\Gamma_{imp}}{2}$.

Electron-electron interaction

Multiple processes contribute to the decay of quasiparticles due to electron-electron interaction, such as *single* electron-hole pair production, *multiple* electron-hole pair production, or excitation of plasmon modes. For particles near the Fermi level, energy and momentum conservation forbid the latter two processes, so it is enough to consider single electron-hole production, illustrated in Figure 2.4a.

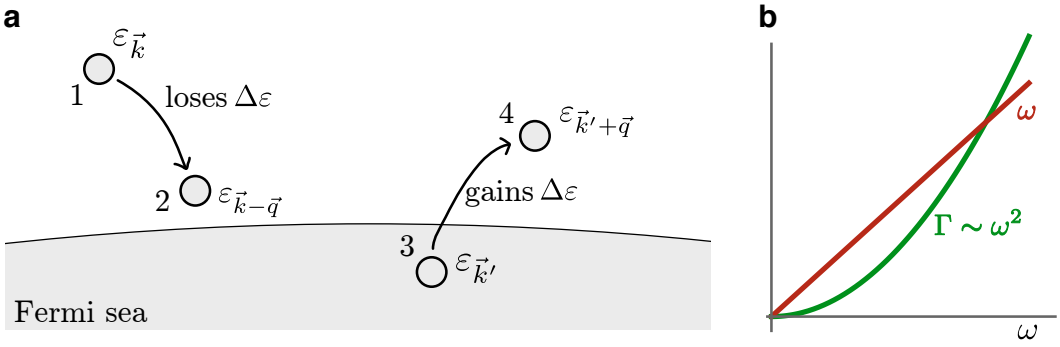

Figure 2.4.: (**a**) Quasiparticle scattering due to electron-electron interaction. (**b**) There is always a range of $\omega = \varepsilon - \varepsilon_F$ where the scattering rate is smaller than the energy of a quasiparticle

An excited quasiparticle 1 loses energy $\Delta\varepsilon$, and excites the particle-hole pair 3-4, conserving both energy and momentum. A simple analysis of Figure 2.4a can be used to qualitatively understand the dependence of the scattering rate on the quasiparticle energy. The total scattering rate from the state 1 is proportional to the number of ways states 2 and 3 can be chosen. The state 2 is initially unoccupied, so its energy $\varepsilon_{\vec{k}-\vec{q}}$ is higher than the Fermi energy. At the same time, energy conservation dictates

that it has to be smaller than the initial energy, $\varepsilon_{\vec{k}-\vec{q}} < \varepsilon_{\vec{k}}$. The number of such states is proportional to the difference between the initial state energy and the Fermi energy, $\omega_{\vec{k}} = \varepsilon_{\vec{k}} - \varepsilon_F$. In a similar way, state 3 has to be initially occupied, and have energy within $\omega_{\vec{k}}$ of the Fermi level. Once states 2 and 3 are chosen, the conservation laws completely determine state 4. Thus, the scattering rate of a quasiparticle with energy ω away from the Fermi level is expected to depend on the quasiparticle energy as $\Gamma \sim \omega^2$. This simple analysis yields the correct functional dependence for a three dimensional electron gas, while additional corrections appear in the two dimensional case. It also justifies the Fermi liquid theory as such, because, as shown in Figure 2.4b, there is always a range of excitation energies close to the Fermi level where the energy is larger than the decay rate, i.e. the quasiparticle concept is justified.

Although the approach outlined above is sufficient to grasp the energy dependence of the scattering rate, a more detailed treatment is needed if experimental values of scattering rates are to be compared to model predictions. Here I outline the derivation of the scattering rate of a 3D and a 2D Fermi liquid, following Ref. [38]. A free-electron like parabolic dispersion is assumed, and the only interaction taken into account is the screened Coulomb interaction, $W(\vec{q}) = \frac{V(\vec{q})}{\varepsilon(\vec{q},\omega)}$, with $V(\vec{q})$ denoting the Fourier transform of the unscreened interaction, and $\varepsilon(\vec{q},\omega)$ the dielectric function. The inverse lifetime, proportional to the scattering rate, is given by Fermi's golden rule:

$$\frac{1}{\tau_{\vec{k}}} = \frac{2\pi}{\hbar} \sum_{q,k'} \left| \frac{W(\vec{q})}{L^d} \right|^2 \delta\left(\varepsilon_{\vec{k}-\vec{q}} + \varepsilon_{\vec{k}'+\vec{q}} - \varepsilon_{\vec{k}} - \varepsilon_{\vec{k}'}\right), \tag{2.23}$$

where L^d is the size of the d dimensional space. The energy is related to momentum via the parabolic dispersion, the sums over momenta are turned into integrals, and the integrals over the angular part of the momentum evaluated explicitly. After these steps are taken, the expression for the scattering rate in 3D reads:

$$\frac{1}{\tau_{\vec{k}}} \sim \frac{\omega^2 + (\pi k_B T)^2}{1 + e^{-\beta\omega}} \int_0^{2k_F} dq \, |W(\vec{q})|^2 . \tag{2.24}$$

The first part of the expression describes the number of electron-hole pairs that can be excited with the phase space restrictions given by the Fermi sphere at temperature T, and qualitatively behaves as expected from the simple analysis given above (Figure 2.4). The integral describes the screened interaction, which can be approximated by the long-wavelength static limit, i.e. the Thomas-Fermi approximation.

It is found to be equal to

$$\int_0^{2k_F} dq \left|W\left(\vec{q}\right)\right|^2 \approx \frac{2k_F}{g\left(\varepsilon_F\right)^2}\xi_3\left(r_s\right), \tag{2.25}$$

where $g\left(\varepsilon_F\right)$ is the density of states at the Fermi level, and $\xi_3\left(r_s\right)$ a function of the average distance between electrons expressed in Bohr radii, r_s. For metallic densities $\xi_3\left(r_s\right)$ does not vary much, and is of order one. After relating the Fermi energy and the density of states using the parabolic dispersion, the inverse scattering time is found to be equal to

$$\frac{1}{\tau_{\vec{k}}^{3D}} = \frac{\pi}{8\hbar\varepsilon_F}\frac{\omega^2 + \left(\pi k_B T\right)^2}{1 + e^{-\beta\omega}}\xi_3\left(r_s\right). \tag{2.26}$$

In the 2D case both the phase space restriction and the functional form of the screened interaction are modified. Analogous calculation yields

$$\frac{1}{\tau_{\vec{k}}^{2D}} = \begin{cases} \xi_2\left(r_s\right)\frac{\omega^2}{4\pi\hbar\varepsilon_F}\ln\left|\frac{4\varepsilon_F}{\omega}\right| & k_B T \ll \omega \\ \\ \xi_2\left(r_s\right)\frac{\left(\pi k_B T\right)^2}{8\pi\hbar\varepsilon_F}\ln\left|\frac{4\varepsilon_F}{k_B T}\right| & k_B T \gg \omega \end{cases}, \tag{2.27}$$

where $\xi_2\left(r_s\right)$ is another function of the average distance between electrons, also very weakly dependent on the density and of order one at metallic densities. The dependence of the scattering rate on the quasiparticle energy is now modified by a logarithmic correction.

While the ω dependence of the scattering rate is a consequence of very general arguments related to the available phase space, the exact form of the equations can depend on the Fermi surface geometry. Thus, while the $\sim \omega^2$ and $\sim \omega^2 \ln\left|\frac{4\varepsilon_F}{\omega}\right|$ functional forms of the scattering rate are frequently observed [31, 39–41], the proportionality constant has to be determined experimentally. In particular, it was assumed throughout the derivation that there is only one circular Fermi surface. The delafossite Fermi surfaces are however hexagonal, and it will therefore be interesting to study the influence of this hexagonality on the scattering rate.

Once the scattering rate is known, so is the imaginary part of the self-energy, $\Sigma'' = \Gamma/2$. The real part of the self-energy could in principle be determined by the Kramers-Kronig relations, but that would require the knowledge of $\Sigma''\left(\omega\right)$ for all ω,

whereas the above derivation is valid only in a small energy range around the Fermi level. Nonetheless, the fact that Σ'' is even around $\omega = 0$ indicates that Σ' is odd, and can therefore be expanded as $\Sigma'_{el}(\omega) = -\alpha\omega$ near the Fermi level. In the low temperature limit the electron-electron self-energy in three dimensions is then given by

$$\Sigma^{3D}_{el}(\omega) = -\alpha\omega + \imath\beta\omega^2. \tag{2.28}$$

The logarithm in equation 2.27 for a two dimensional gas can be rewritten as $\ln\left|\frac{4\varepsilon_F}{\omega}\right| = \ln 4\left(1 + \frac{1}{\ln 4}\ln\left|\frac{\varepsilon_F}{\omega}\right|\right)$, leading to the following expression for total self-energy:

$$\Sigma^{2D}_{el}(\omega) = -\alpha\omega + \imath\beta\omega^2\left(1 + 0.72\left|\ln\left|\frac{\omega}{\varepsilon_F}\right|\right|\right). \tag{2.29}$$

Electron-phonon interaction

A system containing electrons and phonons can be described by the Hamiltonian

$$H = \sum_k \varepsilon_k c^\dagger_k c_k + \sum_q \omega_q a^\dagger_q a_q + \sum_{k,k'} g(k,k')\, c^\dagger_{k'} c_k \left(a^\dagger_{k-k'} + a_{k'-k}\right), \tag{2.30}$$

where spin and polarisation indices are omitted [42]. The first term describes electrons, while the second term describes phonons in the presence of these electrons. In other words, it is assumed that the correct phonon spectrum in the metal, ω_q, has already been calculated. The third term corresponds to the scattering of electrons due to emission ($a^\dagger_{k-k'}$) and absorption ($a_{k'-k}$) of phonons.

It can be shown that the electron-phonon coupling is too strong to be treated in second order perturbation theory. If a proper many-body treatment is employed instead, the renormalised electron spectrum is found to be equal to $\varepsilon^*_k = \varepsilon_k + \Sigma(k, \varepsilon^*_k)$, with the self-energy $\Sigma(k, \varepsilon^*)$ given by

$$\Sigma(k,\varepsilon^*) = \sum_{k'} |g(k,k')|^2 \left(\frac{1 + n_B(k'-k) - n_F(k')}{\varepsilon^*_k - \varepsilon_{k'} - \omega_{k'-k} + \imath\delta} + \frac{n_B(k'-k) + n_F(k')}{\varepsilon^*_k - \varepsilon_{k'} + \omega_{k'-k} + \imath\delta}\right), \tag{2.31}$$

where n_B and n_F stand for Bose-Einstein and Fermi distribution, respectively, and δ is an infinitesimally small parameter [43]. This expression has been proven to be correct to the order of $\sqrt{m_e/M_{ion}}$, where m_e is the mass of free electrons, and M_{ion}

that of the relevant ions. If the Fermi surface is isotropic, the explicit k dependence of the self-energy can be neglected to the same order.

The matrix element $g(k,k')$ has so far been treated as a function of momentum, but it is often more useful to think of it as a function of energy. A new function, called the Eliashberg function $\alpha^2F(\omega)$, is introduced:

$$\alpha^2F(\omega) = \frac{1}{(2\pi)^3}\frac{\int \frac{dk^2}{v_F}\int \frac{dk'^2}{v_F}\left|g(k,k')\right|^2\delta\left(\omega-\omega_{k'\text{-k}}\right)}{\int \frac{dk^2}{v_F}}. \tag{2.32}$$

If the matrix element $\left|g(k,k')\right|^2$ were omitted from the integral, the equation 2.32 would be reduced to the expression for the phononic density of states, $F(\omega)$. The Eliashberg function therefore corresponds to the phononic density of states, weighted by the interaction strength. The symbol used, $\alpha^2F(\omega)$, emphasises this interpretation, but it should be noted that $\alpha^2F(\omega)$ is a single function; it can be factorised into the density of states and a coupling parameter only if the momentum dependence of the matrix element $\left|g(k,k')\right|^2$ is neglected.

Using the Eliashberg function the self-energy can be expressed as:

$$\Sigma(\varepsilon^*) = \int_{-\infty}^{\infty}d\varepsilon\int_0^{\infty}d\omega'\alpha^2F(\omega')\left(\frac{1+n_B(\omega')-n_F(\varepsilon)}{\varepsilon^*-\varepsilon-\omega'+\imath\delta}+\frac{n_B(\omega')+n_F(\varepsilon)}{\varepsilon^*-\varepsilon+\omega'+\imath\delta}\right). \tag{2.33}$$

The parameter that is most often used to describe the strength of the electron-phonon interaction is the mass renormalisation factor, λ (equations 2.19 and 2.20), proportional to the energy derivative of the real part of the self-energy. Using the expression 2.33 for self-energy, it can be related to the Eliashberg function by

$$\lambda = 2\int_0^{\infty}d\omega'\frac{\alpha^2F(\omega')}{\omega'}. \tag{2.34}$$

This framework can be used to find energy and temperature dependent self-energies in simple models for acoustic and optical phonons, i.e. the Debye and Einstein models, respectively. If the matrix element $\left|g(k,k')\right|^2$ is assumed to be independent of momentum, the self-energy can be parametrised by a single number, λ. In this approximation the Eliashberg function $\alpha^2F(\omega)$ is proportional to the density of states, which is of known form in the two models, with a prefactor related to λ by

requiring equation 2.34 to hold at low temperatures. $\alpha^2F(\omega)$ found in this way is combined with the general expression for electron-phonon self-energy (equation 2.33) to find the self-energy in the Debye and Einstein models.

In the low temperature limit of the Debye model with the Debye frequency ω_D [31], the real part of the self-energy is found to be equal to

$$\Sigma'(\varepsilon^*) = -\lambda\frac{\hbar\omega_D}{3}\left[\frac{\varepsilon^*}{\hbar\omega_D} + \left(\frac{\varepsilon^*}{\hbar\omega_D}\right)^3 \ln\left|1-\left(\frac{\varepsilon^*}{\hbar\omega_D}\right)^2\right| + \ln\left|\frac{1+\frac{\varepsilon^*}{\hbar\omega_D}}{1-\frac{\varepsilon^*}{\hbar\omega_D}}\right|\right], \tag{2.35}$$

and the imaginary to be equal to

$$\Sigma''(\varepsilon^*) = \begin{cases} \lambda\frac{\pi}{3}\frac{\varepsilon^{*2}}{(\hbar\omega_D)^2} & |\varepsilon^*| < \hbar\omega_D \\ \lambda\frac{\pi}{3}\hbar\omega_D & |\varepsilon^*| > \hbar\omega_D \end{cases}. \tag{2.36}$$

Similarly, the Einstein model with the Einstein frequency ω_E yields

$$\Sigma'(\varepsilon^*) = -\lambda\frac{\hbar\omega_E}{2}\ln\left|\frac{1+\frac{\varepsilon^*}{\hbar\omega_E}}{1-\frac{\varepsilon^*}{\hbar\omega_E}}\right|, \tag{2.37}$$

and

$$\Sigma''(\varepsilon^*) = \begin{cases} 0 & |\varepsilon^*| < \hbar\omega_E \\ \lambda\frac{\pi}{2}\hbar\omega_E & |\varepsilon^*| > \hbar\omega_E \end{cases}. \tag{2.38}$$

The self-energy in the two models is shown in Figure 2.5. The real part has a peak at the maximum phonon energy, and approaches zero at higher binding energies. Qualitatively this has to be true, because electrons at binding energies much higher than the phonon energy cannot be significantly perturbed. The imaginary part has a step at the same energy, because there are no electrons that can fill a hole of a binding energy smaller than the phonon energy (ε_1^* in the inset of Figure 2.5). On the other hand, if the hole binding energy is higher than the phonon energy (ε_2^*), the hole can be filled with a probability independent of its energy. In the Einstein model there is only one phonon mode, so the imaginary self-energy is zero up to the Einstein energy, while in the Debye model it increases continuously because there are phonon modes at all energies lower than the Debye energy.

The expression 2.33 for the self-energy is temperature dependent, so it can be

used to predict the temperature dependence of the photoemission linewidth. For an arbitrary temperature the self energy has to be calculated numerically, but at temperatures much higher than the characteristic phonon energy the imaginary self-energy limits to

$$\Sigma''\left(\varepsilon^*, T \gg \hbar\omega_{ph}/k_B\right) = \lambda\pi k_B T, \tag{2.39}$$

in both models and at all binding energies.

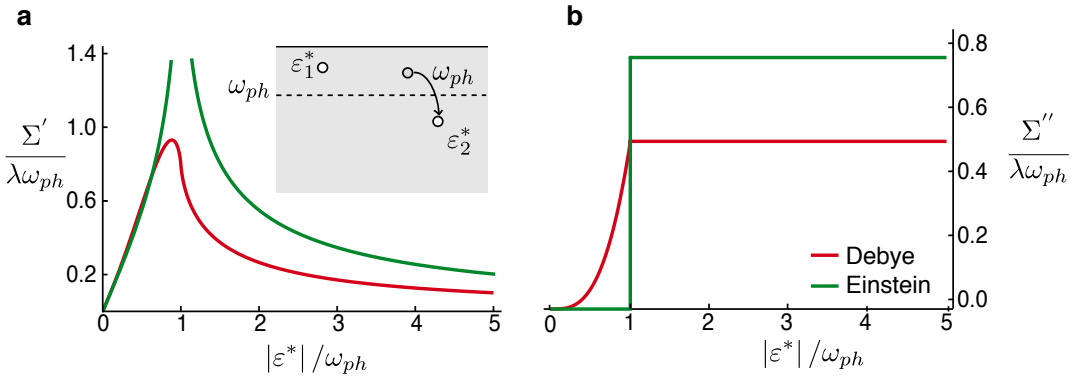

Figure 2.5.: The real (a) and imaginary (b) part of the phonon self-energy in the Debye (red) and Einstein (Green's) model. The inset illustrates the energy constraint on the phonon emission.

2.5. Model spectra and analysis

In the last section I discussed Green's functions and the self-energy formalism, with the aim of gaining understanding of how the features of the one-electron spectral function, measurable by photoemission, arise. The spectral function, proportional to the imaginary part of the Green's function (equations 2.16 and 2.17), of a system described by a bare band dispersion $\varepsilon(k)$ and self-energy $\Sigma(\omega)$ is given by

$$A(k,\omega) = \frac{1}{\pi}\frac{\Sigma''(\omega)}{\left(\omega - \varepsilon(k) - \Sigma'(\omega)\right)^2 + \left(\Sigma''(\omega)\right)^2}. \tag{2.40}$$

I will use this form of the spectral function to simulate photoemission spectra assuming the self-energies calculated in Section 2.4.2. In doing this I will assume that the

band structures are two-dimensional. This simplifies the discussion for two reasons. First of all, as the in-plane dispersion is the same at all values of the out-of-plane momentum, there is no k_z - broadening (described in Section 2.1). Furthermore, the linewidths of observed features are a direct measure of the lifetime of the hole created by photoemission only if the initial state is perfectly two-dimensional [44]. In a general case the measured linewidth is related both to the lifetime of the photo-hole, governed by the self-energy, and the lifetime of the photoexcited electron, which depends on the scattering processes as the electron leaves the solid.

Simulated spectra are helpful in interpreting real ARPES data, as they facilitate recognising characteristic features when they appear in experiments. I will therefore analyse them using methods similar to those used for real data in the rest of the thesis. ARPES data are usually analysed by extracting one-dimensional cuts of the spectral function. The cuts taken at constant energy are called the momentum distribution curves (MDCs), while those taken at constant momentum are called the energy distribution curves (EDCs). The line shapes of the two types of cuts differ because the self-energy in the first approximation depends explicitly on energy, but not on momentum. As long as this approximation is valid the MDCs are of Lorentzian line shape, while the EDC line shape depends on the form of the self-energy. Quantitative analysis of ARPES spectra is therefore usually performed by fitting Lorentzian peaks to the extracted MDCs. This type of analysis was performed for all of the photoemission data in this thesis, so I will take the same approach in analysing the simulated spectra.

To show explicitly how the Lorentzian shape of the MDCs arises from the spectral function given by equation 2.40, it is useful to rewrite the equation as a function of momentum at a fixed energy, $A_\omega(k)$. The spectral function peaks at a momentum k_ω, defined by $\omega = \varepsilon(k_\omega) + \Sigma'(\omega)$. The bare band can be linearised in the vicinity of this momentum as

$$\varepsilon(k) = \varepsilon(k_\omega) + v_B(k_\omega)(k - k_\omega), \tag{2.41}$$

where $v_B(k_m)$ denotes the *bare* band slope ($v_B = d\varepsilon/dk$), at the momentum at which the spectral function peaks. With this linearisation the spectral function at a fixed

energy takes the form of

$$A_\omega(k) = \frac{\Sigma''(\omega)}{\pi v_B^2(k_\omega)} \frac{1}{(k-k_\omega)^2 + (\Sigma''(\omega)/v_B(k_\omega))^2}. \tag{2.42}$$

The full width at half maximum (FWHM) of this Lorentzian, a quantity directly extracted from the fits to experimental data, is given by $\Delta k_\omega = 2\Sigma''(\omega)/v_B(k_\omega)$. It depends on the self-energy at the binding energy at which the MDC is extracted ($\Sigma''(\omega)$), and the bare band slope at the momentum at which the MDC peaks ($v_B(k_\omega)$). $\Sigma''(\omega)$ therefore cannot be extracted directly from the measurements; rather, an assumption about the bare band dispersion needs to be made. This is also true of the real part of the self-energy, $\Sigma'(\omega)$. The information about it is contained in the difference of the spectral function and the bare band dispersion; as only the former is experimentally accessible, an assumption about the latter needs to be made. What is more, not only the value of the extracted self-energy depends on the assumed bare band; its binding energy dependence does too.

The MDC peak position as a function of binding energy can be used to extract the Fermi velocity, or more generally the band slope. This is done by performing a linear fit to the peak positions in the binding energy range of choice; the inverse of the slope of this fit corresponds to the band slope, $d\varepsilon/dk$. The Fermi velocity is related to the band slope at the Fermi energy as

$$v_F = \frac{1}{\hbar}\frac{d\varepsilon}{dk}\bigg|_{\varepsilon_F}. \tag{2.43}$$

As they differ only in the constant $\hbar$, the terms 'band slope' and 'band velocity' are often used interchangeably, and Fermi velocities are quoted in eVÅ. This is particularly convenient in relating momentum changes to energy changes in the electronic structure. Nonetheless, it is often informative to convert the Fermi velocity to m/s; the relevant conversion is given by

$$v\,[\mathrm{m/s}] = 151926.8v\left[\mathrm{eV\AA}\right]. \tag{2.44}$$

The effective mass m^* in units of the free electron mass can be calculated from the

fitted band slope and Fermi momentum as

$$\frac{m^*}{m_e} = \frac{1}{m_e}\frac{\hbar k_F}{v_F} = 7.61996\frac{k_F\left[\text{Å}^{-1}\right]}{v_F\left[\text{eVÅ}\right]}. \tag{2.45}$$

In the following three sections I will simulate the spectral functions of a system interacting only with impurities (section 2.5.1), as well as of systems in which electron-electron (section 2.5.2), and electron-phonon interactions (section 2.5.3) are added to the impurity scattering. In all cases I will assume a free-electron parabolic bare band dispersion,

$$\varepsilon(k) = \frac{\hbar^2}{2m_e}\left(k^2 - k_F^2\right), \tag{2.46}$$

with $k_F = 1\,\text{Å}^{-1}$. The Fermi velocity of this band is equal to $v_F = 7.62\,\text{eVÅ} = 1.16\times 10^6\,\text{m/s}$, and the bare band mass is equal to the free electron mass by construction.

2.5.1. Non-interacting electrons

If the electrons do not interact with each other or the lattice, the removal of one of them cannot perturb the rest of the system. Both initial and final state many-body wave functions are products of the same eigenstate of the $N-1$ particle system, $\Psi_{m_0}^{N-1}$, and a single Bloch state. The difference between the energies of the N and the $N-1$ particle ground states is exactly equal to the binding energy of the extracted electron, which depends on momentum, $\omega_m^{N-1} = \varepsilon(k)$. The spectral function (equation 2.10) is therefore equal to a delta function, $A^-(k,\omega) = \delta(\omega - \varepsilon(k))$ reflecting the infinite lifetime of a quasiparticle in a non-interacting system. To put the same statement in the language of Green's functions, the self-energy vanishes. In any realistic system, however, impurities are present to some degree, leading to a finite imaginary part of the self-energy.

A spectral function simulated assuming only an impurity contribution to the self-energy, which is purely imaginary and has no binding energy dependence, is shown in Figure 2.6a for $\Sigma'' = 20\,\text{meV}$. The bare band dispersion underlying it (dashed line) coincides with the maximum intensity of the spectral function because the self-energy contains no real part. The spectral function is, however, broadened by impurity scattering, introducing a binding energy dependence of the MDC linewidth. The linewidth is given by $\Delta k_\omega = 2\Sigma''_{imp}/v_B(k_\omega)$; it increases as the band slope

decreases at higher binding energies due to the parabolic bare band (Figure 2.6(b, c)).

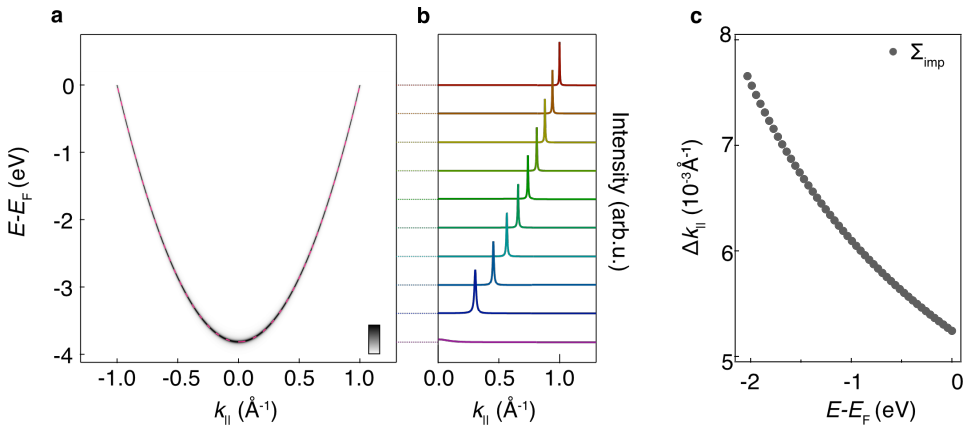

Figure 2.6.: (**a**) Spectral function simulated for a free-electron dispersion, with an impurity self-energy of $\Sigma''_{imp} = 20\,\text{meV}$. (**b**) MDCs extracted from (a), at energies indicated by the dashed lines. (**c**) The full width at half maximum of Lorentzian fits to MDCs extracted from (a) as a function of binding energy.

2.5.2. Electron-electron interactions

In Figure 2.7a I show the simulated spectral function with an electron-electron self-energy of a three dimensional Fermi liquid (equation 2.28):

$$\Sigma_{el}^{3D}(\omega) = -\alpha\omega + \imath\beta\omega^2, \tag{2.47}$$

with $\alpha = 0.5$ and $\beta = 0.1\,\text{eV}^{-1}$. As the real part of the self-energy is now finite, the maximum intensity in the spectral function does not coincide with the bare band dispersion, but is offset by the real part of the self-energy, Σ', as indicated in Figure 2.7a. As Σ' is finite at all binding energies, the whole bandwidth is reduced, reflecting the high energy scale of the electron-electron interactions.

The renormalised band can be analysed by extracting momentum distribution curves as a function of binding energy, and fitting them to Lorentzian line-shapes, as was done for the non-interacting case above. The position of these Lorentzian

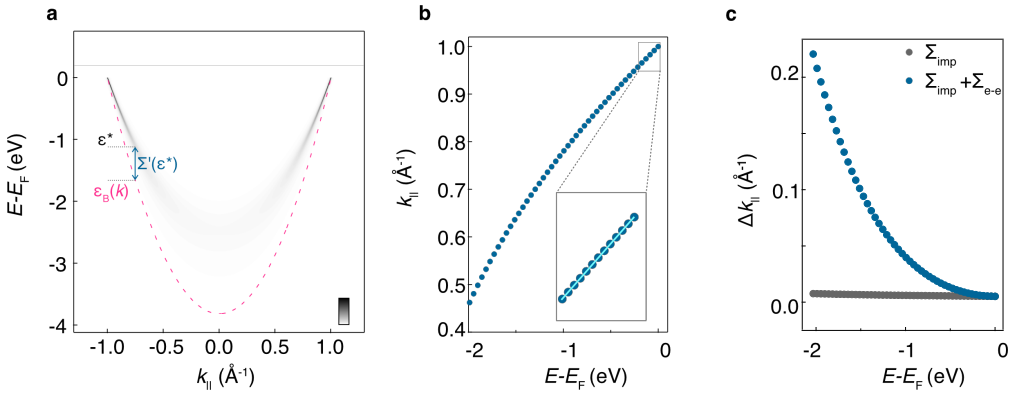

Figure 2.7.: (**a**) Spectral function simulated for a free-electron dispersion, with an impurity self-energy of $\Sigma''_{imp} = 20\,\text{meV}$, and an electron-electron self-energy given by equation 2.47. (**b**)The positions of Lorentzian fits to MDCs extracted from (a) as a function of binding energy. A linear fit to the band close to the Fermi level is shown in the inset. (**c**) The full width at half maximum of Lorentzian fits to MDCs extracted from (a) as a function of binding energy (blue), compared to the same with only impurity self-energy (same as in Figure 2.6c).

fits as a function of binding energy is shown in Figure 2.7b[2]. In order to find the Fermi velocity of this renormalised band, a linear fit to the momentum as a function of binding energy needs to be performed in the narrow region in the vicinity of the Fermi level, as shown in the inset of Figure 2.7b. The Fermi velocity extracted from this fit is 5 eVÅ, suggesting a mass renormalisation of $m^*/m_e = 1.53$. However, as discussed in Section 2.4.2, the mass renormalisation is related to the real part of the self energy as

$$\frac{m^*}{m} = 1 - \frac{d\Sigma'}{d\omega}. \tag{2.48}$$

For the self-energy employed here (equation 2.47, with $\alpha = 0.5$) this expression predicts the mass renormalisation to be $m^*/m = 1.5$. The small difference arises because the linear fit in Figure 2.7b is performed over a binding energy range of 200 meV; although the fit appears to be very good, the band curvature affects the extracted slope. This effect would be minimised if the fitting range was reduced,

[2]In the rest of the thesis I will plot the fitted data of this type as binding energy vs momentum, as is usually done. Here I plot the extracted momentum as a function of binding energy, in order to emphasise the way in which the data are extracted: momentum at which the intensity is maximum is found as a function of fixed binding energy.

but this is often not possible with real data, which require a larger fitting range to enable a robust fit, not overly sensitive to noise and other experimental artefacts. For each spectrum a fitting range needs to chosen to compromise between the effects of band curvature and experimental artefacts. In Appendix C I show how a fitting range was chosen for a few example data sets from this thesis.

The extracted full-width at half-maximum of the Lorentzian fits to the MDCs as a function of binding energy is shown in Figure 2.7c. As expected, the linewidth increases with binding energy, at a considerably higher rate than for the case of only impurity scattering. To summarise, electron-electron interactions in the simplest case continuously shrink the bandwidth and increase the linewidth.

2.5.3. Electron-phonon interactions

The situation is very different for electron-phonon interactions because the characteristic phonon energy is typically much smaller than the bandwidth. Both the real and the imaginary part of the phononic self-energy have features at the phonon energy (Figure 2.5), which are reflected in the simulated spectral function, shown in Figure 2.8a for a self-energy within the Debye model (equations 2.35 and 2.36, $\lambda = 0.5$, $\hbar\omega_D = 100\,\mathrm{meV}$). The spectral function exhibits a sudden change of slope at the Debye energy, often referred to as a 'kink', characteristic of electron-boson coupling. The slope of the renormalised band is reduced at energies smaller than the phonon energy. The deviation from the bare band dispersion is the largest at the phonon energy, where the real part of the self-energy peaks, and is reduced at higher binding energies (inset of Figure 2.8a). The band slope can be extracted in the same way as described in the section 2.4.2 above; the Fermi velocity is found to be equal to $4.83\,\mathrm{eV\AA}$, corresponding to the mass renormalisation of $m^*/m_e = 1.58$. In other words, if this fit were used to estimate the electron-phonon coupling strength λ, it would be deduced to be equal to 0.58, $\sim 15\%$ higher than the actual value used in the simulation, 0.5. This is of course again a consequence of the finite fitting range; a slope fitted just at the Fermi level yields the expected value of 0.5. The analysis of these simulated spectra points to the importance of careful fitting range determination for real data (Appendix C).

The linewidth as a function of binding energy, shown in Figure 2.8c, inherits the discontinuity of the self-energy at the Debye energy. It increases rapidly from the

Fermi level towards the Debye energy. At higher binding energies the linewidth increases at a moderate rate; it is in fact equivalent to a system with only an effective impurity self-energy of $\Sigma''_{eff} = \left(\lambda\pi\hbar\omega_D/3 + \Sigma''_{imp}\right)$. This is also seen in the simulated spectral function (Figure 2.8a): at high binding energies the spectral function follows the bare band dispersion, as it does in absence of interactions, but with a larger linewidth (*cf.* Figure 2.6a).

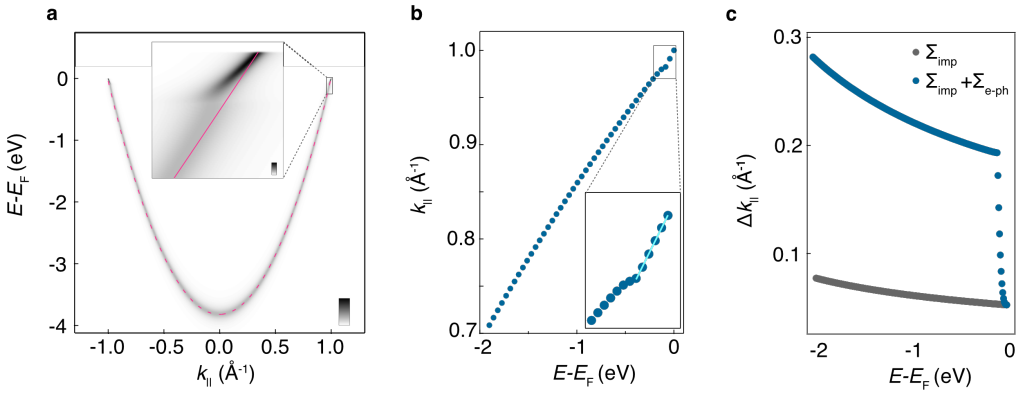

Figure 2.8.: (**a**) Spectral function simulated for a free-electron dispersion, with an impurity self-energy of $\Sigma''_{imp} = 20\,\text{meV}$, and an electron-phonon self-energy within the Debye model, with the Debye energy of 100 meV and coupling of $\lambda = 0.5$. A zoom-in of the states close to the Fermi level is shown in the inset. The bare band dispersion is shown by the line. (**b**) The positions of Lorentzian fits to MDCs extracted from (a) as a function of binding energy. A linear fit to the band close to the Fermi level is shown in the inset. (**c**) The full width at half maximum of Lorentzian fits to MDCs extracted from (a) as a function of binding energy (blue), compared to the same with only impurity self-energy (same as in Figure 2.6c).

2.6. ARPES experiment

I have now discussed the theory behind the ARPES experiments, as well as the type of information that can be gained through them. In this section I will describe some of the practicalities of those experiments. All of the data in this thesis were taken at synchrotron beamlines, so I will concentrate on describing those setups, although ARPES can also be done using laser light, or the ultraviolet light from a gas-discharge lamp. The majority of the data in this thesis were taken at the i05 beamline at the Diamond Light Source, with the exception of the soft x-ray ARPES data (Figures 5.17, 5.18 and 5.19) and the spin-resolved data (Figure 6.4b), which were taken at the i09 beamline at Diamond and the APE beamline at the Elettra Synchrotron, respectively. The specifics of those experiments will be discussed in Sections 2.6.6 and 2.6.7, respectively. During the course of my PhD I participated in 13 ARPES beamtimes, adding up to a total of 63 days, across the three beamlines: eight beamtimes (38 days) at the i05 beamline at Diamond, three at the i09 beamline (10 days) and two at the APE beamline at Elettra (15 days).

Synchrotron photoemission differs from the lamp or laser based photoemission not only in the type of light source, but also because the experiments performed at large scale facilities present different challenges and opportunities to those done in in-house laboratories. Although the users are typically not sufficiently familiar with the setup to maintain it, it is vital that they understand its various parts well enough to be able to tune them, with the aim of obtaining the data of the highest quality achievable in the specific circumstances. Furthermore, the facility experiments are limited to a few days, typically 5 or 6 at a time, which need to be used efficiently. The users have a 24 hour access to the beamline, requiring a team of people to work together. For all the beamtimes I participated in the team consisted of four group members, each of whom had a 12 hour-long shift. The shifts were staggered, so that everybody overlapped with one person for the first 6 hours and with another for the remaining 6 hours of the shift. This shift schedule is beneficial both to ensure efficient information transfer from shift-to-shift, and because the two people working at the same time are not likely to become tired simultaneously. Although one or two team members usually lead the project, the synchrotron experiments are always a group effort. Good teamwork is therefore vital to ensure efficient (and enjoyable!) beamtimes. During the beamtimes I participated in we collected the data

on delafossites, discussed in this thesis and References [5, 8, 10, 11, 14, 19], but also on a range of transition metal dichalcogenides [45–49], and Sr_2RuO_4 under uniaxial stress [50]. The photoemission data can be collected fairly quickly with modern setups and intense synchrotron radiation; a high-resolution dispersion may be taken in $\sim$ 15 min, while a larger Fermi surface map could be measured in 1-2 hours. However, a considerable fraction of the time is used to optimise the measurement conditions, which entails finding the optimal photon energy and light polarisation, light intensity, momentum and energy resolution and position on the sample, in order to access the relevant information in a reasonable time scale. The experiment as a whole resembles a complex multi-parameter optimisation problem, which requires quick decision taking, based both on the knowledge of the setup and the physics of the material under investigation.

In what follows I will describe the experimental setup of an ARPES beamline. Although the general discussion is not beam-line specific, I will use i05 at Diamond as an example when discussing specific parameters; similar values are found elsewhere. In particular I will focus on the parts of the setup which can be, and often are, tuned by users. The whole experimental setup can be divided into three parts, each of which I will discuss separately: the incoming light, the sample space, and the electron detection. These are all technical details vital to ensuring the quality of the data presented in chapters 4 - 6, but a reader more interested in the results themselves and the theoretical techniques used to model them might prefer at this point to skip directly to chapter 4.

2.6.1. The incoming light

Synchrotron radiation is created by charged particles travelling on curved paths. In a synchrotron facility, schematically shown in Figure 2.9a, electrons are first accelerated in a linear accelerator (LINAC) and the booster ring up to energies of $\sim$ MeV and $\sim$ GeV, respectively. They are subsequently injected into the storage ring, which is composed of alternating straight and curved sections. As the electron trajectories are altered by bending magnets in the curved sections, they produce broadband synchrotron radiation which can be used for experiments. Straight sections of the synchrotron can also be used to produce radiation if insertion devices, creating spatially varying static magnetic fields, are placed in them. The energy electrons lose as

they produce electromagnetic radiation is compensated in the radio-frequency (RF) cavity, where a RF electric field accelerates the electrons. However, as the RF field oscillates, it acts as an accelerator only part of the time. This is why electrons are sent in the storage ring in bunches, tuned such that they pass the RF cavity only in the part of the cycle in which the field accelerates them. In normal operation at Diamond there are 900 electron bunches that are 2 ns apart, and carry 0.62 nC each. Two such trains of bunches are separated by 72 ns, resulting in a total current of 300 mA. The energy at which the electrons move in the storage ring is 3 GeV. In a synchrotron there can be many beamlines, more than 30 at the Diamond synchrotron, each of which receives light from a bending magnet or an insertion device. Since all electrons in the storage ring pass through all the magnets and undulators, synchrotrons have to be designed to minimise the influence of the experiments on different beamlines on each other.

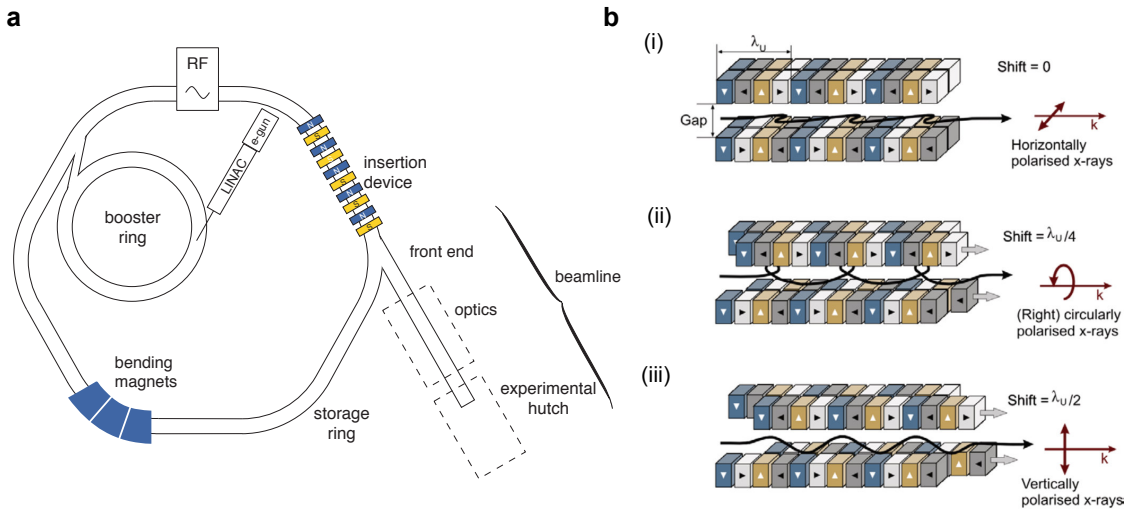

Figure 2.9.: (**a**) Schematic of a synchrotron, taken with permission from Ref . [51]. (**b**) Schematic of an undulator, with arrows and colours corresponding to magnetisation direction of the permanent magnets. Configurations required to achieve (i) linear horizontal (ii) circular right and (iii) linear vertical polarisation are shown. Taken with permission from Ref. [52].

The most commonly used type of insertion device in modern synchrotrons is the undulator, which produces the most intense light concentrated in a narrow spectral range [51, 53]. It consists of two arrays of magnets, above and below the electron

orbit plane, forcing electrons to oscillate. A slightly more complicated design, in which there are two arrays of magnets above and two below the electron plane (Figure 2.9b), allows for the polarisation of the light to be changed. Displacing the magnet rows with respect to each other changes the electron paths, resulting in linearly or circularly polarised light, as indicated in Figure 2.9b. The radiation produced in this way is intense and concentrated in a narrow energy range. The wavelength at which its intensity peaks depends on the period of the undulator, marked λ_u in Figure 2.9b , as well as the magnetic field the electrons feel. Undulators are chosen to match the photon energy range needed on a specific beamline, while the photon energy within that range can be tuned by modifying the size of the gap between the two arrays of magnets, thus changing the magnetic field in the electron plane.

The light produced in a dedicated bending magnet or an undulator is passed into a beamline, where it travels through an array of optical elements, as needed. Although the intensity of the light emitted in an undulator peaks at a specific wavelength, it is not sufficiently monochromatic to be used in an experiment. It therefore needs to be monochromatised using a diffraction grating, which must be chosen to match the relevant wavelengths. For instance, in the hard x-ray range the wavelengths are on the order of Å, enabling the use of single crystals as diffraction gratings. In contrast, the energy range used in a typical photoemission experiment, $10 - 100\,\mathrm{eV}$, corresponds to wavelengths of $\sim 1 - 10\,\mathrm{nm}$, so manufactured periodic gratings are used instead, with the separation between grating lines chosen according to the wavelength. As an example, at i05 it is possible to choose between two gratings, with 800 lines/mm and 400 lines/mm; the first one of those allows for the best light energy definition, as high as $E_l/\Delta E_l > 20000$, while the second one allows for a higher photon flux, with a slightly reduced resolving power [54]. The photon energy of the light used in the experiment is set by the monochromator angle with respect to the beamline axis, usually chosen to match the peak intensity of the undulator light, maximising the intensity of the light incident on a sample. Occasionally, however, high intensity can reduce the measurement resolution in a photoemission experiment, due to the Coloumb interaction of the many outgoing electrons, called the space charge effect [55]. In those cases intensity can be reduced by detuning the undulator such that its peak intensity does not coincide with the energy passed through the monochromator.

The beam exiting the monochromator contains a spread of wavelengths, sorted along the height of the beam. Monochromatic light is obtained by focusing the light onto the so-called exit slit, which allows only a small portion of the beam to pass through. The vertical size of the exit slit can be chosen, directly affecting the energy resolution, as shown in Figure 2.10 for the i05 beamline. It simultaneously affects the photon flux (inset of Figure 2.10), and the vertical size of the light spot on the sample, which varies between 7 and 70 µm for the exit slit heights between 0 and 200 μm at i05. The horizontal beam spot size is fixed to $\sim$ 50 µm. As is often the case, a compromise needs to be made between high resolution and high flux, while also keeping in mind the spot size.

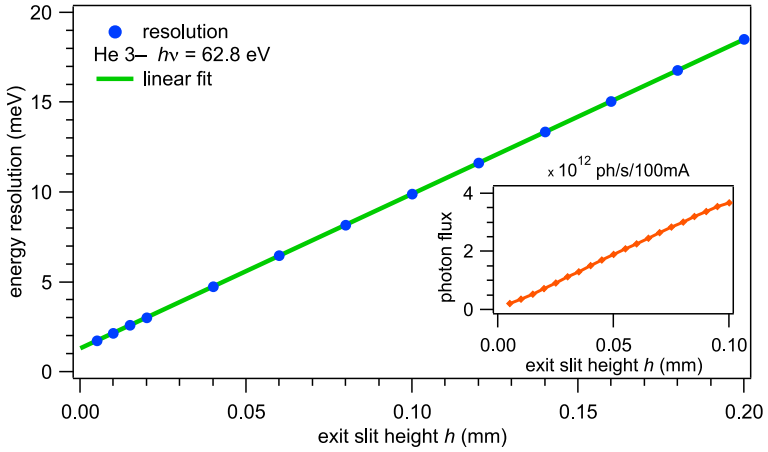

Figure 2.10.: Measured energy resolution as a function of the exit slit height at the i05 beamline at Diamond. Inset: the photon flux as a function of the exit slit height. Reproduced with permission from Ref. [54].

2.6.2. The sample and sample space

Ultra-high vacuum

The synchrotron light with photon energy defined using the above-described techniques is focused on the sample, which is placed in a dedicated sample manipulator in an ultrahigh vacuum (UHV) chamber. There are several reasons for keeping the ARPES setup under vacuum. Firstly, both the incident ultraviolet light and outgoing electrons can be scattered by air molecules. Furthermore, operation of the

electron analyser requires a pressure of $\sim 10^{-7}$ mbar. However, the base pressure specification, typically $\sim 10^{-11}$ mbar , is not ultimately defined by these considerations, but by the surface sensitivity of photoemission. As the mean free path of the outgoing electrons is comparable to the interatomic distance at typical photoelectron kinetic energies, the signal comes only from a thin layer of sample close to the surface. It can therefore be easily dominated by both intrinsic and extrinsic surface contributions. The residual gas molecules adsorbed on the sample surface are a source of disorder scattering, reducing the data quality. As the rate of adsorption of gas molecules scales linearly with their pressure, it is beneficial to achieve as low a pressure as possible [30].

Loading samples into the UHV chamber is achieved through a system of interconnected chambers at varying degrees of vacuum, constantly pumped by turbomolecular pumps backed by scroll pumps, sometimes with added ion pumps and non-evaporable getters to reach the lowest pressures[3]. The only chamber that is exposed to the atmospheric pressure during regular operation is the smallest of them, called the load-lock, where samples are introduced into and taken out of the UHV system. After new samples are added into the load-lock, it is first pumped down to $\sim 10^{-2}$ mbar using a scroll pump, after which a turbomolecular pump is turned on. The pressure needs to reach values of $\sim 10^{-8}$ mbar before the sample can be transferred in the rest of the vacuum system, which typically takes 1-2 hours. It is therefore important to carefully plan sample exchanges in order not to waste time waiting for the pressure to drop. The sample is then transferred through the intermediate chambers into the measurement chamber. In general, when working with UHV systems it is good practice to do all the movements very slowly, constantly monitoring the pressure in order to avoid pressure spikes due to trapped residual gas.

Sample preparation

In order to obtain clean surfaces, single crystals are typically cleaved *in-situ* using a top-post, as was done with all the samples from which data are shown in this thesis. A ceramic post of 500 μm diameter is glued on the sample surface with silver epoxy. Once in the UHV system at the desired pressure and temperature, the top-

[3]There are many resources available to learn about pumps, pressure gauges, and other examples of UHV technology; see for example Ref. [56].

post is hit using a wobble stick, with the aim of breaking the sample and creating a clean surface. It is impossible to fully control the cleaving process; although careful sample mounting does increase chances of a successful cleave, there is no guarantee that, for example, the top post will not detach instead, leaving a sample covered in epoxy. Even if the sample cleaves, the surface may not be flat and uniform. The probability of a successful cleave depends on the material: it is higher for layered materials and crystals which are not too small. The delafossites, the crystals of which can be as thin as $\sim$ 1µm as-grown, often cleave only partially, leaving a small and inhomogeneous surface available for the experiment.

Sample manipulator

Most beamlines have bespoke sample manipulators controlling the sample motion. The manipulator design is particularly important for angle resolved photoemission, because the angle between the sample and the analyser axis is a measurement parameter, directly related to the crystal momentum of the electrons is the solid. The manipulator at the i05 beamline has six independent degrees of freedom, corresponding to the translation along, and rotation around, the three axes. Each one of them is controlled by a stepper motor, and their absolute positions are monitored by encoders. With appropriate backlash corrections, all the angles are reproducible to the precision of 0.05° [54]. Every one of the six degrees of freedom can be controlled by the software, both individually and as a part of a more complex measurement sequence. This high degree of motion precision, control and automatisation is unusual, and is one of the reasons high quality data on samples as demanding as delafossites could be taken at i05. As already mentioned, the cleaved surfaces of delafossites are rarely uniform, so considerable optimisation was needed to find parts of the surface which could yield high resolution data. After cleaving a new sample we would therefore always move the sample in a two dimensional grid, initially with a step size of $\sim$ 100 µm, and take quick measurements at each position. This rough survey of the sample would allow us to identify regions where surface or the bulk contributions dominate the measured signal. After choosing the region in which the signal of interest could be observed, we would optimise the position further, making steps as small as $\sim$ 10 µm until the best position was found. Indeed, in some samples movements of $\sim$ 10 µm would noticeably change the data quality. Crucially, after

finding the best position it was possible to reproducibly return to it and measure.

2.6.3. Electron analyser

Once electrons are photoemitted, their kinetic energy at a specific angle of emission needs to be measured. This is typically done using commercially available concentric hemispherical analysers, whose main components are two hemispheres, with a potential difference $\Delta V = V_{in} - V_{out}$ between them, as shown schematically in Figure 2.11. The electric field produced by the hemispheres makes the electrons which enter the analyser travel on circular paths. The radius of the electron path depends on its kinetic energy, as illustrated in Figure 2.11 by the different colours; the electron on a 'purple' trajectory has the highest, and the one on the 'red' the lowest energy. Only electrons in a narrow energy range can avoid colliding with the hemispheres, and reach the detector. Within this range, the kinetic energy of the electrons determines their position on the detector, enabling its measurement.

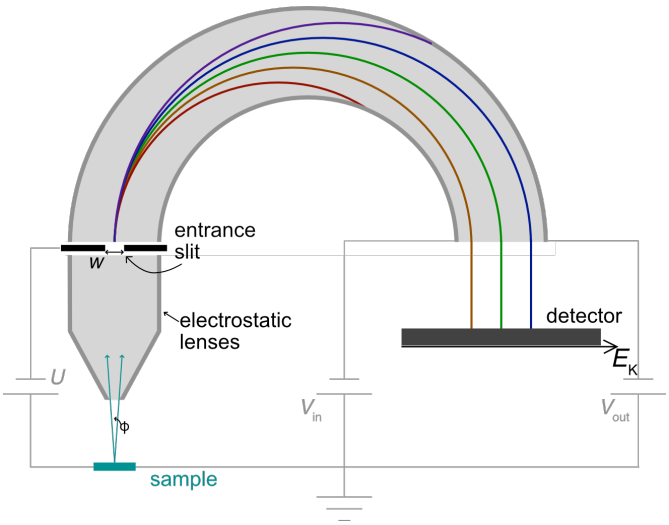

Figure 2.11.: Schematic of the cross-section of a concentric hemispherical analyser.

Details of the energetics of the photoemission experiment and detection are clarified in Figure 2.12. The difference between the photon energy and the binding energy of the electron in the solid is equal to the sum of the sample work function

(W_s) and the electron kinetic energy in vacuum (E_{k1}):

$$h\nu - |E_B| = E_{k1} + W_S; \tag{2.49}$$

this is equivalent to the energetic argument made at the beginning of the chapter (equation 2.1), and illustrated in Figure 2.12a. However, there can be small variations between the work function of the analyser (W_A) and that of the sample (W_S), although both are typically $\sim 4.5\,\text{eV}$ (Figure 2.12b). Crucially, as long as the sample shares the same ground with the analyser there is no variation in the Fermi level between the two. This enables the determination of the binding energy measured from the common Fermi level using the work function of the analyser and the kinetic energy of the electrons in the analyser:

$$h\nu - |E_B| = E_{k2} + W_A. \tag{2.50}$$

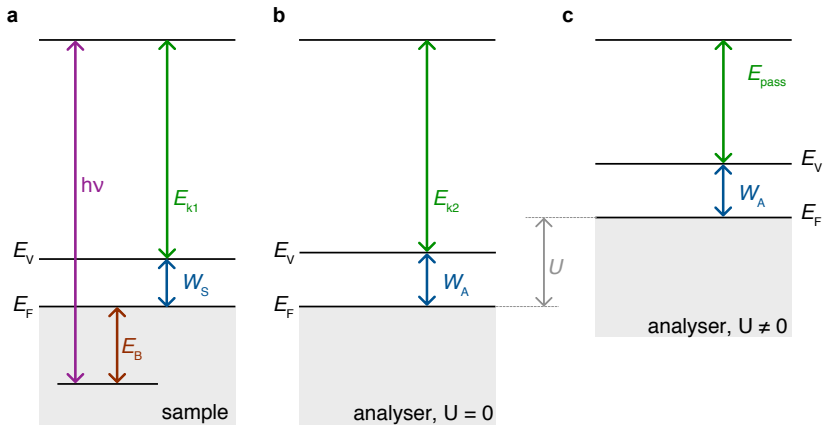

Figure 2.12.: Diagram outlining the energetics of an ARPES experiment, (**a**) in the sample, (**b**) in the analyser if there is no retardation potential, and (**c**) in the analyser with a finite retardation potential, slowing down electrons to the pass energy, E_{pass}.

Kinetic energy in the hemisphere is, however, generically *not* equal to E_{k2}, the kinetic energy of the photoemitted electron, modified by the difference in the work functions. Indeed, elementary electrostatic arguments state that the kinetic energy of the electrons travelling along the mean radius of the hemisphere (the green

trajectory in Figure 2.11) is given by:

$$E_{pass} = \frac{e\Delta V}{\frac{R_1}{R_2} - \frac{R_2}{R_1}}, \tag{2.51}$$

where e is the electron charge, ΔV is the potential difference between the two hemispheres, and R_1 and R_2 their radii. In other words, it is governed only by the hemisphere parameters. It can be tuned by changing the voltage difference between the hemispheres, and it is typically chosen to be in the range of $5 - 20\,\text{eV}$ for an ARPES experiment. Since we may be interested in a kinetic energy E_{k2} which is very different from the pass energy of the analyser, the electrons are slowed down by a retardation potential U, set by the electrostatic lenses (Figure 2.11). The retardation potential is chosen to satisfy $U = E_{k2} - E_{pass}$, leading to the overall energy conservation of the form

$$h\nu - |E_B| = E_{pass} + U + W_A, \tag{2.52}$$

as illustrated in Figure 2.12c.

E_{pass} is an important measurement parameter, as it sets both the energy range that can be accessed in a single measurement, and the energy resolution. Those are of course related: the larger the spread of energies of the electrons sorted according to the energy in the fixed space between the hemispheres, the poorer is the energy resolution. The accessible energy range is typically $\sim 10\%$ of E_{pass}. It is therefore often convenient to chose a large value of E_{pass}, in order to be able to measure the states across a wider binding energy range. If the binding energy range of interest is wider than that accessible in a single measurement with the highest pass energy, measurements are usually performed in the so-called 'swept' mode. This entails keeping the pass energy fixed, while sweeping the lens voltage U to change the kinetic energy detected at the centre of the detector.

The analyser energy resolution is theoretically set by the pass energy, entrance slit width w and the analyser acceptance angle ϕ, both marked in Figure 2.11, as:

$$\Delta E_a = E_{pass}\left(\frac{w}{R_0} + \phi^2\right), \tag{2.53}$$

where R_0 is the mean radius of the hemisphere, $R_0 = (R_1 + R_2)/2$ [33]. Typically

analysers have multiple entrance slits which can be changed by the user. Reducing both the pass energy and the entrance slit width improves the resolution, but reduces the number of electrons that can be detected, i.e. the signal. Assuming independent, random errors, the measurement energy resolution is determined by a combination of the light resolution ΔE_l, discussed in Section 2.6.1, and the analyser resolution ΔE_a, as :

$$\Delta E = \sqrt{(\Delta E_l)^2 + (\Delta E_a)^2}. \tag{2.54}$$

The electrons analysed in the schematic shown in Figure 2.11 are all travelling vertically towards the detector, within the precision given by the acceptance angle ϕ; they have no in plane momentum ($k_{||} = 0$). If the sample were rotated with respect to the analyser axis this would change, allowing for the mapping of the dependence of the photoemission intensity on the emission angle, and thus $k_{||}$. In modern setups it is, however, possible to simultaneously measure a range of electron momenta without sample movement. This is enabled by two-dimensional detectors, and elongated entrance slits, as shown schematically in Figure 2.13a. The electrons arrive on a different place along the length of the slit depending on their in-plane momentum in the direction parallel to the slit, as shown by the colours in Figure 2.13a. Their paths are curved by the electric field in the hemisphere, and their energy is therefore analysed as described above (*cf.* Figure 2.11). The position where the electron arrives on the detector now depends both on its kinetic energy and the in-plane momentum along the slit direction, as indicated in Figure 2.13a. In a single measurement the number of photoelectrons arriving at the detector as a function of their angle of emission and kinetic energy is recorded.

In Figure 2.13a I suggested that the two sides of the detector are parallel to the angle and energy axes. This is, however, strictly true only for the angular axis. To understand why the curves of constant energy are not perpendicular to the curves of constant angle, it is useful to look at a top view of the hemispherical analyser and the electron trajectories, shown in Figure 2.13b. The red, orange and yellow lines represent the electrons photoemitted with the same kinetic energy, but at three different angles, as shown in Figure 2.13a. Because the radius of the trajectory is set by the kinetic energy, the radii of the three trajectories are the same; the three lines are of the same length. However, because they entered the analyser at different positions along the straight entrance slit, their horizontal position on the detector

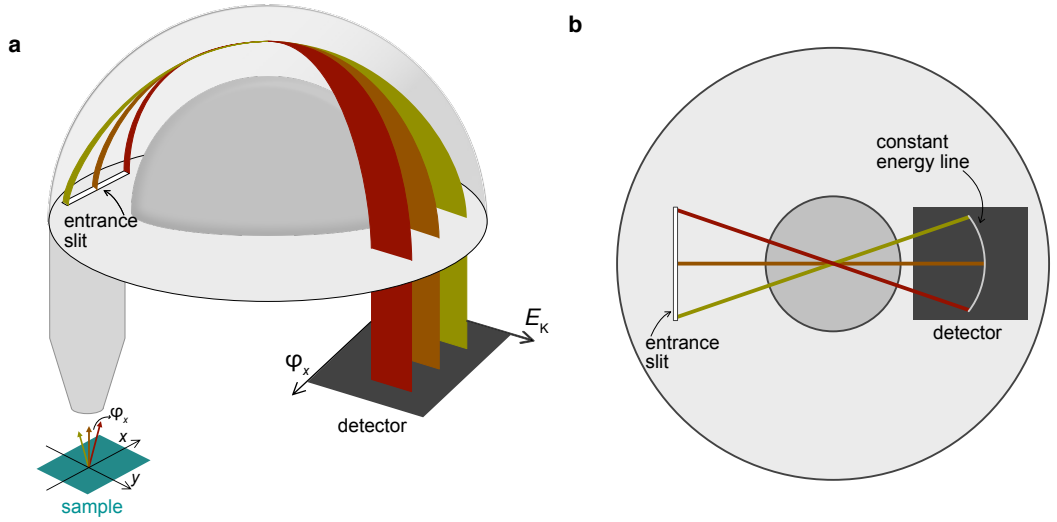

Figure 2.13.: (**a**) Schematic of a concentric hemispherical analyser. (**b**) A view from the top of the analyser. The red, orange and yellow lines represent the trajectories of electrons emitted at different emission angles φ_x.

is not the same. Consequently, a constant energy line is curved on the detector, as shown in Figure 2.13b.

There are two ways to account for this effect. One is to use a curved entrance slit instead of the straight one, with a curvature chosen to compensate the effect. Measured constant energy lines are then parallel to the detector side, thus facilitating the analysis. Curved slits, however, introduce artefacts in the mapping of the emission angle on the detector. Alternatively, a straight slit can be used to minimise experimental artefacts; the curved constant energy curves are then compensated for in the analysis. This was done for all the measurements in this thesis. To analyse the data taken with a straight slit, it is necessary to perform a reference measurement of a constant energy curve, using the same measurement conditions as in the experiment. This is typically done by measuring the spectrum of polycrystalline gold evaporated on the sample manipulator, which therefore shares the ground, and the Fermi level, with the sample. An example of such a measurement is shown in Figure 2.14a. The gold Fermi level is a curve of constant energy, and is evidently not parallel to the detector edge. The fact that the spectrum contains no features other than the Fermi level facilitates an unbiased determination of the Fermi level as a function of emission angle, which can typically be approximated by a polynomial, as shown by

the red line in Figure 2.14b. It is then easy to process all the measurements so that the energies are referenced from the known the Fermi level at every angle, as shown for the gold measurement in Figure 2.14c.

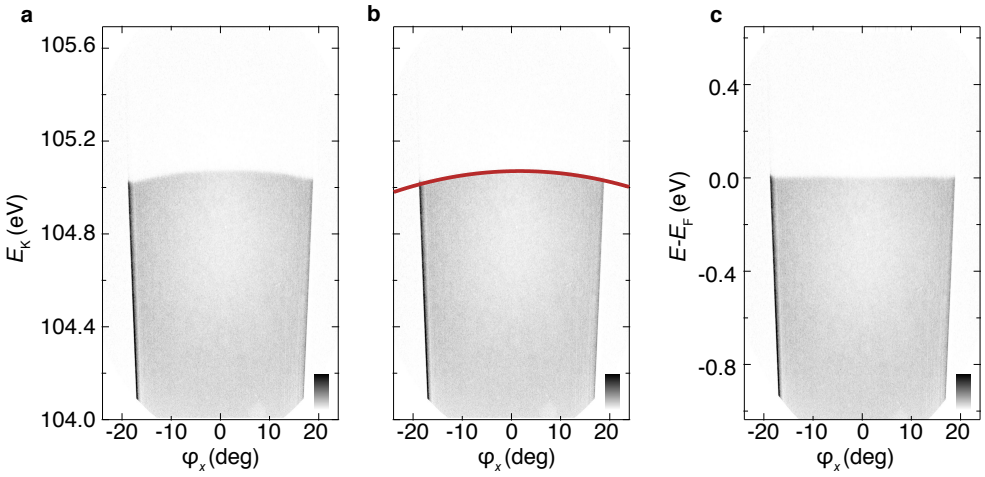

Figure 2.14.: (**a**) Raw measurement of the photoemission spectrum of polycrystalline gold. (**b**) Same as (a), with a fitted polynomial approximating the Fermi edge. (**c**) The same data as in (a), with energy expressed in relation to the fitted Fermi level.

The range of angles focused along the length of the entrance slit can be altered by changing the lens voltages, and the user can usually choose between a few options. The range of $\sim \pm 15°$ is commonly used, as was the case for the measurements of polycrystalline gold in Figure 2.14. At the photon energy of 100 eV this angular range corresponds to $\sim \pm 1.3\,\text{Å}^{-1}$, comparable to a Brillouin zone size of a typical solid. A wider angular range allows for a larger portion of the $k_{||}$ - space to be measured at once, but with a reduced momentum resolution $\Delta k_{||}$. The momentum resolution is proportional to the angular resolution of the analyser $\Delta\varphi_a$. Expressed as a function of the momentum, electron kinetic energy and the angular resolution, the momentum resolution is equal to

$$\Delta k_{||} = \Delta\varphi_a \sqrt{\frac{2mE_K}{\hbar^2} - k_{\|}^2}. \tag{2.55}$$

The finite energy and momentum resolution (Equations 2.54 and 2.55, respectively) broaden the measured signal. The spectral function modulated by the matrix

elements is convolved with a Gaussian of widths $\Delta k_{||}$ and ΔE in the momentum and energy directions, respectively. This broadening can affect the line shapes of the one-dimensional cuts extracted from the measurement. As discussed in Section 2.5, the MDCs of the spectral function are Lorentzian as long as the self-energy is momentum independent. However, the finite energy resolution leads to the mixing of states of different energies in an MDC extracted from a measurement. The Lorentzian shape is therefore not necessarily preserved, although it usually remains a good approximation. This is important to keep in mind whenever a deviation from the Lorentzian MDC shape is observed - this may imply momentum-dependent self-energy, but can also be an artefact of finite measurement resolution. In addition to these considerations due to the measurement of photoelectron energy and momentum, sample imperfections can also impede the extraction of intrinsic properties of the spectral function. For instance, if the sample is slightly curved, electrons of any given crystal momentum may leave the sample in a range of emission angles. Furthermore, the cleaved surface can sometimes contain flakes inclined with respect to each other, leading to the measurement of a few copies of the same feature which may or may not be clearly resolvable. We often saw such feature-doubling in delafossites, and we also suspect some of the samples were slightly bent. The inhomogeneity of the cleaved surface was therefore typically the factor setting the final measurement resolution.

So far I have treated the electron detector as a black box, enabling the detection of electrons arriving at it. In practice the detectors consist of one or several microchannel plates (MCPs), followed by a phosphor plate imaged by a charge-coupled device (CCD) camera. The MCP consists of a series of channels made in a highly resistive material, to which a high electric field is applied. As electrons enter the channels, they collide with their walls, exciting many more electrons and thus amplifying the signal. When the fast electrons reach the fluorescent phosphor screen light is produced, and the image of the screen is then taken by the camera. With an appropriate photon flux and signal intensity it is possible to monitor the live camera image of the electron distribution in k - space, observing how it changes as we modify the measurement settings or sample angles. For a measurement, data are collected for a length of time chosen according to the intensity of the signal and the statistics needed.

Example data sets

As an example of unprocessed ARPES data, in Figure 2.15 I show a data set[4] measured on a CoO_2 layer of $PdCoO_2$. The two axes are the emission angle, and the kinetic energy[5] of outgoing electrons, while the colour of each pixel encodes the number of electrons that were detected on that position in the measurement time. The first step towards understanding a plot of ARPES data is to look at the colour scale used, as shown by the legend which should be available with the plot. In Figure 2.15a a simple grayscale is used, with white representing no counts and black the highest number of counts detected in a pixel. The detector edges, beyond which there are no more counts, are clearly visible. The data in their vicinity can be distorted, so it is good practice to set up the measurements such that the features of interest are far from the detector edges, preferably in its centre.

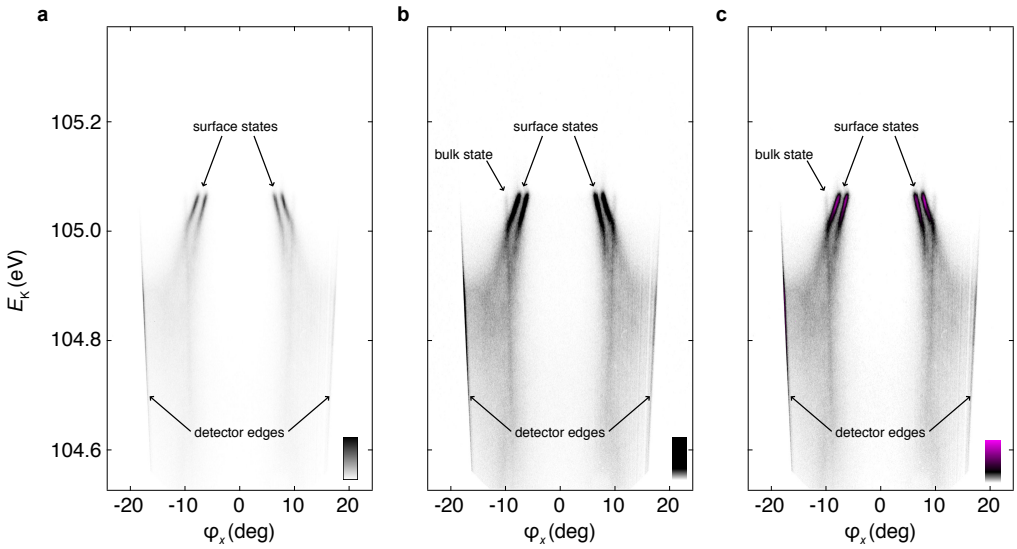

Figure 2.15.: Example data set from a CoO_2 terminated surface (see Chapter 6), plotted in different colour-scales.

[4]The analysed data from the same sample are shown in Chapter 6 and Appendix D. The same data, but processed, are shown in Figure 6.1e. The physics of these states is discussed in Chapter 6 ; here I just use them as an example measurements.

[5]Actually a combination of kinetic energy and emission angle, because a straight analyser entrance slit is used. This is a small enough effect not to impede any qualitative discussion, and is compensated for in the analysis, as described above.

The most intense features are the two states at the Fermi level, each of which appears symmetrically at positive and negative angles; those are in fact the surface states originating from the CoO_2 - terminated surface, and will be discussed in Chapter 6. Additionally, there is a much weaker, hardly visible, fast dispersing band. Those weak features are more prominent if the same data are plotted in a saturated grayscale, as shown in Figure 2.15b. The weak feature, which is in fact a bulk state discussed in Chapter 4, is now more visible. However, all the intense features are now black, and therefore information on the intensity variation between them is lost. For instance, in Figure 2.15a it can be seen that the two positive-angle features at the Fermi level do not have the same intensity; the one at the larger angle is darker. This information is lost in the over-saturated plot. To avoid information loss, while showing features of a range of intensities, more complex colour-scales can be used. A type of colour scale I have used when necessary throughout the thesis is one in which white corresponds to no counts, black to some intermediate count number, chosen to bring out the weak features, while the largest count number corresponds to a bright colour, such as pink or green. When the same data are plotted in this way (Figure 2.15c), the weak bulk band can be seen, but so can the variation of intensity between the intense surface states. Sometimes even more complex colours-scales are used. Whenever this is the case it is important to look at the legend, and understand how the colours used to represent the data correspond to the measured intensities.

To show how the analyser parameters affect the measurable range of angles and energies, in Figure 2.16 I show data similar to those in Figure 2.15, but taken in a range of measurement conditions. In the measurement shown in Figure 2.16a (the same data as in Figure 2.15) a pass energy of 10 eV was used, leading to a measurement range of 0.84 eV across the detector. In the angular lens mode used, called Ang30, the electrons leaving the sample in a $\sim \pm 15°$ range of emission angles are dispersed along the length of the entrance slit. In Figure 2.16b the same pass energy was used, but a different angular mode (Ang14), in which the length of the slit corresponds to the $\sim \pm 7°$ range of emission angles. A smaller portion of k - space is mapped, but with a higher angular resolution. Because of the artefacts due to the sample surface homogeneity, reducing the measured angle range to improve the angular resolution was of limited value in delafossites. The measurements in the two angular modes, but with a pass energy of 5 eV, are shown in Figures 2.16(c,

d). The lower pass energy leads to a smaller accessible energy range of 0.42 eV, but higher energy resolution. The kinetic energy at the centre of the detector was set to be 104.95 eV in all of the measurements shown here.

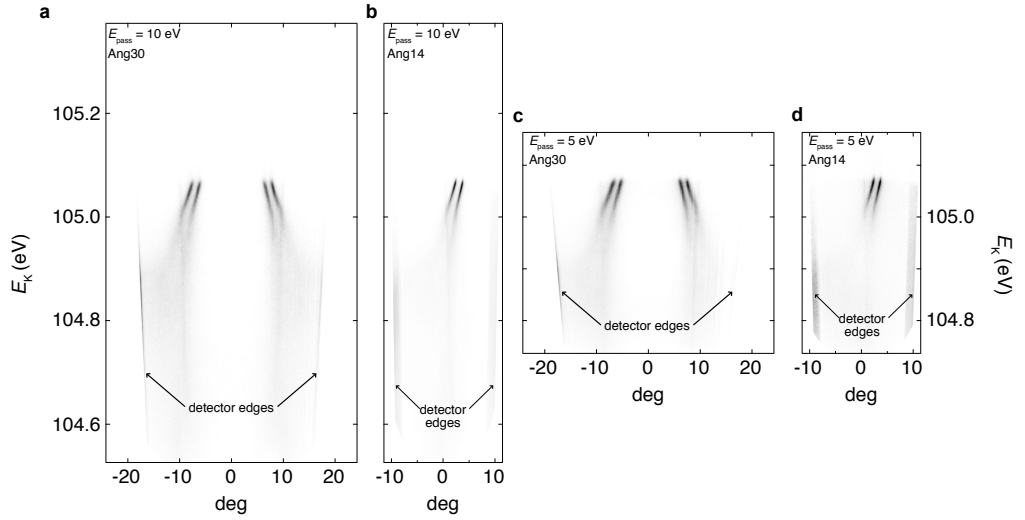

Figure 2.16.: Example data set from a CoO_2 terminated surface (see Chapter 6) measured in different pass energies, and lens angular modes determining the angular range of the electrons along the slit: (**a**) $E_{pass} = 10$ eV, 30 deg range across the slit (Ang30), (**b**) $E_{pass} = 10$ eV, 14 deg range across the slit (Ang14), (**c**) $E_{pass} = 5$ eV, Ang30 and (**d**) $E_{pass} = 5$ eV, Ang14.

2.6.4. Sample angles

In the previous section I discussed the information that can be accessed in a single measurement, without sample movement. However, changing the sample angles with respect to the analyser axis allows for a wider range of k - space to be mapped. This is done in practice by changing the manipulator angles. Ideally the sample is parallel to the manipulator, although small deviations are possible. In this section I will discuss briefly how the rotation around the three axes affects the measurements. The three angles corresponding to the three rotations are called polar, tilt and azimuth, as indicated on Figure 2.17 for a coordinate system in which the x - axis is vertical, and the z axis normal to the sample surface. I will assume here that the analyser entrance slit is vertical; for a horizontal slit the influences of the polar and the tilt angle are reversed.

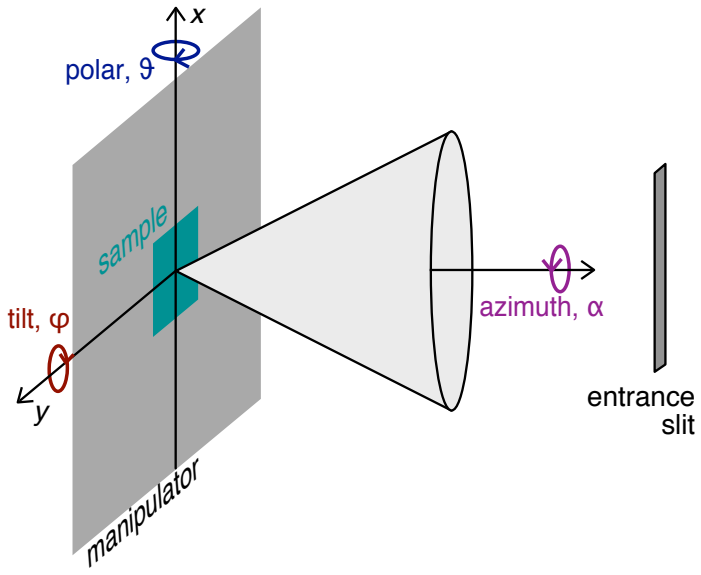

Figure 2.17.: Schematic of a sample on a manipulator plate and the analyser, showing the three angles needed to describe their relative position.

If both the polar and the tilt angle are set to zero, the electrons with no in-plane momentum travel straight towards the entrance slit, and eventually appear in the middle of the detector. States of finite in-plane momentum along the slit direction appear at finite angles. This is the case, for instance, in the measurements shown in Figures 2.16(a, c), leading to the observed symmetrical spectra. However, even when the states of interest have a finite in-plane momentum we may wish to measure them at the centre of the detector. This can be achieved by changing the tilt angle of the sample; the electrons emitted from the sample at a finite angle of emission are now directed towards the middle of the slit, and therefore observed at the centre of the detector, as shown in Figures 2.16(b, d) above. To explicitly show how the states move on the detector as a function of the tilt angle, in Figure 2.18 I plot the same bands measured at different values of φ. As well as the states moving across the detector, it is also clear that the data quality depends somewhat on the tilt; at $\varphi = 16°$ it is noticeably poorer than for example at $\varphi = 8°$. This is probably in part due to the effects of the edge of the detector, but also because the focus of the analyser changes slightly as a function of the tilt, and in this case was optimised for $\varphi = 8°$. In the measurements in which the states are close to the edge of the

detector, such as the $\varphi = 0°$ measurement, the curved Fermi edge is also clearly visible.

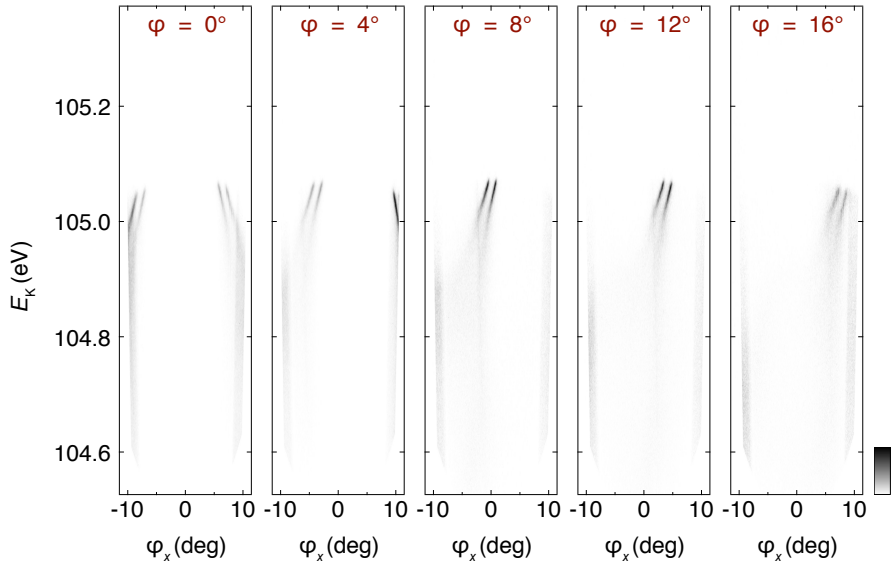

Figure 2.18.: Example data set measured with a varying tilt offsets φ, as indicated in the panels.

In all of the measurements discussed so far the detected electrons had a finite momentum along the slit direction, k_x, but vanishing momentum along the other in-plane direction, k_y. This changes if the polar angle ϑ (Figure 2.18) is finite, allowing for the mapping out of the two dimensional momentum space. As changing the polar angle leads to the probing of a different part of momentum space, the measurements taken at two distinct values of ϑ can look very different, and be difficult to instantly relate to each other. An example of this can be seen in Figures 2.19(a, b), where I show the dispersions measured at two values of the polar angle differing by $\sim 7°$. Measurements at many closely spaced values of ϑ are typically taken, in order to obtain information on the electronic structure evolution across momentum space. All of these data are combined into a three dimensional data set (φ_x, ϑ, E_K), from which arbitrary two-dimensional cuts can be extracted. The most common two-dimensional cut is the constant energy cut at the Fermi level; once angles are converted to momenta this corresponds to the Fermi surface. An example of such a cut is shown in Figure 2.19c. It is built from 250 dispersions, each measured for 10 seconds, with an increment of the polar angle of 0.2° between

them. The dispersions shown in Figures 2.19(a, b) are two of these 250 dispersions, taken at the ϑ values indicated in 2.19c.

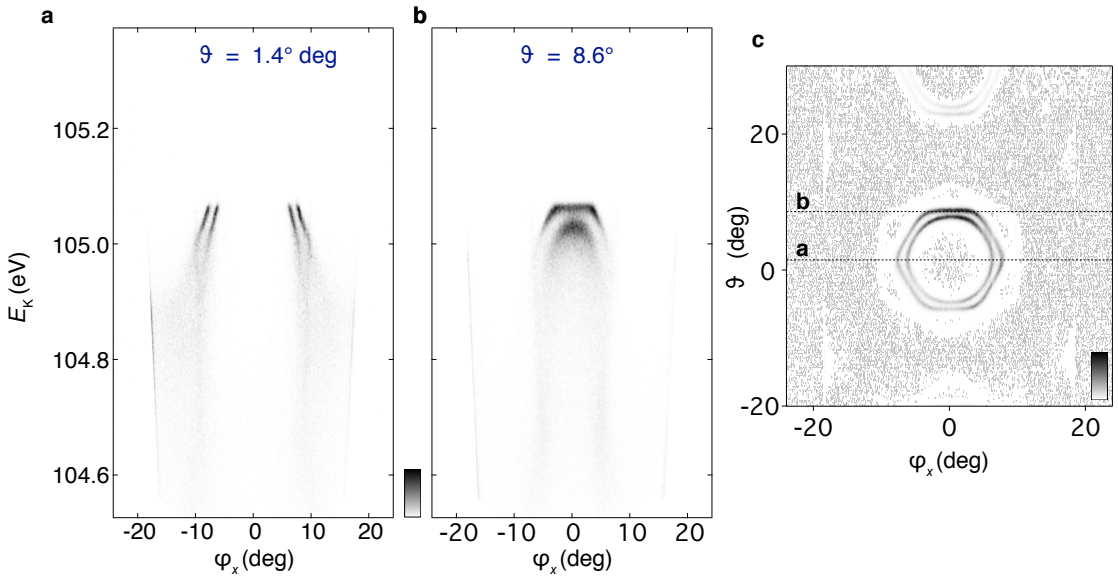

Figure 2.19.: Example data set measured with the polar angle (**a**) $\vartheta = 1.4°$ and (**b**) $\vartheta = 8.6°$. (**c**) A constant energy cut at the Fermi level, extracted from a three dimensional data set consisting of 250 dispersions like the ones shown in (a, b), each taken at a different polar angle, with increments of 0.2° between them.

The polar and the tilt angles can be converted into the two dimensional momentum as

$$k_x = k \sin(\varphi_x - \varphi + \varphi_0) \cos(\vartheta + \vartheta_0) \quad k_y = k \sin(\vartheta + \vartheta_0), \tag{2.56}$$

where φ_x is the angle along the slit direction, while φ and ϑ are the tilt and polar angles as determined by the manipulator. If the sample is not perfectly parallel to the sample plate, there can be a small offset between the manipulator and the sample angle; this is captured by φ_0 and ϑ_0. They can be found by inspecting the symmetry of the measured spectra. For instance, it is evident in Figure 2.19c that the high symmetry cut corresponding to the corner of the hexagon is measured at a finite $\vartheta = 1.4°$, implying a polar offset of the sample of $\vartheta_0 = -1.4°$. The total momentum of the free electrons in vacuum is related to their kinetic energy as

$$k = \sqrt{2mE_K} = 0.5123\sqrt{E_K/\mathrm{eV}}\,\mathrm{\AA}^{-1}. \tag{2.57}$$

The azimuthal angle does not influence k_x and k_y as defined above, but it determines the angle between k_x and k_y and the sample crystalline axes. Practically, this means that changing the azimuth results in the 'rotation' of the measured electronic structure; if the azimuth is rotated by an angle α, so are the measured constant energy contours shown in Figure 2.19c. This enables the measurement of the electronic structure along different high-symmetry directions in the zone in a single measurement. In multiple cases in the thesis I will be showing data taken both along the $\overline{\Gamma} - \overline{K}$ or the $\overline{\Gamma} - \overline{M}$ directions of the hexagonal Brillouin zone; these measurements were obtained by changing the azimuth by 30°. The ability to change the azimuth also means it is not necessary to orient the samples prior to the measurements. Rather, the orientation is determined *in-situ* by a quick version of a map shown in Figure 2.19c, and the relevant direction reached by the azimuthal rotation.

2.6.5. Surface terminations in delafossite oxides

One of the reasons a small light spot and the high degree of motion control is particularly important for measurements on delafossites are the surface states hosted by their polar surfaces, introduced in Section 1.2.1. The example data sets shown in the previous section all show very intense features arising from the CoO_2 - terminated surface, very weak bulk states, and no traces at all of the states expected of a Pd - terminated surface. However, in the course of our photoemission investigation of $PdCoO_2$ we were able to observe both the states originating from the CoO_2-terminated surface and the Pd - terminated surface. By surveying the whole surface of the sample we could often observe signatures of both types of surfaces on the same sample, indicating that surface termination changes across the cleaved crystal, as shown schematically in Figure 2.20a. The ability to reproducibly move between patches of different terminations allowed us to reliably compare their features. A schematic of one such sample we have measured is shown in Figure 2.20b, with the three spots at which measurements were taken marked by yellow ellipses. The size of the ellipses indicates the size of the light spot on the sample, $\sim 90 \times 20\,\mu m$ in the settings used here. To identify the relative composition of the surface in the three locations, we measured the x-ray photoemission spectrum (XPS) at each one of them, across a binding energy range covering both the Co $3p$ and the Pd $4p$ core levels.

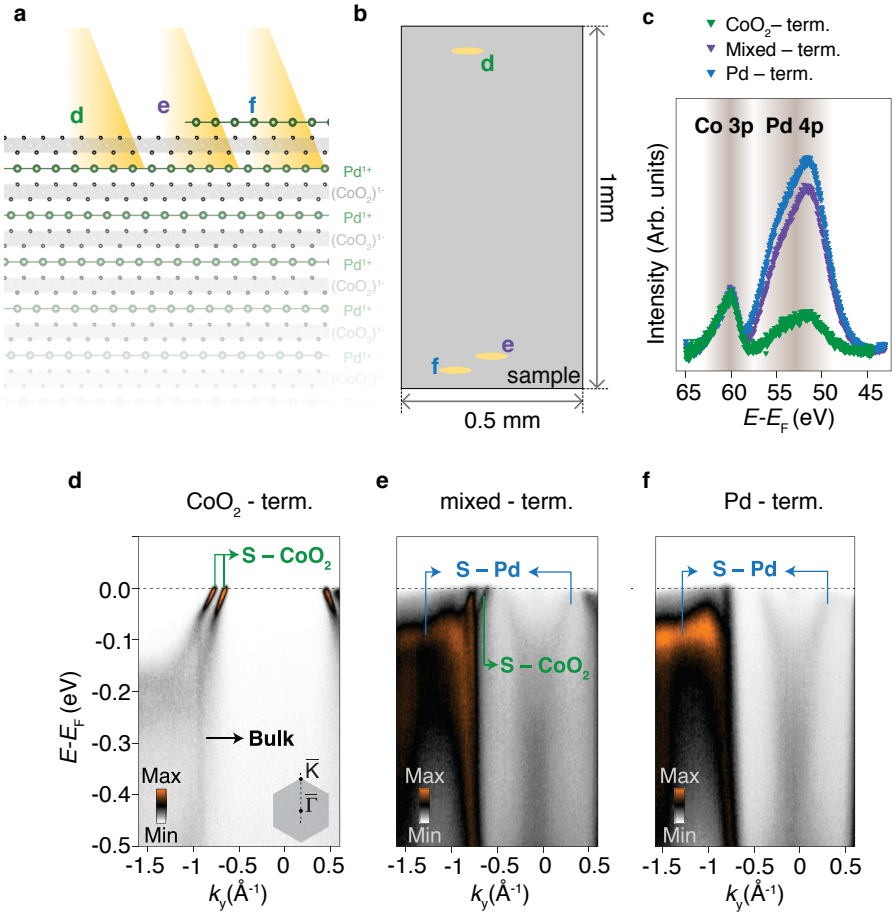

Figure 2.20.: (**a**) Side view of the crystal structure of $PdCoO_2$, showing two expected surface terminations. (**b**) A 'map' of the sample, with the light spot positions at which the measurements in panels (c-f) were taken marked by yellow ellipses. The size of the rectangle corresponds to the nominal light spot size. (**c**) XPS spectra ($h\nu = 120\,\mathrm{eV}$), after subtraction of a linear background and normalised by the area of the Co 3p peak, at different spatial locations of a cleaved crystal, as indicated in (b). The electronic structure measured (**d**) on the CoO_2- termination, (**e**) on the mixed termination and (**f**) on the Pd - termination. Panels c-f courtesy of Federico Mazzola [10].

As evident in 2.20c, the relative intensity of the two peaks changes across the sample, with the highest Co and Pd contributions in the positions marked d and f in Figure 2.20b, respectively. The angle resolved photoemission spectra measured at the same three positions are shown in Figures 2.20(d-f). The spectrum measured at the position with the highest Co contribution (Figure 2.20d) shows two surface

bands crossing the Fermi level, as predicted by the calculations for the CoO_2 - termination. The spectrum at the Pd-rich position (Figure 2.20f) shows an electron like-pocket centred at the $\overline{\Gamma}$ - point, as well as a fully occupied flat band at the $\overline{K}$ - point, consistent with the DFT prediction for a Pd - terminated surface. A spectrum measured at an intermediate point (Figure 2.20e) exhibits both types of features, therefore showing that both types of terminations can be present in a region covered by the light spot.

In practice, the vast majority of the spectra we measured on $PdCoO_2$ showed signatures of the CoO_2 - derived surface states. Those states also appeared to be very robust. When we attempted to remove them using thermal cycling, or by exposing a cleaved surface to a pressure as high as $\sim 10^{-8}$ mbar in in the load lock, they would still remain observable, although less intense and not as sharp as immediately after cleaving. What is more, the signal tended to become better defined again after a prolonged measurement in the high intensity light beam, indicating a surface photochemical reaction 'cleaning' the surface. We also observed similar states on the transition metal oxide terminated surfaces of $PtCoO_2$ and $PdRhO_2$. They, and the physics underlying them, are described in detail in Chapter 6.

In contrast, the surface states originating from the Pd - terminated surface appeared to be much more sensitive to the purity of the surface, and were removed by thermal cycling. Although statistically both surface terminations should appear with equal probability, we did not observe the features originating from the Pd-terminated surface as often as those originating from the CoO_2 - terminated surface. In addition to the Pd-surface states being more purity - sensitive, it is possible that a larger homogeneous region of uniform surface termination is needed to support coherent surface states on the Pd-terminated surface. In the vast majority of measurements in which we were able to observe the Pd-terminated states, the spectra contained features of both terminations, similar to the spectrum shown in Figure 2.20e, testifying to the surface inhomogeneity. We were also able to observe similar surface states in our measurements of $PdCrO_2$, consistent with previous findings of Sobota et al [28]. The basic phenomenology and physics of the Pd - terminated surface states are described in Appendix B.

In addition to the measurements showing signatures of one of, or both, surface terminations, we twice measured cobaltate samples which showed no signs of surface states, once in each $PdCoO_2$ and $PtCoO_2$. In both cases the samples cleaved

badly, leaving only a very small patch of the surface available for measurements. It is likely that in those cases the surfaces were too disordered to support coherent surface states. We were, however, able to measure the bulk states originating from the subsurface layers. Because the surface states were not there to complicate the analysis, those two samples are most suitable to deduce the bulk properties of delafossites, and I analyse them in detail in Chapter 4.

2.6.6. Resonant photoemission

As I have already mentioned, the best in-plane momentum resolution is achieved when using low photon energies. On the other hand, the probing depth is larger, and the k_z determination more precise, when the measurements are performed with high photon energies, in the soft x-ray energy range of $100 - 1000\,\mathrm{eV}$. Another motivation to perform photoemission measurements at these high photon energies is the opportunity to use resonant photoemission to investigate the atomic character of electronic states. We used soft x-ray ARPES for this reason in the study of $PdCrO_2$ when we wanted to identify the states derived from the Cr $3d$ orbitals, as described in Section 5.3.2.

Resonant photoemission can be used to investigate atomic contributions of any atom which has a well-defined x-ray absorption edge in the accessible photon energy range. To understand how resonant photoemission allows for the determination of atomic character, it is necessary to first understand the basics of x-ray absorption. A photon creates a hole in a core level of an atom, displacing an electron to an unoccupied state of the same atom (Figure 2.21a). Those electrons can be detected in form of the 'drain current' I_D, measured between the sample and ground, and are often used as a measure of the x-ray absorption cross-section. The core hole lifetime is on the order of a femtosecond, after which it is filled by an electron from a shallower core level, or the valence band. Crucially, as the hole is localised at the atom, the electron filling it also originates from the same atom, indicated by the green colour in Figure 2.21. The energy of the electron filling the hole is reduced in the process, and released either as a photon or as a photoemitted electron, corresponding to the fluorescent and Auger decay channels, respectively (Figure 2.21(b, c)).

Both of these decay channels, however, treat the creation of the core hole and its decay as independent processes. This need not be the case, as the excited electron

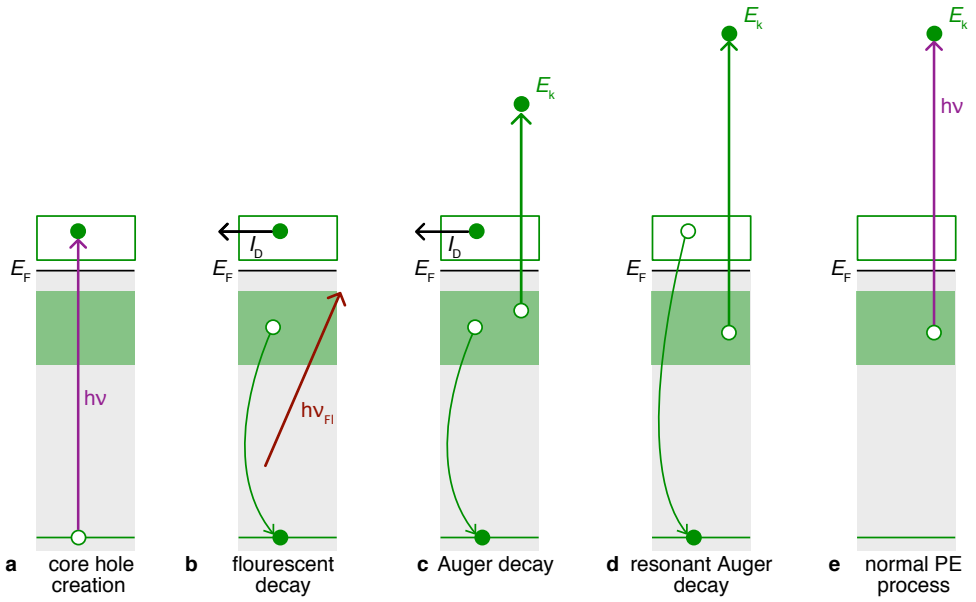

Figure 2.21.: Schematic representing the (**a**) creation of a core level hole by x-ray absorption, and the decay of this hole via (**b**) emission of a photon (fluorescent decay), (**c**) emission of an electron (Auger decay) and (**d**) emission of an electron using the excited electron (resonant photoemission). The resonant photoemission process had the same initial and final states as a regular photoemission process (**e**). The full and empty green rectangles indicate the occupied and unoccupied states, respectively, derived from the atom in whose core level the hole is created. E_F and E_V mark the Fermi level and the vacuum level, respectively.

displaced from the core level can also fill the hole at a later time (Figure 2.21d). Crucially, the energy released in this process is exactly equal to the energy of the photon which created the hole in the first place. The final state of the electron emitted in this *resonant* Auger process is therefore the same as the final state of an electron emitted in a regular photoemission process, with the same photon energy, and originating from the same initial state (Figure 2.21e). Both the resonant and the normal photoemission processes happen simultaneously and constructively interfere, leading to the atom-specific resonant enhancement of the photoemission signal.

We used the i09 beamline at the Diamond synchrotron for our resonant ARPES measurements. The general discussion of photoemission experiments in sections 2.6.1-2.6.4 applies to our soft x-ray measurements as well. However, the overall cross-section for soft x-ray ARPES is small, so high energy resolution usually has to

be sacrificed to increase the photon flux. For instance, pass energy as high as 80 eV, instead of ~ 10 eV at the high resolution i05 beamline, is used. In $PdCrO_2$ we used the Cr L x-ray absorption edge, corresponding to the transitions between the Cr $2p$ and the Cr $3d$ orbitals. The Cr L edge is split by the atomic spin-orbit coupling into two peaks, labelled L_2 and L_3, in the energy range $570 - 600$ eV [57]. The exact shape of the absorption peaks depends on the bonding environment and the interactions of the core-hole. We therefore determined the x-ray absorption cross-section of $PdCrO_2$ *in-situ*, by measuring the drain current as a function of photon energy. We see two clear absorption peaks, corresponding to the $L_{2,3}$ edge (Figure 2.22). When photon energy coincides with the absorption peak the photoemission signal originating from the Cr $3d$ orbitals is enhanced, due to the process sketched in Figure 2.21d.

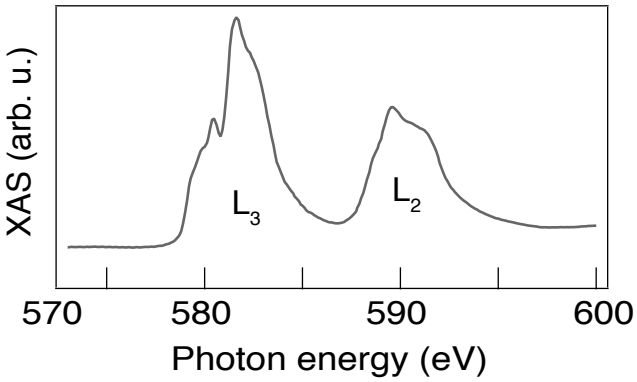

Figure 2.22.: X-ray absorption spectrum across the $L_{2,3}$ edge of Cr.

2.6.7. Spin-resolved photoemission

So far I have described how the hemispherical analysers enable the mapping of the dependence of the quasiparticle energy on its momentum. In the vast majority of solids each state which is detected in this way is degenerate, because the states of opposite spin, but same momentum and band index, have the same energy. This, however, need not be the case; as discussed in Chapter 6, if either the time reversal symmetry or the inversion symmetry are broken, band structures can lose their spin degeneracy. To experimentally determine whether a band structure is spin-split, and

learn more about the k-dependence of this splitting, it is necessary to measure the spin of photoemitted electrons, while keeping the information on their momentum and energy. This can be done in several ways. A hemispherical analyser of the type described in Section 2.6.3 is used to sort the electrons according to their energy and momentum. However, not all of the electrons are passed onto the MCP. Rather, the ones of chosen momentum and energy pass through apertures placed above and below the MCP, and are guided towards a spin-sensitive detection system. One method of providing spin contrast which is commonly used is the Mott scattering of fast electrons off heavy-element targets, whereby the spin-orbit coupling of the heavy element causes a scattering asymmetry of the spin-polarised electrons. The spin-resolved measurements in this thesis were done using a different technique, namely very low energy electron diffraction (VLEED). The technique relies on the spin-dependent reflectivity of very low energy electrons at a magnetised ferromagnetic target, usually an oxygen-passivated Fe(001) film, as described in Reference [58]. Such setups currently exist as user facilities at Hiroshima Synchrotron Radiation Center [59, 60], and at the APE beamline at the Elettra synchrotron in Italy [61]; we used the latter setup, shown schematically in Figure 2.23.

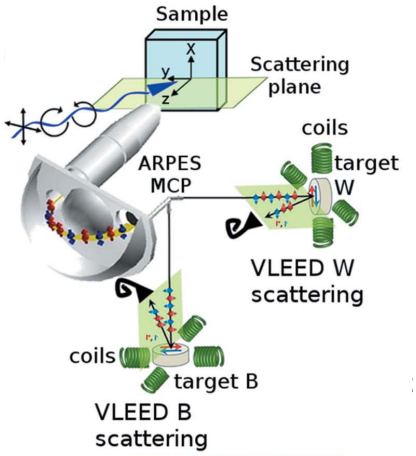

Figure 2.23.: Schematic of the spin-resolved ARPES setup at the APE beamline at Elettra synchrotron. Reproduced with permission of the International Union of Crystallography from Reference [61].

A set of lenses and deflectors is used to focus the electrons of specified energy and momentum onto two targets, labeled W and B, for white and black. Each of the targets can be magnetised using pairs of Helmholtz coils, either in the direction perpendicular to the sample plane, or in one of the directions parallel to the sample plane; x for the 'white' and y for the 'black' detector in the coordinate system outlined in Figure 2.23. This in principle allows the measurement of the spin projection on each of the three axes in consecutive measurements. The out-of-plane spin can be measured independently with the two targets, providing a natural way to compare the target efficiencies, and to estimate measurement uncertainty. To measure spin polarisation in a single direction two measurements need to be performed, with the opposite magnetisations of the target. In practice, we always take at least four measurements, two of each magnetisation. The target magnetisation is chosen as $\uparrow\downarrow\downarrow\uparrow$ for the four measurements, where $\uparrow$ and $\downarrow$ denote the two magnetisation directions, in order to compensate for any systematic errors which may arise due to the ageing of the target, or other time-dependent artefacts. If the band structure is spin degenerate, the measurements with different target magnetisations yield the same intensity, while any differences in the intensity encode the spin polarisation of the electronic structure. If $I^{\uparrow}$ and $I^{\downarrow}$ are the intensities measured with the target magnetised in the opposite directions, the intrinsic spin polarisation is given by

$$P = \frac{1}{S}\frac{I^{\uparrow} - I^{\downarrow}}{I^{\uparrow} + I^{\downarrow}}, \tag{2.58}$$

where S, called the Sherman function, quantifies the discriminatory power of the detector. The larger the Sherman function, the larger is the measured asymmetry of the signal for a given intrinsic polarisation. In the VLEED detectors it depends highly on the target quality, so every target needs to be individually characterised. Practically this is done by comparing the spin polarisation measured on a well-known system, typically the (111) surface of gold, with the literature values [62]. For VLEED detectors S is usually in the range $0.1-0.4$; it was 0.3 for our measurements.

The efficiency of the technique is not governed by the Sherman function alone, but also by the reflectivity of the target, which is $\sim 10^{-1}$ at the kinetic energy of the electrons used in the experiment [59, 61]. In other words, a measurement done using VLEED detection is 10 times less efficient than using regular ARPES detection. What is more, a measurement of spin-polarisation requires the differ-

ence of the signals measured with the two target magnetisations to be larger than the statistical noise. As the statistical noise decreases with total electron count N only as $1/\sqrt{N}$, long measurements are usually needed to obtain reliable information on spin polarisation. A measurement of a single momentum resolved curve of spin polarisation may take on the order of $2-3$ hours. Because of the poor efficiency of the technique the beamline and analyser settings are usually chosen to prioritise high flux over the energy resolution.The energy resolution of the spin resolved measurements is determined by a combination of the factors affecting the resolution of spin-integrated ARPES, and the size of the apertures through which electrons pass before reaching the magnetised targets. The size of the aperture also determines the angular integration range of the measured electrons, therefore setting the momentum resolution. At the APE beamline there are four different apertures which can be exchanged *in-situ.*

We used spin-resolved photoemission to look into the spin-character of the surface states on the CoO_2 - terminated surface of $PtCoO_2$. More specifically, we were interested in the difference of the spin polarisation of the two intense bands, shown for $PdCoO_2$ in Figures 2.15 - 2.19 above. The energy resolution in the settings we used was $\sim 100\,\mathrm{meV}$, comparable to the energy scale of the features in the electronic structure of interest (*cf.* Figures 2.15 - 2.19). Quantitative determination of the value of the intrinsic spin-polarisation was therefore not possible in this system. However, it was possible to track its variation in momentum space, and in particular its change of sign. In practice, to be confident that the measured spin-polarisation is not an experimental artefact, it is important to measure a spin-degenerate feature in the band structure, for example at high binding energies, and show that the measurement really shows no spin-polarisation in that case. This was done systematically for all of our spin resolved measurements. The result of these is shown in Figure 6.4, and the causes of the observed spin polarisation are the main topic of Chapter 6.

3. Theory and Models

Our experimental motivated a number of calculations, which helped to develop an understanding of the measured electronic structure, as well as motivating additional experiments. Density functional theory calculations, their downfolding onto a set of Wannier orbitals, and minimal tight binding models were all used to understand both the bulk electronic structure of non-magnetic delafossites (discussed in Chapter 4), and the surface states found on their transition metal oxide terminated surfaces (Chapter 6). My aim in this chapter is to describe these theoretical approaches at the level I found useful during the research described in the thesis. For instance, I did not perform the density functional theory calculations myself, but had the pleasure of working with Helge Rosner, the output of whose calculations I have used to address the questions inspired by the experiments. On the other hand, I constructed the tight-binding models which are much less material-specific than the density functional theory calculations, but are easier to manipulate and use to gain direct physical insight. I will briefly describe the theory and approximations underlying each of these approaches, as well as their scope and range of applicability. I will outline the way they were used to study delafossites, and point to the sections where the results of such procedures are shown in this thesis.

3.1. Tight binding models

If the aim is conceptual simplicity and isolating the essence of features observed in a band structure, while detailed agreement with experiment is not sought, it is often useful to construct tight-binding models starting from atomic orbitals, using the Slater-Koster parametrisation [63]. While such models can in principle correctly capture the overall features of the band structure, their numerical predictions are physically relevant only if the free parameters of the models are deduced based on some additional information, such as experiments or first principles calculations.

The essence of the tight-binding models is the construction of Bloch wave functions from localised orbitals:

$$\psi_{n,\vec{k}}\left(\vec{r}\right) = \frac{1}{\sqrt{N}}\sum_{i} \exp\left(\imath\vec{k}\cdot\vec{R}_i\right)\varphi_n\left(\vec{r}-\vec{R}_i\right), \tag{3.1}$$

where $\varphi_n\left(\vec{r}-\vec{R}_i\right)$ is the n-th orbital localised on site i. The effective single-particle Hamiltonian $H\left(\vec{r}\right)$, which contains contributions from ionic potentials of all the atoms[1], needs to be expressed in the basis of these Bloch functions. If there are M atomic orbitals, the Hamiltonian is an $M \times M$ matrix, with the components given by:

$$H_{n,m}\left(\vec{k}\right) = \frac{1}{N}\sum_{i,j} \exp\left(\imath\vec{k}\cdot\left(\vec{R}_i-\vec{R}_j\right)\right)\int d\vec{r}\varphi_m^*\left(\vec{r}-\vec{R}_j\right)H\left(\vec{r}\right)\varphi_n\left(\vec{r}-\vec{R}_i\right), \tag{3.2}$$

where the sum goes over all the pairs of atomic orbitals. If the integrals in equation 3.2 had to be calculated for all pairs of orbitals and atomic sites, this approach would be computationally heavy, and of limited value. However, as Slater and Koster pointed out, with a few assumptions the integrals can be replaced with a small set of constants, which are then used as fitting parameters. The first assumption is that the orbitals on different sites are orthogonal to each other. This is not true for actual atomic orbitals, but a transformation between these and the so-called Löwdin orbitals, which are orthogonal, is always possible. These orbitals have the same symmetry as the atomic ones, so unless an explicit calculation of integrals in equation 3.2 is performed, and only symmetry considerations are used, it can be assumed that the transformation was done, and we can proceed with Löwdin orbitals as we would with atomic ones. The second approximation simplifies the Hamiltonian $H\left(\vec{r}\right)$ used to calculate the matrix elements. Specifically, only the central potentials of the two atoms whose wave functions are integrated are kept, simplifying the integrands in equation 3.2 to

$$\int d\vec{r}\varphi_m^*\left(\vec{r}-\vec{R}_j\right)\left(V_c\left(\vec{r}-\vec{R}_j\right)+V_c\left(\vec{r}-\vec{R}_i\right)\right)\varphi_n\left(\vec{r}-\vec{R}_i\right), \tag{3.3}$$

[1]It can also implicitly contain interactions, through renormalised parameter values.

where $V_c\left(\vec{r}-\vec{R}_i\right)$ is a central potential around i-th atom. Within this approximation, called the two-centre approximation, the integrals are the same as the ones which appear when considering a diatomic molecule, with the distance between the two centres, $\vec{R}_i-\vec{R}_j$, defining an effective molecular axis. In this limit the language and methodology developed to describe the molecular bonding of diatomic molecules can be utilised to describe the bonding in solids [64]. In particular, the bonding is allowed only if the orbitals on the two sites have the same symmetry with respect to rotation around the molecular axis. Orbitals are grouped according to their symmetry into the σ, π and δ orbitals, which can be combined into the well-known σ, π and δ bonds. A visual way to determine the symmetry of an orbital is to imagine looking at it from the molecular axis: if it has one lobe it is a σ orbital, if it has two lobes it is a π orbital and if it has four it is a δ orbital. For example, for a molecular axis along the z direction the s, p_z and $d_{3r^2-z^2}$ orbitals are of σ symmetry, p_x, p_y, d_{yz} and d_{zx} are of π symmetry, and d_{xy} and $d_{x^2-y^2}$ are of δ symmetry. The integral between the atomic-like α and β orbitals forming a bond of η symmetry is denoted $V_{\alpha\beta\eta}$. Crucially, in this approach these integrals are not actually calculated, but rather treated as free parameters, whose number is limited by the symmetry considerations outlined above. For instance, hopping between p orbitals is governed by two integrals, $V_{pp\sigma}$ and $V_{pp\pi}$, as is hopping between p and d orbitals, $V_{dp\sigma}$ and $V_{dp\pi}$. On the other hand, there are three independent integrals describing the hopping between d orbitals: $V_{dd\sigma}$, $V_{dd\pi}$ and $V_{dd\delta}$. The values of the integrals depend on the radial parts of the wave functions, and the interatomic distance; they are usually the largest for nearest neighbours, so often only the nearest neighbours, or next-nearest neighbour terms are kept.

Many such 'diatomic molecules' need to be considered in a solid, with molecular orbitals pointing in directions governed by the vectors connecting the relevant pairs of atoms, $\vec{R}_i-\vec{R}_j$. For each bond direction the σ, π and δ states can be defined, but they correspond to *different* atomic-like orbitals depending on the bond orientation; for example, the p_x orbital is the σ orbital of a bond along the x direction, and the π orbital of a bond along the y direction. It is of course possible to find the σ and π orbitals for every bond direction in a crystal structure, but this is not necessary. Rather, a global basis can be used to parametrise all the hopping integrals. In Reference [63], Slater and Koster listed the dependence of the hopping integrals between cubic orbitals on the bond direction, making this a particularly convenient

basis choice. To cite two examples, the hopping integral between the p_x and p_y orbitals is given by

$$E_{x,y}(l,m,n) = lmV_{pp\sigma} - lmV_{pp\pi}, \tag{3.4}$$

and that between d_{xy} and d_{yz} by

$$E_{xy,yz}(l,m,n) = 3lm^2nV_{dd\sigma} + ln\left(1-4m^2\right)V_{dd\pi} + ln\left(m^2-1\right)V_{dd\delta}, \tag{3.5}$$

where $n = \cos\vartheta$, $l = \sin\vartheta\cos\varphi$ and $m = \sin\vartheta\sin\varphi$ are directional cosines describing the relative positions of the two atoms in the global coordinate system.

This offers a clear recipe for constructing the tight binding Hamiltonians. The crystal, with cubic orbitals on atomic sites, needs to be placed in a global coordinate system. If only nearest neighbour interactions are considered, the Hamiltonian matrix element relating orbitals γ and δ is given by

$$H_{\gamma,\delta}\left(\vec{k}\right) = \sum_{n.n} \exp\left(\imath\vec{k}\cdot\vec{R}_i\right) E_{\gamma,\delta}(l_i,m_i,n_i), \tag{3.6}$$

where $\vec{R}_i$ are the vectors connecting the central site to nearest neighbours, and (l_i, m_i, n_i) the relevant directional cosines; the extension to include further hoppings is straightforward. The integrals $E_{\gamma,\delta}$ as a function of directional cosines can be directly taken from Reference [63]. The number of free parameters of such a model depends on the number and the symmetry of the included orbitals.

It is worth emphasising that the Slater-Koster framework allows for a construction of a tight-binding Hamiltonian which respects the symmetry of the lattice *without* an explicit construction of orbitals of this symmetry. Rather, cubic harmonics in a global coordinate system can be used; the symmetry of the lattice is included through the hopping integrals which depend on the bond angles. This fact makes the implementation of the Slater-Koster method straightforward even for non-cubic lattices, as I will show for the specific examples of p orbitals on a triangular lattice (Section 6.4.1), as well as the more complex case of d and p orbitals in a transition metal oxide layer of delafossites (Section 6.6).

3.2. Density functional theory

In contrast to the tight binding models described above, the aim of density functional theory is to deduce the physical properties of solids and molecules from first principles, with no additional assumptions. In solids, this would require solving the Schrödinger equation of $\sim 10^{23}$ electrons, all of which interact with each other and the external lattice potential. Although this problem is clearly not soluble, it is possible to make approximations which simplify it enough to make its solution computationally feasible, while still adequately describing the electronic structure of numerous materials. Density functional theory (DFT) relies on the fact that the many-body problem can be recast in terms of the ground state electron density, instead of the much more complicated complete electron wavefunction. This is mathematically an exact statement, based on the two Hohenberg-Kohn theorems [65]. The first of the theorems states that the external potential is uniquely determined by the ground state electron density ($n_0(\vec{r})$). The second theorem states that the total energy of the system can be expressed as a functional of the electron density, $E[n(\vec{r})]$, and that the ground state corresponds to the global minimum of this functional. In other words, if the dependence of the total energy on the electron density is known, all the other ground-state properties of the many-body system can be calculated. This is a powerful statement, but it is not very practical by itself, since it only guarantees the existence of such a functional, but does not say anything about its form. In practice density functional theory calculations are done using the Kohn-Sham ansatz [66], whereby a system of interacting particles is replaced by a system of non-interacting particles moving in an effective potential. The form of this potential, and in particular of its part describing the electron correlations and exchange, is not known. Most exchange-correlation potentials used in practice are based either on the local density approximation (LDA), or the generalised gradient approximation (GGA), which assume that the exchange-correlation functional depends only on the local electron density, or on the local electron density and its gradient, respectively. It is important to keep in mind that all of these approximations mean that density functional theory is generically expected to be able to accurately describe only weakly correlated systems. In particular, strong on-site Coloumb repulsion between electrons can never be correctly described in a single electron picture, as it depends on the orbital occupations. It might then

seem that density functional theory can never be relevant for any system which contains strongly correlated electrons, but this is not entirely true. Corrective approaches may be taken, in which an energetic penalty for a double occupancy of a specific state is introduced, in the spirit of a Hubbard Hamiltonian. These effective exchange-correlation functionals are labelled LDA+U or GGA+U, where U is the energy cost of the double occupancy. While not expected to correctly describe the correlated states themselves, this procedure has extended the range of utility of density functional theory.

Once an exchange-correlation potential is chosen, the problem is mathematically well defined, and can be numerically solved in a self-consistent manner: an initial electron density is chosen, the energy functional with this electron density calculated and minimised, resulting in a new density. This is repeated until the density converges within the required precision, to a value which would ideally depend only on the choice of the exchange-correlation potential, and be independent of the code used. However, the basis in which the wave functions are expressed varies between the codes. If the bases were complete this would not change the final results, but working with such large basis sets is not possible. Different DFT implementations use various schemes to address this issue, as is nicely summarised in Reference [67], where it was also shown that the results of all modern DFT implementations are consistent, at least when calculating the energy of the crystalline ground state of elemental materials.

3.2.1. DFT of delafossite oxides

All the density functional theory calculations whose results are shown in this thesis were done by Helge Rosner, using the FPLO code (www.fplo.de, [68, 69]) developed in Dresden. Unlike the majority of DFT implementations which are based on plane waves, the FPLO code uses an atomic-like basis set, which makes it particularly useful for looking into the orbital character of the electronic states. The general gradient approximation was used for the exchange-correlation potential [70]. Comparison with experiments showed that including the on-site interaction of the Co $3d$ orbitals was necessary to correctly describe the bulk electronic structure of delafossites [17], so this was done through the GGA+U functional. Relativistic effects were always included, in the scalar-relativistic formalism in cases where spin-orbit

coupling was neglected, or by solving the four - component Kohn–Sham–Dirac equation when including the spin-orbit coupling. For the cases where the band structure becomes spin-split (Chapter 6), the calculation was repeated with the three different quantisation axes, in order to calculate spin-projection along each one of them.

The Kohn-Sham equation can be represented by a $N_B \times N_B$ matrix, where N_B is the number of basis orbitals used, including spin. In band structure calculations the eigenvalues of this matrix are calculated at a number of momentum points, N_k, typically chosen along the high symmetry directions. The output are therefore the $N_k \times N_B$ eigenvalues, corresponding to the N_B bands calculated at N_k points; when plotted these make the typical 'spaghetti plots'. Additionally, the code can return the band weights, i.e. the N_B - dimensional eigenvector corresponding to each of the calculated eigenvalues. As the FPLO code uses an atomic-like basis set, these are the overlaps of the wave functions with the atomic-like orbitals. The code returns only the amplitude, but not the phase of these overlaps, a point I return to below.

The output thus contains a large body of information (up to 1GB in some of the surface state calculations!), but to access the physically relevant quantities the right questions need to be asked. As a somewhat trivial example, if we are interested in the orbital character of the bulk band in $PtCoO_2$ at the Fermi level, it is reasonable to look into the contribution of Pt $5d$ orbitals to the electronic structure, but not of Pt $3d$ orbitals. I have worked with the output of Helge Rosner's calculations to extract the information needed to address the physical questions relevant to understanding my experimental data, and enable the construction of the plots shown in the thesis; unless otherwise stated, all the plots were made by myself.

3.3. Downfolding on a Wannier basis

The density functional theory and Slater-Koster tight binding models are in some sense the opposite approaches to band structures: the first is computationally demanding but in principle offers exact description of specific materials, while the second is easily manipulated to gain insight, but is not very specific or accurate. An intermediate route, in which a tight binding model is constructed based on the results of the density functional theory, is available. This process is known as the 'downfolding' of a density functional theory calculation onto a Wannier basis.

The eigenstates of the Kohn - Sham Hamiltonian solved by the density functional

theory calculation are of Bloch form, and as such are delocalised in real space. An equivalent description of an electronic system can be obtained with a different set of wave functions, related to the Bloch ones by a unitary transformation. In particular, the so-called Wannier orbitals, in which the localisation in momentum space is replaced by localisation in real space, are often invoked [71]. The transformation between the Bloch and Wannier functions is gauge dependent, and thus not unique. For instance, one choice of Wannier orbitals are the so called maximally-localised Wannier orbitals, for which a well-defined mathematical criterion is used to find a set of basis states of the smallest spatial extent. Another choice is orbitals centred on atomic sites which obey the symmetry of the atomic orbitals, but with a radial shape which depends on the bonding environment. As the Wannier orbitals are not physical observables, no choice is 'more correct' than others, although some may be more useful for specific applications. It is important to note that the mapping between Wannier and Bloch wave functions is exact only if the same number of wave functions is used. As there are as many Bloch wave functions as there are electronic states in a unit cell, in practice the transformation is done for a subset of bands, rather than for a full band structure. It is therefore exact only if it is possible to isolate the bands of interest from others, either by band gaps, or if hybridisation is forbidden by symmetry.

The FPLO code can be used to project the Kohn-Sham wave functions on the highly localised atomic-like Wannier functions. Bloch wave functions with those Wannier functions as basis sets are constructed, and used to find the matrix elements of the tight-binding Hamiltonian expressed in the Wannier basis. Such Wannier tight binding Hamiltonians were constructed both for the surface electronic structure of $PtCoO_2$ by Maurits Haverkort, using the Quanty program package (http://www.quanty.org, [72]), of which he is the author. The resulting tight-binding matrix can be easily used and manipulated using Wolfram Mathematica, as I will show in example calculations in Section 6.7.2.

If the downfolding is done for an isolated set of bands, as it is the case for delafossites, the band structure calculated using the Wannier tight binding Hamiltonian will by construction exactly match the density functional theory band structure at the k points where the latter was calculated, and interpolate between them. The downfolding is therefore particularly useful when calculating properties which require integrals over the whole Brillouin zone. Crucially, and in contrast to density

functional theory output, the complex eigenvectors are known, and consequently so are the complex wave functions corresponding to each eigenvalue. This gives access to information that either cannot be gained directly from a density functional theory calculation, or would be computationally very heavy to obtain. To use an example mentioned above, if the spin polarisation along three different axes needs to be calculated, the density functional theory calculation has to be performed three times, with the three different quantisation axes. In contrast, the same information can be gained from the tight binding Hamiltonian by calculating the expected values of the three spin operators using the known tight binding wavefunctions. In general, the expected value of any operator can be calculated using the Wannier downfolding as long as it is known how that operator acts on the basis functions. Specifically, since the Wannier functions provided by the FPLO code have the same angular dependence as the atomic orbitals, it was easy to use them to calculate the orbital angular momentum of the tight binding wave functions describing the surface states in delafossite oxides (Section 6.7.2).

4. Bulk states in $PtCoO_2$ and $PdCoO_2$

Understanding the exceptionally high conductivity of delafossite oxides, as well as the unconventional transport properties it causes, requires a good knowledge of their electronic structure. As discussed in Section 1.1.3, prior to the work presented here both quantum oscillation and photoemission measurements were performed on the Pd based delafossites, $PdCoO_2$ and $PdCrO_2$ [7, 12, 17, 26–28], while the available $PtCoO_2$ crystals were too small to make such experiments feasible. In Sections 4.1 and 4.2 of this chapter I report the first measurements of the electronic structure of $PtCoO_2$, as well as new ARPES measurements on $PdCoO_2$ which will be used to compare the two compounds. As discussed in Section 2.6.5, the majority of the photoemission measurements on delafossites reveal signatures of both bulk and surface states. However, one of our cleaves from each of $PtCoO_2$ and $PdCoO_2$ showed no signs of surface states arising from either of the surface terminations. This greatly simplifies the analysis and interpretation of the bulk electronic structure, so I will concentrate on the results obtained from these two samples. The effective masses and electron counts extracted from the photoemission data will also be compared to density functional theory calculations and bulk - sensitive quantum oscillation measurements.

As was already discussed in the context of the previous measurements on $PdCoO_2$, the band which crosses the Fermi level in the Pd and Pt - based delafossite metals is very two dimensional. The experimental line-width is therefore simply related to the self-energy, making the delafossites candidate model systems to investigate the influence of many-body interactions on the quasiparticle dispersions. Additionally, the large bandwidth of the metallic band in principle allows for the analysis of electron-electron interactions over a large energy range of $\sim 1\,\mathrm{eV}$. Such analysis is performed, and its limitations discussed, in Section 4.3.

4.1. The Fermi surface

In Figure 4.1 I show our measurements of the Fermi surfaces of (a) $PtCoO_2$ and (b) $PdCoO_2$. Both Fermi surfaces consist of a single electron-like pocket of a nearly hexagonal cross-section, consistent with previous measurements on $PdCoO_2$ [73]. The measured Fermi surfaces are sharp and well-defined, indicating that the states at the Fermi level have essentially no out-of-plane dispersion. This is consistent with previous quantum oscillation measurements on $PdCoO_2$ [17].

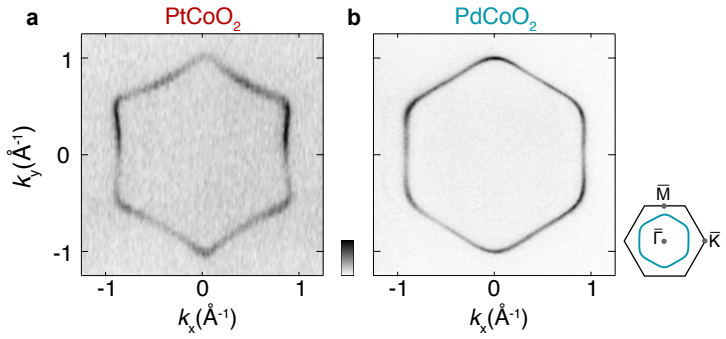

Figure 4.1.: The measured Fermi surface of (**a**) $PtCoO_2$ ($h\nu = 110\,\mathrm{eV}$, p - polarised light) and (**b**) $PdCoO_2$ ($h\nu = 100\,\mathrm{eV}$, p - polarised light).

The dimensionality of electronic structure can also be checked by photoemission, if the in-plane quasiparticle dispersions are measured as a function of the probing photon energy, as described in Section 2.1. We have performed such a measurement along the $\overline{\Gamma} - \overline{K}$ direction in $PtCoO_2$, and found no resolvable variation of the Fermi crossing vectors with photon energy (Figure 4.2a), proving that the $PtCoO_2$ Fermi surface is indeed two-dimensional within our resolution. This finding is consistent with the density functional theory calculations, if the on-site correlations on the Co site are included. The change of the Fermi surface cross-section with the out-of-plane momentum k_z predicted by DFT in the GGA+U approximation is very small, and not possible to resolve visually in Figure 4.2b. As in $PdCoO_2$ [17], this is not the case if the on-site correlations on the Co sites are not included; DFT in this approximation predicts significant admixing of Co states at the Fermi level, introducing a degree of out-of-plane dispersion which is not consistent with either the photoemission or quantum oscillation experiments [5].

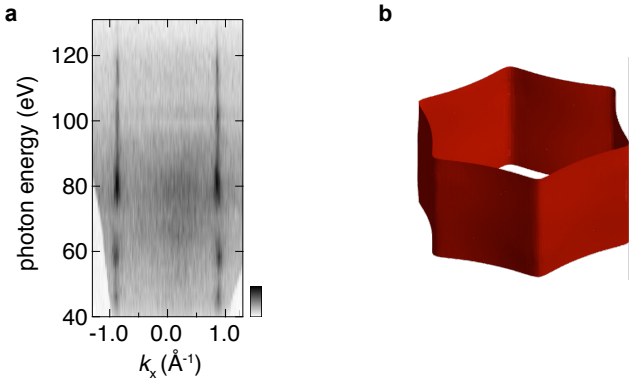

Figure 4.2.: (**a**) The dependence of Fermi crossing vectors on photon energy in $PtCoO_2$. (**b**) The three dimensional Fermi surface of $PtCoO_2$ calculated by DFT within the GGA+U approximation ($U = 4\,\mathrm{eV}$).

The Fermi momenta as a function of angle are extracted by radially fitting momentum distribution curves (MDCs) around the measured Fermi surface (dots in Figures 4.3(a, d)). Those fits are integrated to find the areas enclosed by the Fermi surfaces: in $PtCoO_2$ the area is (2.62±0.05) Å^{-2}, corresponding to a Luttinger count, assuming perfect two-dimensionality, of $n = (0.92\pm0.04)\,e^-$, while for $PdCoO_2$ it is (2.78±0.06) Å^{-2}, corresponding to $n = (0.98\pm0.04)\,e^-$. Although the area extracted from $PtCoO_2$ is smaller than expected for a half-filled band, quantum oscillations on the crystals from the same batch indicate a Luttinger count of $0.98e^-$[5], which is within the experimental error of the expectation for half-filling. In fact, in all of our measurements of the bulk Fermi surfaces of delafossites, as well as in the Fermi surface of $PdCrO_2$ measured in reference [28], the extracted area is slightly smaller than would be expected from half-filling, although quantum oscillations confirm that the compounds are stoichiometric [5, 17, 27]. The deviations of the ARPES-derived Fermi volumes from half filling are therefore likely to be caused by a small difference in surface chemistry, such as oxygen vacancies, or charge transfer towards subsurface layers. Nonetheless, the steepness of the bands ensures that the measured shape of the Fermi surface reflects the true shape of the bulk Fermi surface.

The shape of the two Fermi surfaces is slightly different, as the $PtCoO_2$ Fermi surface sides are more warped than those in $PdCoO_2$. The warping is quantified by fitting the extracted Fermi momenta as a function of angle φ around the Fermi

surface to a periodic function reflecting the 6 - fold symmetry:

$$k_F(\varphi) = k_0 + k_{6,0}\cos(6\varphi) + k_{12,0}\cos(12\varphi), \tag{4.1}$$

where we employ the nomenclature for warping terms introduced by Bergemann et al. [74] in relation to analysis of quantum oscillation experiments [17]. This is a simple way to parametrise the Fermi surface shape, and can easily be incorporated in numerical calculations of transport properties. The results of such fits to the Fermi surfaces of the two materials are shown as lines in Figures 4.3(b, c, e, f), while the fit parameters are listed in Table 4.1. I also list the parameters scaled to make the Fermi surface area correspond to half the Brillouin zone, which should be used to describe the true bulk Fermi surface.

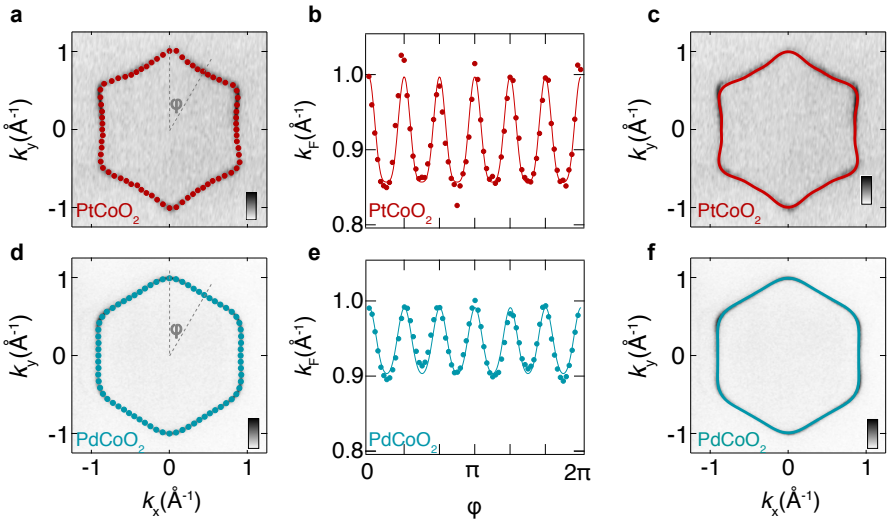

Figure 4.3.: Measured Femi surface of **(a)** $PtCoO_2$ and **(d)** $PdCoO_2$, with dots representing the Fermi momenta extracted by radially fitting MDCs. **(b, c)** Extracted momenta (dots) as a function of angle φ around the Fermi surface, with a sinusoidal fit (lines) describing the Fermi surface shape (Equation 4.1). **(c, f)** The same fit as lines in **(b, c)**, superimposed on measured data to demonstrate good agreement.

The different shape of the two Fermi surfaces is reflected in the values of the warping parameters. For instance, in an ideal hexagon the first warping term ($k_{6,0}$) is 5.8% of the constant term (k_0), in $PtCoO_2$ it is 7.7%, while in $PdCoO_2$ it is 4.7%. To visualise this point in Figure 4.4 I plot the fits to the Fermi surface of $PtCoO_2$ and $PdCoO_2$, scaled to make the Fermi surface area half the relevant Brillouin zone, and

normalised by the size of the Brillouin zone. While the $PdCoO_2$ Fermi surface can be thought of as a hexagon with flat sides and slightly rounded corners (Figure 4.4b), the $PtCoO_2$ Fermi surface sides curve inwards (Figure 4.4a). The Fermi vectors of the two compounds as a function of angle around the Fermi surface, compared with that of a perfectly hexagonal Fermi surface, are shown in Figure 4.4c.

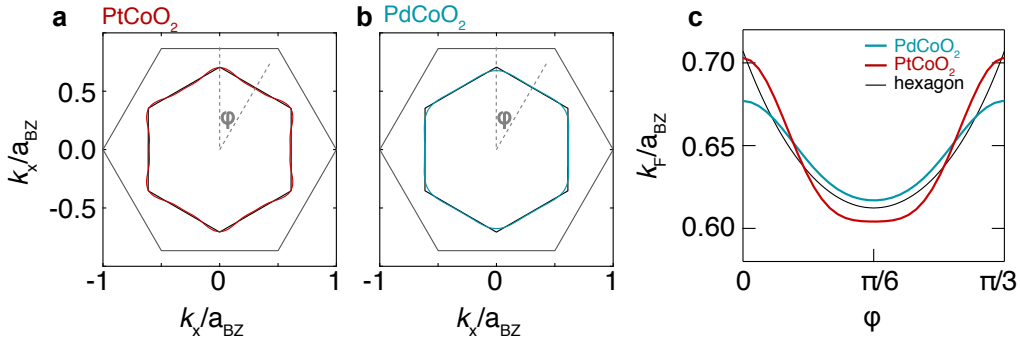

Figure 4.4.: Fits to the Femi surface of **(a)** $PtCoO_2$ and **(b)** $PdCoO_2$, scaled to the side of the respective Brillouin zone (a_{BZ}), and compared to a hexagon of the same area (black line). **(c)** The same as (**a**, **b**), but shown as a function of angle to emphasise the small differences in shape.

	fitted		scaled	
	$PtCoO_2$	$PdCoO_2$	$PtCoO_2$	$PdCoO_2$
k_0	0.9112 ± 0.0005	0.9425 ± 0.0005	0.9542	0.9518
$k_{6,0}$	0.0701 ± 0.0007	0.0440 ± 0.0006	0.0734	0.0444
$k_{12,0}$	0.0158 ± 0.0007	0.0048 ± 0.0006	0.0165	0.0048

Table 4.1.: Parameters of fits of a periodic function (Equation 4.1) to the bulk Fermi surfaces of $PtCoO_2$ and $PdCoO_2$, as well as the values scaled to make the Fermi surface area half the Brillouin zone, while keeping the experimental shape.

4.2. The dispersions

In Figure 4.5 I show the bulk band dispersion measured along the $\overline{\Gamma} - \overline{K}$ direction in (a) $PtCoO_2$ and (b) $PdCoO_2$. Consistent with the Fermi surface shown in Figure 4.1 there is a single steep band crossing the Fermi level. The peak positions of the fits to the MDCs along the $\overline{\Gamma} - \overline{K}$ and $\overline{\Gamma} - \overline{M}$ directions in both compounds are shown in Figure 4.5c. There are no resolvable deviations from linearity of the band in a range shown in Figure 4.5c, exceeding 0.25 eV below E_F. In each compound the band slopes are the same along the two directions within out measurement resolution. The Fermi velocity in $PtCoO_2$, $(8.9 \pm 0.5) \times 10^5$ m/s [5.8 ± 0.3 eVÅ/ħ], is somewhat higher than the one found in $PdCoO_2$, $(6.6 \pm 0.3) \times 10^5$ m/s [4.3 ± 0.2 eVÅ/ħ]. Because of the difference in the Fermi crossing vectors the effective mass obtained from the Fermi velocity is different for the two directions, and it averages to $m^* = 1.26m_e$ in $PtCoO_2$ and $m^* = 1.69m_e$ in $PdCoO_2$. In both cases this is approximately 10% higher than the value obtained from quantum oscillations ($m^* = 1.14m_e$ for $PtCoO_2$ [5], $m^* = 1.5$ for $PdCoO_2$ [27]). A likely cause of this small

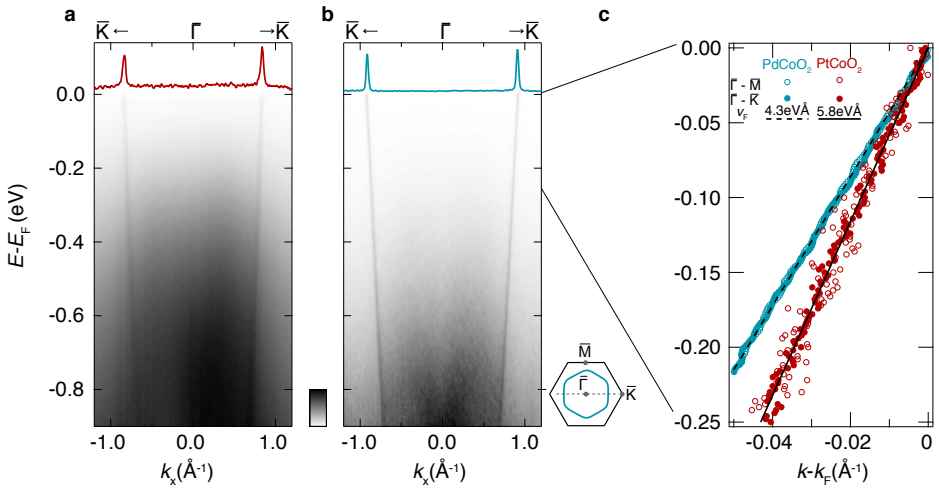

Figure 4.5.: The dispersion along the $\overline{\Gamma} - \overline{K}$ direction measured in (**a**) $PtCoO_2$and (**b**) $PdCoO_2$, and corresponding momentum distribution curves at the Fermi level (lines in (a, b), $E_F \pm 10$ meV). (**c**) The peak positions of the fits to the MDCs along the $\overline{\Gamma} - \overline{K}$ (full symbols) and $\overline{\Gamma} - \overline{M}$ (open symbols) directions in both compounds, as well as lines representing Fermi velocity fits.

difference is the fact quantum oscillations probe only the states right at the Fermi level, while the photoemission data need to be fitted over a larger energy range to obtain a reliable fit. Details of the fitting procedure, and in particular fitting range determination, are given in Appendix C. In spite of these potential issues, both photoemission and quantum oscillations state that the effective electron mass is about 35% higher in $PdCoO_2$ than in $PtCoO_2$, reflecting the larger orbitals, and thus larger orbital overlaps, in $PtCoO_2$.

4.3. Interactions

As discussed in Chapter 2.4.1, ARPES can probe interactions as well as the band structure. In the measured spectral function (Figure 4.5a) neither linewidth broadening below the Fermi level characteristic of electron-electron interactions, nor the typical electron-phonon kink discussed in Sections 2.5.2 and 2.5.3, are immediately obvious. In the following sections I will look at the data more carefully to see if linewidth analysis can reveal signatures of interactions. I will compare the experimental results to known models of electron-electron and electron-phonon interactions, in order to assess whether signatures of interactions are expected to be observed with the given experimental resolution.

4.3.1. Resolution and surface quality effects

The dispersions in Figure 4.5 were measured with the energy resolution of $\sim 5\,\mathrm{meV}$ and angular resolution of 0.1°, at the photon energy of $\sim 100\,\mathrm{eV}$, yielding the momentum resolution of $0.01\,\mathrm{\AA}^{-1}$, or 1% of the bulk Fermi vector. This momentum resolution appears to be very high, however due to the large band slope it actually limits the effective energy resolution to $\Delta E \sim v_F \Delta k \sim 50\,\mathrm{meV}$. The large low temperature transport mean-free path suggests that impurity scattering in delafossites is negligible, and that therefore the linewidth at the Fermi level should be resolution-limited. However, the linewidths measured at the Fermi level are $0.03\,\mathrm{\AA}^{-1}$ and $0.04\,\mathrm{\AA}^{-1}$ in $PdCoO_2$ and $PtCoO_2$ respectively, about three times larger than the momentum resolution, decreasing the effective energy resolution further. Measurements on multiple samples and multiple spots on the same sample lead us to believe that the quality of the cleaved surface, rather than intrinsic disorder or pho-

toemission resolution, is the factor setting the linewidth. It is difficult to obtain an atomically flat cleaved surface, so the light spot shines on multiple flat surfaces, which can be slightly inclined with respect to each other. What is more, the crystals are typically very thin ($\sim 10\,\mu$m) and tend to bend, so the angle of emission is not well-defined. Consequently, each measurement consists of a few copies of the single band, too close to each other to resolve, but increasing the effective linewidth. In each experiment special care was taken to find the most uniform spot on the sample, and to keep the light on the same spot if sample was rotated, for example during Fermi surface measurements. Occasionally sample movements as small as $10\,\mu$m would change the linewidth, testifying to the surface inhomogeneity.

A good way to check if the bare band dispersion and the effective impurity scattering alone can account for the experimental observations is to simulate the spectrum that would be observed in these simple conditions, and compare it to the experimental one. I will do this for $PdCoO_2$, as a combination of lower background, smaller Fermi level linewidth and less steep band makes the effective resolution higher than in the $PtCoO_2$ measurement. Although impurity scattering is not the underlying cause of the measured linewidth, the broadening due to surface inhomogeneity can be incorporated in the simulations via an effective impurity self-energy contribution of $\Sigma'' = v_F \Delta k/2 \approx 65\,$meV in $PdCoO_2$. In Figure 4.6a I plot a simulated photoemission spectrum, using the experimental Fermi velocity and wave vector, assuming a parabolic dispersion and the impurity self-energy of 65 meV. The points correspond to the momenta extracted from the measurement shown in Figure 4.5b, proving that the parabolic band is a reasonable approximation in this energy range. In Figure 4.6b I show the full width at half maximum (FWHM) of Lorentzian fits to momentum distribution curves extracted from Figure 4.5b at different binding energies, compared to the same quantity extracted from the spectrum simulated assuming only impurity broadening (Figure 4.6a). As discussed in Section 2.5.1, although the impurity self-energy is a constant, the momentum distribution curve linewidth increases as the band slope decreases with binding energy (line in Figure 4.6b). This linewidth increase caused by impurity scattering alone cannot account for the rate of linewidth increase in the measurement, motivating the analysis of potential interaction effects. It is important to keep in mind however that the incoherent background, which also increases with binding energy, causes a large scatter in the extracted linewidths. It is therefore not possible to make precise quantitative

statements about different contributions to the scattering rate, but it is possible to compare the scattering rate observed in $PdCoO_2$ to the one that would be expected in simple models, as I do below.

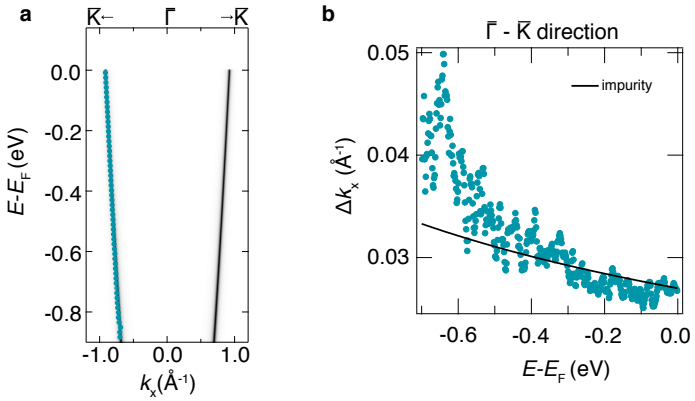

Figure 4.6.: (**a**) Simulated spectral function, assuming a parabolic dispersion and the impurity self-energy of 65 meV. The symbols are peak positions of Lorentzian fits to MDCs extracted from Figure 4.5b. (**b**) Full width at half maximum of Lorentzian fits to MDCs extracted from the measurement show in in Figure 4.5b (symbols), and from the simulated spectrum (**a**).

4.3.2. Electron-electron scattering

In Figure 4.7a I show a spectral function simulated assuming the same parabolic dispersion as in Figure 4.6a, now broadened by both an effective impurity scattering and electron-electron interactions within the Fermi liquid theory, assuming a circular Fermi surface and a parabolic band in a two-dimensional system, as discussed in Section 2.4.2 (equation 2.27). Under those assumptions the theory has no free parameters; its prediction for a linewidth increase with binding energy in shown by the dashed line in Figure 4.7b. Comparing the model to the scattering rate extracted from the measurement along the $\overline{\Gamma}-\overline{K}$ direction (symbols in Figure 4.7b) shows that the model overestimates the scattering rate; the experimental observation is better matched by a scattering rate three times smaller than the parameter-free prediction (solid line in Figure 4.7b). While it is not surprising that the experiment does not numerically agree with such a simple model, it is interesting that the observed scattering rate is lower than the predicted one. Possible reasons for the reduction

in the scattering rate are the hexagonal shape of the Fermi surface. Indeed, the variation of orbital character around the hexagonal Fermi surface was suggested as a possible cause of scattering suppression in $PtCoO_2$, leading to the low room temperature resistivity[6]. Experimentally, they motivate looking at the scattering rate along the $\overline{\Gamma} - \overline{M}$ direction, i.e. at the corner of the hexagonal Fermi surface (Figure 4.7c). A few observations can be made. First of all, the scattering rate is approximately 10% higher in the measurement along this direction, likely because the light moved to a slightly different spot on the sample. The overall binding energy dependence is still well-described by a combination of impurity scattering and one third of Fermi liquid scattering rate (solid line in Figure 4.7c), so the scattering rates along the two directions are indistinguishable with the present experimental resolution. However, the detailed shape of the binding energy dependence is slightly different along the two directions, and would be a very interesting topic of future experimental study, using smaller light spots. Regardless of these details, the fact that the linewidth continuously increases as a function of binding energy strongly suggests that there is detectable electron-electron scattering in the system.

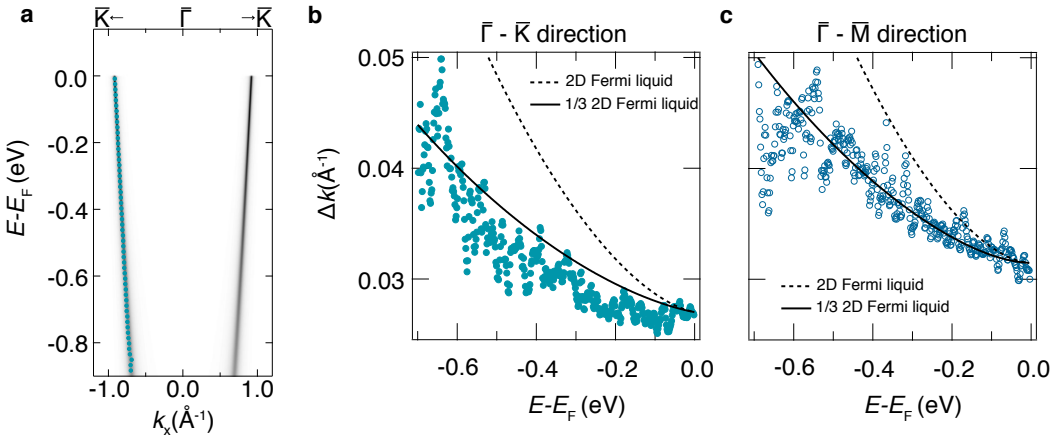

Figure 4.7.: (**a**) Simulated spectral function, assuming a parabolic dispersion, impurity self-energy of 65 meV, and a Fermi liquid scattering (equation 2.27). The symbols are peak positions of Lorentzian fits to MDCs extracted from Figure 4.5b. (**b**) Full width at half maximum of Lorentzian fits to MDCs extracted from the measurement along the $\overline{\Gamma} - \overline{K}$ direction show in in Figure 4.5b (symbols), from the spectrum simulated assuming Fermi liquid scattering (dashed line), and from the spectrum simulated assuming one third of Fermi liquid scattering (solid line). (**c**) Same as (**b**), but for the measurement along the $\overline{\Gamma} - \overline{M}$ direction.

4.3.3. Electron-phonon scattering

The measured dispersions exhibit no obvious signs of electron-phonon coupling, discussed in Section 2.5.3: there are no resolvable kinks in the spectral function, nor does the binding energy dependent linewidth show a step at a phonon energy. In Figure 4.8 I simulate the spectral function using the same bare-band parabolic dispersion as above, with a self-energy describing the electron-phonon interaction within the Debye model. The Debye temperature is set to 340 K, as deduced from heat capacity measurements [75]. The electron-phonon coupling constants of $\lambda = 0.1$ and $\lambda = 0.2$ are used to calculate the spectral functions in Figures 4.8a and 4.8b, respectively; no kinks are obvious in either of them. In Figure 4.8c I compare the experimentally extracted linewidth broadening with that expected from the Debye model with $\lambda = 0.1$ (solid line) and $\lambda = 0.2$ (dashed line). For $\lambda = 0.1$ the step in linewidth at the Debye energy is smaller than the scatter in our data, so we would probably not be able to resolve the coupling of that strength. On the other hand, we would be able to resolve the electron-phonon coupling with $\lambda = 0.2$. Therefore, although we observe no evidence of electron-phonon coupling, we can use our data to set an upper limit on the electron-phonon coupling strength to $\lambda = 0.2$. For comparison, the bulk value in copper is reported to be 0.15, while the electron-phonon coupling strength of the states localised on copper surface is found to be 0.14 in photoemission measurements [76].

As the number of occupied phonon modes increases with temperature, so does the self-energy due to electron-phonon coupling. Another way to assess the strength of the coupling is to perform measurements at higher temperatures. We have therefore measured the dispersion along the $\overline{\Gamma} - \overline{K}$ direction in $PtCoO_2$ as a function of temperature up to 100 K. As seen in Figures 4.9(a, b), no broadening is obvious in this temperature range. The experiment was later repeated on a different sample, for temperatures up to 250 K. The linewidth at the binding energy of 50 meV, which is larger than the Debye energy of 30 meV, is shown as a function of temperature for both samples in Figure 4.9c. It is constant within our resolution, and the scatter in the data is larger than the change of linewidth predicted by the Debye model with $\lambda = 0.2$. We would therefore not be able to resolve the temperature dependence of the linewidth even for the largest possible coupling of 0.2.

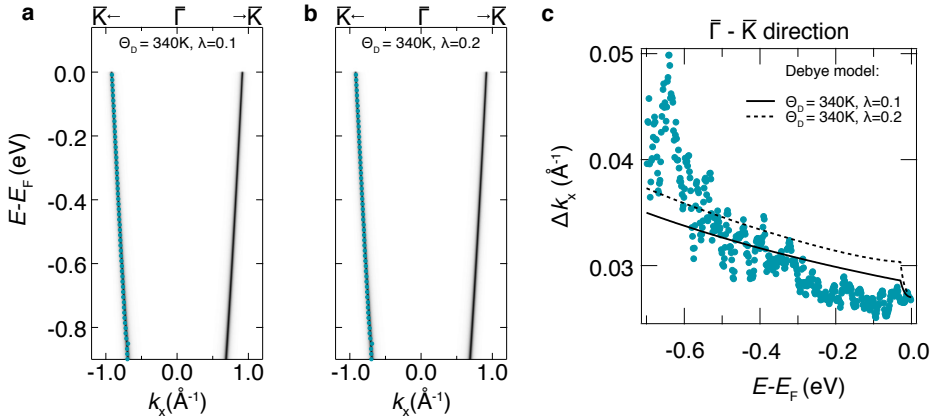

Figure 4.8.: Simulated spectral function, assuming a parabolic dispersion, impurity self-energy of 65 meV, and a electron-phonon self-energy in the Debye model, with (**a**) $\Theta_D = 340\,\mathrm{K}, \lambda = 0.1$, and (**b**)$\Theta_D = 340\,\mathrm{K}, \lambda = 0.2$. The symbols are peak positions of Lorentzian fits to MDCs extracted from Figure 4.5b. (**c**) Full width at half maximum of Lorentzian fits to MDCs extracted from the measurement along the $\overline{\Gamma} - \overline{K}$ direction show in in Figure 4.5b (symbols), from the spectrum simulated assuming electron-phonon coupling with $\Theta_D = 340\,\mathrm{K}, \lambda = 0.1$ (solid line), and with $\Theta_D = 340\,\mathrm{K}, \lambda = 0.2$ (dashed line).

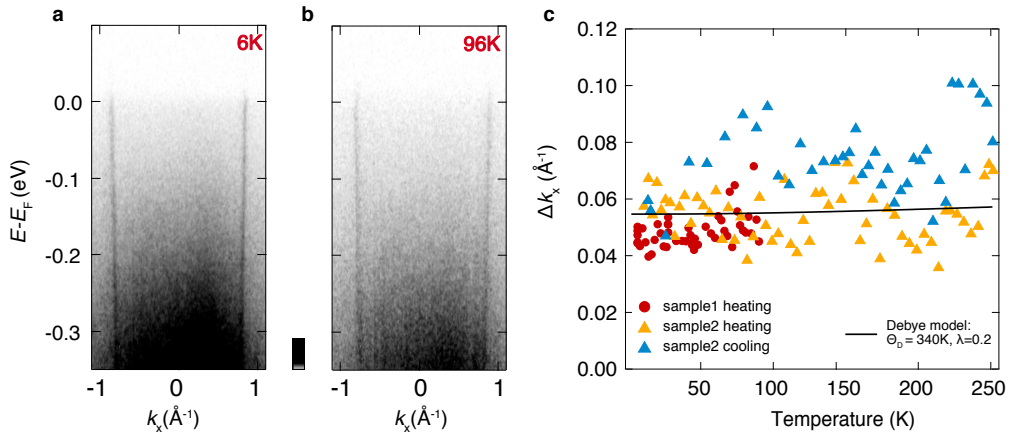

Figure 4.9.: The dispersion along the $\overline{\Gamma} - \overline{K}$ direction measured in $PtCoO_2$ at (**a**) 6 K and (**b**) 96 K. (**c**) Full width at half maximum of Lorentzian fits to MDCs extracted at the binding energy of 50 meV as a function of temperature from measurements on the same sample as dispersions in (**a**) and (**b**) (sample1, circles), and a different sample (sample2, triangles). The line is a prediction of the Debye model, with $\Theta_D = 340\,\mathrm{K}, \lambda = 0.2$.

It is interesting to note that the scatter in the extracted linewidth is larger as a function of temperature than as a function of binding energy. Again, this is a consequence of surface inhomogeneity. As we vary the temperature the whole manipulator holding the sample changes length, and the light shines on a slightly different spot on the sample. We have moved the sample in order to correct for this, enabling us to collect the data shown in Figure 4.9. This correction, however, cannot perfectly track the manipulator contraction, causing the observed scatter. This is also the reason the linewidths measured while warming up are systematically lower than the ones measured while cooling back down (yellow and blue symbols in Figure 4.9c); the most uniform part of the surface was found at low temperatures, but the sample systematically drifted during the warmup and subsequent cool-down.

4.3.4. Summary

The discussion of interactions in the bulk electronic structure of delafossites emphasises the importance of careful analysis of ARPES spectra, as well as comparisons to simulated spectral functions. As the measured dispersions appear very sharp, and do not show obvious signs of interactions, it would be tempting to conclude that the interactions are weak, and to relate this fact to the high conductivity. However, the large band velocity impedes our ability to resolve interactions; to put it simply, steep bands always look sharp. Linewidth analysis, however, reveals that the electron-electron interactions are present, and are approximately three times weaker than predicted by the Fermi liquid theory for a two dimensional electron system with a simple, isotropic, circular Fermi surface. Signatures of electron-phonon coupling are not observed, and would be detected only if the coupling were stronger than $\lambda = 0.2$. A comparison with other systems suggests that this is not a particularly weak coupling; in other words the photoemission measurements offer no indications that the electron-phonon coupling is weaker in delafossites than in other metals.

A particularly interesting open question is the dependence of the electron-electron scattering rate on the angle around the Fermi surface; while it is the same within our resolution, it is possible that there are subtle differences between the scattering rate at the Fermi surface corners and sides. As the overall measurement resolution is set by the quality of the cleaved surface, the best way to obtain this information would be to try the measurement with a smaller light spot, ideally ensuring that the

measurement signal is arising from a single flat surface. A smaller light spot would also reduce the incoherent background, especially visible in the $PtCoO_2$ measurement (Figure 4.5a), as this is likely to arise from the electrons photoemitted from amorphous silver epoxy around the sample.

5. Coupling of Metallic and Mott-insulating states in $PdCrO_2$

As described in Chapter 4, the non-magnetic delafossites $PtCoO_2$ and $PdCoO_2$ host bulk metallic states in their Pt and Pd layers, while the contribution of the CoO_2 layer to the bands at the Fermi level is negligible. In this chapter I will concentrate on $PdCrO_2$, the magnetic counterpart of $PdCoO_2$. Its transition metal oxide layer is a correlated Mott insulator, hosting localised spins 3/2 on chromium sites, which at 37.5 K undergo a transition towards an antiferromagnetic state with a 120° order, as described in Section 1.1.4. The main question I will address in this chapter is how the coupling between the itinerant and antiferromagnetic Mott insulating subsystems affects the spectroscopic signatures, and what information can be obtained from the spectral function of such a coupled system. I will first show the measured spectra, and compare them to the bulk states of $PtCoO_2$ and $PdCoO_2$ (Section 5.1). In trying to understand the magnitude of the observed signal it became clear that our experimental observations cannot be explained in terms of simple models of electrons in a periodic potential. Reaching this conclusion required a general analysis of photoemission intensity in systems with periodic potentials of varying strength, given in Section 5.2. This discussion is not relevant only for $PdCrO_2$, but for all systems with periodic potentials of varying strength, such as charge- or spin- density wave materials. A reader primarily interested in $PdCrO_2$ may choose to read Section 5.2.4, in which the discrepancy between the measurement and the simple model becomes apparent, immediately after Section 5.1. The discrepancy motivated a many body calculation, done by our collaborators Sota Kitamura and Takashi Oka, which I outline in Section 5.3. This calculation in turn motivated additional experiments, described in Section 5.3.2, which both confirmed the theory and offered novel insight about the types of information accessible to angle resolved photoemission.

5.1. The measured electronic structure

In Figure 5.1 I show an experimental overview of electronic structure of $PdCrO_2$ in the binding energy range of $\sim 1\,\text{eV}$. The spectral function (Figure 5.1a) contains an intense electron-like band, reminiscent of that found in the non-magnetic delafossites, but also a weaker feature dispersing in the opposite direction. I will refer to the more and less intense features as the main band and the reconstructed weight, respectively. The main band makes a hexagonal Fermi surface, similar to the one measured in $PdCoO_2$; weaker copies of the main hexagon, made of the reconstructed weight, are also observed (Figure 5.1b). These findings are consistent with the photoemission measurements of Noh et al. [7], while Sobota et al. observed the main band and signatures of states localised on the Pd surface, but no reconstructed weight [28].

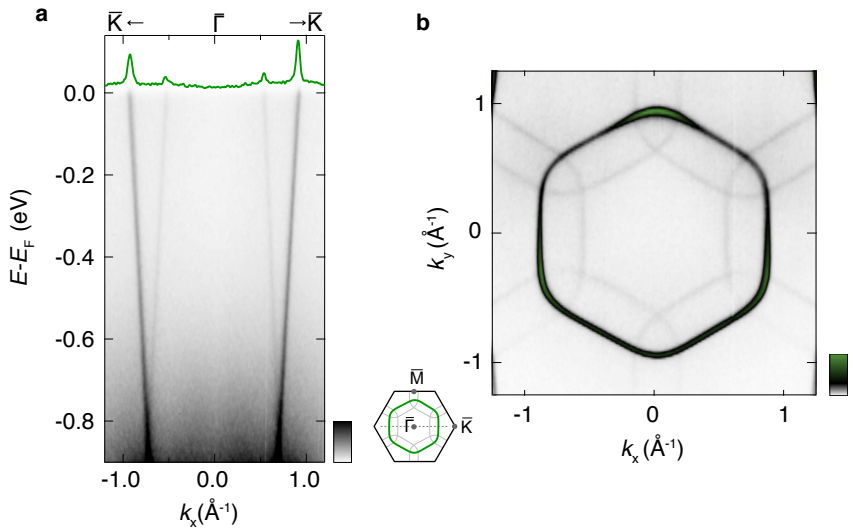

Figure 5.1.: Measured (**a**) dispersion ($h\nu = 110\,\text{eV}$) along the $\overline{\Gamma} - \overline{K}$ direction, with a momentum distribution curve at the Fermi level ($E_F \pm 10\,\text{meV}$), and (**b**) Fermi surface ($h\nu = 120\,\text{eV}$) of $PdCrO_2$.

5.1.1. The main band

To check how similar the main band Fermi surface really is to that of $PdCoO_2$, I have extracted the Fermi momenta as a function of angle by radially fitting momentum

distribution curves around the measured Fermi surface (dots in Figures 5.2(a, b)). The area enclosed by the Fermi surface is (2.53±0.05) $Å^{-1}$, corresponding to the Luttinger count of $n = (0.95 \pm 0.04)\, e^-$, slightly smaller than expected for a half-filled band, as was also found for the non-magnetic delafossites (Chapter 4) and for $PdCrO_2$ by Sobota et al. [28]. The shape of the Fermi surface was parametrised in the same way as the Fermi surfaces of the non-magnetic delafossites, using a periodic function of the form:

$$k_F(\varphi) = k_0 + k_{6,0}\cos(6\varphi) + k_{12,0}\cos(12\varphi)\,. \tag{5.1}$$

The corresponding fit is shown as lines in Figures 5.2(b, c), while the fit parameters are listed in Table 5.1. I also list the parameters scaled to make the area of the Fermi surface equal to half the Brillouin zone while keeping the experimental shape; these are relevant for calculating bulk transport properties.

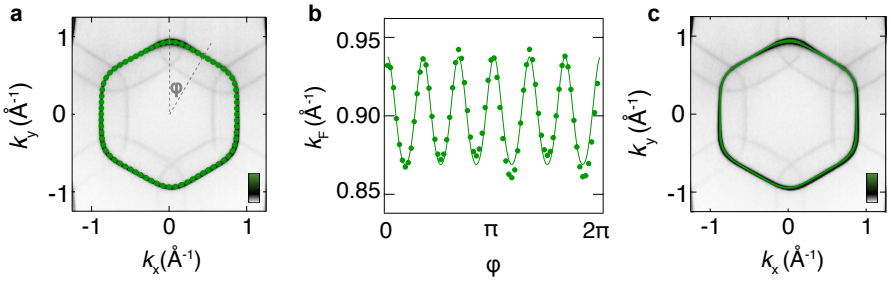

Figure 5.2.: **(a)** Measured Femi surface of $PdCrO_2$, with dots representing the Fermi momenta extracted by radially fitting MDCs. **(b)** Extracted momenta (dots) as a function of angle φ around the Fermi surface, with a sinusoidal fit (lines) describing the Fermi surface shape (Equation 5.1). **(c)** The same fit as lines in **(b)**, superimposed on measured data to demonstrate good agreement.

As mentioned in Chapter 4, in an ideal hexagon the first warping term ($k_{6,0}$) is 5.8% of the constant term (k_0). In $PtCoO_2$ it is 7.7%, in $PdCoO_2$ it is 4.7%, while in $PdCrO_2$ it is 3.8%, confirming that the $PdCrO_2$ Fermi surface is very similar, although not identical, to that of $PdCoO_2$. The similarity is emphasised by plotting fits to the two Fermi surfaces superimposed on each other, each scaled to the respective Brillouin zone (Figure 5.3a). The excellent agreement of the Fermi surface shapes reaffirms that the states at the Fermi level have the same origin in the two compounds, i.e. they are arising from the Pd 4*d* orbitals. Slight differences in the

	fitted	scaled
k_0	0.9001 ± 0.0003	0.9214
$k_{6,0}$	0.0343 ± 0.0004	0.0351
$k_{12,0}$	0.0031 ± 0.0004	0.0032

Table 5.1.: Parameters of fits of a periodic function (Equation 5.1) to the bulk Fermi surface of $PdCrO_2$, as well as the values scaled to make the Fermi surface area half the Brillouin zone, while keeping the experimental shape.

shape are visible if the Fermi momenta are plotted as a function of angle around the Fermi surfaces (Figure 5.3b). This is most likely arising from the different ratio of next nearest neighbour and nearest neighbour hopping in the two compounds, caused by a difference in the lattice parameter, which is $\sim 3.5\,\%$ larger in $PdCrO_2$ than in $PdCoO_2$ [4].

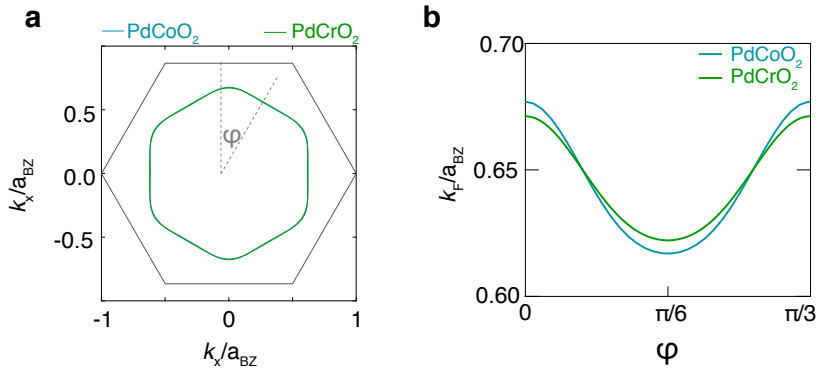

Figure 5.3.: **(a)** Fits to the Femi surface of $PdCrO_2$ and $PdCoO_2$, scaled to the side of the respective Brillouin zone (a_{BZ}). **(c)** The same as (**a**), but shown as a function of angle to emphasise the small differences in the Fermi surface shape.

In Figure 5.4b I compare the slopes of the bands of the two compounds. As evident from the points extracted from momentum distribution curves, the band slope is slightly smaller in $PdCrO_2$ than in $PdCoO_2$; the fitted Fermi velocity is 4.07 eVÅ in $PdCrO_2$, compared to 4.30 eVÅ in $PdCoO_2$. The difference in slope could have two origins: either interactions with the correlated CrO_2 layer enhance the effective mass in $PdCrO_2$, or the bare band velocity is slightly different due to the difference

in the lattice constant. If the band can be described by a nearest - neighbour tight binding model, $E = t\cos(ka)$, the Fermi velocity is given by $v_F = \hbar ta$. The hopping parameter t naturally decreases as the lattice constant increases; if this were a linear relationship the Fermi velocity would remain unchanged as the lattice constant varies. However, the hopping parameter is set by the overlap of charge densities originating from two neighbouring atoms, and as such can have a much stronger dependence on the interatomic distance. It is therefore not possible to exclude the change in lattice constant as the origin of different Fermi velocities in $PdCoO_2$ and $PdCrO_2$. Although we have not directly confirmed the isotropy of Fermi velocity in $PdCrO_2$, the similarity of the main band to the one in $PdCoO_2$ strongly suggests that the velocity is the same along the $\overline{\Gamma}-\overline{M}$ and $\overline{\Gamma}-\overline{K}$ directions. Under this assumption, and using the extracted Fermi velocity of 4.07 eVÅ and the mean Fermi wave vector of 0.92 Å, the average electron mass is found to be $1.73m_e$, slightly higher than in $PdCoO_2$ ($1.69m_e$).

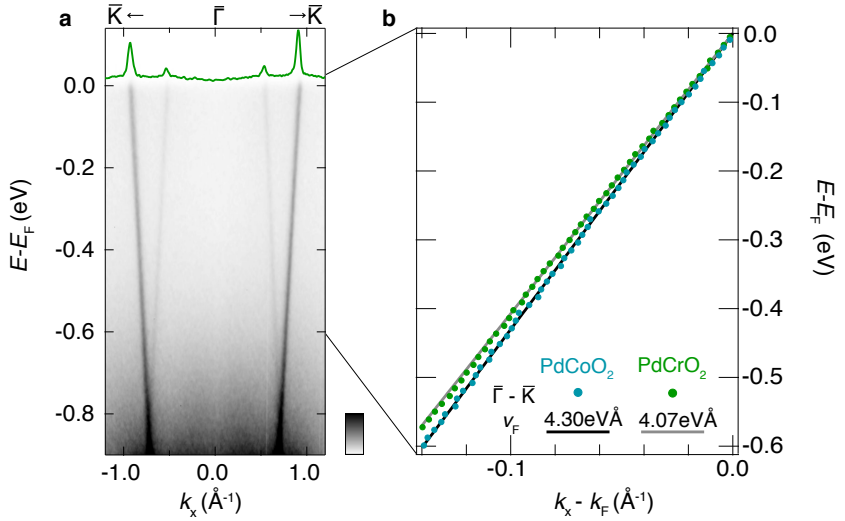

Figure 5.4.: (**a**) The dispersion along the $\overline{\Gamma}-\overline{K}$ direction measured in $PdCrO_2$, and a momentum distribution curve at the Fermi level momentum distribution curve (green line, $E_F \pm 10$ meV) (**c**) The peak positions of the fits to the MDCs along the $\overline{\Gamma}-\overline{K}$ direction in $PdCrO_2$ (green) and $PdCrO_2$ (blue), as well as lines representing Fermi velocity fits.

5.1.2. The reconstructed weight

Our data confirm that, unless very fine detail of the electronic structure is relevant, the main band in $PdCrO_2$ can be thought of as having the same properties as the bulk band in $PdCoO_2$, consistent with previous photoemission studies [7, 28]. It is also consistent with quantum oscillation measurements [26, 27], which reported a Fermi surface consisting of the $PdCoO_2$ Fermi surface backfolded across the antiferromagnetic Brillouin zone boundary. The interpretation of this backfolding is straightforward: electrons in the Pd layer, which have the same properties in $PdCoO_2$ and $PdCrO_2$, feel an additional periodic potential arising from the antiferromagnetic order. New bands, which are copies of the original ones offset by the wavevectors of the antiferromagnetic order $\vec{Q}_{AFM}$, appear. They hybridise with the original bands, opening small gaps at the boundaries of the magnetic Brillouin zone, the area of which is a third of the area of the non-magnetic zone. Quantum oscillations can measure the electron orbits corresponding to this reconstructed band structure. When Noh et al.[7] observed the reconstructed weight in photoemission, they interpreted it as arising from the same reconstruction due to the antiferromagnetic potential. Indeed, the reconstructed weight does consist of copies of the main band offset by the wavevectors of the antiferromagnetic order, as shown in Figure 5.5 for (a) the dispersion and (b) the Fermi surface, so this is a natural starting assumption. However, in order to fully understand the observed signal, it is necessary to explain its intensity, as well as the position in momentum space.

To judge whether the observed spectral features are consistent with such a band-folding picture, it is necessary to revisit the fundamentals of photoemission, and think about how it probes the initial state wave function. I do this in the following Section, at the level I found helpful to fully grasp the origin and the intensity of the photoemission signal in a band-folding picture, with the hope that a reader encountering a similar experimental situation will find it useful. A reader who is more interested specifically in $PdCrO_2$ may wish to skip immediately to Section 5.2.4; the main conclusion of previous sections is that in the band-folding picture intensity should drop very quickly away from the new Brillouin zone boundary.

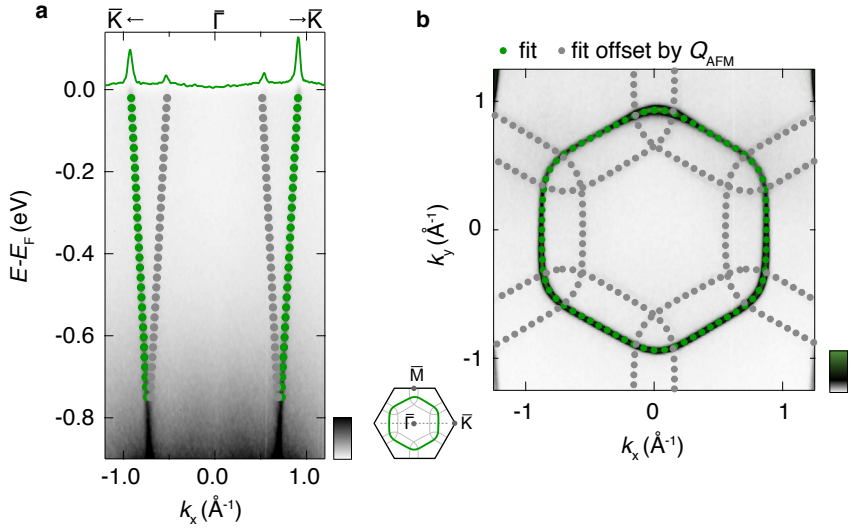

Figure 5.5.: (**a**) Measured dispersion along the $\overline{\Gamma} - \overline{K}$ direction, with a momentum distribution curve at the Fermi level ($E_F \pm 10\,\text{meV}$), and (**b**) Femi surface of $PdCrO_2$. In both (a) and (b) the green dots correspond to fits to the 'main' band, while the grey points are copies of the green ones, offset by the wavevectors of the antiferromagnetic order.

5.2. Reconstructed weight intensity

As discussed in Section 2.3, the photoemission intensity can be thought of as a product of the square of the one-electron matrix element ($\left|M_{if}^{k}\right|^2$) and the single electron removal spectral function ($A^{-}(k,\omega)$). In a non-interacting system the spectral function consists of a series of delta functions centred at momenta and energies set by the dispersion, $E_B(k)$, leading to photoemission intensity is proportional to

$$I(k,\omega) = \left|M_{if}^{k}\right|^2 \delta\left(\omega - E_B(k)\right). \tag{5.2}$$

The delta function allows for the mapping of the band structure, while the intensity variation of the signal is given by the matrix element, M_{if}^{k}. It is therefore necessary to understand how the periodic potential affects the photoemission matrix element. In general, the matrix element is given by $M_{if}^{k} = \left\langle \varphi_{f,k} \left| \vec{A} \cdot \vec{p} \right| \varphi_{i,k} \right\rangle$, where $\vec{A}$ is the vector potential of the incoming light, $\vec{p}$ the momentum operator, and $\varphi_{i,k}$ and $\varphi_{f,k}$ the initial and final state one-electron wave functions (Section 2.3). The final state can be approximated by a plane wave, $\varphi_{f,k} = \exp\left(i\vec{k}_f \cdot \vec{r}\right)$, which is an eigenstate of

the momentum operator, with $\hbar\vec{k}$ as an eigenvalue. The matrix element therefore takes the form of

$$M_{if}^{k} = \hbar\vec{A}\cdot\vec{k}_f \left\langle \varphi_{f,k} | \varphi_{i,k} \right\rangle , \tag{5.3}$$

resulting in an intensity directly governed by the overlap of the initial wave function in the solid, and the final state free-electron wave function which is measured[1]. The initial state wave function in a periodic potential has the Bloch form, $\varphi_{\vec{k}}\left(\vec{r}\right) = \exp\left(\imath\vec{k}\cdot\vec{r}\right) u_{\vec{k}}\left(\vec{r}\right)$, with $u_{\vec{k}}\left(\vec{r}\right)$ inheriting the periodicity of the lattice, and the initial state momentum $\vec{k}$ restricted to the first Brillouin zone. The Bloch wave function can be expanded in a Fourier series as

$$\varphi_{i,k}\left(\vec{r}\right) = \exp\left(\imath\vec{k}_i x\right) \sum_{n,\vec{G}} c_n\left(\vec{k}_i\right) \exp\left(\imath n\vec{G}x\right) , \tag{5.4}$$

where $\vec{G}$ are the reciprocal lattice vectors, and n an integer. Using this form of the initial state wave function the matrix element is given by

$$M_{if}^{k} = \hbar\vec{A}\cdot\vec{k}_f \sum_{n} c_n\left(\vec{k}_i\right) \delta\left(\vec{k}_i + n\vec{G} - \vec{k}_f\right) . \tag{5.5}$$

The $\vec{A}\cdot\vec{k}_f$ term introduces the dependence of the intensity on the measurement geometry, as it depends on the angle between the polarisation vector and the final state momentum direction. It can often explain the variation of photoemission intensity with changing measurement conditions. For instance, in the Fermi surface map shown in Figure 5.1b the measured intensity is not the same at every corner of the main band hexagonal Fermi surface. In particular, the corner at $k_x = 0$ and $k_y > 0$ appears to be much more intense than the one at $k_x = 0$ and $k_y < 0$. The symmetry of the system guarantees that the initial state wave functions are the same in all the corners. However, as the polar angle is changed during the measurement of the map, the angle between the light polarisation vector and the final state momentum is changed, causing the observed variation in intensity. This is an example of a so-called 'matrix element effect,' and it is not relevant for the

[1] This is in fact a simplification, as the final state in the three step process is actually an unoccupied Bloch state. For high photon energies it can be approximated by a free-electron state, but even in these circumstances this is not the measured state, as the electron still needs to travel to the surface, and escape into vacuum (steps two and three of the three step process). These distinctions are however not important for the qualitative discussion outlined here.

present discussion. I will therefore assume that $\vec{A} \cdot \vec{k}_f$ is a constant, and will not consider it further. I will instead consider in detail how is the sum in Equation 5.5 affected by the periodic potential, and demonstrate that the intensity of the reconstructed band cannot be understood in this framework.

Assuming for simplicity a one dimensional solid of lattice spacing a, the relevant part of the matrix element takes the following form:

$$\tilde{M}(k_f) = \sum_n c_n(k_i)\,\delta(k_i + nG - k_f), \tag{5.6}$$

where $G = 2\pi/a$ is the reciprocal lattice constant. The matrix element is a function of the *final state* momentum, which is measurable and can assume any value, while the coefficients $c_n(k_i)$ are functions of the crystal momentum in the first zone, as they are a property of the initial state wave function. The expression 5.6 states that if the final state wave vector is in the first zone ($k_f = k_i$), the intensity of the signal is set by $|c_0(k_i)|^2$, that is by the weight of the plane wave $\exp(\imath k_i x)$ in the initial state wave function. Equivalently, if the final state momentum is in a higher zone labelled by n ($k_f = k_i + nG$), the intensity is proportional to the corresponding Fourier component of the Bloch wave function, $|c_n(k_i)|^2$. Photoemission could therefore in principle be used to decompose the Bloch wave function into its Fourier components; in practice this is complicated by experimental considerations. This analysis of the matrix elements also immediately emphasises that the photoemission intensity need not follow the periodicity of the solid, therefore explaining how the reconstructed weight intensity can be weaker than the main band intensity in $PdCrO_2$. This qualitative discussion does not, however, offer any insight into the expected intensity ratio between the two. In what follows I will look at how the matrix elements influence the photoemission signal in two extreme cases, that of a nearly free electron system and that of a tight binding band. The insights developed using these examples will help in understanding the intensity distribution caused by a weak periodic potential superimposed on a tight binding band, a situation approximating the case of $PdCrO_2$.

5.2.1. Nearly free electron system

The wave functions of electrons in vacuum are plane waves, $\exp(\imath k x)$, and their energy exhibits a quadratic momentum dependence, $E = (\hbar k)^2 / (2m)$, as illustrated

in Figure 5.6a. If the kinetic energy of electrons in a solid is sufficiently larger than the strength of the periodic potential, plane-wave wave functions, and the corresponding parabolic dispersion, can be a useful starting point in determining the electronic structure, leading to the so-called nearly-free electron approximation. The periodic potential allows for the free electron states whose momenta differ by the wave vector of the potential to mix and interfere with each other. A band structure of such a system is illustrated in Figure 5.6b, for a cosine potential of amplitude $V = 0.1\,\mathrm{eV}$, and wave vector $G = 1\,\mathrm{Å}^{-1}$. In addition to the 'original' band (orange in Figure 5.6b), the band structure now contains copies of the same band offset by nG, where n are integers, as shown for $n = 1$ and $n = -1$ in Figure 5.6b (pink and red, respectively). While the wave function away from the points where bands cross can be well described by a single plane wave, $\exp(\imath\,(k \pm nG)\,x)$, as indicated in Figure 5.6b, at the band crossing points those plane waves hybridise. The resulting band structure, shown in green, resembles the offset parabolas everywhere in momentum space except at the boundaries of the Brillouin zones (dashed lines in Figure 5.6b), at which energy gaps proportional to the Fourier components of the periodic potential open; the analytical form of the band structure and the wave functions in this region is taken from Reference [77].

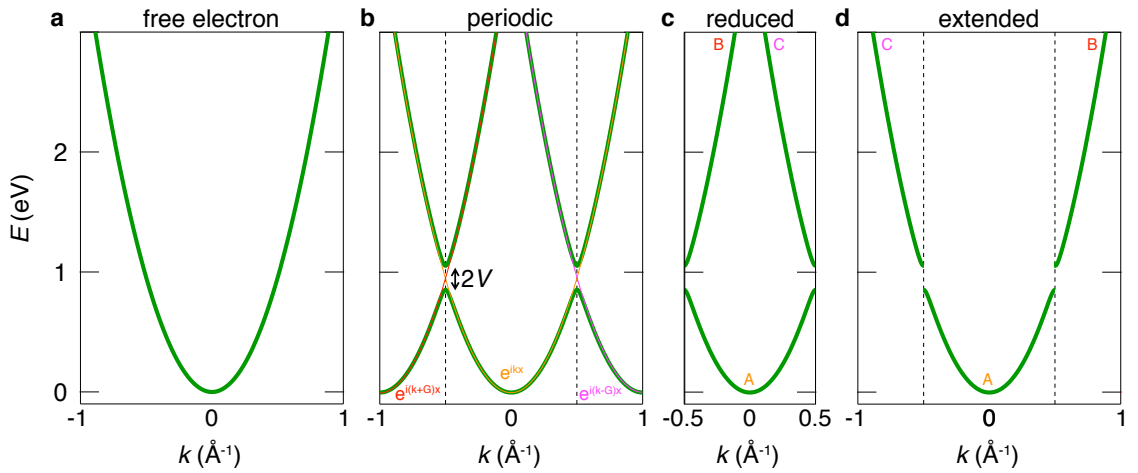

Figure 5.6.: (**a**) Dispersion of free electrons. Band structure of free electrons perturbed by a periodic potential of cosine form, $V\cos(xG)$, for $V = 0.1\,\mathrm{eV}$ and $G = 1\,\mathrm{Å}^{-1}$, shown in the (**b**) periodic, (**c**) reduced and (**d**) extended zone scheme. The orange, red and pink lines in (b) are the free-electron dispersion, a free electron dispersion offset by $-G$ and by G, respectively.

There are three commonly used ways to represent a band structure of a periodic solid. In the periodic zone scheme (Figure 5.6b), all the bands are drawn in all the Brillouin zones, emphasising the fact that there are n solutions to the Schrödinger equation for every momentum, where n is the number of bands ($n = 2$ in the example outlined here). This is, however, highly redundant, as all the Brillouin zones are equivalent. In the reduced zone scheme therefore all the bands are shown only in the first zone, emphasising the fact that every state in the crystal can be labelled by k in the first zone and a band index n (Figure 5.6c). The third representation is the so-called extended zone scheme, in which different bands are plotted in different zones (Figure 5.6d). Although this may seem somewhat arbitrary for a system in a periodic potential, in a nearly free electron system it emphasises the relation to the parabolic dispersion of free electrons. All of these representations are well-defined, and thus equally correct, however some may be more useful than others in specific situations. For instance, the one electron spectral function $A(k, \omega)$ peaks at all energies which are the solutions of the Schrödinger equation, for every value of crystal momentum, and therefore follows the periodic zone scheme (Figure 5.7a). It is an intrinsic property of the solid, and as such obeys its periodicity, but it is not a direct physical observable.

To find out which of the zone schemes, if any, is relevant for the intensity of the photoemission experiment it is necessary to consider the matrix element variation as a function of the final state momentum. This requires the Fourier decomposition of the initial state wave function, which is particularly simple in the case of nearly-free electrons, as already indicated by the plane wave labels in Figure 5.6b. Neglecting the regions in the vicinity of the Brillouin zone boundary, for each of the three sections of bands seen in the reduced zone scheme, labelled A, B and C, only one of the coefficients c_n in the Fourier expansion (equation 5.4) is finite: c_0, c_1 and c_{-1} for sections A, B and C, respectively. The matrix element therefore allows each band section to be observed for a final state wave vector in one of the zones only: the first zone ($k_f = k_i$) for section A, the zone to the right of it ($k_f = k_i + G$) for section B and the zone to the left of the first one ($k_f = k_i - G$) for section C, as indicated in the extended zone scheme diagram (Figure 5.6d). The photoemission intensity is therefore expected to dominantly follow the extended zone scheme. Indeed, a calculation of the matrix elements taking properly into account the regions in the vicinity of the zone boundary confirms this conclusion (Figure 5.7b). A closer look

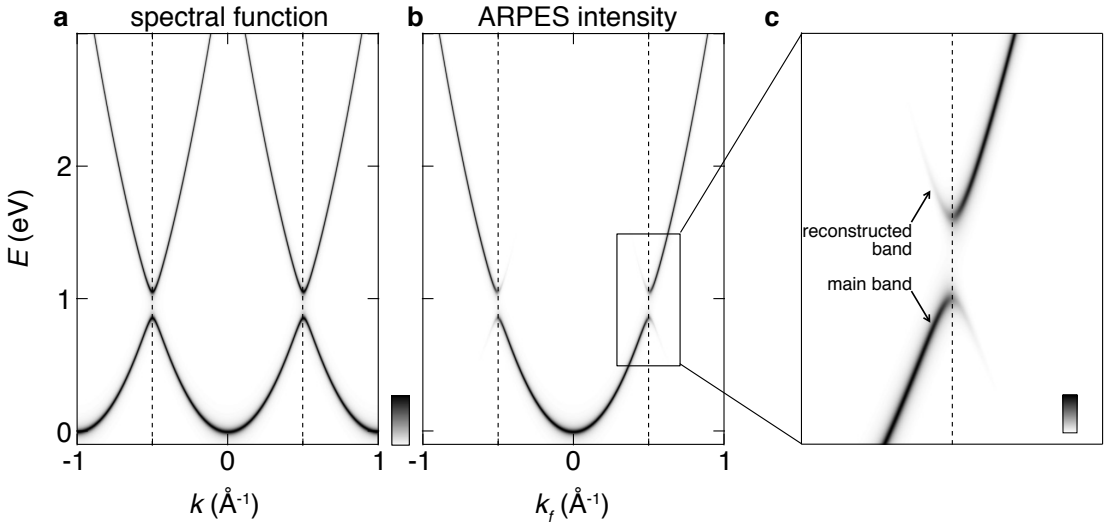

Figure 5.7.: (**a**) Spectral function and (**b**) photoemission intensity of a nearly free electron system, with $V = 0.1\,\mathrm{eV}$ and $G = 1\,\mathrm{Å}^{-1}$. (**c**) Expanded region around the Brillouin zone boundary, indicating the difference in intensity of the 'main band' and the 'reconstructed weight'.

at the zone boundary reveals additional features. In addition to the 'main band', which follows the extended zone scheme, weaker traces of the 'reconstructed band' are also visible (Figure 5.7c). This happens because in this region of momentum space two Fourier components are needed to describe the wave functions:

$$\varphi_{i,k_i}(x) = c_0(k_i)\exp(\imath k_i x) + c_1(k_i)\exp(\imath(k_i + G)x). \tag{5.7}$$

To determine the intensity of the two bands in, for example, the first zone, it is necessary to calculate the variation in $|c_0(k_i)|^2$. As the wave function at the zone boundary is an equal superposition of the two plane waves, $|c_0|^2 = 0.5$ for both bands at this point. For the main band this fraction rapidly increases towards one away from the crossing point, while for the reconstructed band it decreases, resulting in the higher visibility of the main band; equivalent statements can be made about the second zone. This is really just a description of hybridisation - the 'original' wave functions can mix in the regions of momentum space in which their energy would be similar in the absence of hybridisation. As their energy difference increases away from the crossing point, the wave functions become more

similar to the 'original ones'. Unsurprisingly, the rate of intensity decrease of the reconstructed band depends on the strength of the periodic potential, as illustrated in Figure 5.8; the reconstructed weight is less visible for $V = 0.1\,\mathrm{eV}$ (Figure 5.8a) than for $V = 0.5\,\mathrm{eV}$ (Figure 5.8b). Even for such a strong periodic potential the reconstructed band intensity is much weaker than that of the main band. Crucially, the intensity always decreases away from the crossing point, as illustrated in Figure 5.8c for a range of potential strengths. All of those potential strengths are chosen to be smaller than the kinetic energy scale; if the periodic potential is very strong the nearly free electron picture is not valid any more. An interesting question is what happens with intensity in that case; in particular, is it still be true that each band is dominantly visible in only one zone?

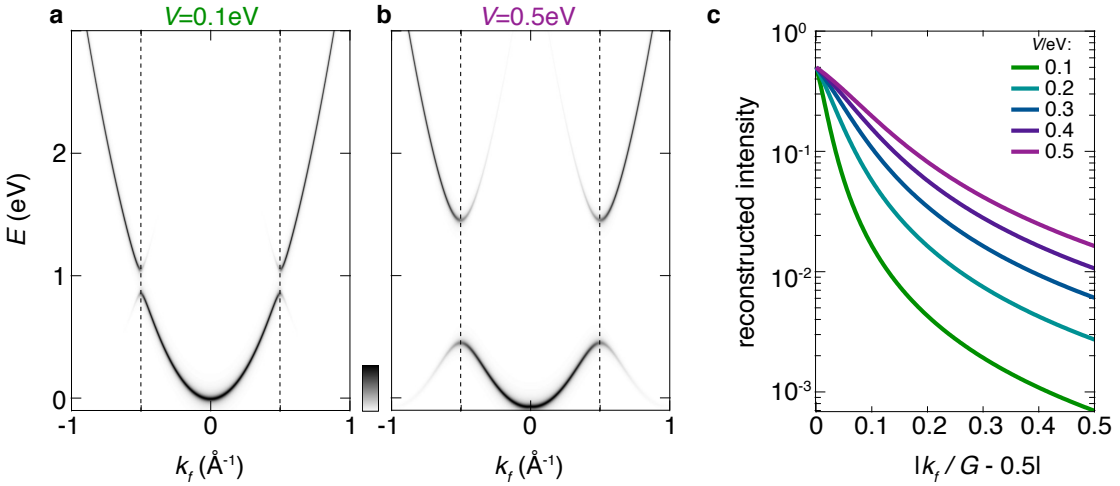

Figure 5.8.: Photoemission intensity of a nearly free-electron system, for (**a**) $V = 0.1\,\mathrm{eV}$ and (**b**) $V = 0.5\,\mathrm{eV}$. (**c**) The variation of intensity of the reconstructed band as a function of distance from the Brillouin zone boundary, for a range of potential strengths V.

5.2.2. Tight binding system

In the limit of very strong periodic potential the band structure can be modelled using the tight binding approximation. For a one-dimensional solid, and considering only nearest neighbour hopping of amplitude t, the tight binding band has a cosine dispersion, $E = -t\cos(ka)$. The wave function of momentum k_i is a sum of orbitals localised on every site, $\varphi(x - na)$, with the phase change of $k_i a$ between sites:

$$\psi_{k_i}(x) = \frac{1}{\sqrt{N}}\sum_n \varphi(x - na)\exp(\imath k_i na), \tag{5.8}$$

where k_i is defined in the first zone, and a is the lattice constant. The tight binding wave function is of course of the Bloch form:

$$\psi_{k_i}(x) = \exp(\imath k_i x)\frac{1}{\sqrt{N}}\sum_n \varphi(x - na)\exp(-\imath k_i(x - na)) = \exp(\imath k_i x)\, u_{k_i}(x), \tag{5.9}$$

with $u_{k_i}(x)$ inheriting the lattice periodicity. A discussed above, the variation of photoemission intensity with the final state momentum is governed by the Fourier transform of $u_{k_i}(x)$ (Equation 5.5). The intensity distribution therefore necessarily depends on the form of the tight binding basis, $\varphi(x - na)$, out of which $u_{k_i}(x)$ is constructed. This is why useful information on the symmetry of the initial state wave function can be extracted from photoemission matrix elements. For simplicity I will assume a Gaussian charge distribution of width σ on every site, and study the form of the resulting intensity variation. With this assumption the periodic part of the Bloch wave function, $u_{k_i}(x)$, has the following form:

$$u_{k_i}(x) = \frac{1}{\sqrt{N}}\frac{1}{(2\pi\sigma^2)^{1/4}}\sum_n \exp\left(-\frac{(x - na)^2}{4\sigma^2} + \imath k_i(x - na)\right). \tag{5.10}$$

As the Fourier transform of a Gaussian is also a Gaussian, the coefficients $c_n(k_i)$ of the transform are given by

$$c_n(k_i) = \frac{1}{\sqrt{\pi N}}\left(2\pi\sigma^2\right)^{1/4}\exp\left(-\sigma^2(nG - k_i)^2\right), \tag{5.11}$$

with G denoting the reciprocal lattice vector, $G = 2\pi/a$. The width of this momentum - space Gaussian is inversely proportional to the width of the charge distri-

bution in real space, reflecting the basic property of Fourier transforms. The more localised the tight binding orbitals are, the more $c_n\,(k_i)$ coefficients are relevant, and the band can be observed in further zones. This is shown explicitly in Figure 5.9, in which I plot the photoemission intensity expected of a tight binding band as a function of final state momentum, varying the width of the charge distribution σ. For a charge distribution localised to within 1% of the lattice spacing ($\sigma = 0.01a$, Figure 5.9a), no variation of photoemission intensity is observable in the first three zones, as shown in Figure 5.9b. If the change distribution is made wider, the intensity in the higher zones is visibly reduced ($\sigma = 0.05a$, Figure 5.9c, d). The suppression is larger and quicker for an even wider charge distribution ($\sigma = 0.1a$, Figure 5.9e, f). While the intensity in the nearly free-electron model is best understood as a projection of the initial state wave function onto a plane wave final state, it is more useful to think about the intensity in the tight binding model as a Fourier transform of the initial state wave function. These are of course equivalent statements, useful in the opposite limits.

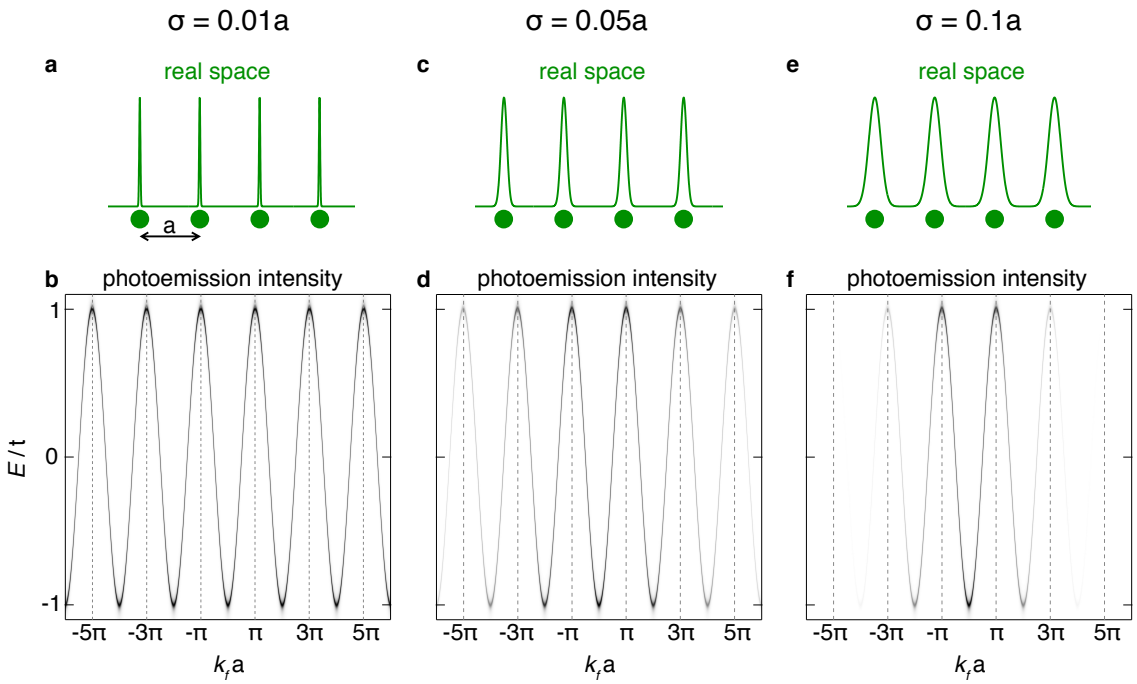

Figure 5.9.: Real space distribution of charge density (**a**, **c**, **e**) and the variation of photoemission intensity (**b**, **d**, **f**) for a Gaussian charge distribution on every site of width $\sigma = 0.01a$ (**a**, **b**), $\sigma = 0.05a$ (**c**, **d**) and $\sigma = 0.1a$ (**e**, **f**).

5.2.3. Tight binding band in a weak periodic potential

The remaining question is how the measurable intensity of a tight binding band changes if a weak periodic potential is superimposed onto the strong potential leading to the tight binding description in the first place. This is the model relevant for describing the $PdCoO_2$ - like conduction electrons in a weak periodic potential caused by the local moment antiferromagnetism. It should therefore qualitatively reproduce the features observable in $PdCrO_2$, as long as the interaction of metallic electrons and the weak periodic potential really captures the relevant physics. As will become apparent in the following section, this is not the case.

The band structure in a weak periodic potential consists of the original tight - binding band, and its copy offset by the wave vector of the periodic potential. Such a band structure is shown in Figure 5.10a in the limit of the vanishing periodic potential, by the orange and red lines representing the 'original' and 'offset' band, respectively. The wave vector of the weak periodic potential is half the reciprocal lattice vector, $G/2$. The boundaries of the 'new' zone are marked by vertical dashed lines, and the bands are plotted in the repeated zone scheme. The periodic parts of the Bloch wave functions corresponding to those two bands, $u^I_{k_i}(x)$ and $u^{II}_{k_i}(x)$, are given by:

$$u^I_{k_i}(x) = \sum_n c_n(k_i) \exp(\imath n G x), \quad u^{II}_{k_i}(x) = \sum_n c_n(k_i) \exp\left(\imath \left(n + \frac{1}{2}\right) G x\right). \quad (5.12)$$

A Hamiltonian expressed in the basis of these wave functions has the following generic form:

$$H(k) = \begin{pmatrix} E(k) & V \\ V & E(k + G/2) \end{pmatrix}, \quad (5.13)$$

where $E(k)$ is the dispersion of the original tight-binding band. A finite periodic potential V allows hybridisation between the original band and its offset copy, so gaps open at the new Brillouin zone boundary, as shown in Figure 5.10a by the green lines. The two wave functions of this hybridised system are both linear combinations of $u^I_{k_i}(x)$ and $u^{II}_{k_i}(x)$:

$$u_{k_i}(x) = \alpha(k_i)\, u^I_{k_i}(x) + \beta(k_i)\, u^{II}_{k_i}(x), \quad (5.14)$$

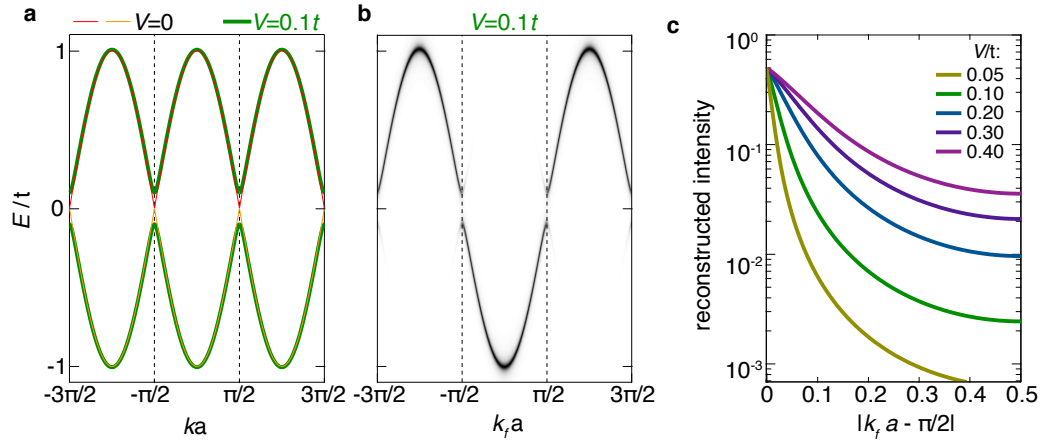

Figure 5.10.: (**a**) Tight binding bands in the limit of the vanishing additional periodic potential (red, orange), and for an additional periodic potential of strength $V = 0.1t$ (green). (**b**) Photoemission intensity for $V = 0.1t$. (**c**) Photoemission intensity as a function of the distance from the boundary of the new Brillouin zone, for varying potential strength V.

with momentum-dependent prefactors $\alpha(k_i)$ and $\beta(k_i)$, which are different for the two bands. The hybridised wave functions are of course also periodic, with Fourier transforms given by:

$$u_{k_i}(x) = \sum_n d_n(k_i) \exp(inGx/2). \tag{5.15}$$

As always, the photoemission intensity in the first zone ($n = 0$) is given by the $n = 0$ coefficient of the Fourier expansion, $|d_0(k_i)|^2$ here. A comparison of the two expressions for the wave function (equations 5.14 and 5.15) makes it clear that $d_0(k_i) = \alpha(k_i)\, c_0(k_i)$. Therefore, the ratio of the intensity of the band in a weak periodic potential ($|d_0(k_i)|^2$) to the one without the weak potential ($|c_0(k_i)|^2$) is given by $|\alpha(k_i)|^2$, i.e. the admixture of the $u^I_{k_i}$ state in the wave function. In the first zone the $u^I_{k_i}$ state corresponds to the unperturbed wave function, so this is equivalent to stating that the photoemission intensity of a tight binding band in a superimposed weak periodic potential is proportional to the overlap of the corresponding wave function with the 'original' tight binding one. It is straightforward to show that this conclusion is valid in every zone, resulting in the photoemission intensity following the dispersion of the 'original' cosine band, as shown in Figure 5.10b and discussed

previously by Voit at al. [78]. The intensity of the reconstructed band is weak, and quickly reduces away from the boundary of the new Brillouin zone. Unsurprisingly, the rate of the decrease depends on the strength of the periodic potential V, as shown in Figure 5.10c.

The analogy with the nearly-free electron case is evident. In both cases a new periodicity perturbs a system dominated by a different energy scale. Copies of the original band offset by the wave vector of the periodic potential appear, and hybridise with the 'original' band, opening gaps proportional to the periodic potential at the boundaries of the new zone. The intensity of the 'reconstructed' band is proportional to the admixture of the 'original' band in the hybridised one, and is therefore quickly reduced away from the zone boundary, as the mixing with the original band is suppressed. Crucially, this behaviour does not rely on any specific properties of the system. The intensity in every zone is always set by a term in the Fourier expansion of the wave function, $c_n \exp(\imath n G x)$, with the *integer* n varying from zone to zone. An additional periodic potential of wave vector G_1 introduces new components of the form $c_m \exp(\imath (m + G_1/G) G x)$ to the expansion. However, as G_1 is smaller than G, G_1/G is never an integer, those components cannot contribute to the observable intensity in any of the original zones. Therefore, once the 'original' and 'new' bands are allowed to hybridise, the observable intensity is proportional to the admixture of the 'original' band in the hybrid one, as shown explicitly both for a free-electron band and a tight binding band in a weak periodic potential above.

5.2.4. Reconstructed intensity in $PdCrO_2$

In order to see how the above discussion applies to $PdCrO_2$, it is useful to construct a tight - binding model using realistic parameters. Since details of the band structure are not relevant for the arguments presented here, I will use a simplified tight binding model taking into account only the nearest - neighbour hopping on a triangular lattice. The dispersion in this model is given by

$$E(k_x, k_y) = -t\left(\cos(k_x a) + 2\cos\left(\sqrt{3}k_y a/2\right)\cos(k_x a/2)\right) - E_0. \tag{5.16}$$

The hopping integral t and the offset E_0 are chosen to match the experimental Fermi wave vectors and the energy at which the 'original' and reconstructed band intersect, leading to $t = 0.9\,\mathrm{eV}$ and $E_0 = 0.4\,\mathrm{eV}$. The wavevectors of the periodic potential due

to the antiferromagnetic order are $\vec{G}_1 = 4\pi/(3a)\,\hat{x}$ and $\vec{G}_{2,3} = 2\pi/(3a)\left(\hat{x} \pm \sqrt{3}\hat{y}\right)$. A crucial parameter is of course the magnitude of the periodic potential V, which can be related to the gap at the magnetic Brillouin zone boundary Δ as $V = \Delta/2$. The gap is too small to be resolved in the photoemission spectra, but it can be deduced indirectly from the so-called breakdown field in quantum oscillation measurements. The breakdown field is a characteristic field setting the probability for an electron to tunnel across the gaps opened by the periodic potential, and move on the 'original' Fermi surface instead. It depends on the gap size roughly as $\hbar\omega_c \sim \Delta^2/\varepsilon_F$, where $\omega_c = eH/m$ is the corresponding cyclotron frequency and ε_F the Fermi energy [79]. Ok et al. [26] measured a breakdown field of $\sim 7\,\mathrm{T}$ in $PdCrO_2$, corresponding to a gap size of $\sim 40\,\mathrm{meV}$. I therefore simulate the photoemission intensity assuming $V = 20\,\mathrm{meV}$, broadened by an effective impurity self-energy of $80\,\mathrm{meV}$ to reproduce the experimental linewidth of $\sim 0.04\,\mathrm{\AA}^{-1}$ at the Fermi level. As evident in Figure 5.11a, the reconstructed band is not visible at all, a consequence of the quick suppression of its intensity away from the zone boundary. The reconstructed band weight is plotted as a function of binding energy in Figure 5.11b, showing that it is four orders of magnitude smaller than the main band intensity at the Fermi level! This is in clear contrast to the measured electronic structure (Figure 5.1), in which the intensity is visible all the way to the Fermi level. To directly compare the measured intensity of the reconstructed weight to the one predicted by the periodic potential model, I normalise both by the intensity at the binding energy of $0.7\,\mathrm{meV}$, at which the main band and the reconstructed weight are separated well enough to ensure a reliable fit. It is clear that the simple periodic potential model is inadequate to explain our experimental observation, predicting a qualitatively different binding energy dependence of the intensity.

To confirm that the observed signal is not an artefact of the specific experimental conditions chosen to perform the measurement in Figure 5.1a, we measured the same dispersion using a range of photon energies and different light polarisations, as shown for p - and s- polarised light in Figures 5.12a and 5.12b, respectively.The intensity variation with binding energy does slightly depend on the experimental conditions, however it was never observed to change by more than a factor of two over the $700\,\mathrm{meV}$ binding energy range, whereas the simple model would predict a change of two orders of magnitude in the same energy range. It is particularly interesting to note that in the measurements with s- polarised light the intensity

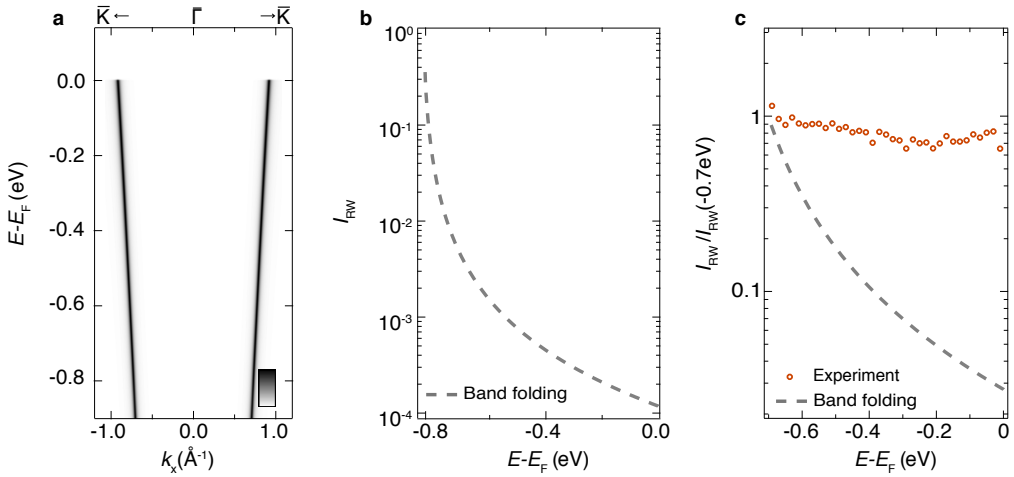

Figure 5.11.: (**a**) Simulated photoemission spectrum of $PdCrO_2$, assuming the strength of the periodic potential to be $V = 20\,\text{meV}$. (**b**) The dependence of the reconstructed weight on binding energy, extracted from (a). (**c**) The dependence of the reconstructed weight on binding energy normalised at $-0.7\,\text{eV}$, extracted from the band folding model (line, extracted from (a)) and the experiment (symbols, extracted from Figure 5.1a)

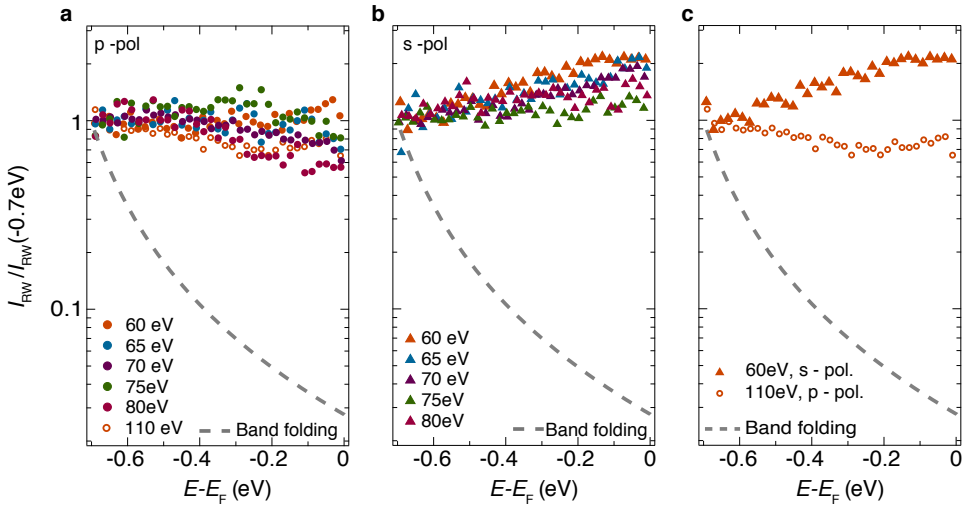

Figure 5.12.: The dependence of the reconstructed weight on binding energy normalised at $-0.7\,\text{eV}$ measured using a range of photon energies, as indicated by the legends, using (**a**) p - polarised and (**b**) s - polarised light, and compared to the prediction of the band-folding model. (**c**) The same, shown only for two measurement conditions illustrating the range of observed binding energy dependencies.

actually increases towards the Fermi level, an effect that could never be explained in the hybridisation picture. For clarity in Figure 5.12c I plot only the intensity variation measured at 110 eV with p - polarised light and at 60 eV with s - polarised light, representative of the range of observed intensity variations.

5.3. Coupling of metallic and Mott insulating layers

The evident disagreement between the 'backfolding' model and the experiment indicates that the weak periodic potential arising from the antiferromagnetic order in the chromium layer is not the cause of the reconstructed spectral weight. A crucial ingredient neglected so far is the correlated nature of the Mott layer; it was treated as a source of periodic potential, but its dynamical degrees of freedom were not taken into account. After realising this issue, we addressed it by starting a collaboration with Roderich Moessner, Sota Kitamura and Takashi Oka. Kitamura and Oka developed a minimal model describing the coupling between the metallic Pd and Mott insulating CrO_2 layers. I will outline their calculation, and in particular discuss its implications for the measured spectra. More technical details of the calculations are available in Reference [8].

The starting point is a Hubbard Hamiltonian, combining the hopping within and between the Pd and Cr layers with the Coulomb repulsion in the Cr layer:

$$H = -\sum_{ij\sigma}^{n.n} \left(t_p p^\dagger_{i\sigma} p_{j\sigma} + t_c c^\dagger_{i\sigma} c_{j\sigma} \right) + U \sum_i \left(n^c_{i\uparrow} - \frac{1}{2} \right) + \sum_{i\sigma} g \left(p^\dagger_{i\sigma} c_{i\sigma} + h.c. \right), \quad (5.17)$$

where t_p (t_c) denote the hopping integrals between the Pd (Cr) sites, g is the interlayer hopping and U the on-site Coulomb repulsion on the Cr sites, as illustrated in Figure 5.13a. The full calculation, the results of which I will compare to the experiment, includes the three t_{2g} orbitals of Cr and the $d_{3z^2-r^2}$ orbital of Pd, and considers nearest neighbour and next-nearest neighbour hopping on a staggered triangular lattice, as is appropriate for $PdCrO_2$. For simplicity, in Equation 5.17 I assume only nearest neighbour hopping, and one state per site; $p^\dagger_{j\sigma}$ ($p_{j\sigma}$) and $c^\dagger_{j\sigma}$ ($c_{j\sigma}$) therefore correspond to the electron creation (annihilation) operators for an electron of spin σ on the Pd and Cr site j, respectively (Figure 5.13a). All the hopping parameters were informed by downfolding a density functional theory calculation onto a Wan-

nier basis model [8]; while this effectively single-particle calculation cannot correctly capture the electronic structure of $PdCrO_2$, its estimates for orbital overlaps are relevant. The resulting hopping parameter in Pd layer is $t_p \sim 1\,\text{eV}$, while the hopping in the Cr layer t_c and the hopping between the layers g are both $\sim 0.1\,\text{eV}$. The on-site repulsion U is typically on the order of 4 eV for $3d$ orbitals [80], making it the dominant energy scale in the problem considered here; this value was also confirmed specifically for $PdCrO_2$ by dynamical mean field theory [8, 81]. Because U is so large compared to other coupling constants, it is justified to express the Hamiltonian in a reduced basis, which contains only wavefunctions in which the Cr sites are singly-occupied. This is technically achieved using a Schrieffer-Wolff transformation, yielding the following low-energy Hamiltonian, valid at energies significantly smaller than U:

$$H_{eff} = -t_p \sum_{ij\sigma}^{n.n} p^\dagger_{i\sigma} p_{j\sigma} + \frac{4t_c^2}{U} \sum_{ij}^{n.n} \vec{S}_i \cdot \vec{S}_j + \frac{4g^2}{U} \sum_{i\sigma\sigma'} p^\dagger_{i\sigma} \left(\vec{S}_i \cdot \vec{\sigma}_{\sigma\sigma'} \right) p_{i\sigma'}, \tag{5.18}$$

where $\vec{S}_j$ represents the spin localised on the Cr site j, and $\vec{\sigma}$ is a vector of Pauli matrices, $\{\sigma_x, \sigma_y, \sigma_z\}$. This is the well-known Heisenberg-Kondo Hamiltonian, often used to describe the systems where itinerant electrons are coupled to localised spins [82].

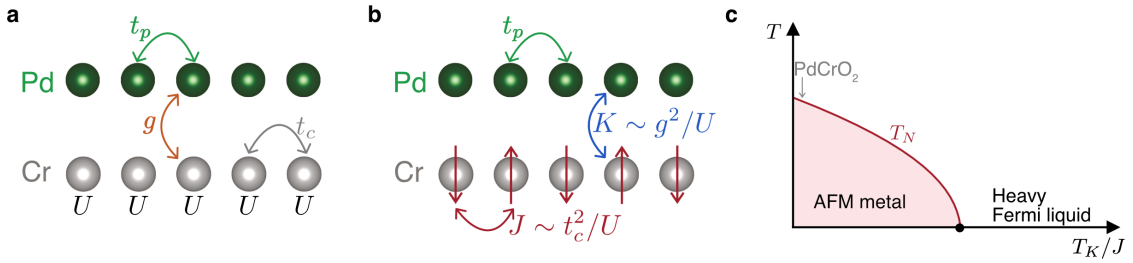

Figure 5.13.: A 1D schematic of the metallic (Pd) and Mott insulating (Cr) layers of $PdCrO_2$, indicating the terms in the Hamiltonian describing the system within the (**a**) starting Hubbard model (Equation 5.17), and (**b**) the Kondo - Heisenberg model valid at low energies (Equation 5.19). (**c**) The Doniach phase diagram (after Reference [83]), indicating the position of $PdCrO_2$.

It is instructive to analyse how its three terms, illustrated in (Figure 5.13b), arise from the original Hamiltonian (Equation 5.17, Figure 5.13a). The first term, describ-

ing the hopping in the metallic Pd layer, remains unchanged. This in not surprising, as the Pd layer is not significantly affected by the strong correlations in the Cr layer. However, the hopping in the Cr layer ($t_c c^\dagger_{i\sigma} c_{j\sigma}$) is suppressed because the on-site repulsion introduces a large energy cost for double occupancy. It is replaced by an effective nearest neighbour antiferromagnetic spin exchange, $4t_c^2/U\left(\vec{S}_i \cdot \vec{S}_j\right)$. This term arises because the virtual process by which an electron hops to a neighbouring site and returns to the original one is forbidden by the Pauli principle if the neighbouring spins are ferromagnetically aligned. Such virtual processes, however, reduce the total kinetic energy, as they allow the wave functions to become more delocalised; antiferromagnetic alignment is therefore favourable. The energy gain associated with the antiferromagnetism scales as t_c^2/U, reflecting the fact that the process underlying it requires two 'hops,' to and from an intermediate state, whose energy is U. This is the standard way in which antiferromagnetic interaction arises in correlated insulators. The last term, known as the Kondo coupling term, describes the interaction of localised spins and conduction electrons. It has the same physical origin as the antiferromagnetic coupling between the localised spins: if the spin of an itinerant electron is the same as the spin of the localised one, the Pauli principle does not allow their wave functions to overlap, leading to a larger degree of wave function localisation, and the corresponding kinetic energy cost. A localised spin therefore 'attracts' conduction electrons of opposite spin. The similar origin of the two terms is emphasised if the Kondo term is rewritten as

$$H_{int} = \frac{4g^2}{U} \sum_i \vec{S}_i \cdot \vec{s}_i, \qquad \vec{s}_i = \sum_{\sigma\sigma'} p^\dagger_{i\sigma} \vec{\sigma}_{\sigma\sigma'} p_{i\sigma'}, \tag{5.19}$$

where $\vec{s}_i$ represents the spin of an itinerant electron on site i. Care should be taken though not to over-interpret this notation; while $\vec{s}_i$ can be used to determine the spatial variation of expected value of the spin of the itinerant electrons, in contrast to $\vec{S}_i$ it does not represent a spin localised at site i.

The antiferromagnetic nature of the Kondo interaction favours the creation of singlet states between the localised spins and the itinerant electrons, with a characteristic binding energy of

$$k_b T_K = \varepsilon_F \exp\left(-1/\left(K\rho\left(\varepsilon_F\right)\right)\right) \sim \varepsilon_F \exp\left(-\varepsilon_F/K\right), \tag{5.20}$$

where T_K is the so-called Kondo temperature, ε_F the Fermi energy, $K = 4g^2/U$ the Kondo coupling, and $\rho(\varepsilon_F)$ the density of states at the Fermi level [37]. The exponential suppression makes this energy scale typically much smaller than the Fermi energy. Varying the relative strength of the antiferromagnetic exchange and the Kondo temperature results in the rich phase diagram of the Heisenberg - Kondo Hamiltonian, known as the Doniach phase diagram, sketched in Figure 5.13c. If the antiferromagnetic exchange dominates, the localised spins order antiferromagnetically, while the itinerant electrons feel a spatially varying spin-dependent potential arising from this antiferromagnetic order. On the other hand, if the Kondo temperature is the dominant energy scale, the itinerant electrons tend to form singlet states with the localised spins, thus screening them and preventing the antiferromagnetic order from arising. The resulting state is a heavily renormalised Fermi liquid, where the effective Fermi energy is not set by the hopping t_p, but by the Kondo energy scale, T_K. This is the limit relevant for the so-called heavy fermion systems.

It is worth emphasising that the Doniach phase diagram offers a valid description even in the absence of the direct antiferromagnetic exchange, for the so-called Kondo lattice Hamiltonian, which contains only terms describing the kinetic energy of itinerant electrons and their Kondo coupling to a lattice of localised spins. This Hamiltonian is relevant for f - electron systems, because the negligible direct orbital overlap of the f orbitals cannot cause a direct antiferromagnetic exchange. The antiferromagnetism is instead provided through the Ruderman – Kittel – Kasuya – Yosida (RKKY) interaction, which arises as a consequence of coupling of the local moments and the conduction electrons, and as such is already implicitly included in the Kondo coupling term. As with the Kondo temperature, the energy scale associated with the RKKY interaction is also governed by a combination of the Fermi energy and the Kondo coupling, in this case as $J_{RKKY} \sim K^2/\varepsilon_F$. However, this simple model governed by only two microscopic parameters, K and ε_F, is often not sufficient to describe realistic materials containing many atoms and orbitals. The direct exchange can then be added empirically to the Hamiltonian, with a value chosen to match the experimental findings. In contrast, as the $3d$ orbitals are more extended than the f orbitals, the direct antiferromagnetic exchange is present in $PdCrO_2$, leading to the observed antiferromagnetic ground state. The fact that the $PdCrO_2$ is in the antiferromagnetic part of the Doniach phase diagram is confirmed by a comparison of the relevant energy scales. If estimated from the first principles

calculations both the antiferromagnetic exchange J and the Kondo coupling are found to be of similar magnitude, $J \sim K \sim 5\,\mathrm{meV}$. This is not surprising, as the hopping in the chromium layer and the hopping between the layers are of a comparable magnitude ($t_c \sim g \sim 0.1\,\mathrm{eV}$). The Fermi energy is very large, on the order of 5 eV, so the Kondo energy scale $k_b T_K \sim \varepsilon_F \exp(-\varepsilon_F/K)$ is indeed very small. $PdCrO_2$ is therefore an example of a system that can be described by a Kondo - Heisenberg Hamiltonian using realistic microscopic parameters, and is found to be in the antiferromagnetic limit of the model.

5.3.1. Spectral functions

To see if this model can account for our experimental findings it is necessary to calculate the one-electron removal spectral function, separately for the Pd layer and the Cr layer because of their different nature. In what follows I will use the term 'spectral function' to refer to the spectral function already modulated by the overlap of the initial state and the final free-electron like state. Although not precise, this is commonly done as the spectral function itself is not physically observable[2].

The one-electron removal spectral function of metallic Pd describes the process in which an electron is removed from the Pd layer, in our experiment by photoemission, as illustrated in Figure 5.14a. The hole created in this way propagates in the Pd layer, occasionally tunnelling into the Cr layer, thus feeling the periodic potential arising from the antiferromagnetic order. The resulting spectral function therefore looks dominantly like the Pd dispersion (Figure 5.14b). Zooming in at the boundary of the new magnetic Brillouin zone (inset in Figure 5.14b) reveals a small gap opening, and a very weak spectral weight in the reconstructed band. This is precisely the band folding due to a weak periodic potential introduced in Section 5.2.3; it does take place, but it cannot account for the signal we observe.

In contrast, the removal of electrons from Cr orbitals is drastically altered by the coupling to the Pd layer. In an isolated Mott layer electrons can be removed only from the lower Hubbard band, which is found at the binding energy of $\sim U/2$; therefore, electron removal spectral function of a Mott insulator has no features at smaller energies. However, for finite interlayer coupling g, a hole created in the Mott

[2] Calling this quantity the 'simulated intensity', as I did in the simple models above, is misleading if we wish to compare it to the experimental findings, as it does not account for the experimental geometry, or the symmetry of the underlying orbitals.

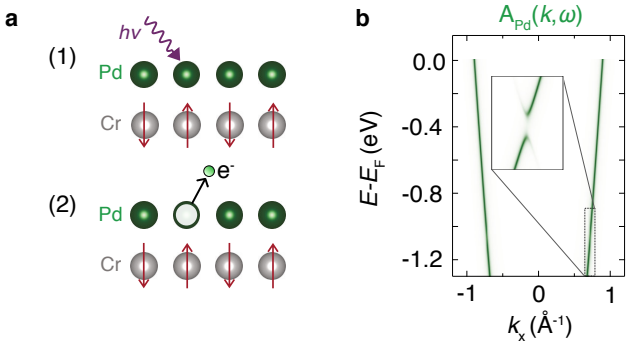

Figure 5.14.: (**a**) Photoemission from a Pd layer leaves a hole which propagates in the Pd layer. (**b**) One-electron removal spectral function for electrons in the Pd layer. The inset shows as small gap opening at the magnetic zone boundary and weak weight in the reconstructed band.

layer can rapidly move to the itinerant layer, where it can propagate. This can be seen formally, as the Schrieffer–Wolff transformation leads to an effective real space Cr removal operator of the form:

$$(c_{j\sigma})_{eff} = \frac{2g}{U} \sum_{\sigma\sigma'} \left(\vec{S}_j \cdot \vec{\sigma}_{\sigma\sigma'} \right) p_{j\sigma'}. \tag{5.21}$$

An attempt to remove an electron from the Cr layer therefore results in a hole in the Pd layer. There are two important features of the transformed operator. Firstly, the process is perturbatively small in g/U. Secondly, it provides a connection between the itinerant Pd electrons ($p_{j\sigma'}$) and Mott spins ($\vec{S}_j$). To develop an intuitive feeling for this coupling in the limit of a magnetically ordered system it is useful to consider its form if the local spin orientation is fixed, for instance along the positive z direction, $S_j^z = 1/2$. The removal operator for a spin up (parallel to the localised spin, $c_{j\uparrow}$) and down ($c_{j\downarrow}$) electron are then given by

$$(c_{j\uparrow})_{eff} = \frac{g}{U} p_{j\uparrow}, \quad (c_{j\downarrow})_{eff} = -\frac{g}{U} p_{j\downarrow}. \tag{5.22}$$

The first of these expressions is easy to understand: it is possible to remove a spin-up electron ($c_{j\uparrow}$) from a site where there exists a localised spin up ($S_j^z = 1/2$), as long as the hole is instantly filled by an electron from the Pd layer, which happens with a probability proportional to g/U (Figure 5.15a). At first it may seem unusual

that it is also possible to remove an electron of the opposite spin, with the same probability of g/U. This is in fact not contradictory, as an electron may be removed from a virtually doubly occupied site. As the double occupancy is also enabled by the coupling between the two layers, its probability is also given by g/U (Figure 5.15b). The operators for the removal of the 'correct' and 'wrong' spin therefore do not differ in amplitude, but they do differ in sign (Equation 5.22). The wave function of a Pd layer hole created by this process therefore encodes the localised spin of the site where it was first created through its phase.

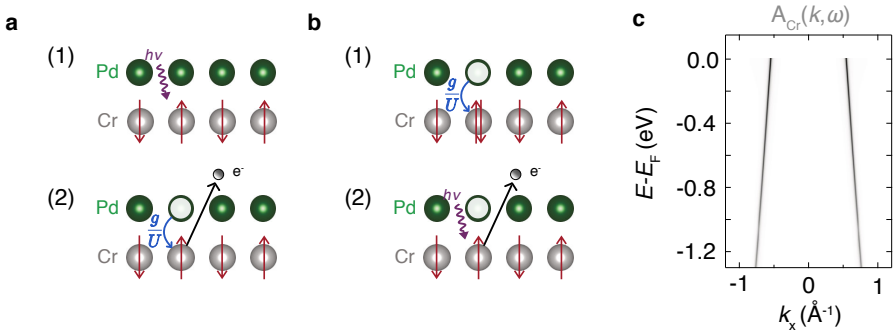

Figure 5.15.: (**a**) A hole created by photoemission from a Cr layer immediately tunnels to the Pd layer. (**b**) Alternatively, a photo can remove an electron from a double occupied site, again leaving a hole in the Pd layer. (**c**) One-electron removal spectral function for electrons in the Cr layer.

This spin-dependent tunnelling process is crucial in determining the final form of the chromium removal spectral function, which is found to be equal to

$$A_{Cr}\left(\vec{k},\omega<0\right)=-\int_{-\infty}^{0}\frac{d\omega'}{2\pi}\int\frac{d^3\vec{q}}{(2\pi)^3}\frac{32\left|g_{\vec{k}+\vec{q}}\right|^2}{U^2}A_{Pd}\left(\vec{k}+\vec{q},\omega'\right)\left\langle\vec{S}_{\vec{q}}\cdot\vec{S}_{-\vec{q}}(\omega-\omega')\right\rangle. \tag{5.23}$$

It is a convolution of the itinerant layer spectral function and the spin-spin correlation function of the Mott layer, with an amplitude determined by the interlayer coupling[3], through the $(g/U)^2$ term. The Pd spectral function appears because the holes tunnel to the Pd layer and propagate there, while the Cr spin-spin correlation

[3]The inter-layer coupling g here exhibits a weak momentum dependence, and is thus labelled as $g_{\vec{k}}$. This is a consequence of the fact that in the real material each atom has more than one nearest neighbour in the neighbouring layer. The coupling therefore has a spatial structure, reflected in a momentum structure of its Fourier transform. For more details see Ref. [8].

function appears because those holes retain a memory of the localised spin in the Mott layer. Indeed, if the spins were not correlated at all, holes would appear in the Pd layer with arbitrary phases on different sites, and therefore would not lead to a coherent photoemission signal. A finite spin-spin correlation function is reflected in the phase of the created holes, and consequently in the spectral function. In this way the spin response of the Mott layer and the charge response of the itinerant layer become intertwined, and photoemission is sensitive to both.

In the case of the antiferromagnetically ordered $PdCrO_2$, the mean-field spin correlation function is a delta function peaked at zero energy and the wavevectors of the antiferromagnetic order $\vec{Q}_{AFM}$, leading to the chromium removal spectral function which is just a copy of the Pd removal spectral function, offset by $\vec{Q}_{AFM}$:

$$A_{Cr}\left(\vec{k}, \omega < 0\right) \sim \frac{32g^2}{U^2} A_{Pd}\left(\vec{k} + \vec{Q}_{AFM}, \omega\right), \tag{5.24}$$

as illustrated in Figure 5.15c. It peaks at the same momenta as a band reconstructed by a weak periodic potential would, but its intensity does *not* depend strongly on binding energy. This is illustrated explicitly in Figure 5.16a, in which I plot the calculated intensity normalised at $-0.7\,\mathrm{eV}$, together with experimental points and the prediction of the band folding model. The calculated variation in spectral weight is in good agreement with the experiment. The exact slope of the reconstructed intensity as a function of binding energy depends on the detailed structure of $PdCrO_2$, and in particular of the ratio of the nearest-neighbour and next-nearest neighbour Kondo coupling. This is best seen by plotting the reconstructed weight for various combinations of nearest neighbour (nn) and next-nearest neighbour (nnn) hopping; small parameter-dependent quantitative variations are observed, although the overall binding energy dependence of the reconstructed weight intensity remains weak for all choices of parameters (Figure 5.16b). The exact form of the binding energy dependence of the reconstructed weight therefore depends on details both in the experiment and in the theory, but the weight never changes by more than a factor of two, in clear contrast to the 'band folding' model which predicts a change of two orders of magnitude.

In addition to this agreement with experiment, the intertwined spin-charge response theory makes an independent prediction: it states that the reconstructed weight is a feature of the chromium one electron removal spectral function, not of

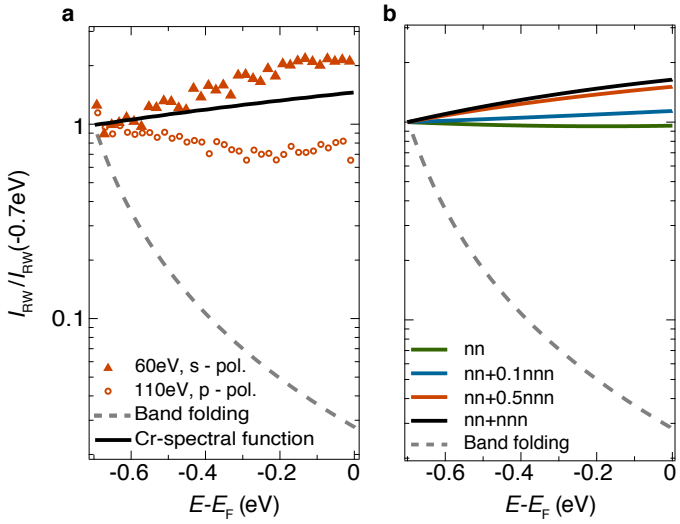

Figure 5.16.: (**a**) Comparison of experiments (symbols), the band folding model (dashed line) and the Cr spectral function calculated within the intertwined spin-charge theory (full line). (**b**) The comparison of the predictions of the theory for different ratios of nearest-neighbour and next-nearest neighbour Kondo couplings (full lines), with that of the band folding model (dashed line).

the Pd spectral function. This is in fact a very surprising prediction, as the spectral functions of Mott insulators are naturally associated with broad, weakly dispersing features, while the reconstructed weight in $PdCrO_2$ is well-defined and dispersive. The prediction motivated us to perform resonant photoemission measurements enabling us to determine the atomic character of the observed states, as I describe in the following section.

5.3.2. Orbital character of the reconstructed weight

In order to check the orbital character of the reconstructed weight we performed resonant angle resolved photoemission measurements in the soft x-ray photon energy range, coinciding with the $L_{2,3}$ x-ray absorption edge of chromium, which we measured on the same sample. The physics behind this technique is described in Section 2.6.6. We first used it to identify the orbital character of the dominant features of the spectral function by comparing on- to off- resonant spectra measured across a wide binding energy range of 4 eV (Fig. 5.17 (a, b)). Consistent with meas-

urements at lower photon energies, we observe the main band crossing the Fermi level. Additionally, we observe a large resonant enhancement of spectral weight of a very weakly dispersing and broad feature centred at approximately 2 eV below E_F, emphasised in energy distribution curves integrated over $0 \pm 0.5\,\text{Å}^{-1}$ (Fig. 5.17c). This weight would be expected in an isolated Cr-derived Mott insulator: a hole created by photoemission has a short lifetime and cannot propagate, leading to the broad, non-dispersive 'lower Hubbard' band, centred at approximately $U/2$ below the Fermi level, in agreement with the DFT+DMFT calculations [8, 81], and confirming $U \sim 4\,\text{eV}$ as a reasonable value for the on-site Coloumb repulsion. While the spectral weight of the main band (I_{MB}) shows negligible change across the resonances, the integrated intensity of the weakly-dispersive feature (I_{LHB}) tracks the Cr $L_{2,3}$ - edge x-ray absorption spectrum (Fig. 5.17d). These measurements therefore establish both the Pd origin of the main band and the Cr origin of the lower Hubbard band, entirely consistent with the picture of $PdCrO_2$ as a natural heterostructure of a nearly-free electron metal alternating with a Mott insulator.

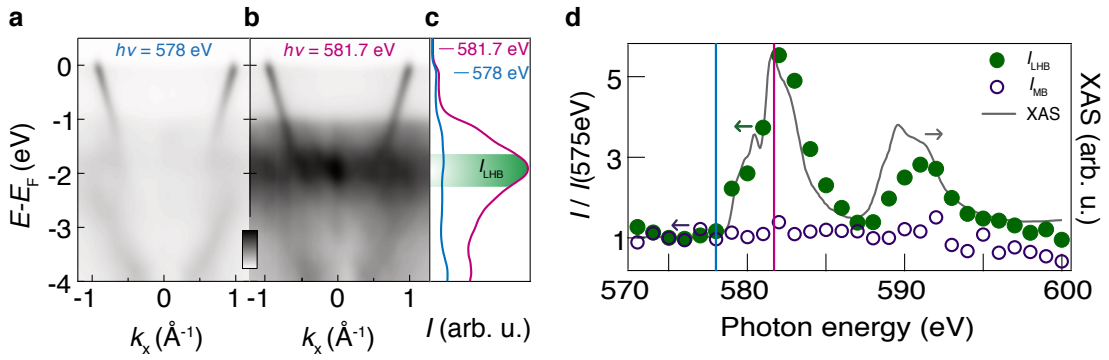

Figure 5.17.: Soft x-ray ARPES ($T = 13\,\text{K}$) at photon energies of (**a**) 578 eV and (**b**) 581.7 eV, respectively tuned off- and on- resonance with the Cr L_3 edge. (**c**) Energy distribution curves extracted from (a, b) and integrated over $0 \pm 0.5\,\text{Å}^{-1}$. (**d**) The intensity of the main band (I_{MB}, extracted from fits to momentum distribution curves at the Fermi level) and of the feature associated with the lower Hubbard band (I_{LHB}, extracted from energy distribution curves (c)) as a function of probing photon energy compared to the measured x-ray absorption spectrum (XAS) across the Cr $L_{2,3}$ – edge.

Our intertwined spin-charge model, however, predicts that if the Mott insulator is coupled to a metal, its spectral weight can also be observed at lower energies in the form of the reconstructed weight. This reconstructed weight is too weak to be immediately obvious in Fig. 5.17(a, b), both because of the intrinsic suppression of $\sim (g/U)^2$ predicted by our model, and because of the small cross section for Cr photoemission at the soft x-ray energies. Just off-resonance the ratio of the cross sections for Cr $3d$ and Pd $4d$ orbitals is only ~ 0.15 [84]; for comparison, this is ~ 100 times smaller than at 110 eV at which the data in Figure 5.1 were measured. However, the reconstructed spectral weight is revealed by comparing momentum distribution curves measured on- and off- resonance (Fig. 5.18a, extracted from Fig. 5.17(a, b)), demonstrating how it is in fact enhanced when the photon energy is tuned to promote photoemission from Cr orbitals. The enhancement is made even clearer by comparing Fermi surfaces measured on- and off- resonance (Figure 5.18(b, c)); the copies of the Fermi surface are visible only in the resonant measurement, strongly supporting a chromium origin of the reconstructed weight.

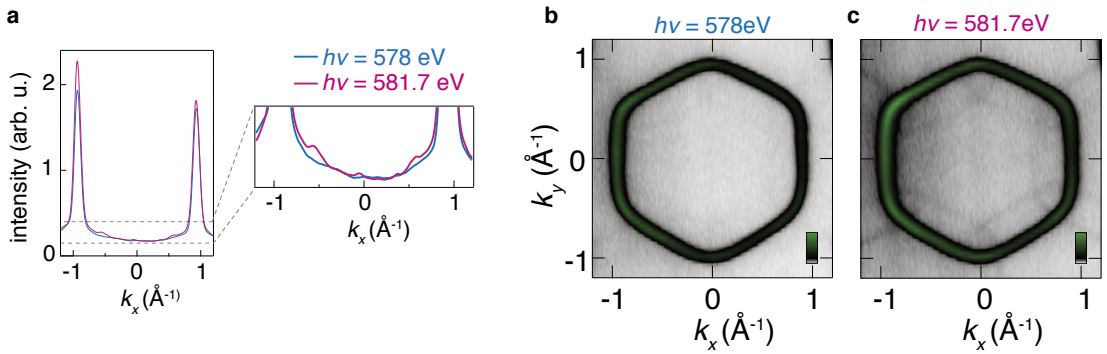

Figure 5.18.: (**a**) Momentum distribution curves ($E_F \pm 50$ meV) extracted from dispersions measured at photon energies of 578 eV and 581.7 eV(shown in Fig. 5.17 (a, b)), respectively tuned off- and on- resonance with the Cr L_3 edge. The MDCs are offset to account for a small increase in background at resonance. The Fermi surface measured ($T = 13$ K, integrated over $E_F \pm 200$ meV) (**b**) off-resonance and (**c**) on-resonance with the Cr L_3-edge.

An additional independent confirmation of the chromium character of the reconstructed weight can be obtained from the photon energy dependent measurements at non-resonant photon energies. Away from resonances the variation of photoemission intensity with photon energy is dominantly caused by the changing overlap of the

radial part of the initial state wave function and the final state plane wave. This overlap changes with the wavelength of the final state plane wave, at a rate dependent on the initial state wave function. We therefore compare the photon energy dependence of the lower Hubbard band intensity with that of the reconstructed feature in the $100 - 350\,\text{eV}$ photon energy range. They follow the same functional form (Figure 5.19a); as the lower Hubbard band is proven to be chromium derived (Figure 5.17), this measurement strongly suggests that so is the reconstructed weight. To check that this agreement is not an artefact of an overall intensity variation with photon energy, in Figure 5.19b I plot the ratio of the reconstructed weight and the main band intensity. First of all, the ratio is not constant, showing that the Pd - derived intensity does change at a rate different to the Cr derived-intensity. Moreover, this measured ratio follows the functional form of the ratio of the calculated Cr $3d$ and Pd $4d$ ionic cross-sections [84]. Taken together, the resonant enhancement and the variation of intensity as a function of photon energy at non-resonant photon energies offer strong experimental evidence of the chromium character of the reconstructed weight.

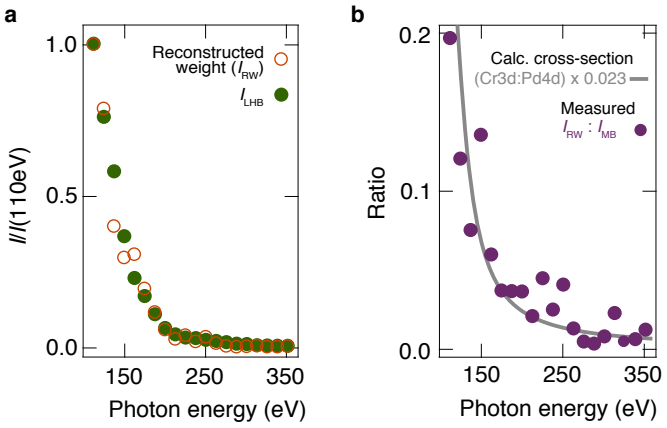

Figure 5.19.: (**a**) The photon energy dependence of the reconstructed weight (I_{RW}) at lower photon energies closely tracks that of the Cr-derived lower Hubbard band (I_{LHB}). (**b**) The ratio of I_{RW} to the weight of the 'main band' I_{MB}, compared to the Cr $3d$: Pd $4d$ ionic cross-section ratio [84], scaled by a factor of ~ 0.023.

The ratio of the intensities of the reconstructed weight and the main band as a function of photon energy contains additional information. It follows the form of the calculated ratio for Cr $3d$ and Pd $4d$ orbitals, but it is ~ 0.02 (Figure 5.19b) smaller. This is our best estimate of the *intrinsic* ratio of spectral weights of the reconstructed and the main band feature. The intertwined spin-charge model predicts the reconstructed weight to be suppressed by $\sim 32(g/U)^2$ from the main band weight (equation 5.23). Assuming $U = 4\,\mathrm{eV}$ and the suppression of 0.02, this yields $g \sim 0.1\,\mathrm{eV}$, as estimated independently from first principles calculations. Our model therefore agrees both qualitatively and quantitatively with the experiment.

5.4. Conclusion and implications

The combination of the weak binding energy dependence of the reconstructed weight and its chromium character taken together rule out not only the simple band folding model, but also other potential explanations for the observed spectral weight. For example, diffraction of the outgoing electrons from the superlattice potential caused by e.g. a structural distortion would lead to a reconstructed spectral weight with a weak binding energy dependence, as observed e.g. in graphene grown on SiC [85]. However, this picture could never explain the Cr-derived character of the spectral features; if they were due to the diffraction of the Pd-derived states, they would exhibit Pd character. On the other hand, a very strong hybridisation between Cr and Pd layers could explain the Cr character, but in this scenario the backfolded weight would quickly drop away from the hybridisation points, as it does in the band folding model. Indeed, this was the model used in Ref. [7], but gaps needed to be as large as $\sim 1\,\mathrm{eV}$ to explain a backfolded weight observable at the Fermi level (Fig. 4 of Ref. [7]), in clear contrast to both photoemission and quantum oscillation measurements.

We can therefore be confident that $PdCrO_2$ is indeed described by the Heisenberg-Kondo Hamiltonian, whose parameters are experimentally constrained (equation 5.18), establishing $PdCrO_2$ as a simple and clean model system to study the physics arising from this Hamiltonian. The implications of our measurements and theory are however even broader, as we were able to show that in certain circumstances angle-resolved photoemission can be used as an energy- and momentum- resolved probe of spin-spin correlations. The necessary condition to achieve this is coupling

between two subsystems, one of which can support only spin excitations, and the other one only charge excitations. This situation occurs naturally in $PdCrO_2$ because of the close proximity of metallic and Mott insulating layers, but it could also be engineered artificially, with the aim of investigating the structure of spin-spin correlation function in systems which are not suitable for the more traditional probes, such as neutron scattering. A case in point are the van der Waals magnets [86], which offer the opportunity to study the magnetic ordering in a two-dimensional limit. However, as they are only a few atomic layers thick, and often not larger than a few micrometers in lateral size, probing them poses a considerable experimental challenge. Is is, however, possible to stack layers of different van der Waals materials, creating the so-called van der Waals heterostructures. If a coupling between the correlated magnet of interest and a metallic layer was achieved, ARPES could be used to obtain otherwise inaccessible information about the spin-spin correlation function of the magnet. More generally, our experiment and theory together point to a type of spectroscopic signal that was not considered before. As well as motivating completely new types of experiments, this also invites revisiting known systems in which correlated and itinerant states coexist, and a careful investigation of the origin of any 'replica features' that may be observed.

6. Rashba-like spin-split surface states

The surfaces of $PtCoO_2$ and $PdCoO_2$ support states with properties very different from those of the bulk, as discussed in the Introduction (Section 1.2.1), and shown in Section 2.6.5 on the example of $PdCoO_2$. The surface states found on their CoO_2 - terminated surfaces are the topic of this chapter, which I will start by describing the experimental observations, and the conclusions that can be drawn based on the experiments and symmetry arguments alone (Section 6.1). I will go on to introduce the density functional theory (DFT) calculations of these surface states performed by Helge Rosner, compare them to the experiment, and show how this comparison was necessary to correctly interpret the calculations, but also to motivate further measurements (Section 6.2). Both the experiment and the first principles calculations show that the surface states exhibit a spin-splitting that is unusually large for a system based on $3d$ orbitals, motivating a careful examination of the basic principles underlying the appearance of spin-split band structures in solids (Sections 6.3 - 6.5). This analysis, although motivated by our measurements, in not at all specific to delafossites. In contrast, it outlines a general framework which can be used to think about systems exhibiting spin-splitting. In section 6.4 I work with a didactic model based on p - orbitals, as originally introduced by Petersen and Hedegård [87], which is very useful for establishing and illustrating the main principles behind spin-splitting. In section 6.5 I discuss the generality of the conclusions drawn from the p - orbital model, and finally, in section 6.6 I extend the analysis to a tight binding model whose ingredients are directly relevant to the CoO_2 layer of the delafossites. I show how this model gives a new perspective on the density functional theory calculations, and how its predictions were confirmed by measurements on a new compound, $PdRhO_2$ (Section 6.7). A reader more interested in the results specifically relevant for the delafossite surface states than in the general

analysis of the development of spin splitting and orbital angular momentum in solids may prefer to jump directly from section 6.2 to section 6.6, and back-refer to sections 6.3 - 6.5 as necessary.

6.1. Experimental observations

In figure 6.1 I show the surface electronic structure measured along the two high symmetry directions of $PtCoO_2$ and $PdCoO_2$, as well as the corresponding Fermi surfaces. In both compounds there are two surface hole-like bands centred at the $\overline{\Gamma}$ point of the Brillouin zone, which I will refer to as the *inner* (smaller k_F) and *outer* (larger k_F) band. The outer band forms a hexagonal Fermi surface of the same orientation as the zone, while the Fermi surface of the inner band is circular, consistent with the previous observation in $PdCoO_2$ [12]. The surface states in $PtCoO_2$ and $PdCoO_2$ are very similar, so the discussion below is valid for both materials. For simplicity the majority of data in this chapter is shown for $PtCoO_2$ only; equivalent plots for $PdCoO_2$, as well as numerical values extracted from them, can be found in Appendix E. I will point to the Appendix when appropriate, but referring to it is not necessary to follow the rest of this chapter.

6.1.1. Dispersions

The high resolution dispersions (Figure 6.1 a, b, d, e) can be used to determine the Fermi crossing vectors (k_F), as well as Fermi velocities (v_F) along the high symmetry directions. In Figures 6.2(a, d) I show zoom-ins of the data measured close to the Fermi level along the $\overline{\Gamma} - \overline{M}$ and the $\overline{\Gamma} - \overline{K}$ directions in $PtCoO_2$ (same data as in Figure 6.1 (a, b)). The dots mark the positions of Lorentzian peaks fitted to extracted momentum distribution curves (MDCs) as a function of binding energy; the same extracted points are shown in Figures 6.2(b, e). The dispersions are linear on the energy scale of $\sim 50\,\text{meV}$, however a slight curving away from this linear trend can be seen in the immediate vicinity ($\sim 10\,\text{meV}$) of the Fermi level. This apparent change of slope is an artefact both of Coloumb interactions between the outgoing electrons, known as the space charge effect [55], and the finite resolution. The space

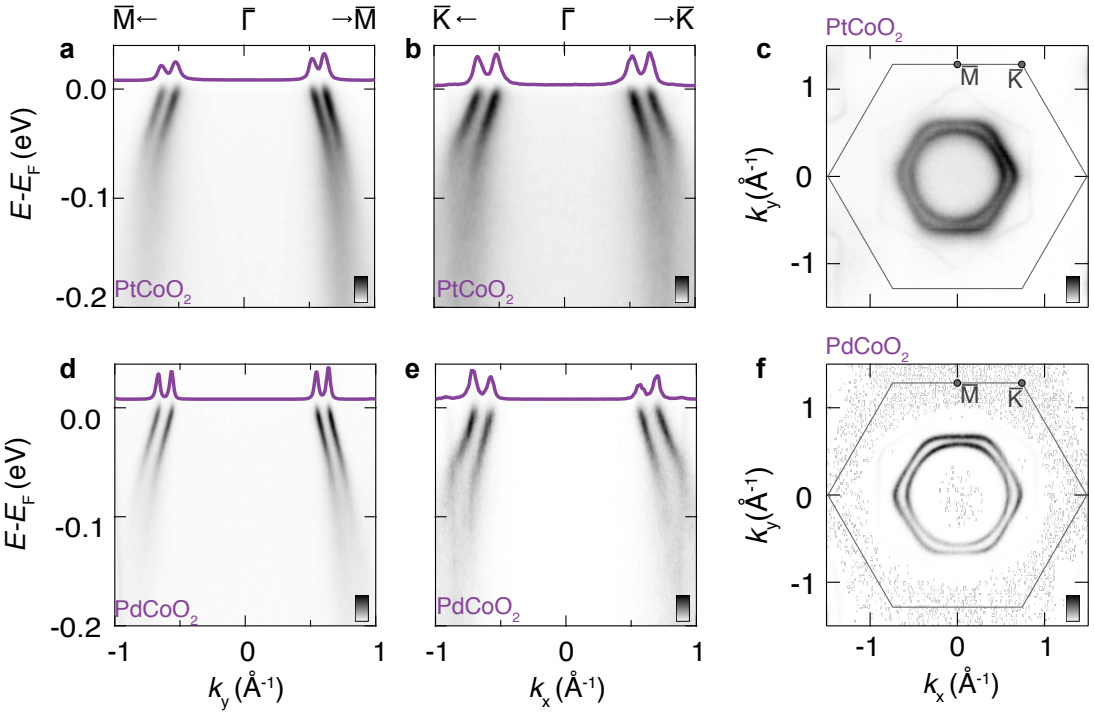

Figure 6.1.: Overview of the experimental results on the spin-split surface states of $PtCoO_2$ (**a**, **b**, **c**) and $PdCoO_2$ (**d**, **e**, **f**). Dispersions in **a** and **d** are measured along the $\overline{\Gamma} - \overline{M}$ direction, while those in **b** and **e** are along $\overline{\Gamma} - \overline{K}$. The purple lines in **a**, **b**, **d** and **e** are momentum distribution curves integrated over $E_F \pm 5\,\text{meV}$. Fermi surfaces ($E_F \pm 5\,\text{meV}$) of the two compounds are shown in panels **c** and **f**. All the data were measured using photon energy of 110 eV and p-polarised light.

charge effect can be minimised by reducing the photon energy, light intensity[1] or increasing the light spot size. The non-uniform surfaces of delafossites required the use of the smallest possible light spot, and the photon energy was chosen to maximise the matrix element for photoemission from Co 3d orbitals. We did reduce the light intensity as much as possible while still allowing collecting high-quality data in a reasonable timescale. Nonetheless, special care needs to be taken in analysis not to be misled by the artificial curving near the Fermi level when extracting band

[1]The synchrotron radiation is not continuous, but arrives in pulses, as determined by electron bunches in the synchrotron ring (see section 2.6.1). The relevant parameter for space charge is actually the number of photons per pulse, rather than the average intensity. However, from the point of view of the user, tuning the number of photons per pulse is equivalent to tuning the intensity.

slopes and Fermi momenta. Specifically, it is crucial to decide on the fitting range which is large enough for the fit to be reliable, but includes only the linear part of the band, as described in detail in Appendix C.2. This has been done individually for every dispersion, measured on three different samples, the data from which are shown in Figure D.2. Examples of such linearised bands, with slopes and crossing points determined by careful fitting, are shown by black lines in Figures 6.2(b, e), while extracted values of Fermi momenta and velocities are listed in Table 6.1. The values of both velocities and momenta confirm that the inner band, unlike the outer one, is isotropic. The equivalent plots and extracted values for $PdCoO_2$ are shown in Figure D.1 and Table D.1 of Appendix D.

		inner	outer
$\overline{\Gamma} - \overline{K}$	$k_F \left(\text{Å}^{-1}\right)$	0.50 ± 0.01	0.64 ± 0.02
	$v_F \left(\text{eVÅ}\right)$	0.40 ± 0.01	0.31 ± 0.02
	m/m_e	9.5 ± 0.5	15 ± 1
$\overline{\Gamma} - \overline{M}$	$k_F \left(\text{Å}^{-1}\right)$	0.50 ± 0.01	0.60 ± 0.01
	$v_F \left(\text{eVÅ}\right)$	0.40 ± 0.02	0.41 ± 0.02
	m/m_e	9.6 ± 0.5	11.5 ± 0.8

Table 6.1.: The Fermi momenta, velocities and effective masses of the two surface state bands in $PtCoO_2$, averaged over three samples, the measurements from which are shown in Figure D.2. The uncertainties reflect both the measurement and fitting precision, as well as sample-to-sample variation. The equivalent data extracted from $PdCoO_2$ are listed in Table D.1, while the measurements underlying it are shown in Figure D.3.

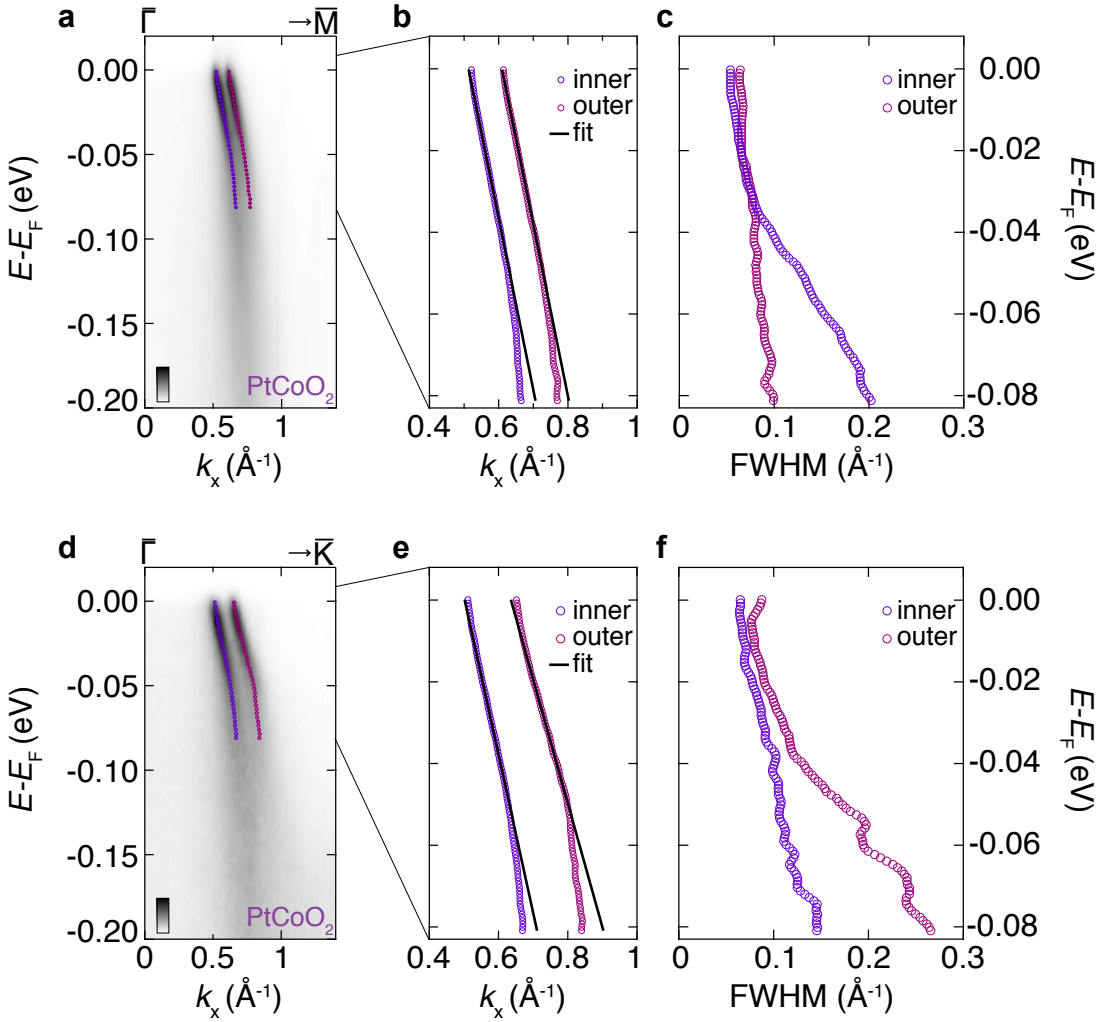

Figure 6.2.: (**a**, **d**) Dispersion measured along the $\overline{\Gamma} - \overline{K}$ and the $\overline{\Gamma} - \overline{M}$ directions in $PtCoO_2$ (110 eV, *p*-polarised light), respectively. The dots in (**a**, **b**, **d**, **e**) are the peak positions of Lorentzian fits to extracted MDCs. The lines in (**b**, **e**) are linearised bands, defined by fitted band slopes and Fermi momenta of the relevant dispersion. (**c**, **f**) The full width at half maximum of Lorentzian fits to the MDCs as a function of binding energy. Equivalent plots for the two high symmetry directions in $PdCoO_2$ are shown in Appendix D, Figure D.1.

The effective quasiparticle masses of the inner (outer) band, calculated from the extracted band slopes and the Fermi vectors, are found to be $(9.5 \pm 0.5)\, m_e$ ($(15 \pm 1)\, m_e$) along the $\overline{\Gamma} - \overline{K}$ direction, and $(9.6 \pm 0.5)\, m_e$ ($(11.5 \pm 0.8)\, m_e$) along the $\overline{\Gamma} - \overline{M}$ direction (Table 6.1). The extracted masses are rather large, especially compared to the free-electron like bulk band. It is evident from the dispersions that the mass is enhanced by interactions. Especially prominent are kinks characteristic of electron-boson coupling, seen at the binding energy of $\sim 50\,\mathrm{meV}$ (*cf.* simulated spectra in Figure 2.8). However, if this were the only type of interaction the rate of increase of the linewidth would be expected to suddenly decrease at the characteristic energy of the boson. In contrast, the extracted full width at half-maximum of the Lorentzian fits (FWHM, Figure 6.2c) does not show any sharp features at the kink energy, pointing to the influence of electron-electron interactions. While the presence of both types of interactions is a robust experimental fact, estimating their numerical strength requires making an assumption about the bare, non-interacting band.

6.1.2. Fermi Surfaces

In Figure 6.3a I show the Fermi surfaces resulting from the surface bands of $PtCoO_2$, with dots representing the Fermi momenta extracted by radially fitting momentum distribution curves (MDCs) around the measured Fermi surface. To analyse the shape of the Fermi surface, it is useful to plot the extracted momenta as a function of angle φ (dots in Figure 6.3b). Clearly visible oscillations in the outer band reflect the 6-fold symmetry of the larger Fermi surface. In contrast, the inner band Fermi vector does not appear to depend on the angle in a systematic way. These statements can be made more quantitative by fitting the extracted momenta as a function of angle to a periodic function reflecting the 6-fold symmetry, as was already done for the bulk Fermi surface (Section 4.1):

$$k_F(\varphi) = k_0 + k_{6,0}\cos(6\varphi) + k_{12,0}\cos(12\varphi)\,. \tag{6.1}$$

The results of fits to the two bands are shown as lines in Figures 6.3(b, c); averaged parameters from fits to Fermi surfaces in two samples are listed in Table 6.2. In an ideal hexagon the first warping term ($k_{6,0}$) is 5.8% of the constant term (k_0), in the outer band in $PtCoO_2$ it is 3.3%, while in the inner band it is only 0.7% of the

constant term, which is within the error of the experiment. The next warping term, $k_{12,0}$, is barely larger than the experimental error for the outer band and negligible for the inner band. All higher terms are negligible for both bands.

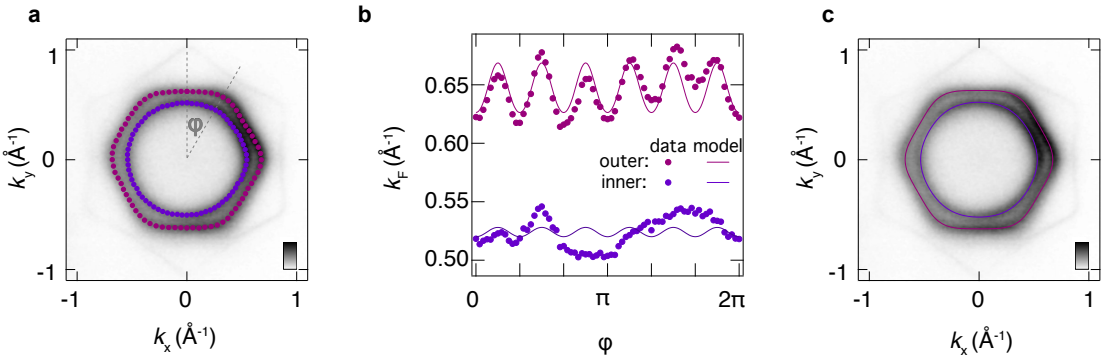

Figure 6.3.: **(a)** Measured Fermi surface of $PtCoO_2$, with dots representing the Fermi momenta extracted by radially fitting MDCs. **(b)** Extracted momenta (dots) as a function of angle φ around the Fermi surface, with a sinusoidal fit (lines) describing the Fermi surface shape (Equation 6.1). **(c)** The same fit as in **b** (lines), superimposed on measured data to demonstrate good agreement. The equivalent plots of the data extracted from $PdCoO_2$ are shown in Figure D.4.

	inner	outer
k_0	0.5248 ± 0.0008	0.6483 ± 0.0007
$k_{6,0}$	-0.003 ± 0.001	-0.022 ± 0.001
$k_{12,0}$	0.000 ± 0.001	0.0011 ± 0.0009

Table 6.2.: Parameters of fits of a periodic function (Equation 6.1) to the inner and outer surface state Fermi surfaces of $PtCoO_2$. An example of such a fit is shown in 6.3(b, c). The quoted values are weighted averages of values extracted from two samples. The equivalent parameters extracted from the measurements on $PdCoO_2$ are listed in Table D.2.

While the agreement between the measured data and the sinusoidal fit for the outer surface demonstrated that the above analysis is a good way to parametrise the Fermi surface shape, it is important to remember that the numerical values of Fermi momenta extracted from the maps are systematically overestimated, due to

the combined effect of the finite integration window of the Fermi surface ($E_F \pm 5\,\text{meV}$) and the space charge. Comparison with the momenta extracted from fits to dispersions (Table 6.1) suggests this is an effect on the order of 4% for both bands. This information is relevant for extracting the areas of the two Fermi surfaces, as it means that direct integration of the fitted data will give an area 8% larger than the intrinsic one. Once this is taken into account, the best estimates for the areas of the inner and outer Fermi surface are 15% and 23% of the Brillouin zone, respectively, adding up to 38%. Assuming spin degeneracy, this would suggest a carrier density of ~ 0.78 holes per unit cell. While effective hole-doping of the surface transition metal oxide layer with respect to the insulating bulk is not unexpected, a simple ionic argument outlined in Section 1.2.1 would suggest there should be 0.5 holes per unit cell. The total charge of the surface states is therefore the first experimental indication that the surface states might not be spin degenerate.

6.1.3. Spin-splitting

A direct confirmation of the lifting of the spin degeneracy comes from our spin resolved ARPES measurements. We measured the expected value of spin perpendicular to momentum along the $\overline{\Gamma}-\overline{K}$ direction of the zone (turquoise line in Figure 6.4a), and found that the spin polarisation is indeed finite, and of different sign on the two bands (Figure 6.4b).

The values of intrinsic spin polarisation are difficult to extract due to the energy resolution of spin resolved ARPES, which is $\sim 100\,\text{meV}$ in the settings used here (Section 2.6.7, [61]), about twice the energy of the kink in the dispersions (Figure 6.2a). Nonetheless, much can be deduced about the spin texture of the surface states from this experiment alone. Since all $\overline{\Gamma}-\overline{K}$ directions in the zone are equivalent, we know there is non-zero spin polarisation perpendicular to momentum along at least three in-plane directions in the zone, as illustrated in Figure 6.4c. In other words, the spin direction becomes "locked" to momentum, circling along the Fermi surface in opposite direction on the two bands. Such spin-momentum locking is reminiscent of the Rashba spin-splitting that is often observed on surfaces of systems with strong spin-orbit coupling. However, the states observed here are features of the CoO_2 terminated surfaces, for which the bare spin-orbit coupling is rather weak, only 70 meV for Co $3d$ orbitals [88]. For comparison, the (111) surface of copper, another

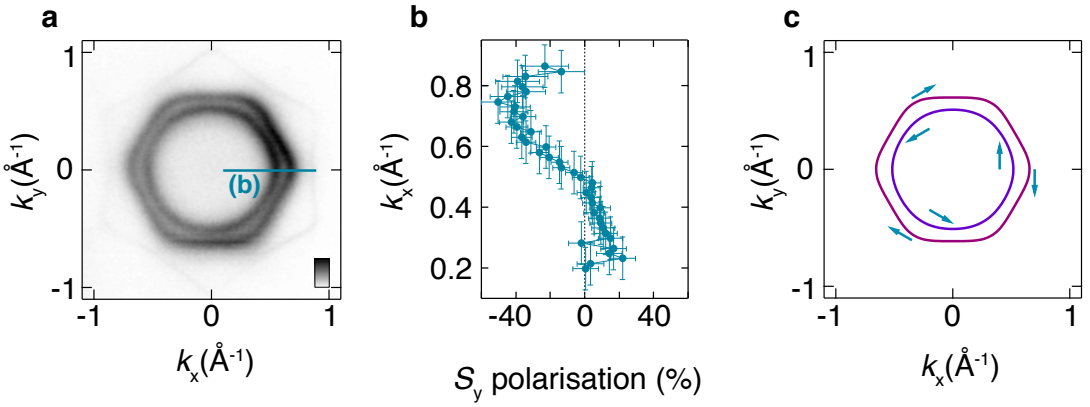

Figure 6.4.: (**a**) Measured Fermi surface of $PtCoO_2$. The turquoise line indicates the cut in momentum space along which the spin polarisation was measured. (**b**) Spin-resolved ARPES measurements ($h\nu = 65\,\text{eV}$, p-polarised light) of an in-plane spin polarisation ($\langle S_y \rangle$) of the Fermi surface for the cut shown in **a**. Error bars reflect an estimate of the uncertainty in extracting the spin polarisation from the experimental measurements as a function of in-plane momentum, incorporating statistical and systematic errors. (**c**) Fits to the Fermi surfaces (same as Figure 6.3c), with arrows representing the information on the direction of spin polarisation that can be extracted based on experiment and symmetry arguments alone. The length of the arrows is arbitrary.

$3d$ orbital system with similar spin-orbit coupling of 100 meV, supports Rashba spin-splitting, but the size of the splitting observed at the Fermi level is only $0.0057\,\text{Å}^{-1}$ [89], and would not be resolvable at all in our experiment. The splitting in $PtCoO_2$ is as large as $0.13\,\text{Å}^{-1}$ and $0.1\,\text{Å}^{-1}$ along the $\overline{\Gamma}-\overline{K}$ and $\overline{\Gamma}-\overline{M}$ directions, respectively. This magnitude is comparable to some of the largest Rashbla-like splittings known [90, 91], found in systems containing Bi $6p$ orbitals which have a very large atomic spin-orbit coupling of 1500 meV.

The above comparison of our experimental observations and well-known systems in the literature therefore suggests that the CoO_2 terminated surfaces of delafossite oxides support unusually large spin-splitting, the origin of which needs to be understood. A first thought might be that there is significant admixing of Pt $5d$ states, which have much larger atomic spin-orbit coupling. Additionally, we may wonder if correlation effects play a significant role in enhancing the splitting, or if surface distortions are relevant. A way to address these questions is to perform density

functional theory calculations of the surface electronic structure. This allows us to directly ask questions about the orbital character, to artificially change the surface structure, and to eliminate correlation effects.

6.2. Comparison of DFT and experiment

The surface electronic structure was calculated for a symmetric slab, containing nine CoO_2 and eight Pt layers. It was terminated with CoO_2 layers on both sides, with a vacuum gap of 15 Å above the surface. The ideal crystal structure was used, with no surface relaxation. The corresponding band structure is shown in Figure 6.5a, where the colour represents the wave function weight in the surface CoO_2 layer.

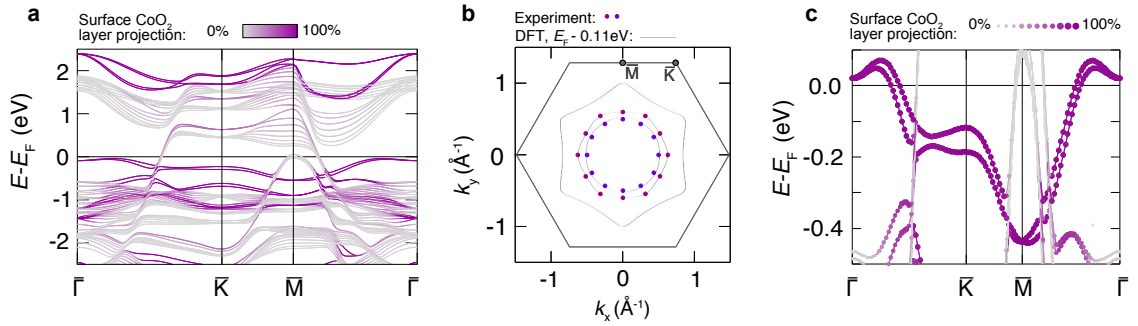

Figure 6.5.: (**a**) Electronic structure from the DFT supercell calculations projected onto the first CoO_2 layer. There are two bands in the bulk band gap in the vicinity of, but not crossing the Fermi level. (**b**) The experimental Fermi momenta of the surface state (dots) match the calculated wavevectors at the binding energy of 110 meV. (**c**) DFT electronic structure, shifted by 110 meV to match the experiment at the Fermi level.

6.2.1. Setting the Fermi level

It is evident that the calculated band structure shown in Figure 6.5a cannot match the experiment: there are no surface bands at the Fermi level, in clear contrast to the measured electronic structure. However, there are two bands just below the Fermi level which are mainly isolated from bulk bands, and disperse in the same direction as the experimentally observed surface states. In fact, as will soon become

clear, these are the bands that are observed experimentally to cross the Fermi level. Their occupation is an artefact of the slight non-stoichiometry of the slab, necessary to make the slab symmetric: a stoichiometric slab would have the same number of Pt and CoO_2 layers, while a slab terminated with CoO_2 layers on both sides has an additional CoO_2 layer. The non-stoichiometry is not expected to change the shape of the bands, but it does necessarily affect their filling, as well as relative energies of different bands. We therefore set the Fermi level in the calculations to match the experimental crossing vectors of the surface states (Figure 6.5b). Applying a shift of +110 meV to all the bands (Figure 6.5c) results in a good agreement of the calculated and measured surface states at the Fermi level. However, it causes the hole-like bulk bands near $\overline{M}$ to intersect the Fermi level in the slab calculation, contrary to the case for the true bulk electronic structure (Figure 4.1). I will neglect these pockets in plotting the calculated Fermi surfaces.

6.2.2. Fermi velocities and interactions

The fact it is possible to set the Fermi level in the calculation such that the Fermi momenta of both bands match the experiment means the interactions are not affecting the relative filling of the two bands. However, they decrease the Fermi velocities, as evident in the measured dispersions (Figure 6.1 a, b, d, e), thus increasing the effective masses. The mass renormalisation, quantified through λ (equations 2.19, 2.20) can be estimated by comparing the calculated and measured Fermi velocities:

$$\lambda = 1 - \frac{m^{exp}}{m^{DFT}} = 1 - \frac{v_F^{DFT}}{v_F^{exp}}. \tag{6.2}$$

To determine the DFT Fermi velocities, I extracted the band slope as a function of energy in the vicinity of the Fermi level (Figure 6.6), and fitted it to a quadratic function. It is worth emphasising that the fact a *quadratic* function was needed to correctly describe the band slope in the range of $E_F \pm 50$ meV means the use of a linear or a parabolic bare band, as is often done, would introduce systematic errors here. The fits are used to extract the band slope at the Fermi level, i.e. the Fermi velocity, as well as to estimate the error of that Fermi velocity caused by the uncertainty in the Fermi level, assumed to be ± 5 meV (Table 6.3).

The mass renormalisation extracted in this way is smaller for the inner band ($\lambda =$

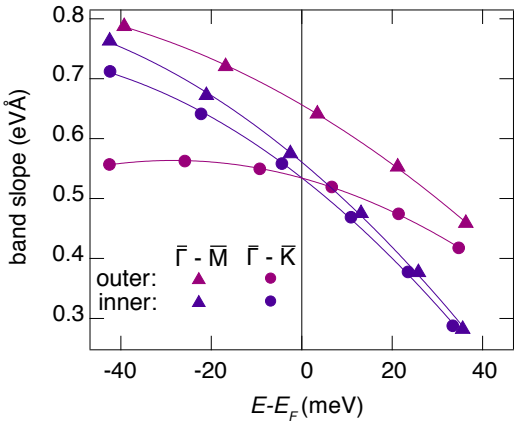

Figure 6.6.: Band slope of for the two bands along the two high symmetry directions, as a function of energy. The lines are quadratic fits to the plotted range, used to extract the value at E_F and the error.

0.4) than the outer band ($\lambda\left(\overline{\Gamma}-\overline{M}\right)=0.6$, $\lambda\left(\overline{\Gamma}-\overline{K}\right)=0.7$) along both directions (Table 6.3). If really true, this is a very interesting result which invites several questions. Is the self-energy intrinsically k-dependent, or is it different for different orbital states found on the two bands? Is the electron-electron or the electron-phonon interaction the one responsible for the difference in the renormalisation of the two bands? However, reliably disentangling the influence of electron-electron and electron-phonon interactions is known to be a difficult problem even when the bare band is well known [92], made even more complicated in delafossites by the close proximity in momentum space of the two surface-state bands and the bulk band. Additionally, the finite band curvature in the range in which the fits were performed affects the extracted values of velocities. A different curvature of the outer and inner band could contribute to the apparent difference in Fermi velocity. Answering detailed questions about self-energies will therefore require both more reliable calculations, and experiments with better resolution, possibly using laser photoemission.

	$v_F^{DFT}\left(\text{eV}\mathring{\text{A}}\right)$	λ
inner, $\overline{\Gamma}-\overline{K}$	0.53 ± 0.03	0.4 ± 0.1
inner, $\overline{\Gamma}-\overline{M}$	0.56 ± 0.03	0.4 ± 0.1
outer, $\overline{\Gamma}-\overline{K}$	0.53 ± 0.01	0.7 ± 0.1
outer, $\overline{\Gamma}-\overline{M}$	0.66 ± 0.02	0.6 ± 0.1

Table 6.3.: Fermi velocities extracted from DFT (v_F^{DFT}, see figure 6.6), and mass renormalisation λ (Equation 6.2) for the two bands along the two high symmetry directions.

6.2.3. Spin polarisation

As well as reproducing the basic band dispersion, the calculation should show the experimentally observed spin polarisation. To check for this, I have coloured the bands according to the expected value of spin (Figure 6.7). Non-vanishing spin polarisation is found in-plane for the direction perpendicular to the momentum (Figure 6.7a, $\langle S_\perp \rangle$), as well as out-of plane (Figure 6.7b, $\langle S_z \rangle$). The in-plane component parallel to the momentum ($\left\langle S_\parallel \right\rangle$, not shown) vanishes along the high symmetry directions. As well as the chiral in-plane component consistent with the experiment, the calculation also finds a smaller out-of-plane spin polarisation at the Fermi level. This is summarised in Figure 6.7c, in which the length of arrows encodes the calculated $\langle S_\perp \rangle$, and the colour the $\langle S_z \rangle$. $\langle S_\perp \rangle$ is $\sim 0.9\hbar/2$ at the Fermi level for both bands along both high-symmetry directions, while $\langle S_z \rangle$ vanishes along the $\overline{\Gamma}-\overline{M}$ direction. Its absolute value is approximately $0.2\hbar/2$ for both bands along the $\overline{\Gamma}-\overline{K}$ direction.

Once the basic agreement with the experiment has been established, the calculation can be used to gain further insight in the bands and wave functions, in particular away from the Fermi level, where the correlations broaden out the experimental features. The band structure plots in Figures 6.7(a, b) show that the spin-splitting persists throughout the bandwidth of the relevant bands, vanishing only at the $\overline{\Gamma}$ and $\overline{M}$ points of the zone, where a combination of translation and time-reversal symmetry ensures spin degeneracy. While the direction of the polarisation changes, from out-of plane in the vicinity of the $\overline{K}$ point, towards dominantly in-plane in the rest of the zone, the expected value of the spin operator is always close to the max-

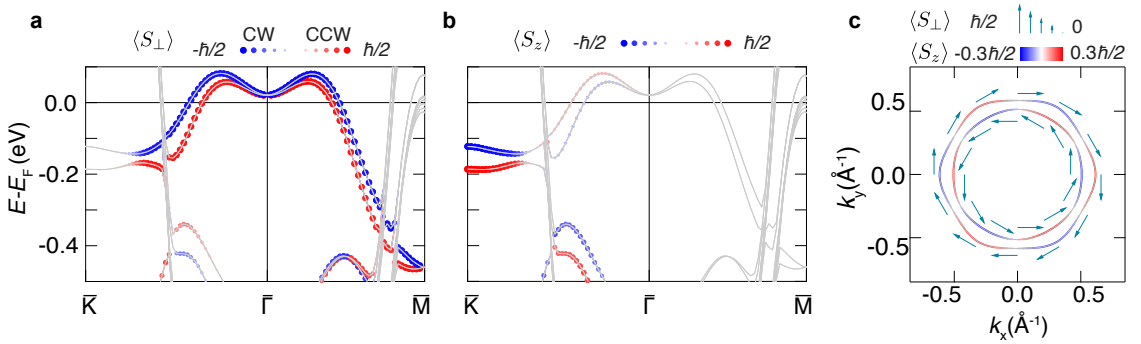

Figure 6.7.: DFT band structure, coloured according to the spin projection (**a**) in the in-plane direction perpendicular to momentum ($\langle S_\perp \rangle$, with red is denoting the counterclockwise rotation) and (**b**) in the out-of-plane direction ($\langle S_z \rangle$). (**b**) Fermi surface calculated by DFT, coloured according to $\langle S_z \rangle$, with the length of arrows encoding $\langle S_\perp \rangle$.

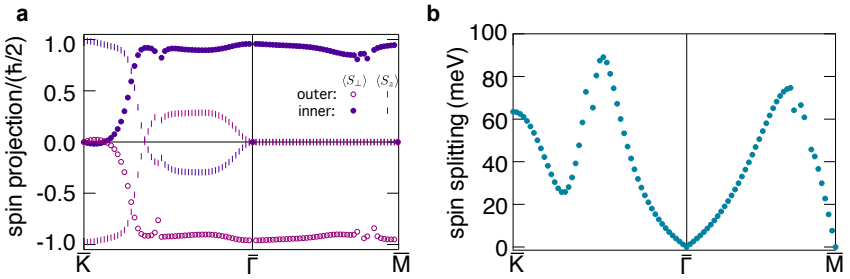

Figure 6.8.: (**a**) Expected value of in-plane spin perpendicular to momentum ($\langle S_\perp \rangle$, circles) and out-of plane spin ($\langle S_z \rangle$, dashes). (**b**) Energetic splitting between the spin-polarised bands. Both are calculated by DFT.

imum possible value, $\hbar/2$ (Figure 6.8a). This is true even in the immediate vicinity of the $\overline{\Gamma}$ and $\overline{M}$ points; the spin polarisation does not decrease continuously, but stays large as long as the splitting is allowed. In contrast, the bands have to be continuous, and consequently the energetic splitting between them decreases smoothly toward the time-reversal invariant points (Figure 6.8b). The requirement for the splitting to vanish at the $\overline{\Gamma}$ and $\overline{M}$ points means it needs to reach a local maximum between them, which indeed happens, with a splitting of 74 meV. The momentum dependence of the splitting is more complicated along the $\overline{\Gamma} - \overline{K}$ direction, where it increases from zero at $\overline{\Gamma}$ to a maximum value of 87 meV, followed by a local minimum at the momentum where the spin changes orientation from in-plane to out-of-plane,

to another maximum of 64 meV at $\overline{K}$. The most striking feature of the momentum dependence of the spin-splitting is the size it can assume; the splitting is on the order of the atomic spin-orbit coupling of Co $3d$ orbitals (70 meV) in a large part of the zone, reaching a maximum 25% larger than the atomic value.

6.2.4. Influence of Pt spin-orbit coupling

The large splitting quite naturally raises the question of the importance of the Pt $5d$ orbitals, whose local spin-orbit coupling of 550 meV is much larger than that of Co $3d$ orbitals, in determining the spin-splitting. The similarity of the data in the vicinity of the Fermi level in $PtCoO_2$ and $PdCoO_2$ (Figure 6.1) already suggests the A-site contributions in negligible. To address the issue of the Pt influence across a wider binding energy range, I first plot the calculated wave function weight contribution of the Pt orbitals in the two bands (Figure 6.9a).

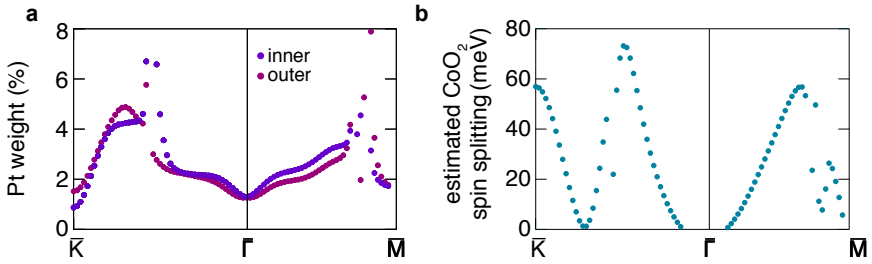

Figure 6.9.: (**a**) The percent of wave function weight coming from Pt orbitals. (**b**) An estimate for the minimum size of the splitting caused by Co SOC, obtained by subtracting the Pt weight (plotted in **(a)**) multiplied by the atomic SOC of Pt $5d$ orbitals (550 meV) from the full spin-splitting (Figure 6.8b)

Neglecting the isolated points where band crossings make it difficult to define individual bands, the Pt weight varies between 1% and 5%, and is about 2.5% at the Fermi wavevectors. A very naive estimate of its contribution to spin-splitting can be obtained by multiplying the Pt $5d$ wave function weight by the Pt $5d$ spin-orbit coupling constant. Subtracting this value from the total spin-splitting gives a rough estimate of the lower bound for the CoO_2 contribution to the energetic splitting (Figure 6.9b). The 'CoO_2 splitting' estimated in this way still reaches the full value of Co spin-orbit coupling at its maximum, and is as high as 57 meV at the $\overline{K}$ point. The above analysis neglects the orbital character (more precisely, the value

of $\left\langle \vec{L} \cdot \vec{S} \right\rangle$) of the admixed Pt bands, and is therefore not quantitatively correct. Nonetheless, the simple estimate it provides is enough to rule out Pt contribution as a driving mechanism of the splitting, and confirms that the spin-splitting is unusually large.

6.2.5. Spin-splitting at the $\overline{K}$ point

The large spin-splitting found in DFT along the $\overline{\Gamma}-\overline{K}$ direction of the zone motivated us to carefully measure the dispersion along the same direction in both $PtCoO_2$ and $PdCoO_2$; the results are shown in Figure 6.10. Although the data are broadened by interactions, we find a clearly resolvable splitting of $\sim 60\,\text{meV}$ at the $\overline{K}$ point in both compounds. The fact the splitting is the same in the two compounds with different A - site cations offers additional, purely experimental, evidence that the strength of the spin-orbit coupling of the A-site cation is not the origin of the large spin-splitting.

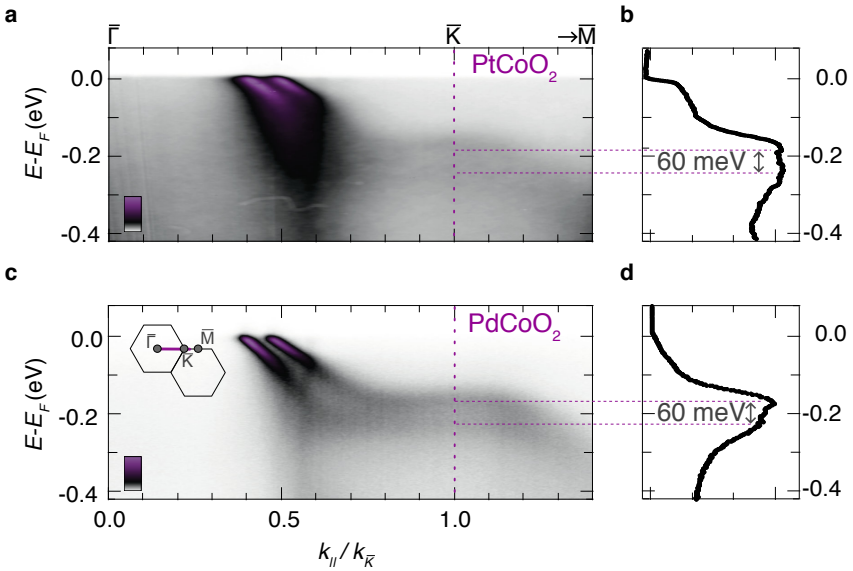

Figure 6.10.: Spin-split surface states of (**a**) $PtCoO_2$ and (**c**) $PdCoO_2$ measured along the $\overline{\Gamma} - \overline{K}$ direction. The inset in a shows the first two Brillouin zones, with the purple line indicating the direction along which the measurements were taken. $k_{\|}$ is the value of in-plane crystal momentum along this direction and $k_{\overline{K}}$ the momentum at the $\overline{K}$ point. Energy distribution curves (EDCs) for for $k/k_{\overline{K}} = 1 \pm 0.05$ are shown in (**b**) and (**d**) for $PtCoO_2$ and $PdCoO_2$, respectively.

The observed splitting size is consistent with the DFT calculations, proving once again that the DFT correctly captures essential features of the spin-splitting. However, it is also important to note that the mean binding energy of the two bands at the $\overline{K}$ point is 200 meV, while the calculated value is 140 meV. Generically, interactions are expected to shrink the bandwidth, not extend it as appears to be the case here. This discrepancy is not so surprising given the approximations used in the calculations, but it does warn against over-reliance on the calculation for the extraction of quantitative interaction parameters.

6.2.6. Conclusions from experiments and DFT

The agreement between the experiment and the density functional theory calculation is very good, but this does not offer direct insight into the basic physics underlying the observed phenomenon. Nonetheless, it does allow us to draw a few important conclusions. First of all, the fact that the DFT calculations capture the relevant physics means that the correlations are not driving the spin-splitting. Furthermore, the calculations are performed for an ideal slab without surface relaxation, so surface distortions of the crystal structure can almost certainly also be ruled out as a cause of the large splitting. Finally, both the experiment and the calculations confirm that the large spin-orbit coupling of Pt $5d$ orbitals is not significantly contributing to the observed spin-splitting. Taken together, these findings suggest that the key physics of the large splitting is contained in a bulk-like CoO_2 layer placed at a surface, and can be understood in a single-particle picture. This motivated me to revisit the question of how spin-splitting arises at all (Section 6.3), and to investigate minimal tight binding models (Sections 6.4 and 6.6) with the aim of isolating the main ingredients necessary to achieve the observed large spin-splitting.

6.3. Spin-splitting

6.3.1. Symmetry requirements

In the vast majority of solids spin degeneracy is protected by a combination of time reversal and inversion symmetry. The time reversal symmetry ensures degeneracy

of states of opposite momentum and opposite spin:

$$E\left(-\vec{k},\uparrow\right) \overset{TR}{=} E\left(\vec{k},\downarrow\right), \tag{6.3}$$

while the inversion symmetry requires degeneracy of states of opposite momentum, but same spin:

$$E\left(-\vec{k},\uparrow\right) \overset{inv}{=} E\left(\vec{k},\uparrow\right). \tag{6.4}$$

Taken together, these symmetries ensure that there are two degenerate states of opposite spin at every momentum:

$$E\left(\vec{k},\uparrow\right) = E\left(\vec{k},\downarrow\right). \tag{6.5}$$

This requirement can be lifted in two ways, either by breaking time reversal symmetry or by breaking inversion symmetry. If time reversal symmetry is broken, the resulting spin-split band structure causes an imbalance in the number of spin-up and spin-down electrons, producing an overall magnetic moment (Figure 6.11(a, b)).

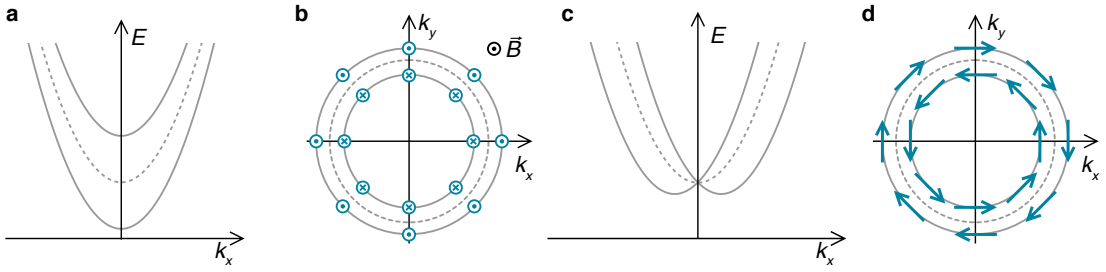

Figure 6.11.: Schematic spin-split band structures (**a**, **c**) and Fermi surfaces (**b**, **d**). Spin-splitting of a spin-degenerate band (dashed line) is allowed either due to the breaking of time reversal symmetry (**a**, **b**) or inversion symmetry (**c**, **d**). Blue arrows mark the direction of spin on the spin-split Fermi surfaces.

If time reversal symmetry is preserved, but broken inversion symmetry allows the band structure to become spin-split, the energetic splitting and spin polarisation direction have to be momentum dependent (Figure 6.11(c, d)). This is a direct consequence of the time reversal condition, which requires the states of opposite momentum to have opposite spin, without creation of any overall magnetic moment. In particular, the splitting needs to vanish at the zero momentum $\overline{\Gamma}$ point of the

zone, as is evident both in the model band structure shown in Figure 6.11c and in the DFT band structure of $PtCoO_2$ (Figure 6.5c).

In addition to this degeneracy at the $\overline{\Gamma}$ point, the $PtCoO_2$ band structure is also spin-degenerate at the $\overline{M}$ point of the zone. This is not accidental; it follows from time reversal symmetry combined with the periodicity of the lattice. The momenta related by inverse lattice vectors ($\vec{G}$) are equivalent:

$$E\left(\vec{k}-\vec{G},\uparrow\right)=E\left(\vec{k},\uparrow\right). \tag{6.6}$$

While true for every point in momentum space, this statement is especially relevant for a subset of momenta for which $\vec{k}=\vec{G}/2$, such as the $\overline{M}$ point of the hexagonal Brillouin zone (Figure 6.12a). For those points $\vec{k}-\vec{G}=-\vec{k}$, so the translation invariance condition (Equation 6.6) is formally equivalent to the inversion symmetry condition (Equation 6.4). In combination with time-reversal symmetry it thus ensures the spin degeneracy at those points in momentum space, called the time-reversal invariant momenta (TRIM).

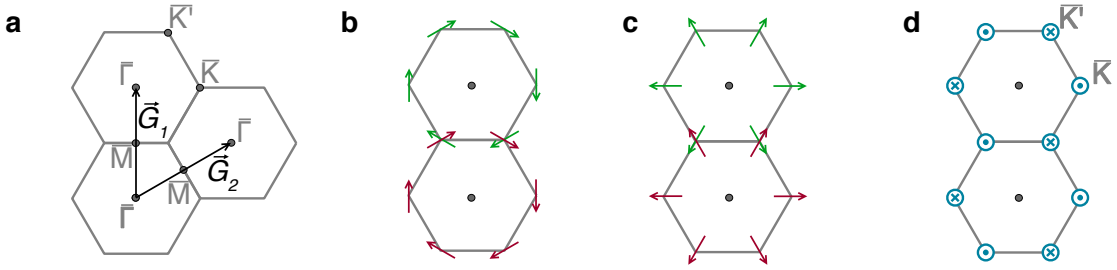

Figure 6.12.: (**a**) Three neighbouring Brillouin zones, and the two inverse lattice vectors $\vec{G}_1$ and $\vec{G}_2$, showing how $\vec{k_M}=\vec{G}/2$ for the $\overline{M}$ point of the zone. Considering two neighbouring Brillouin zones makes it clear why there can never be any (**b**) chiral or (**c**) radial *in-plane* spin polarisation at the $\overline{K}$-point, but out-of plane polarisation is allowed (**d**).

Furthermore, a combination of time-reversal symmetry and periodicity forbids *in-plane* spin polarisation at the $\overline{K}$ point of the zone. This is made obvious by considering spin polarisation in two neighbouring zones. If there were any, for example, clockwise chiral in-plane spin polarisation (Figure 6.12b), it would assume the direction of red arrows in the first zone and green arrows in second zone; clearly there is no way to make the spin polarisation direction consistent at the points common

to both zones. The same is true for radial polarisation (Figure 6.12c). In contrast, *out-of-plane* polarisation is allowed, as shown in Figure 6.12d. This is of course consistent with the findings of density functional theory in $PtCoO_2$; bands are spin-split at the $\overline{K}$ point, but the spin polarisation is purely out-of-plane (Figures 6.7(a, b) and 6.8(a)).

6.3.2. Spin dependent Hamiltonian

The above discussion outlines the cases in which spin-splitting is not forbidden by symmetry, but it does not address the question of whether it will actually take place, and by which mechanism. For a band structure to become spin-split, there needs to be a term in the Hamiltonian which can couple to spin; it is important to understand its physical origin and magnitude. Neglecting exchange interactions, spin can directly couple only to magnetic fields, absent in the time-reversal invariant problem considered here. However, electric and magnetic fields transform into each other under the Lorentz transformation. Consequently, a spin moving with velocity $\vec{v}$ in a static electric field $\vec{E}$ experiences an effective magnetic field:

$$\vec{B}_{eff} = -\frac{1}{c^2}\vec{v} \times \vec{E}. \tag{6.7}$$

For an electron spin this results in a Zeeman coupling term:

$$H_Z = -\vec{\mu} \cdot \vec{B}_{eff} = \frac{e}{m_e c^2}\left(\vec{v} \times \vec{E}\right) \cdot \vec{S}, \tag{6.8}$$

where $\vec{\mu}$ and $\vec{S}$ are the magnetic moment and spin of the electron, respectively, and c is the speed of light. In addition to an electric field due to nuclear charge which is present in every material, the effect of a surface electric field can be relevant for surfaces states.

Surface electric field

Perpendicular to every surface there is an electric field $\vec{E} = E\hat{z}$, caused by the potential difference between the sample and vacuum, i.e. the work function. The transformation of the surface electric field into an effective magnetic field is an appealing way to explain spin-splitting, as it quite naturally incorporates both the

symmetry breaking at the surface, and the coupling of the spin and momentum direction in a single term in the Hamiltonian.

The magnitude of the field can be estimated as a ratio of the work function and the distance over which the potential changes, which is found to be on the order of the Fermi wavelength in the jellium model. For gold (work function $W = 4.3\,\mathrm{eV}$, Fermi wavelength $\sim 5\mathring{A}$), the field is on the order of $\sim 1\,\mathrm{eV/\mathring{A}}$. Using this value the splitting estimated according to equation 6.8 is $10^{-6}\,\mathrm{eV}$ [87], while the measured value at the (111) surface of gold is 100000 times larger, 0.11 eV [93]. This discrepancy of several orders of magnitude rules out the effective magnetic field arising from the surface electric field as a cause of spin-splitting.

Spin-orbit coupling

Another electric field present in all solids is the Coloumb field of the nuclear charge:

$$\vec{E}_C = \frac{1}{e}\vec{\nabla}V_C = \frac{1}{e}\frac{dV_C}{dr}\frac{\vec{r}}{r}, \tag{6.9}$$

which results in the well known spin-orbit coupling term in the Hamiltonian [94]:

$$H_{SOC} = \frac{1}{2}\frac{1}{m_e^2c^2}\frac{1}{r}\frac{dV_C}{dr}\vec{L}\cdot\vec{S} = \lambda(r)\,\vec{L}\cdot\vec{S}, \tag{6.10}$$

where $\vec{L} = \vec{r}\times\vec{p}$ is the angular momentum operator[2]. Given its atomic origin, it is reasonable to first estimate the strength of spin-orbit coupling for an isolated atom, where it acts as a weak perturbation on the central Coulomb potential. The position-dependent part of the coupling can thus be estimated using the unperturbed atomic wave functions, Ψ_{nl}:

$$\lambda = \frac{1}{2}\frac{1}{m_e^2c^2}\left\langle \Psi_{nl}\left|\frac{1}{r}\frac{dV_C}{dr}\right|\Psi_{nl}\right\rangle = \frac{1}{2}\frac{1}{m_e^2c^2}\frac{1}{4\pi\epsilon_0}Z\left\langle \Psi_{nl}\left|\frac{1}{r^3}\right|\Psi_{nl}\right\rangle, \tag{6.11}$$

[2]This is actually half the value that would be obtained by simply combining the Coulomb field (equation 6.9) and the general expression for the coupling of a moving spin and static electric field (equation 6.8). The additional factor of 1/2 is a consequence of a relativistic kinematic effect called the Thomas correction, which is related to the fact the energy is evaluated in a rotating coordinate system [94, 95].

where Z is the nuclear charge. It is enough to know that the size of an electron orbit scales as the ratio of the Bohr radius ($a_B = (4\pi\varepsilon_0\hbar^2)/(m_e e^2)$) and nuclear charge to reach an estimate for the strength of spin-orbit coupling:

$$\lambda \sim \alpha^2 Z^4 \frac{\mathrm{Ry}}{\hbar^2}, \tag{6.12}$$

where $\alpha = e^2/(4\pi\varepsilon_0\hbar) = 1/137$ is the fine structure constant[3]. A proper calculation [96] gives the same trend, with a prefactor dependent on quantum numbers n and l:

$$\lambda_{nl} = \frac{1}{n^3 l\left(l+\frac{1}{2}\right)(l+1)} \alpha^2 Z^4 \frac{\mathrm{Ry}}{\hbar^2}. \tag{6.13}$$

A striking feature of the above expression is the strong dependence of the spin-orbit coupling on the nuclear charge, Z^4. However, using this dependence to estimate the relative strength of spin-orbit coupling in compounds containing different atoms would be very misleading. First of all, the quantum numbers n and l of the outermost electrons, most relevant for material properties, change as a function of Z. Furthermore, the above argument neglects the screening of the nuclear charge by core electrons. The wave function of an outermost electron in an atom spreads from the core region ($r_{core} \leq a_B/Z$) where there is no screening, to the outer region ($r_{out} \geq a_B$) where only the charge of one proton remains unscreened, and the wave function resembles the one of hydrogen, with $Z = 1$. Landau and Lifshitz [97] gave an estimate for the scaling of the spin-orbit coupling strength for the outermost electrons with Z, without worrying about any details of the wave function. They noticed that the dominant contribution to the spin-orbit coupling comes from the core region where the potential gradient is the strongest, and where the $\lambda \sim Z^4$ scaling is valid. Requiring only the continuity of the wave function between the core and the outer region, they found that the probability of finding an electron in the core region scales as $1/Z^2$. The spin-orbit coupling for outermost electrons is thus

[3] This is in fact the origin of the term 'fine structure constant'; while atomic spectra are dominantly governed by the Coloumb interaction, making Rydberg (1 Ry = 13.6 eV) the relevant energy scale, the spin-orbit interaction gives rise to their *fine structure*, with level splittings reduced by the factor of α^2.

expected to obey an overall scaling of

$$\lambda_{out} \sim \alpha^2 Z^2 \frac{\mathrm{Ry}}{\hbar^2}. \tag{6.14}$$

These simple estimates are useful to gain physical intuition, but it is important to check how well they describe real atoms. Shanavas et al. [98] compared them with the values of spin-orbit coupling calculated using Hartree - Fock wave functions [99], and found that the Z^4 scaling works reasonably well for inner electrons with specific values of n and l, although expression 6.13 does always overestimate the magnitude of the coupling because of the neglected screening. The Z^2 scaling describes the rough overall systematic variation of the spin-orbit interaction strength of the outermost electrons, although it clearly cannot capture the specific atom-to-atom and orbital-to-orbital variations (Figure 6.13). As evident in Figure 6.13, the strength of atomic spin-orbit coupling for the outermost electrons in d orbital systems varies between $\sim 10\,\mathrm{meV}$ and $\sim 1\,\mathrm{eV}$ ($10^{-3}\,\mathrm{Ry}$ and $10^{-1}\,\mathrm{Ry}$). These values are also relevant for atoms in solids, as the core atomic region is not significantly affected by bonding. Unlike the surface electric field, the energy scale of atomic spin-orbit coupling is large enough to influence band structures. It is the main mechanism of including spin in time reversal symmetric Hamiltonians, and crucial for spin-splitting, in keeping with received wisdom that spin-splitting is larger in systems with larger spin-orbit coupling.

6.4. Model Hamiltonian: p orbitals on a triangular lattice

It is now clear that the underlying Hamiltonian of a spin-split band structure needs to contain an inversion symmetry breaking term (H^{ISB}) and a spin-orbit coupling term (H^{SOC}). Petersen and Hedegård [87] used a tight-binding model incorporating both of these to describe the spin-split surface states on the (111) surface of gold; a similar approach has been used many times since [98, 100]. I will reproduce the original model constructed by Petersen and Hedegård, containing p orbitals on a triangular lattice, starting from the kinetic Hamiltonian parametrised using the Slater-Koster model, as described in Section 3.1. I will then separately add an

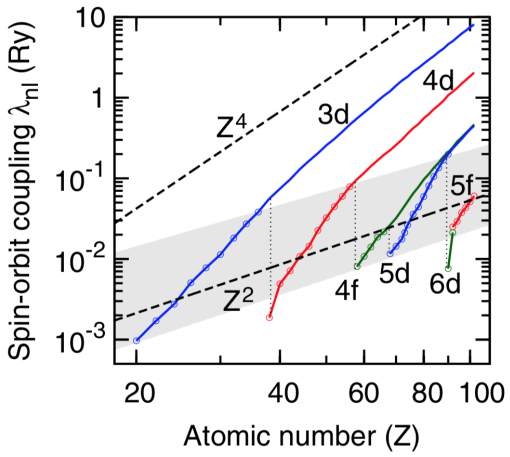

Figure 6.13.: Dependence of the spin-orbit coupling strength λ_{nl} for atoms as a function of the atomic number Z. The results of Herman and Skillman [99], calculated using the Hartree-Fock method (coloured lines and symbols) are compared to the hydrogenic Z^4 dependence for the $3d$ series (equation 6.13, upper dashed line), and the Landau-Lifshitz Z^2 scaling (lower dashed line). Outermost electrons are indicated by the circles and the shaded area. Reproduced from reference [98].

inversion symmetry breaking term and a spin-orbit coupling term, to study how each of them influences the band structure. Finally, I will combine all the terms to see how spin-splitting arises, and how its size depends on the relative strength of the model parameters. The simplicity of this model makes it a useful starting point to establish general principles.

6.4.1. Kinetic Hamiltonian

The kinetic Hamiltonian describing hopping between orbitals localised on different lattice sites is generically given by:

$$H^K = \sum_{ij,\alpha\beta} t_{\alpha\beta}\left(\vartheta_{ij}\right) a^\dagger_{\alpha,i} a_{\beta,j}, \tag{6.15}$$

where $a^\dagger_{\alpha,i}$ ($a_{\alpha,i}$) is a creation (annihilation) operator for an electron on site i in the orbital α, ϑ_{ij} is the angle between the line connecting sites i and j and the x axis, while $t_{\alpha\beta}\left(\vartheta_{ij}\right)$ denotes the hopping integral between the orbital α on site i and the orbital β on site j. In the model considered here the lattice is triangular (Figure

6.14a), and nearest neighbour hopping between three p orbitals, expressed in the cubic basis $\{p_y, p_z, p_x\}$, is included.

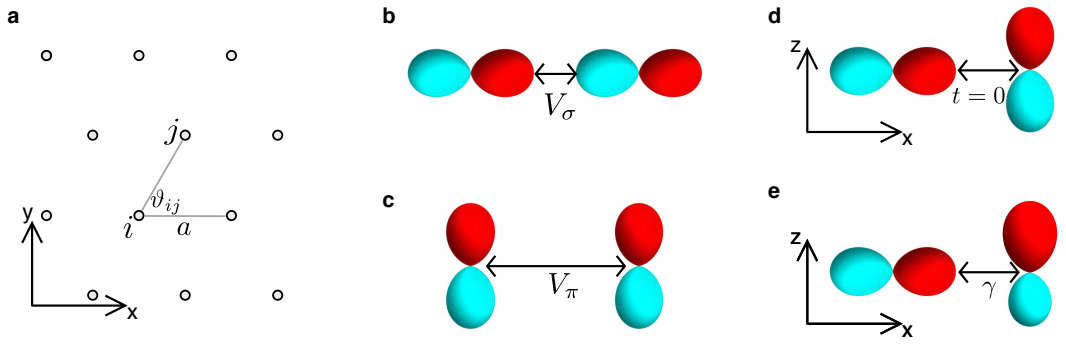

Figure 6.14.: (**a**) A triangular lattice, with ϑ_{ij} marking the angle the line connecting atoms i and j closes with the x axis, and a as the lattice constant. The hopping Hamiltonian can be parametrised with overlap integrals V_σ (**b**) and V_π (**c**). Hopping between in-plane p orbitals and the p_z orbital is zero while inversion symmetry is preserved (**d**), and finite once it is broken (**e**).

The angle and orbital dependent hopping parameters, $t_{\alpha\beta}(\vartheta_{ij})$, can be found in Reference [63], as described in Section 3.1[4]. They can be parametrised using two Slater-Koster integrals: V_σ is the overlap of two p orbitals if their lobes are pointing towards each other (Figure 6.14b), while V_π is the overlap if the lobes are parallel (Figure 6.14c). The angle dependant hopping integrals expressed in terms of these parameters are [63]:

$$t_{yy}(\vartheta_{ij}) = V_\sigma \sin^2(\vartheta_{ij}) - V_\pi \cos^2(\vartheta_{ij}) \tag{6.16}$$

$$t_{zz}(\vartheta_{ij}) = -V_\pi \tag{6.17}$$

$$t_{xx}(\vartheta_{ij}) = V_\sigma \cos^2(\vartheta_{ij}) + V_\pi \sin^2(\vartheta_{ij}) \tag{6.18}$$

$$t_{xy}(\vartheta_{ij}) = (V_\sigma + V_\pi) \sin(\vartheta_{ij}) \cos(\vartheta_{ij}). \tag{6.19}$$

Evaluating the sum 6.15 on a triangular lattice with the above angle dependent hopping leads to the following Hamiltonian matrix elements:

[4]The simplified notation in this section is slightly different from the one used in Section 3.1, which is consistent with Reference [63]. They are related by: $t_{\alpha\beta}(\vartheta_{ij}) = E_{\alpha,\beta}(\cos(\vartheta_{ij}), \sin(\vartheta_{ij}), 0)$.

$$H^K_{yy}(k_x,k_y) = -2V_\pi \cos(k_x) - (V_\pi + 3V_\sigma)\cos\left(\frac{k_x}{2}\right)\cos\left(\frac{\sqrt{3}k_y}{2}\right) \tag{6.20}$$

$$H^K_{zz}(k_x,k_y) = -2V_\pi \left(\cos(k_x) + 2\cos\left(\frac{k_x}{2}\right)\cos\left(\frac{\sqrt{3}k_y}{2}\right)\right) \tag{6.21}$$

$$H^K_{xx}(k_x,k_y) = -2V_\sigma \cos(k_x) - (V_\sigma + 3V_\pi)\cos\left(\frac{k_x}{2}\right)\cos\left(\frac{\sqrt{3}k_y}{2}\right) \tag{6.22}$$

$$H^K_{xy}(k_x,k_y) = \sqrt{3}(V_\sigma - V_\pi)\sin\left(\frac{k_x}{2}\right)\sin\left(\frac{\sqrt{3}k_y}{2}\right). \tag{6.23}$$

For simplicity, all the momenta are expressed in units of $1/a$, where a is the lattice constant.

The band structure found by diagonalising the above Hamiltonian with the parameters used by Petersen and Hedegård [87] ($V_\pi = -0.3V_\sigma$) is shown in Figure 6.15, coloured according to the orbital character. There are three bands, arising from the three p orbitals. The band whose dispersion is electron-like around the $\overline{\Gamma}$ point (green in Figure 6.15) is of well-defined p_z character throughout the zone and intersects the other bands without hybridising. This is possible because there is no hopping between the p_z orbital and the in-plane p orbitals ($t_{yz}(\vartheta_{ij}) = t_{zx}(\vartheta_{ij}) = 0$), as required by inversion symmetry (Figure 6.14d): the overlaps of an in-plane orbital with the positive and negative lobe of the p_z orbital cancel each other. In other words, those band crossing points are protected by inversion symmetry. Additionally, the two in-plane p - orbitals cross at the $\overline{K}$ point, forming a Dirac cone.

This crossing point is protected by symmetries of the triangular lattice, specifically by a combination of the mirror symmetry with zx as a mirror plane, labelled σ_h, and the three-fold rotation, $R_{2\pi/3}$ (Figure 6.16a). Two equivalent $\overline{K}$ points are related by both of these symmetries, requiring all wave functions at these points to be invariant under the two symmetry operations (Figure 6.16c). Their effect on the in-plane p-orbitals is most transparent in the basis of the spherical harmonics, where the two orbitals are p_1 and p_{-1}:

$$p_{-1} = \frac{1}{\sqrt{2}}(p_x - \imath p_y) \quad p_1 = -\frac{1}{\sqrt{2}}(p_x + \imath p_y). \tag{6.24}$$

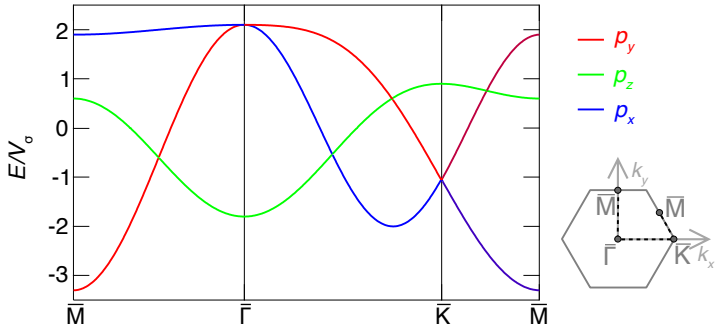

Figure 6.15.: Band structure of p orbitals on a triangular lattice, calculated using the kinetic Hamiltonian (equations 6.20-6.23), and coloured according to the orbital character. The Brillouin zone in the coordinate system is shown on the right, with the path along which the band structure is calculated shown by the dashed line.

As demonstrated in Figure 6.16(c, d) for the p_1 orbital, each p_α state ($\alpha = \pm 1$) transforms into itself (up to a trivial phase factor) under $R_{2\pi/3}$, but into the *different* p_α state under σ_h. Therefore, the two states have to be degenerate at the $\overline{K}$ point of the Brillouin zone as long as both $R_{2\pi/3}$ and σ_h are preserved.

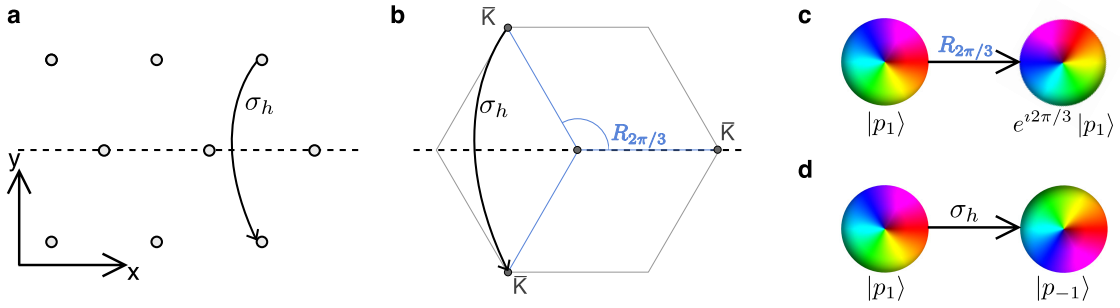

Figure 6.16.: (**a**) Mirror symmetry with the zx plane as the mirror plane, σ_h, is a symmetry of a triangular lattice. (**b**) Two equivalent $\overline{K}$ points of a triangular lattice are connected by σ_h , as well as the three-fold rotation symmetry, $R_{2\pi/3}$. (**c**) The p_1 state transforms into itself under rotation, (**d**) but into the p_{-1} state under the mirror symmetry.

6.4.2. Inversion symmetry breaking Hamiltonian

A term breaking inversion symmetry generically has the form of $H^{ISB} = E\hat{r}$, where $\hat{r}$ is the position operator. Specifically, if inversion is broken along the direction normal to a surface ($\hat{z}$), but preserved in plane, the Hamiltonian is reduced to

$$H^{ISB} = E\hat{z}. \tag{6.25}$$

If the inversion symmetry is broken by a surface electric field E, this term describes the dipole energy. However, it is important to realise that the inversion symmetry breaking (ISB) Hamiltonian has the above form in the first order regardless of its microscopic origin. At the tight binding level the effect of inversion symmetry breaking can be included by considering how the asymmetric deformation of orbitals it causes alters effective hopping parameters [87, 98]. Although every hopping integral can be affected, the largest effect by far is to allow the otherwise forbidden hopping between orbitals that are symmetric under inversion $z \to -z$, and the asymmetric ones. Specifically, once the p_z orbital is deformed the overlaps of its positive and negative lobe with the in-plane p orbital do not cancel anymore (Figure 6.14e), leading to the following hopping terms:

$$t_{zx}\left(\vartheta_{ij}\right) = \gamma \cos\left(\vartheta_{ij}\right) \tag{6.26}$$

$$t_{yz}\left(\vartheta_{ij}\right) = \gamma \sin\left(\vartheta_{ij}\right). \tag{6.27}$$

The resulting Hamiltonian matrix elements, considering nearest neighbour hopping on a triangular lattice, are given by:

$$H_{yz}^{ISB}\left(k_x, k_y\right) = 2\imath\gamma\sqrt{3}\cos\left(\frac{k_x}{2}\right)\sin\left(\frac{\sqrt{3}k_y}{2}\right) \tag{6.28}$$

$$H_{xz}^{ISB}\left(k_x, k_y\right) = 2\imath\gamma\left(2\cos\left(k_x\right) + \cos\left(\frac{\sqrt{3}k_y}{2}\right)\right)\sin\left(\frac{k_x}{2}\right). \tag{6.29}$$

It is worth looking into the structure of this Hamiltonian: it is Hermitian, off-diagonal and has no real components. All of these statements are also true of angular momentum operators L^y, L^z and L^x, which, written in the basis of cubic

harmonics $\{p_y, p_z, p_x\}$ have the following form[5]:

$$L^y = \begin{pmatrix} 0 & 0 & 0 \\ 0 & 0 & -\imath \\ 0 & \imath & 0 \end{pmatrix} \quad L^z = \begin{pmatrix} 0 & 0 & \imath \\ 0 & 0 & 0 \\ -\imath & 0 & 0 \end{pmatrix} \quad L^x = \begin{pmatrix} 0 & -\imath & 0 \\ \imath & 0 & 0 \\ 0 & 0 & 0 \end{pmatrix}. \tag{6.30}$$

As H^{ISB} has only two independent elements, it can be expressed as a linear combination of two angular momentum operators, with momentum dependent prefactors:

$$\begin{aligned} H^{ISB}(k_x, k_y) = &-\gamma L^x \left(2\sqrt{3}\cos\left(\frac{k_x}{2}\right)\sin\left(\frac{\sqrt{3}k_y}{2}\right)\right) + \\ &+\gamma L^y \left(2\left(2\cos(k_x) + \cos\left(\frac{\sqrt{3}k_y}{2}\right)\right)\sin\left(\frac{k_x}{2}\right)\right). \end{aligned} \tag{6.31}$$

This relationship shows that breaking of symmetry along the z direction can cause formation of an *in-plane* momentum dependent orbital angular momentum (OAM). To get a better understanding of the nature of the orbital angular momentum structure it is useful to look at the Hamiltonian along the high symmetry directions ($k_x = 0$ for the $\overline{\Gamma} - \overline{M}$ direction, $k_y = 0$ for $\overline{\Gamma} - \overline{K}$):

$$H^{ISB}(0, k_y) = -2\sqrt{3}\sin\left(\frac{\sqrt{3}k_y}{2}\right)\gamma L^x \tag{6.32}$$

$$H^{ISB}(k_x, 0) = \left(2\left(2\cos(k_x) + 1\right)\sin\left(\frac{k_x}{2}\right)\right)\gamma L^y. \tag{6.33}$$

For both of those directions the inversion symmetry breaking Hamiltonian is proportional to the angular momentum operator perpendicular to the momentum direction, indicating that the orbital angular momentum structure emerging as a consequence of the breaking of inversion symmetry is dominantly chiral. At the high-symmetry points ($k_y\left(\overline{M}\right) = 2\pi/\sqrt{3}$, $k_x\left(\overline{K}\right) = 4\pi/3$) the inversion symmetry breaking Hamiltonian vanishes. This specific relationship of inversion symmetry breaking and orbital angular momentum is by no means general; it would not be true if higher-order terms describing changes to V_σ and V_π due to the asymmet-

[5]These can be obtained from the more standard form in the basis of spherical harmonics by the coordinate transformation given in Appendix E.1.

rical orbital deformation were included. What is more, a similar minimal inversion symmetry breaking Hamiltonian in the d- orbital manifold would also couple the asymmetric (d_{yz}, d_{zx} in this case) and symmetric ($d_{3z^2-r^2}, d_{xy}, d_{x^2-y^2}$) orbitals, but it would result in six generally independent matrix elements. It could therefore not be expressed as a linear combination of the three angular momentum operators. All of these observations motivate an examination of the underlying causes of the somewhat surprising relationship between inversion symmetry breaking and orbital angular momentum (section 6.5). However, even without an in-depth analysis of these issues, there can be no doubt that the two are related in the p - orbital Hamiltonian discussed here. This motivates looking for orbital angular momentum structures in band structures formed by inversion symmetry breaking Hamiltonians.

In Figure 6.17 I show the band structure calculated with the same symmetric hopping parameters as in Figure 6.15 ($V_\pi = -0.3V_\sigma$), but with varying inversion symmetry breaking term, γ. I colour them according to the expected value of orbital angular momentum along a quantisation axis perpendicular to momentum ($\langle L_\perp \rangle$, Figure 6.17(a, c, e)), and according to the orbital character (Figure 6.17(b, d, f)). For a small γ ($\gamma = 0.02V_\sigma$, Figure 6.17(a, b)) the band structure is largely unperturbed, except at points where the band of p_z character would cross bands of the in-plane p character in the symmetric case. Once inversion symmetry is broken those crossing points are not protected anymore; small anti-crossing gaps open, bands hybridise and states on either side of the gaps develop chiral orbital angular momentum. Increasing γ results in larger gaps, and an extended region around them where orbital character mixes to produce orbital angular momentum ($\gamma = 0.2V_\sigma$, Figure 6.17(c, d)). If the inversion symmetry breaking energy scale is made larger than the bandwidth ($\gamma = 2V_\sigma$, 6.17(e, f)) states of different orbital character are allowed to mix across the zone, resulting in a band structure significantly different from the initial symmetric one. The three bands now correspond to the three eigenstates of $\langle L_\perp \rangle$: $m = 1, 0, -1$ for the bands of highest, middle and lowest energy, respectively. The splitting between them is momentum dependent, reflecting the momentum dependent prefactors relating inversion symmetry breaking and angular momentum (Equation 6.31). The $m = 0$ band remains unperturbed, and retains a well-defined orbital character of the p orbital perpendicular to momentum (p_y along k_x, p_x along k_y), as seen in Figure 6.17f. The crossing point at the $\overline{K}$ point remains

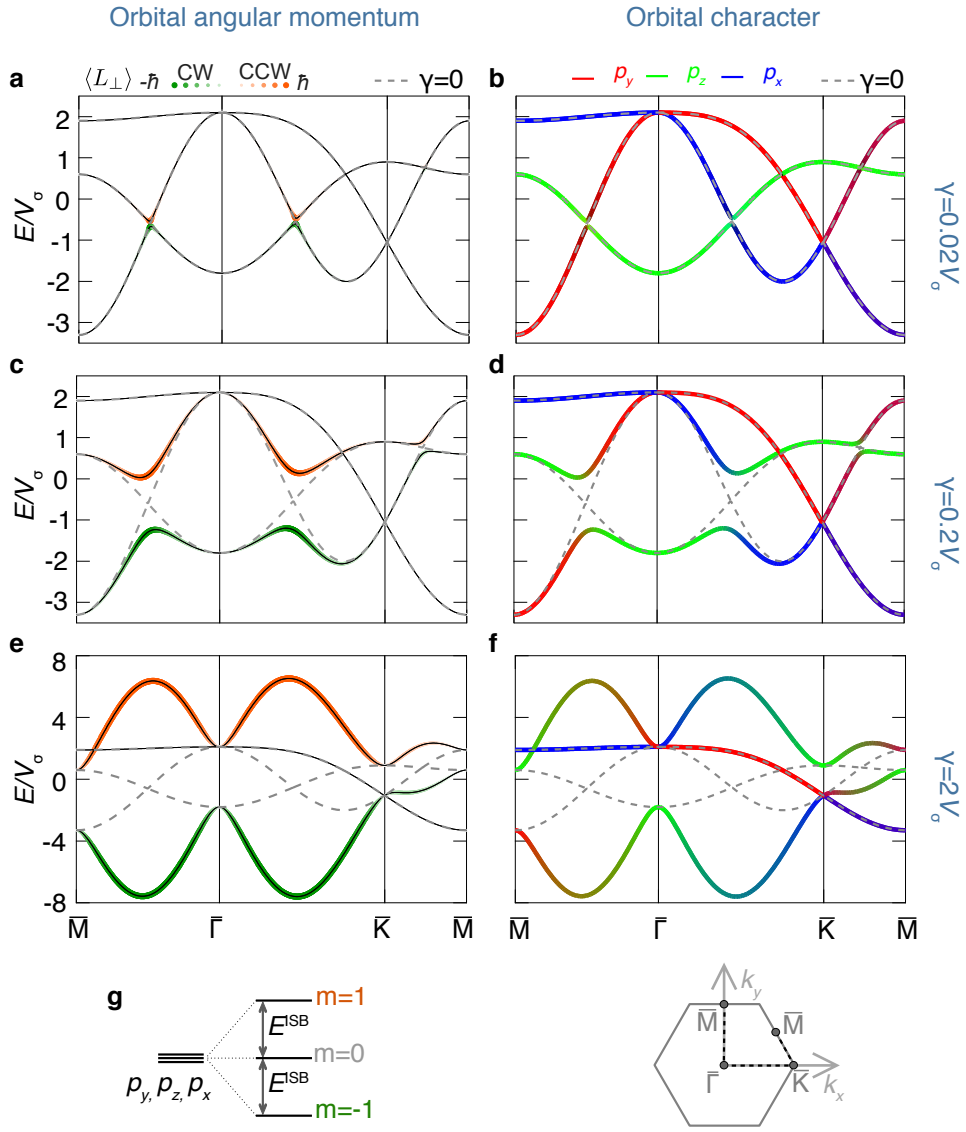

Figure 6.17.: Band structure calculated for the inversion symmetry breaking parameter equal to $\gamma = 0.02$ (**a**, **b**), $\gamma = 0.2$ (**c**, **d**) and $\gamma = 2$ (**e**, **f**). The bands are coloured according to the chiral orbital angular momentum (**a**, **c**, **e**), and orbital character (**b**, **d**, **f**). The dashed line shows the band structure for $\gamma = 0$. The Brillouin zone, with the path along which the band structure is calculated, is shown at the bottom right. (**g**) Schematic representation of the influence of inversion symmetry breaking on p-orbitals. All the calculations are done for $V_\pi = -0.3\,\mathrm{V}_\sigma$.

protected by the combination of mirror and rotation symmetry, both of which are still present.

The influence of strong inversion symmetry breaking on a degenerate set of p orbitals is schematically shown in Figure 6.17g. The atomic states are split into states of defined orbital angular momentum along a specific axis ($\langle L_\alpha \rangle$), which is chiral ($\langle L_\alpha \rangle = \langle L_\perp \rangle$) for the high symmetry directions. The energetic splitting is governed by an inversion symmetry breaking energy scale, $E^{ISB}(k_x, k_y) = \left\langle H^{ISB}(k_x, k_y) \right\rangle$, which is momentum dependent, and proportional to γ. The maximum it reaches in the present geometry is $2\sqrt{3}\gamma \approx 3.5\gamma$ (equation 6.31, and Figure 6.17(e, f)).

6.4.3. Spin-orbit coupling Hamiltonian

The spin-orbit coupling Hamiltonian is easiest to express in the basis of spherical harmonics $\{Y_l\}$, since they are the eigenstates of the angular momentum operator. Of course, it is now necessary to distinguish states of opposite spin, so schematically the basis is $\left\{Y_l^\downarrow, Y_l^\uparrow\right\}$, and the Hamiltonian in that basis:

$$H^{SOC} = \frac{\lambda}{2} \begin{pmatrix} -L^z & L^+ \\ L^- & L^z \end{pmatrix}, \tag{6.34}$$

where 1/2 comes from the value of the electron spin, L^z is the angular momentum operator along the quantisation axis, and L^+ and L^- raising and lowering operators, respectively. This Hamiltonian can be transformed into the cubic basis, $\left\{p_y^\downarrow, p_z^\downarrow, p_x^\downarrow, p_y^\uparrow, p_z^\uparrow, p_x^\uparrow\right\}$ in this case, in the usual way (Appendix E.1), to obtain:

$$H^{SOC} = \frac{\lambda}{2} \begin{pmatrix} 0 & 0 & -\imath & 0 & -\imath & 0 \\ 0 & 0 & 0 & \imath & 0 & 1 \\ \imath & 0 & 0 & 0 & -1 & 0 \\ 0 & -\imath & 0 & 0 & 0 & \imath \\ \imath & 0 & -1 & 0 & 0 & 0 \\ 0 & 1 & 0 & -\imath & 0 & 0 \end{pmatrix}. \tag{6.35}$$

The spin-orbit coupling allows mixing of states of different orbital character; in particular the terms coloured red mix the p_z orbital with the in-plane p orbitals.

However, unlike the inversion symmetry breaking, it mixes states of different spin. It can be diagonalised simultaneously with the total angular momentum operator, $\vec{J}^2 = \left(\vec{L} + \vec{S}\right)^2$, whose eigenvalues are $j\,(j+1)$, with $j = 3/2, 1/2$ in the p orbital case.

I plot the evolution of the band structure with increasing λ in Figure 6.18, colouring the bands according to the expected value of the spin-orbit coupling operator ($\left\langle \vec{L} \cdot \vec{S} \right\rangle$, Figure 6.18(a, c, e)), as well as according to their orbital character (Figure 6.18(b, d, f)). If λ is small ($\lambda = 0.1$ in Figure 6.18(a, b)) only the states in the immediate vicinity of band crossing points are affected. Small gaps open, the states on either side of which develop a finite $\left\langle \vec{L} \cdot \vec{S} \right\rangle$. Increasing λ increases the hybridisation gaps, as well as the portion of the zone in which spin and orbital angular momentum are coupled ($\lambda = 1$, Figure 6.18(c, d)), while making it significantly larger than the kinetic Hamiltonian ($\lambda = 10$, Figure 6.18(e, f)) results in three strongly spin-orbit coupled, but weakly dispersive, bands of undefined orbital character. Unlike inversion-symmetry breaking, the spin-orbit coupling energy scale has no momentum dependence, a consequence of its local origin. No crossing points of the initial band structure are protected against hybridisation due to spin-orbit coupling; in particular a gap opens at the $\overline{K}$ point. This is possible because the mirror symmetry changes the sign of spin, as well as orbital angular momentum, while the rotational symmetry keeps both invariant. Their combination therefore ensures the degeneracy of the $|p_{-1}, \uparrow\rangle$ state with the $|p_1, \downarrow\rangle$ state, but this pair can have a different energy to the ($|p_{-1}, \downarrow\rangle$, $|p_1, \uparrow\rangle$) pair. The two pairs correspond to the states of negative and positive $\left\langle \vec{L} \cdot \vec{S} \right\rangle$, respectively.

The influence of spin-orbit coupling on degenerate p orbitals is shown schematically in Figure 6.18g: they are split into a 4-fold degenerate $j = 3/2$ manifold in which $\left\langle \vec{L} \cdot \vec{S} \right\rangle = 0.5\hbar^2$, and the doubly degenerate $j = 1/2$ manifold in which $\left\langle \vec{L} \cdot \vec{S} \right\rangle = -\hbar^2$, with the energy difference between them set by the spin-orbit coupling energy scale.

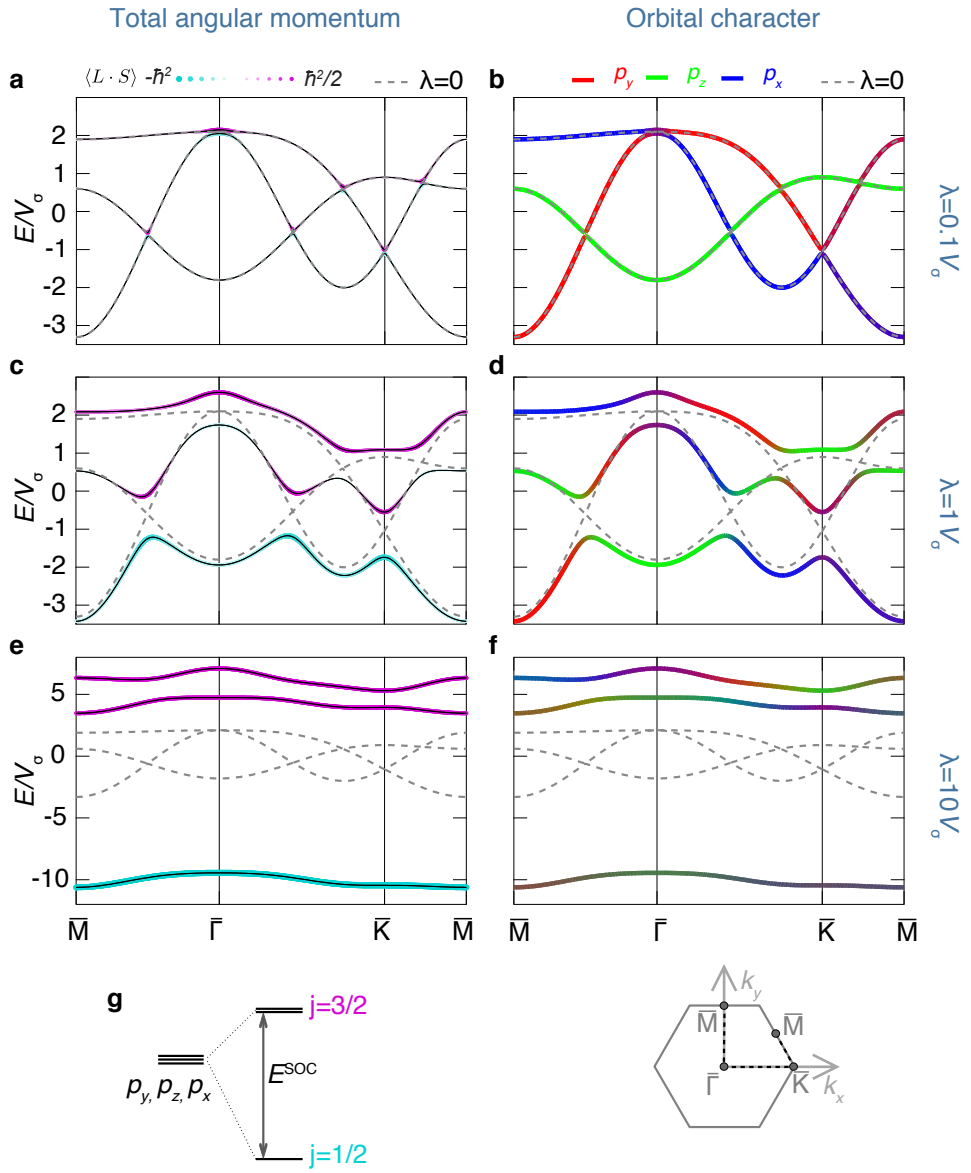

Figure 6.18.: Band structure calculated for the spin-orbit coupling parameter equal to $\lambda = 0.1V_\sigma$ (**a**, **b**), $\lambda = 1V_\sigma$ (**c**, **d**) and $\lambda = 10V_\sigma$ (**e**, **f**). The bands are coloured according to the expected value of the spin-orbit coupling operator $\left\langle \vec{L} \cdot \vec{S} \right\rangle$ (**a**, **c**, **e**), and orbital character (**b**, **d**, **f**). The dashed line shows the band structure for $\lambda = 0$. The Brillouin zone, with the path along which the band structure is calculates, is shown at the bottom right. (**g**) Schematic representation of the influence of spin-orbit coupling on the p-orbitals. All the calculations are done for $V_\pi = -0.3\,\mathrm{V}_\sigma$.

6.4.4. Spin-split band structure

After analysing the separate influence of inversion symmetry breaking and spin-orbit coupling, it is easy to understand how spin-splitting arises when they are combined, especially in the limiting cases where one of the energy scales is much larger than the other. This is best illustrated by looking at an example of two states of different orbital character that are degenerate in the inversion symmetric case with no spin-orbit coupling (Figure 6.19), such as the ones found at band crossing points.

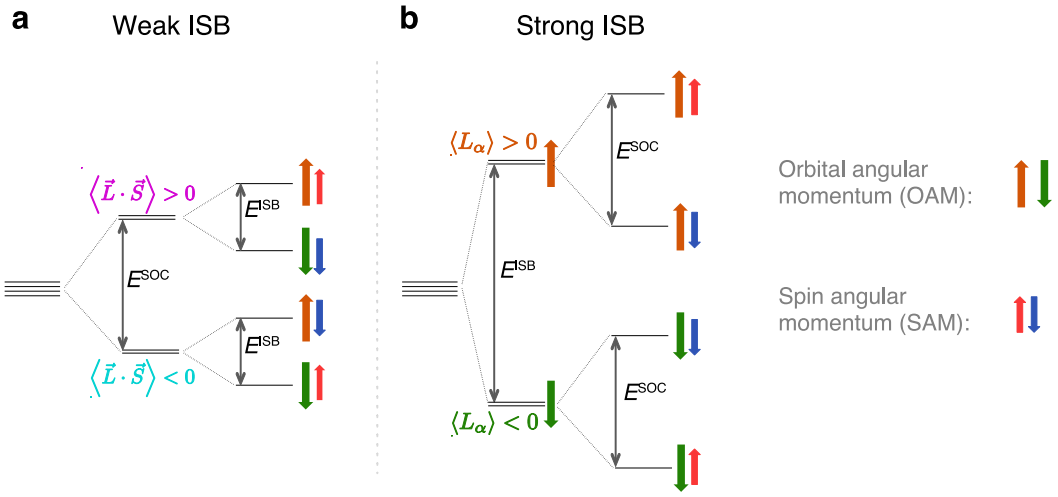

Figure 6.19.: Schematic illustration of how a fourfold-degenerate state becomes split by ISB and SOC if (**a**) the spin-orbit coupling energy scale is dominant, and if the spin-orbit coupling energy scale is dominant.

If a dominant spin-orbit coupling is introduced these initially 4-fold degenerate states (including spin) are split according to their angular momentum. The resulting states need not be the eigenstates of the angular momentum operator, but $\langle \vec{L} \cdot \vec{S} \rangle$ does acquire a finite value, forcing the orbital and spin angular momentum to be either parallel or antiparallel to each other. Breaking inversion symmetry introduces additional splitting according to orbital angular momentum, which is necessarily accompanied by a spin-splitting due to the dominant spin-orbit coupling (Figure 6.19a). In the opposite limit, where inversion symmetry breaking energy scale is dominant, the original states are split into states of finite orbital angular momentum along a specific axis. If weaker spin-orbit coupling is added, it splits the states further into states of spin parallel and anti-parallel to the pre-existing orbital angular

momentum (Figure 6.19b).

The picture that emerges is one of two limiting cases, characterised by strong ($E^{ISB} \gg E^{SOC}$) and weak ($E^{ISB} \ll E^{SOC}$) inversion symmetry breaking. The diagrams in Figure 6.19 suggest that there is a way to distinguish between these limits even if the relative magnitude of the energy scales is not a priori known: the orbital angular momentum of the two bands of opposite spin points in the opposite direction in the weak ISB case, and in the same direction in the strong ISB case. To see how this works in practice in Figure 6.20, I plot the band structure of the p - orbital model in the two limits, choosing the values of parameters such that the weak one alone would open gaps only right at the crossing points, while the strong one affects the larger part of the zone, although in both cases dispersing bands determined by the symmetric, kinetic Hamiltonian remain clearly recognisable ($\gamma = 0.2V_\sigma, \lambda = 0.1V_\sigma$ for the strong ISB case, $\gamma = 0.02V_\sigma, \lambda = 1V_\sigma$ for the weak ISB case; *cf.* Figures 6.17 and 6.18).

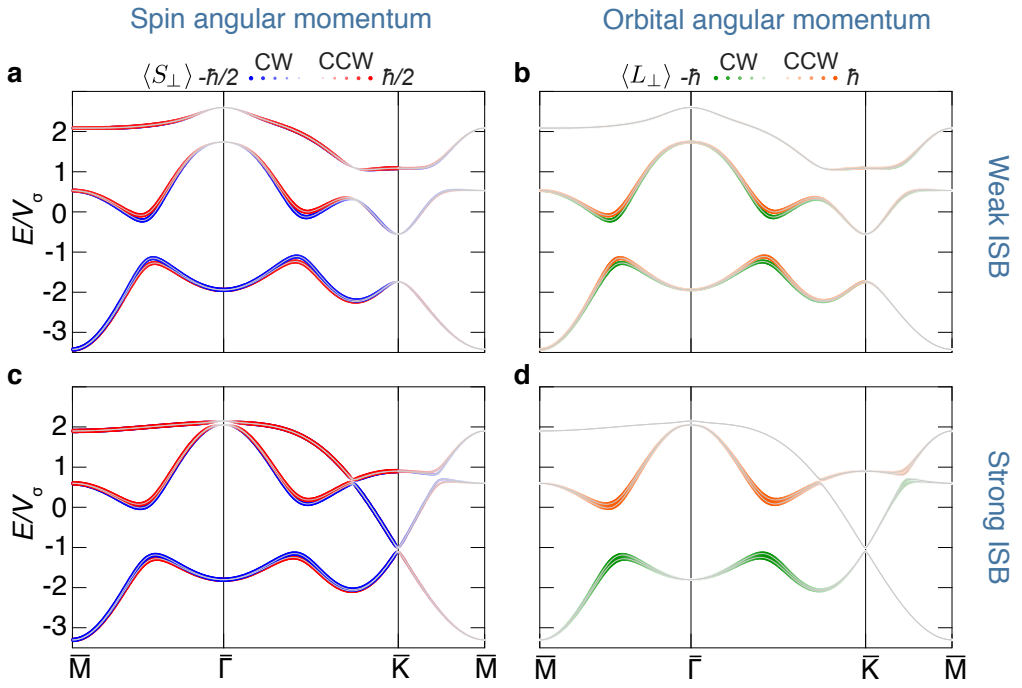

Figure 6.20.: Spin split band structure in the (**a**, **b**) weak inversion symmetry breaking case ($\gamma = 0.02V_\sigma, \lambda = 1V_\sigma$) and (**c**, **d**) strong inversion symmetry breaking case ($\gamma = 0.2V_\sigma, \lambda = 0.1V_\sigma$), coloured according to spin angular momentum (**a**, **c**) and the orbital angular momentum (**b**, **d**).

As evident in Figure 6.20(a, c) the band structure is indeed spin-split in both cases, with the orbital angular momentum pointing in the opposite direction on the two spin-split branches if the inversion symmetry breaking energy is weak (Figure 6.20b), and same if it is strong (Figure 6.20d). Another difference between the two limits is the relative size of the gap between the two spin-split pairs and along the $\overline{\Gamma} - \overline{K}$ line (or, equivalently, the $\overline{\Gamma} - \overline{M}$ line), and the gap at the $\overline{K}$ point. In the weak ISB case both of these are set by the spin-orbit interaction, and thus of a similar magnitude. The inversion-symmetry breaking cannot however open a gap at the $\overline{K}$ point, so the gap size is always determined by the spin-orbit coupling, and is therefore much smaller in the strong ISB case. The transition between the two limits is best studied by keeping one of the parameters fixed while the other one is varied. In Figure 6.21 I plot the band structure along the $\overline{M} - \overline{\Gamma}$ direction for a fixed spin-orbit coupling strength of $\lambda = V_\sigma$ and a variable γ.

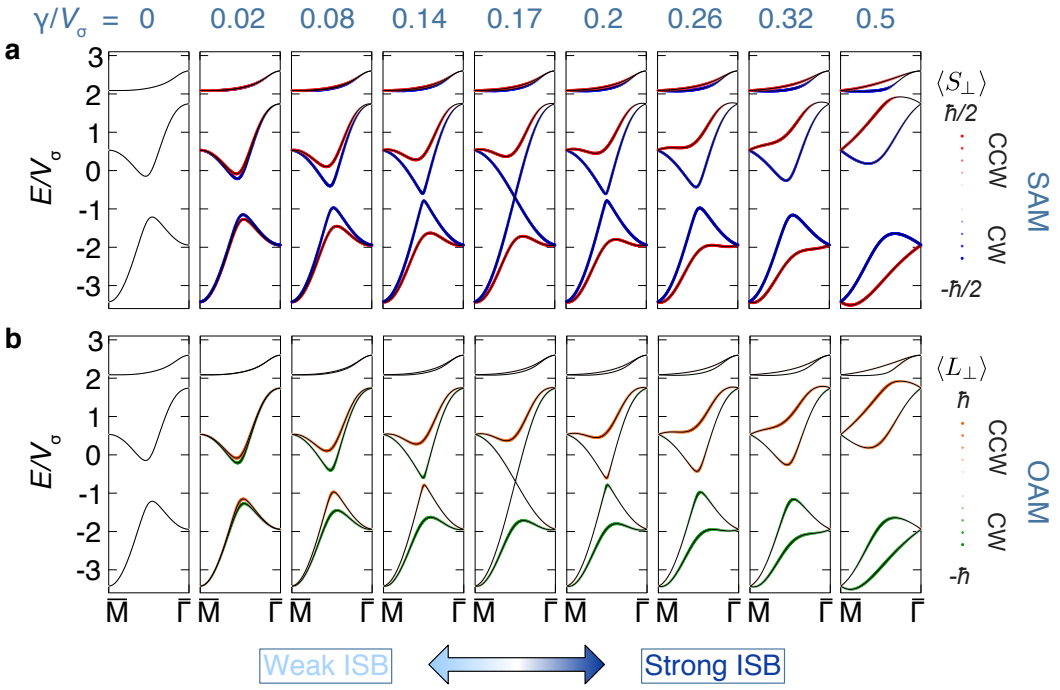

Figure 6.21.: Spin-split band structure along the $\overline{M} - \overline{\Gamma}$ direction for a fixed value of spin-orbit coupling ($\lambda = 1V_\sigma$) and variable inversion symmetry breaking parameter γ, the value of which in units of V_σ is indicated above each plot. The bands are coloured according to (**a**) the spin angular momentum (SAM) and (**b**) the orbital angular momentum (OAM).

As expected, for very small γ the orbital angular momentum has the opposite sign on the bands of opposite spin. As γ is increased this remains true until the spin-splitting becomes large enough for the two clockwise spin polarised bands (blue in Figure 6.21a) to touch, at which point they lose their orbital angular momentum (at $\gamma = 0.17V_\sigma$ in Figure 6.21b). When γ is increased even further they regain the orbital angular momentum, but it is now of the same sign as on their respective spin-split pairs. This confirms that there are indeed two regimes supporting spin-splitting, the weak ISB and the strong ISB regime, which are separated by a well-defined crossover. This crossover is also evident when looking at the maximum size of the spin splitting along the $\overline{\Gamma} - \overline{M}$ line as a function of inversion symmetry breaking, plotted for the lower energy spin-split pair in Figure 6.22a.

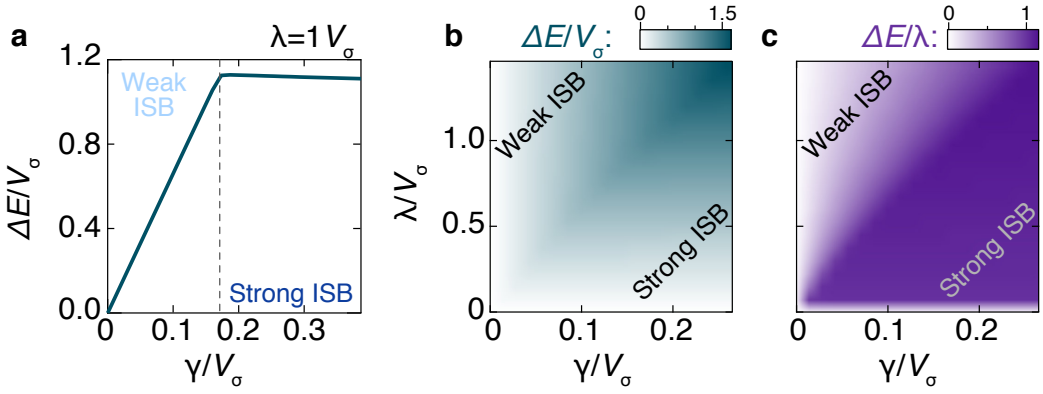

Figure 6.22.: The spin splitting between the two lowest energy bands (Figure 6.21) as (**a**) a function of inversion symmetry breaking γ for fixed spin-orbit coupling $\lambda = 1V_\sigma$, and (**b**) as a function of λ and γ. (**c**) Spin-splitting normalised by the spin-orbit coupling λ, as a function of λ and γ.

The spin-splitting increases linearly with the strength of inversion symmetry breaking in the weak ISB limit. Once the crossover is reached, indicated by the dashed line in Figure 6.22a ($\gamma = 0.17V_\sigma$), the size of the spin-splitting saturates to a value limited by the spin-orbit coupling energy scale. In other words, the size of the spin-splitting is always limited by the weaker of the two energy scales. Another way to see this explicitly is to plot the size of the spin splitting as a function of both inversion symmetry breaking γ and spin-orbit coupling λ (6.22b). If large spin-splitting is the goal, it is not enough to increase one of the energy scales, because the splitting then becomes limited by the weaker one, but rather both energy scales need to be

increased together. Since the spin-splitting can never be larger than either of the energy scales, the largest spin-splitting that can be expected in a material containing given constituent atoms is limited by the atomic spin-orbit coupling of the relevant orbitals of those atoms. Such large splitting can be achieved only if the inversion symmetry breaking scale is dominant, i.e. in the strong ISB case, as illustrated by Figure 6.22c in which I plot the spin-splitting normalised by the spin-orbit coupling constant λ. It should be noted that the fact that spin-splitting is limited by the spin-orbit coupling energy scale does not mean it cannot be larger, or smaller, than λ. The actual value it assumes depends on the underlying orbitals, as well as the relative strength of the kinetic and spin-orbit coupling Hamiltonian. Nonetheless, the largest achievable splitting will be proportional to, and on the order of, λ; it is equal to 1.16λ in the parameter range considered here (Figure 6.22c).

The above picture of a hierarchy of energy scales offers a new perspective on spin-splitting. It emphasises that it is not only the breaking of symmetry that is important, but also the energy scale associated with it. It suggests that the spin-splitting in real materials is usually much smaller that the spin-orbit coupling because it is limited by the inversion symmetry breaking energy scale. It also indicates that the inversion symmetry breaking scale in delafossites might be unusually large, enabling spin-splitting as large as the atomic spin-orbit coupling. However, all of this reasoning is reliant upon the statement that the breaking of inversion symmetry promotes creation of orbital angular momentum along a specific axis. While undoubtedly true for the p - orbital model described in this section, if we wish to use this physical picture to understand real materials it is crucial to understand how general this behaviour is, and its underlying causes.

6.5. Relationship between inversion symmetry breaking and orbital angular momentum

A symmetry-breaking Hamiltonian by definition favours creation of asymmetric wave function weights, raising the question of whether every wave function can be asymmetrically distorted. Park *et al.* [101, 102] and Kim *et al.* [103] described how an asymmetric charge distribution can arise in a tight-binding wave function as a consequence of a surface electric field. The following discussion is based on their

argument, extended to consider the range of validity of the model.

A Bloch wave function of crystal momentum k_x is in the tight binding limit built from orbitals localised on every lattice site, with a phase difference of $k_x a$ between them. For a chain of atoms along the $\hat{x}$ direction the wave function based on the p_x orbital is:

$$\psi^x_{k_x}(\vec{r}) = \frac{1}{\sqrt{N}} \sum_n p_x(\vec{r} - na\hat{x})\, e^{\imath k_x a n}, \tag{6.36}$$

where the sum is taken over all lattice sites and N is the number of atoms. The orbitals building the wave function are schematically shown in Figure 6.23a for $k_x a = 2\pi/5$, with the colours representing the phase. Interference between orbitals on neighbouring sites causes the momentum dependence of the charge distribution. However, the orbital on every site is symmetric under inversion $z \to -z$, and consequently so is the final charge distribution at every momentum. The same argument applies if the phase is antisymmetric, as it is for the p_z orbital; the wave function then has a different sign for positive and negative z, but the wave function weight is still symmetric. A tight-binding wave function composed of a single cubic orbital can therefore never break inversion symmetry. This is not surprising, as the inversion symmetry breaking Hamiltonian is able to modify the band structure only at points where it can mix states of different orbital character (Figure 6.17), for example p_x and p_z character along the k_x direction.

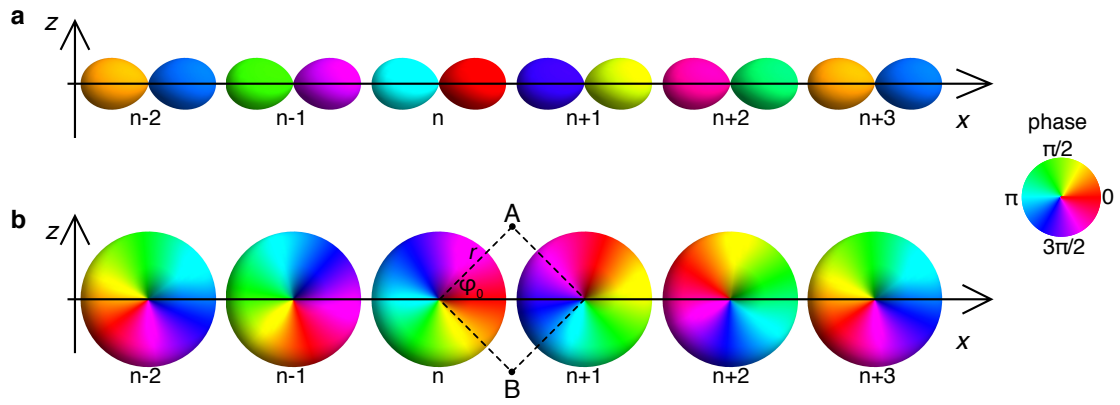

Figure 6.23.: Schematic representation of orbitals composing a tight binding wave function for $k_x a = 2\pi/5$ if the base orbital is (a) p_x orbital and (b) $m_y = 1$ orbital. The phase is shown by colour.

It is therefore reasonable to consider a tight-binding wave function based on a linear combination of two cubic orbitals, such as the eigenstates of L^y, the angular momentum operator quantised along the y axis:

$$p_{m_y=-1} = \frac{1}{\sqrt{2}}\left(-\imath p_z + p_x\right), \quad p_{m_y=1} = \frac{1}{\sqrt{2}}\left(\imath p_z + p_x\right). \tag{6.37}$$

These orbitals are complex, with a phase which depends on the angle φ as $-m_y\varphi$, as shown for the $m_y = 1$ orbital on site n in Figure 6.23b. A tight-binding wave function based on the $m_y = 1$ orbital is schematically shown in Figure 6.23b for $k_x a = 2\pi/5$. The site-to-site phase change of $k_x a$ is equivalent to a site-to-site rotation of the orbital by $-k_x a$. As the orbitals are neither symmetric nor antisymmetric under inversion, it is possible for the Bloch wave function weight to be different for positive and negative z, for example at points A and B between sites n and $n+1$ (Figure 6.23b). Neglecting further orbitals, the wave function at those points is a sum of contribution from sites n and $n+1$, each of which is a product of a radial wave function and a phase factor. At the point A:

$$\psi_{k_x}^{m_y=1}(A) = \frac{1}{\sqrt{2}}\left(R_n(r)\exp\left(-\imath\varphi_0\right) + R_{n+1}(r)\exp\left(\imath\left(-\pi + \varphi_0 + ka\right)\right)\right), \tag{6.38}$$

where $R_i(r)$ is the radial part of the wave function centred at site i. The wave function weight is given by:

$$\left|\left\langle\psi_{k_x}^{m_y=1}(A)\right\rangle\right|^2 = \frac{1}{2}\left(R_n(r)^2 + R_{n+1}(r)^2 - 2R_n(r)R_{n+1}(r)\cos\left(2\varphi_0 + ka\right)\right). \tag{6.39}$$

The last term describes the interference between the wave functions on neighbouring sites. The equivalent expression at the point B is:

$$\left|\left\langle\psi_{k_x}^{m_y=1}(B)\right\rangle\right|^2 = \frac{1}{2}\left(R_n(r)^2 + R_{n+1}(r)^2 - 2R_n(r)R_{n+1}(r)\cos\left(2\varphi_0 - ka\right)\right). \tag{6.40}$$

The interference term is different at the two points, proving that the wave function weight can indeed differ at positive and negative z, as shown explicitly by the plots of the wave function weight (Figure 6.24). The asymmetry is momentum dependent, and disappears at the Brillouin zone centre ($k_x a = 0$) and boundary ($k_x a = \pi$). The tight-binding wave function with the $m_y = -1$ state as the basis also has a

momentum-dependent asymmetrical weight, but pointing in the opposite direction. As long as inversion symmetry is preserved these two states are degenerate, and the total weight distribution symmetrical. However, if the Hamiltonian contains an inversion symmetry breaking term, one of the asymmetrical states is energetically more favourable than the other, and a gap opens between them. As these wave functions with asymmetrical weights are based on eigenstates of L^y, the states on either side of the gap develop orbital angular momentum in the y direction.

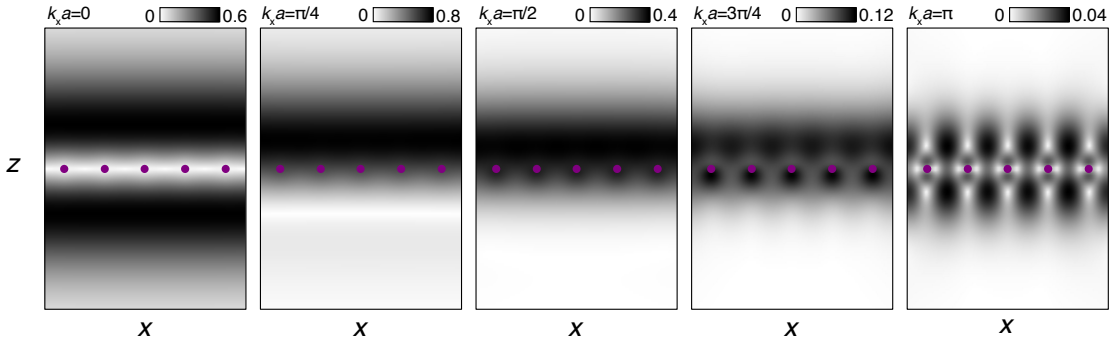

Figure 6.24.: Wave function weight of a tight-binding wave function based on the $m_y = 1$ $2p$ orbital, as a function of x and z. The value of $k_x a$ is indicated above each plot. The hydrogenic radial wave function ($n = 2, l = 1$) is used. Purple dots mark the lattice sites, separated by 2 Å. The sum (equation 6.36) is performed over 2 0 lattice sites to avoid edge effects.

This analysis of wave functions offers an intuitive explanation for the relationship between orbital angular momentum and inversion symmetry breaking for p - orbitals, and is entirely consistent with the conclusions drawn from the tight-binding band structures. The remaining task is to understand how general these conclusions are. A crucial ingredient for an asymmetric wave function weight to develop is the angle dependent phase of the basis orbital, which leads to a constructive interference between neighbouring orbitals for one sign of z, and destructive for the other. If the basis orbital has a constant phase, the interference factor is proportional to $\cos(ka)$ regardless of the sign of z. The remaining question is whether such a wave function necessarily carries an orbital angular momentum in the $\hat{y}$ direction. An orbital which

is a linear combination of spherical harmonics of given l has the general form:

$$\psi_l(\varphi,\vartheta) = \sum_{m=-l}^{l} c_l^m Y_l^m(\varphi,\vartheta), \tag{6.41}$$

where c_l^m are complex coefficients. The phase of the spherical harmonics $Y_l^m(\varphi,\vartheta)$ depends on the angle φ around the quantisation axis, chosen to be $\hat{y}$ here, as $-m\varphi$. Their sum has an angle dependent phase as long as there is at least one m for which it does not contain equal weight of $+m$ and $-m$ states:

$$|c_l^m|^2 \neq \left|c_l^{-m}\right|^2. \tag{6.42}$$

If condition 6.42 is fulfilled, a tight-binding wave function made of $\psi_l(\varphi,\vartheta)$ at every site can support an asymmetric charge distribution. On the other hand, the angular momentum of $\psi_l(\varphi,\vartheta)$ along the quantisation axis is given by

$$\langle L^y\rangle = \hbar \sum_{m=1}^{l} m\left(|c_l^m|^2 - \left|c_l^{-m}\right|^2\right). \tag{6.43}$$

For p orbitals ($l=1$) this is reduced to $\langle L^y\rangle = \hbar\left(|c_l^1|^2 - \left|c_l^{-1}\right|^2\right)$, so the condition to have a finite $\langle L^y\rangle$ is equivalent to the condition to have an angle dependent phase. This is, however, not generically true; for $l>1$ a wave function can be complex and still have vanishing $\langle L^y\rangle$. It is easy to see how this happens for the following d - orbital wave functions:

$$u^+(\varphi,\vartheta) = -\sqrt{\frac{2}{3}}Y_2^1(\varphi,\vartheta) + \sqrt{\frac{1}{3}}Y_2^{-2}(\varphi,\vartheta). \tag{6.44}$$

$$u^-(\varphi,\vartheta) = \sqrt{\frac{2}{3}}Y_2^{-1}(\varphi,\vartheta) + \sqrt{\frac{1}{3}}Y_2^{2}(\varphi,\vartheta). \tag{6.45}$$

$\langle L^y\rangle$ clearly vanishes for both of the wave functions:

$$\left\langle u^+ \left| L^y \right| u^+ \right\rangle = \hbar\left(\frac{2}{3}1 + \frac{1}{3}(-2)\right) = 0, \quad \left\langle u^- \left| L^y \right| u^- \right\rangle = \hbar\left(\frac{2}{3}(-1) + \frac{1}{3}2\right) = 0.$$

They do however have an angle dependent phase, as shown in Figures 6.25a and

6.25b for u^+ and u^-, respectively. Consequently, tight-binding wave functions based on them can support an asymmetric charge distribution at finite k_x, as shown in Figure 6.25(c, d) for $k_x a = \pi/2$.

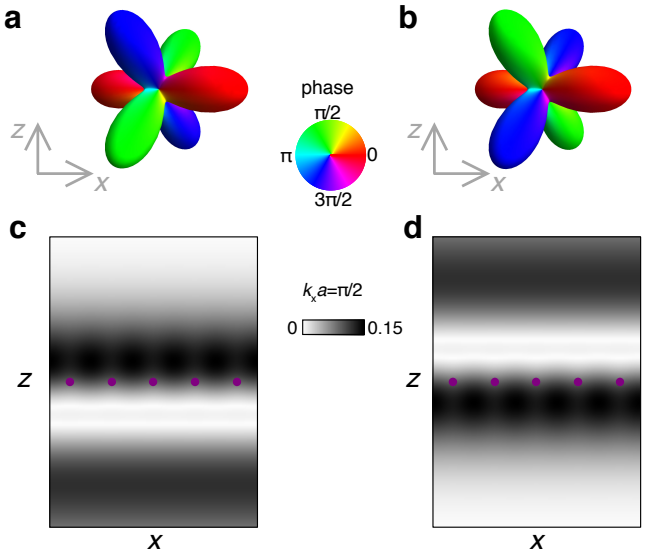

Figure 6.25.: (a) The u^+ and (b) the u^- orbitals (equation 6.44) coloured according to their phase. The tight binding wave functions based on the (c) u^+ and (d) u^- $3d$ orbitals, for $k_x a = \pi/2$. The hydrogenic radial wave function ($n = 3, l = 2$) is used. Purple dots mark the lattice sites, separated by 2 Å. The sum (equation 6.36) is performed over 50 lattice sites to avoid edge effects.

To summarise, a tight binding wave function of a finite crystal momentum $\vec{k}$ can become asymmetric with respect to a direction $\hat{d}$ if its base orbital has an angle dependent phase in the plane containing both $\vec{k}$ and $\hat{d}$. Such a wave function *can*, but *does not have to,* develop a finite expectation value of angular momentum along a specific quantisation axis, determined both by $\hat{d}$ and the orbital character of the wave function in question. An inversion symmetry breaking Hamiltonian always causes a splitting between asymmetric wave functions of opposite weight distributions, which may be followed by a splitting of states of opposite angular momentum and, in combination with spin-orbit coupling, of opposite spin. In those cases the picture of energy scale hierarchy developed in section 6.4.4 is valid and relevant. However, it is also possible that a splitting between asymmetric wave functions does not cause a splitting of states of opposite angular momentum. In

those cases no observable spin-splitting will occur even if the Hamiltonian contains both the inversion symmetry breaking and spin-orbit coupling term.

The above discussion points to two practical considerations for analysing spin-splitting in specific materials. First of all, it is important to check for every material whether the relevant orbital manifold supports creation of orbital angular momentum, and consequently spin-splitting. In majority of systems, and all real materials I can think of, this is the case. Indeed, the example of u^+ and u^- states above is finely tuned to prove that this relationship between orbital angular momentum and inversion symmetry breaking does not arise from fundamental principles; rather it is a consequence of the fact that both orbital angular momentum and wave function asymmetry are related to the spatial variation of the wave function phase, but in different ways. This leads to the second conclusion, which needs to be taken into account when using model Hamiltonians to describe the arising of spin-splitting. It is often convenient to mathematically relate the inversion symmetry breaking term with the orbital angular momentum operator, as was done for p orbitals in Section 6.4.2. However, no such relation can be completely general, and it always needs to be reconsidered in the context of the studied compound.

6.6. CoO_2 tight binding model

The p - orbital model described in the last section demonstrates how a tight-binding analysis can lead to crucial insights on the nature of spin-splitting. The orbitals on which the tight-binding wave functions are based determine whether spin-splitting can occur at all, while the resulting band structure is governed by the relative size of the two relevant energy scales, the spin-orbit coupling and the inversion-symmetry breaking energy scale. This motivates the construction of a second tight-binding model, with the aim of investigating the nature of spin-splitting in the surface states arising on the transition metal oxide terminated surfaces of delafossite oxides. The analysis of such a model entails looking into the relevant basis orbitals, to see which ones amongst them can support spin-splitting, as well as determining the relative magnitude of the two energy scales governing spin-splitting. The spirit of the approach is similar to that adopted above; the aim is not to correctly capture the detailed band structure, but rather to isolate the minimal ingredients necessary to achieve the large effect that is observed experimentally. As the density-functional

theory calculations (Section 6.2) proved that the spin-split wave functions are predominantly localised in the top CoO_2 layer, a good starting point is to consider this layer only.

As discussed in the Introduction (Section 1.1), the Co atoms are arranged on a triangular lattice of lattice constant $a = 2.82\,\text{Å}$, with each Co in the centre of an oxygen octahedron (Figure 6.26(a, b)). The octahedra are edge sharing, so a single CoO_2 layer can be thought of as three triangular layers of equal spacing - a layer of cobalt between two oxygen layers (Figure 6.26a). In the ideal structure the distance between Co and O atoms is equal to $a/\sqrt{2} = 1.99\,\text{Å}$, but in the real materials the octahedra are trigonally distorted [5], bringing oxygen and cobalt layers closer to each other, and decreasing the Co - O distance to 1.88 Å.

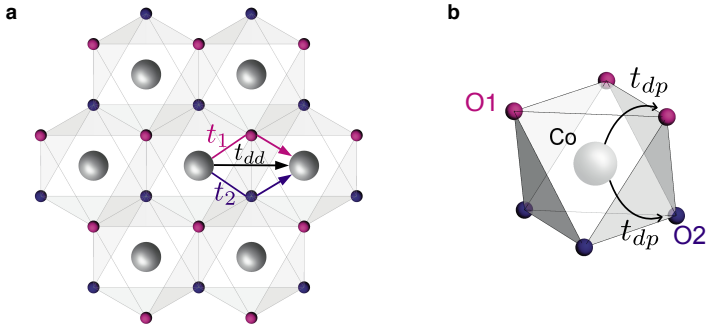

Figure 6.26.: (**a**) A top-view of the CoO_2 layer of delafossite oxides. Effective hopping paths are indicated by the arrows. (**b**) The CoO_2 octahedron, a structural unit building the CoO_2 layer.

As usual, the octahedral crystal field splits the d orbitals into the e_g and t_{2g} manifolds, while the trigonal distortion introduces an additional, smaller, splitting of the t_{2g} manifold. The full crystal field Hamiltonian is diagonal in the so-called trigonal basis, $\{u^+, u^-, x^0, x^1, x^2\}$, where u^+ and u^- are the two e_g^σ orbitals, x^0 is of a_{1g} symmetry, and x^1 and x^2 are of e_g^π symmetry (Figure 6.27, Reference [104]). The basis transformation between the trigonal basis and the spherical basis with z as a quantisation axis is given in Appendix E.2. In the bulk electronic structure of the Co - based delafossites the Co t_{2g} orbitals are fully occupied, and the e_g orbitals empty. The surface layer is effectively hole-doped with respect to the bulk, giving rise to the surface states, which are therefore t_{2g} - derived. Hence, the spin-split

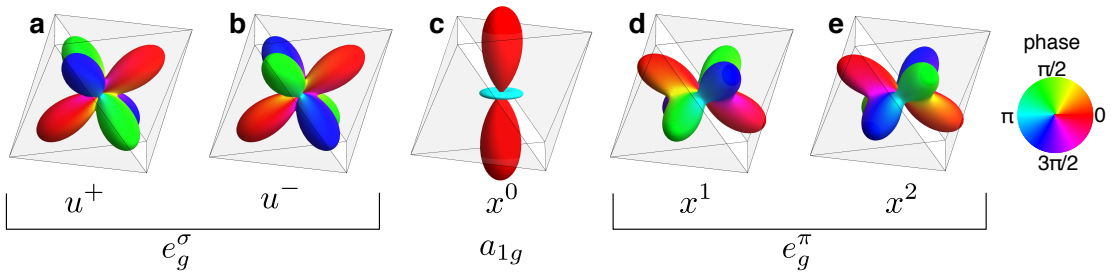

Figure 6.27.: The five $3d$ orbitals of Co, expressed in the trigonal basis which diagonalises the crystal field Hamiltonian. The colour marks the phase of the wave function.

wave functions are based on the orbitals shown in Figures 6.27(c - e). The x_0 orbital is in fact the $d_{3z^2-r^2}$ in the global cubic system; it is real, and a wave-function based on it alone cannot support an asymmetric charge distribution, or orbital angular momentum along a specific axis. The other orbitals are complex, with a phase changing as a function of angle. As discussed in Section 6.5, this means that the wave functions based on them can support asymmetric charge distributions, but it is not a guarantee that they can carry an orbital angular momentum as well. The simplest way to find out if they can is to inspect the orbital angular momentum operator along the $\hat{z}$ axis, expressed in the trigonal basis, as found by utilising the basis transformation given in Appendix E.2:

$$L^z_{trig} = \begin{pmatrix} 0 & 0 & 0 & 0 & -\sqrt{2} \\ 0 & 0 & 0 & \sqrt{2} & 0 \\ 0 & 0 & 0 & 0 & 0 \\ 0 & \sqrt{2} & 0 & 1 & 0 \\ -\sqrt{2} & 0 & 0 & 0 & -1 \end{pmatrix}. \tag{6.46}$$

In the large crystal field limit the terms which mix the e_g^σ and t_{2g} - like orbitals, shown in black in equation 6.46, can be neglected. The upper diagonal 2 x2 block (marked blue in equation equation 6.46) is relevant for the bands derived from the e_g^σ orbitals, while the lower 3x3 block (purple in equation equation 6.46) is relevant for those derived from the t_{2g} - like orbitals. As all the blue terms vanish, there can be

no angular momentum developed in the e_g^σ bands. This is not surprising, as the two orbitals of this symmetry, u^+ and u^-, are precisely the ones used in section 6.5 as an example of complex orbitals which cannot support any orbital angular momentum along a specific quantisation axis. As the e_g orbitals are unoccupied in delafossites, this is not relevant for any of the observations. On the other hand, L^z is diagonal in the subspace spread by the three t_{2g} - like orbitals, with eigenvalues of 0, 1 and -1 for the x^0, x^1 and x^2 states, respectively. Although they are d - orbitals with $l = 2$, the isolated t_{2g} states are therefore expected to behave similarly to p orbitals from the point of view of developing angular momentum along a specific axis. In direct analogy with the p - orbital case, we therefore expect that the band structure based on the t_{2g} orbitals can become spin-split. The spin-splitting can occur in the bands based on the x^1 or x^2 orbital alone, or if they are allowed to mix with the x_0 orbital. In the following few sections I will refer to the x_0 orbital as the $m_z = 0$ state, and to the x^1 and x^2 states as the $|m_z| = 1$ states.

The considerations so far are valid for any system based on the t_{2g} orbitals. To find out how the spin-splitting occurs specifically in the structure of the delafossite surface layer, a band structure needs to be calculated. The kinetic part of the tight binding Hamiltonian is constructed in the geometry outlined above (Figure 6.26), using the Slater-Koster [63] parametrisation of the energy integrals. The cubic $\{xy, yz, 3z^2 - r^2, xz, x^2 - y^2, p1_y, p1_z, p1_x, p2_y, p2_z, p2_x\}$ basis is used, where $p1$ and $p2$ refer to the orbitals on the oxygen layers above and below cobalt, respectively, and the $\hat{z}$ axis is taken to be normal to the crystal surface. Three different types of hopping can be included: direct hopping between Co $3d$ orbitals, direct hopping between O $2p$ orbitals, and hopping between Co $3d$ and O $2p$ orbitals. Although I have constructed a tight-binding model containing all of these hoppings, I found that the essential physics can be captured even if only the nearest neighbour Co - O - Co hopping between cobalt t_{2g} and oxygen p_z orbitals is retained, and the crystal field caused by the trigonal distortion neglected. For illustrative purposes and maximum simplicity in what follows I will show results from this minimal model. Technically this simplification is achieved by applying a very large on-site energy on all the orbitals which are not included in the model. Hopping between d and p orbitals is parametrised by two Slater-Koster integrals, $V_{dp\sigma}$ and $V_{dp\pi}$, which can be related by the empirical relation $V_{dp\pi} = -\sqrt{3}/4 V_{dp\sigma}$ [105] to reduce the number of free parameters even further.

6.6.1. The band structure

Before discussing the spin-splitting, it is useful to look at a spin-degenerate band structure, and in particular at its orbital character, shown in Figure 6.28a. The parameters of the model are chosen so that the bandwidth and energies of all the states approximately match those found by DFT (the first column in Table 6.4). The bands are coloured according to their orbital character, demonstrating that the three bands shown are dominantly derived from the three t_{2g} orbitals, although there is a small oxygen admixture. The electronic structure closely resembles that of a kagome model, which has been used previously to describe the CoO_2 layer of Na_xCoO_2 [106]: the lowest band is flat, and the other two bands cross at the Brillouin zone corner, $\overline{K}$, and along the $\overline{\Gamma} - \overline{K}$ line.

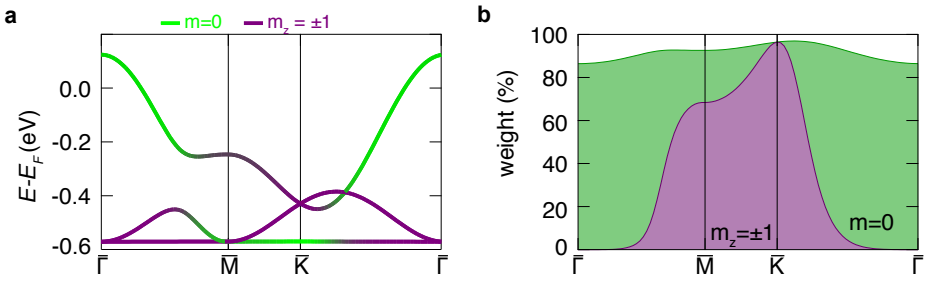

Figure 6.28.: (**a**) The band structure of the CoO_2 layer of delafossite oxides, coloured according to its orbital character. (**b**) Orbitally resolved wave function weight of the band crossing the Fermi level. In both of the plots the green colour corresponds to the weight of the $m_z = 0$ x_0 orbital, while purple corresponds to the sum of the two orbitals with $|m_z| = 1$.

The orbital character of the band crossing the Fermi level changes from dominantly x^0 (green in Figure 6.28a) at the zone centre, to an equal combination of the x^1 and x^2 states (purple in Figure 6.28a) at the zone edge. However, unlike in the case of the p - orbitals on the triangular lattice, the hybridisation between those states is not forbidden by symmetry. As evident in the plot of the wave function weights of the band crossing the Fermi level (Figure 6.28b), in the majority of the zone all of the t_{2g} orbitals contribute, although of course not an equal amount. This implies that a finite orbital angular momentum can be developed in a large part of the zone. The contributions of the three t_{2g} orbitals do not add up to 100% of the wave function weight because they are hybridised with the O $2p$ orbitals.

Parameter	no ISB	strong ISB	weak ISB
$V_{dp\sigma}$	-1.2	-1.2	-1.2
$V_{dp\pi}$	0.52	0.52	0.52
C_o	1000	1000	1000
C_t	0	0	0
E_1^z	-4.3	-3.2	-3.91
E_2^z	-4.3	-7	-4.77
E_{Co}	-0.57	-0.57	-0.57
λ	0.0	0.07	0.07

Table 6.4.: Parameters used to calculate the band structure within the minimal tight binding model without ISB or spin-orbit coupling (Figure 6.30), in the strong ISB limit relevant for delafossites (Figure 6.31), and in the weak ISB limit (Figure 6.32(b)). E_{Co} referred to an overall on-site energy shift applied to the Co orbitals; the other symbols are explained in the text.

To study the development of orbital angular momentum, a term breaking inversion symmetry needs to be added to the Hamiltonian. One way to do that is to consider how the asymmetric orbital deformation influences tight-binding parameters, as was done for the p - orbital model above. For d orbitals this approach would result in three different free parameters describing the inversion symmetry breaking [98]. The crystal structure of the CoO_2 layer suggests another, physically more relevant, way to include inversion symmetry breaking. The effective hopping between Co sites can proceed via two paths which are equivalent in the bulk: either through the oxygen atoms in the layer above cobalt, or through those in the layer below (O1 and O2 in Figure 6.26(a, b)). Crucially, the two paths are not equivalent in a surface CoO_2 layer, because only one of the oxygens, O2 , is bonded to platinum. This insight motivates looking into explicit density functional theory calculations of the partial density of states (PDOS) of the two oxygens, shown in Figure 6.29a for the p_z orbitals, which are the only ones included in the minimal tight binding model.

Close to the Fermi level the partial density of states of the surface oxygen p_z orbital is much larger than that of the subsurface oxygen. Except for this added

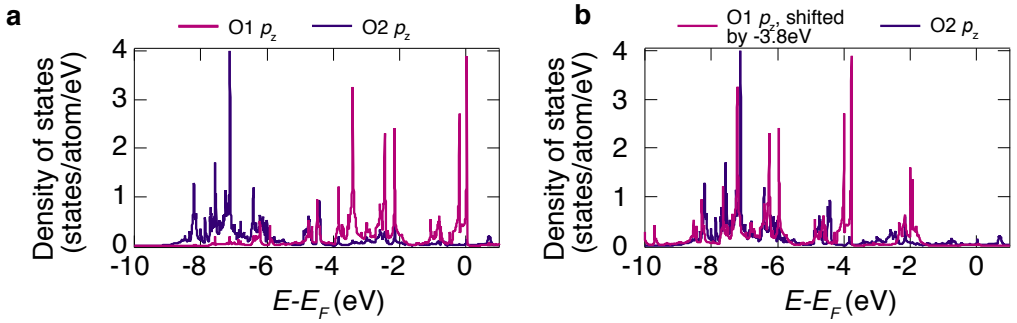

Figure 6.29.: (**a**) The oxygen p_z PDOS for layers above (O1, pink) and below (O2 , purple) the Co layer. (**b**) The same, but with the O1 PDOS shifted by $-3.8\,\mathrm{eV}$.

weight, the O1 PDOS approximates that of O2 if it is shifted by $-3.8\,\mathrm{eV}$ (Figure 6.29b). The relative energies of the O1 and O2 states can be understood as a consequence of bonding to Pt, which moves the predominantly oxygen-derived levels to a higher binding energy in O2, as observed in the calculation. The first principles calculation therefore confirms the intuition-based assumption that the two oxygens are inequivalent, and enables us to quantify the difference between them. It is therefore easy to make the minimal tight-binding Hamiltonian break inversion symmetry in a physically meaningful way: the on-site energy of O1 has to be $3.8\,\mathrm{eV}$ higher than that of O2. This difference in oxygen on-site energy also affects the states at the Fermi level, as the hopping through the oxygen layers is the only hopping process included in the model. The effective hopping integral through an oxygen in layer i ($i = 1, 2$) is given by t_{dp}^2/Δ_i , where t_{dp} denotes the direct hopping parameter between cobalt and oxygen, and Δ_i the on-site energy difference between them. The inversion symmetry breaking energy scale relevant for the surface states is the difference of the hopping integrals for the two paths, $t_{dp}^2\,(1/\Delta_1 - 1/\Delta_2)$. This is the energy difference of the wave functions whose weight is dominantly above and dominantly below the Co plane; an analysis of the Co-O hybridisation reveals that the one whose weight is dominantly above the Co plane has a lower binding energy (see Appendix F). As t_{dp}, Δ_1 and Δ_2 can all be roughly estimated from density functional theory calculations, the inversion symmetry breaking scale is not an arbitrary parameter of the model. This enables a meaningful comparison of the inversion symmetry breaking and spin-orbit coupling energy scales.

In Figure 6.30 I show the band structure calculated with the on-site energies of

the two oxygen p_z orbitals chosen to be $-3.2\,\text{eV}$ and $-7\,\text{eV}$ for O1 and O2 (Table 6.4, second column), respectively. The band structure is coloured according to the in-plane chiral (Figure 6.30a, $\langle L_\perp \rangle$) and the out of plane (Figure 6.30b, $\langle L_z \rangle$) orbital angular momentum.

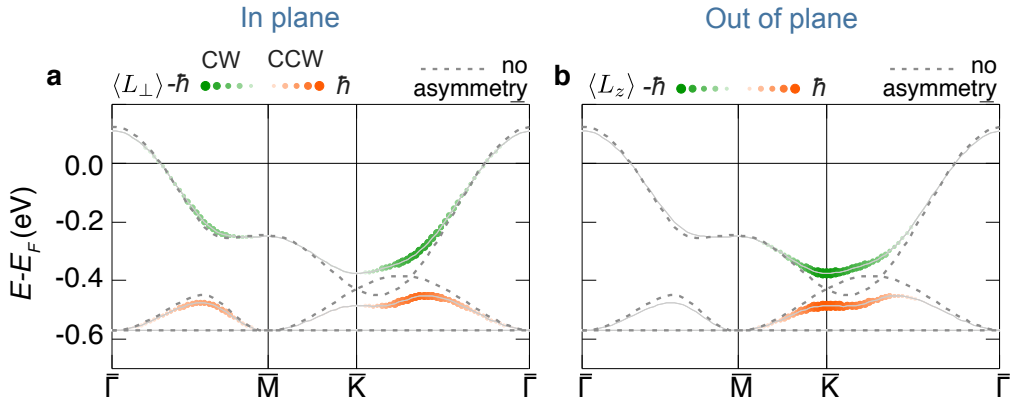

Figure 6.30.: The band structure of the CoO_2 layer of delafossite oxides calculated without spin-orbit coupling, with different on-site energy for the two distinct oxygens, coloured according to (**a**) the expected value of chiral in-plane orbital angular momentum, and (**b**) out-of-plane orbital angular momentum.

As in the example of p - orbitals on a triangular lattice, the breaking of symmetry allows hybridisation at places in the zone where bands cross in the inversion symmetric environment, along the $\overline{\Gamma} - \overline{K}$ line and at the $\overline{K}$ - point here. The opening of a gap at the $\overline{K}$ point is allowed because the CoO_2 layer has no mirror symmetry with respect to the zx plane, which protects the degeneracy of the $m_z = \pm 1$ states in a simple triangular lattice. Once the degeneracy of the $m_z = \pm 1$ orbitals is broken, the bands on either side of the gap develop orbital angular momentum in the z direction. Chiral orbital angular momentum is developed on either side of the hybridisation gap opened along the $\overline{\Gamma} - \overline{K}$ line, much like in the triangular lattice, but also in the part of the zone where there are no avoided crossings, along the $\overline{\Gamma} - \overline{M}$ line here. This is possible because the orbital character is mixed along this line even in the inversion symmetric environment (Figure 6.28(a, b)).

The CoO_2 layer is therefore an example of a system in which inversion symmetry breaking allows for finite orbital angular momentum to be developed along specific axes, determined by the orbital character of the bands and the momentum direction.

If spin-orbit coupling is added to such a system, the band structure becomes spin-split, with the energy scale of the spin-splitting determined by the relative size of the spin-orbit coupling and the inversion symmetry breaking. The latter determines the size of the gap between the states of opposite orbital angular momentum, which is 110 meV the at the $\overline{K}$ point, and 140 meV at the anti-crossing point along the $\overline{\Gamma} - \overline{K}$ line; the values are extracted from Figure 6.30. Both of these energies are larger than the spin-orbit coupling scale of 70 meV, placing the CoO_2 layer in the limit of strong inversion symmetry breaking. The orbital angular momentum is therefore of the same sign on the two spin-split branches, as shown in Figure 6.31.

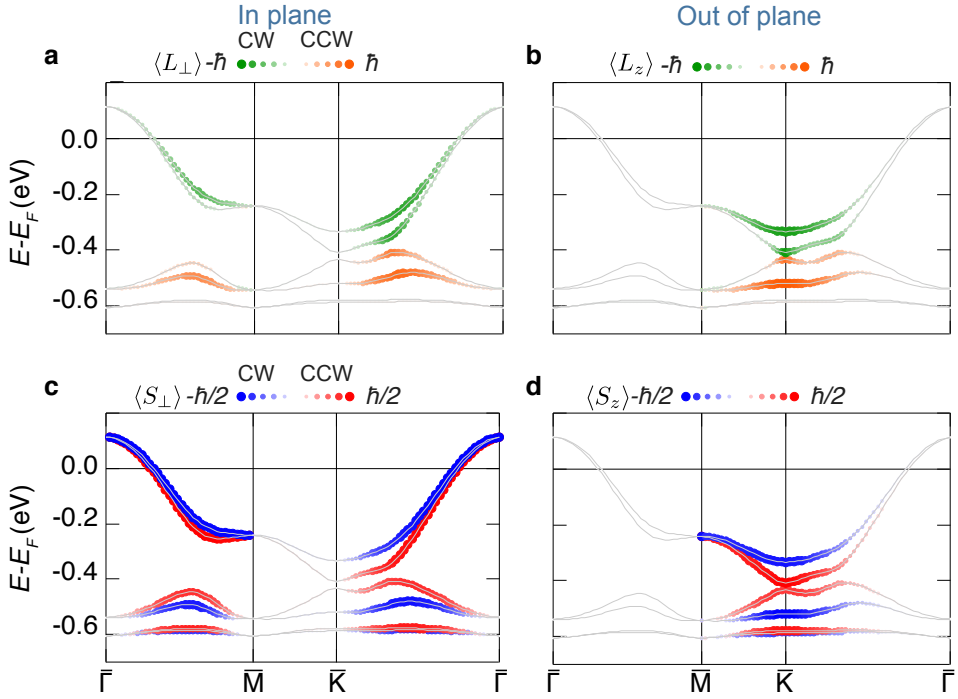

Figure 6.31.: The band structure of the CoO_2 layer calculated with spin-orbit coupling, and with different on-site energy for the two oxygens, coloured according to the expected value of (**a**) chiral in-plane and (**b**) the out-of-plane orbital angular momentum, (**c**) chiral in-plane and (d) out-of-plane spin angular momentum.

This is true across the Brillouin zone, for the in-plane and out-of-plane orbital angular momentum alike. The maximum size of the spin-splitting of the band cross-

ing the Fermi level is 75 meV, on the order of the spin-orbit coupling constant, as expected for a system in the strong spin-orbit coupling limit. This minimal model describing the spin-splitting in the transition metal oxide layer of delafossites therefore suggests an exciting scenario for achieving a large spin-splitting. An asymmetry of *kinetic* energy caused by the structure of the top layer causes an inversion symmetry breaking large enough to place the system in the strong ISB limit. The characteristic signatures of this limit are reproduced by the model: the orbital angular momentum is of the same sign on the two spin-split branches, and the spin-splitting reaches the full strength of the spin-orbit coupling.

To unambiguously show that the two limits identified in the p - orbital case are also relevant for the model considered here, I vary the asymmetry parameter, defined as $\gamma = (E_{O1} - E_{O2}) / (E_{O1} + E_{O2})$, and monitor the evolution of the spin-splitting gap at the $\overline{K}$ point. As for the p - orbital case, the spin-splitting increases linearly with the asymmetry in the weak ISB regime, until it saturates to a value limited by the spin-orbit coupling in the strong ISB regime (Figure 6.32a, *cf.* Figure 6.22a). In a band structure calculated in the weak inversion symmetry breaking regime the orbital angular momentum points in the opposite direction on the two spin-split bands, as shown for $\gamma = 0.1$ in Figure 6.32(b-e). This is in clear contrast to the band structure calculated using parameters relevant for the CoO_2 layer of delafossites ($\gamma = 0.4$, Figure 6.31).

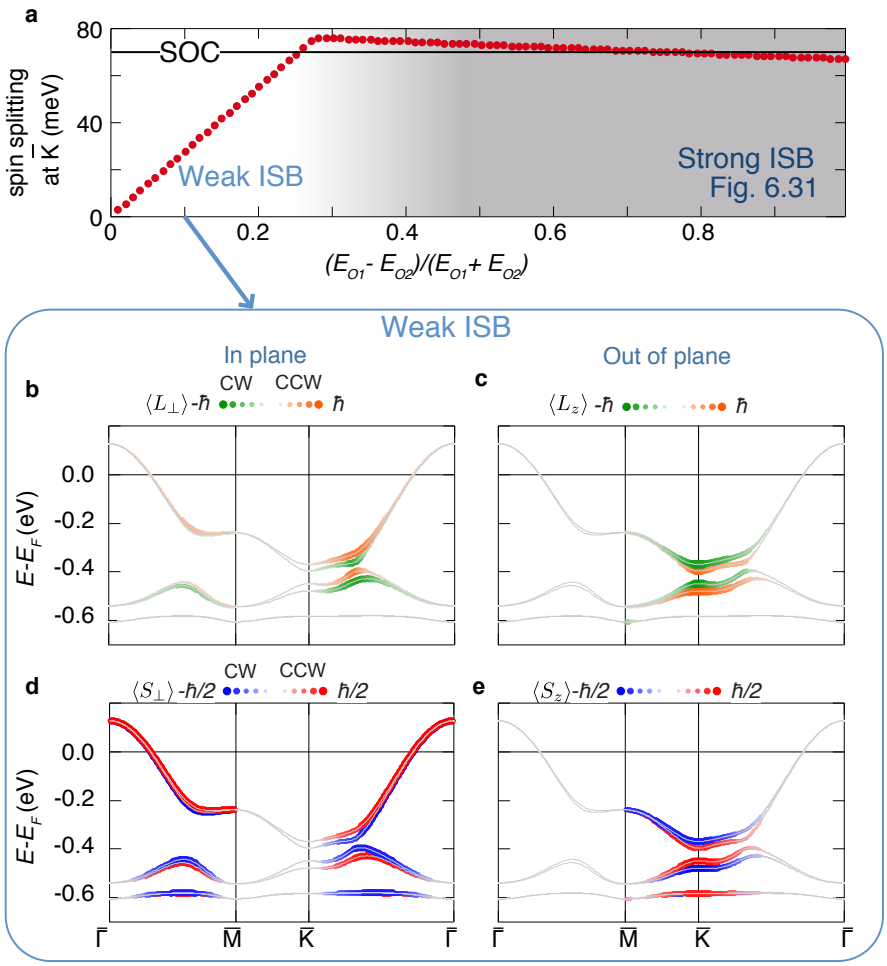

a

Figure 6.32.: (**a**) Spin-splitting at the $\overline{K}$ - point, as a function of the inversion symmetry breaking parameter. The band structure of the CoO_2 layer of delafossite oxides in the weak inversion symmetry breaking limit ($\gamma = 0.1$), coloured according to (**b**) the expected value of chiral in-plane orbital angular momentum, (**c**) out-of-plane orbital angular momentum, (**d**) chiral in-plane spin angular momentum and (**e**) out-of-plane spin angular momentum.

6.7. New insights on the spin-splitting in delafossites

The simple model described in the previous section not only reproduces the large spin-splitting observed in delafossites, but also points to the ingredients necessary for that spin-splitting to develop. First of all, the splitting persists away from the anti-crossing points because the structure supports orbital character mixing. Furthermore, the system is in the strong inversion symmetry breaking limit. Most importantly, the reason for this large inversion symmetry breaking energy scale is the hopping through two oxygen layers, made different by the loss of bonding at the surface. It is important to check that the features observed in the simple model are also present in the real material, rather than being an artefact of the simplifications made. In what follows I will look for their signatures directly in the density functional theory calculations, as well as in further experiments inspired by the understanding brought by the simple model.

6.7.1. Orbital character

In Figure 6.31 I plot the band structure of $PtCoO_2$, coloured according to its orbital character: green represents the $3d_{3r^2-z^2}$ orbital of the cobalt in the surface layer, while purple corresponds to the sum of the weights of all the other $3d$ orbitals of the same atom. As the output of the density functional theory calculation returns the absolute values of overlaps of the wave function with the cubic orbitals, but not their phase, it is not possible to directly extract the weight of the individual trigonal orbitals. However, the $3d_{3r^2-z^2}$ orbital in the global coordinate system is also the x^0 orbital of the trigonal crystal field, while the energetic splitting between the t_{2g} and e_g levels ensures that the orbitals of finite m_z in the energy range shown in Figure 6.31a are dominantly the x^1 and x^2 orbitals of the trigonal crystal field (Figure 6.27). Therefore, the orbital character of the band crossing the Fermi level extracted from the DFT calculation can be compared with the one obtained in the simple tight binding model (Figure 6.28). Indeed, the DFT calculation retains the orbital mixing between states of different m throughout the zone, explaining how the spin-splitting can persist in the whole band, and disappear only at the points where symmetry demands spin degeneracy. The overall contribution from the surface Co $3d$ orbitals is somewhat smaller than in the tight-binding model, indicating that there is a larger degree of hybridisation with oxygen in the real material, as well as

some contribution from subsurface layers.

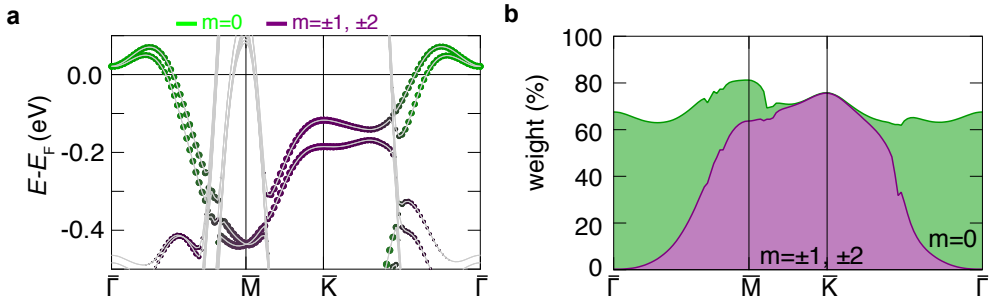

Figure 6.33.: (**a**) The band structure of the CoO_2 layer of delafossite oxides, coloured according to its orbital character. (**b**) Orbitally resolved wave function weight of the band crossing the Fermi level.

6.7.2. Strong ISB limit

As discussed in the context of the tight-binding models, the clearest sign that a spin-split band structure is in the strong inversion symmetry breaking limit is the sign of orbital angular momentum on the two spin-split branches; it is the same in the strong inversion symmetry breaking limit, and opposite in the weak. This motivates calculating the expected value of chiral orbital angular momentum for the density functional theory wave functions, however the lack of information on the phase of these wave functions prevents a direct computation. Instead, the electronic structure was downfolded onto a basis of Wannier functions localised on atomic sites and obeying the symmetry of atomic orbitals. An effective tight-binding Hamiltonian in this basis was obtained, as described in Section 3.3, enabling the calculation of expected values of orbital angular momentum. For computational simplicity the downfolding was done for a band structure calculated without spin-orbit coupling, which was later added at the tight-binding level. In Figure 6.34a I show the Fermi surface calculated without spin-orbit coupling, demonstrating how a chiral orbital angular momentum (arrows), as well as some out-of-plane orbital angular momentum (colours) develop in the absence of spin-orbit coupling. This is similar to the findings of the minimal tight-binding model with inversion symmetry breaking (Figure 6.30).

Adding spin-orbit coupling splits the bands according to their spin, but does not alter the sign of the preexisting orbital angular momentum (Figure 6.34(b, c)), again consistent with the simple model (Figure 6.31).

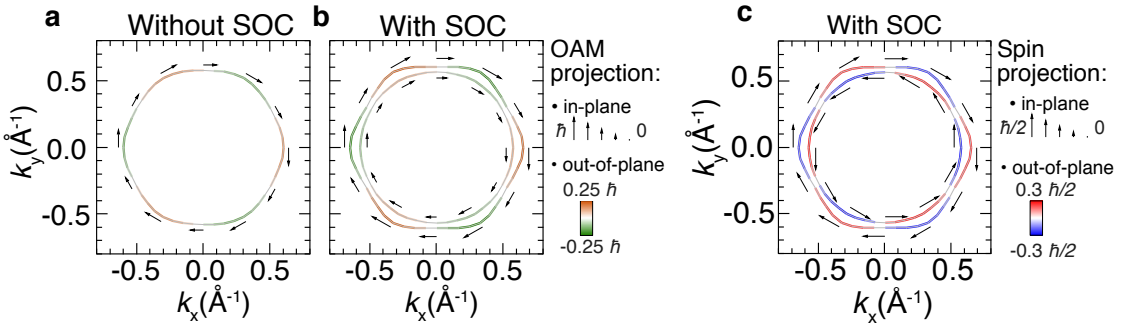

Figure 6.34.: Fermi surface of the surface states calculated (**a**) without spin-orbit coupling (SOC) and (**b**, **c**) with spin-orbit coupling. In (**a, b**) the arrows indicate the expected value of the in-plane orbital angular momentum in the direction normal to the momentum, and the colouring the out-of-plane orbital angular momentum (OAM), while in (**c**) the arrows indicate the expected value of the in-plane spin angular momentum, and the colouring the out-of-plane spin angular momentum.

Although the overall agreement of the theory and the experiment leaves little doubt that the material really is in the strong inversion symmetry breaking limit, the final proof would be an experimental confirmation of the direction of orbital angular momentum. While there is no experimental method that directly measures the orbital angular momentum of a wave function in a solid, circular dichroism in photoemission, i.e. the difference in intensity when measuring with the two circular light polarisations, has been shown to be sensitive to it in many specific cases [107–109]. Motivated by this, in Figure 6.35(a, b) I show the circular dichroism in a measured dispersion and a Fermi surface. Evidently there is a strong circular dichroism of the same sign on the two spin-split states, consistent with the same sign of orbital angular momentum on the two spin-split bands. The result does not depend on the photon energy used, as shown in Figure 6.35c, which also shows that the Fermi momenta do not depend on the photon energy, as expected of two-dimensional electronic states (Section 2.1).

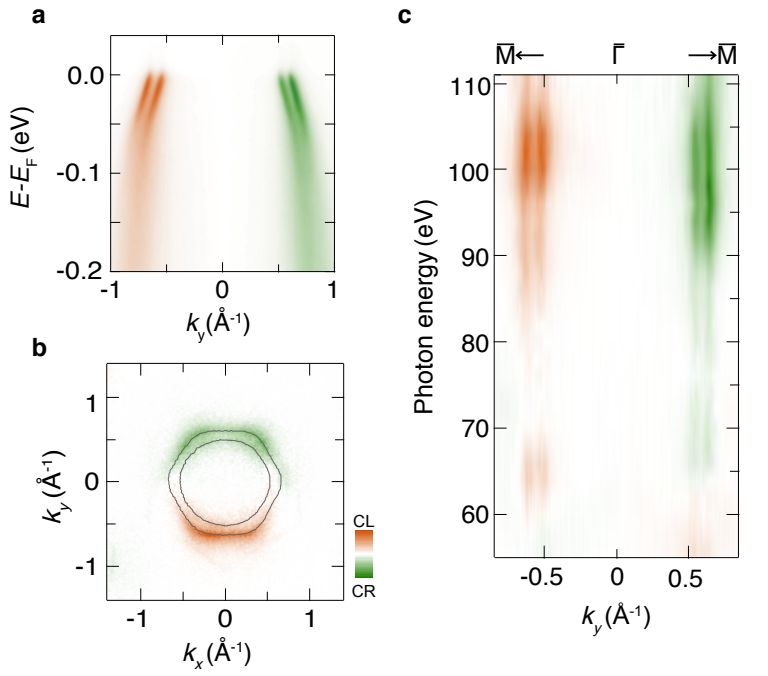

Figure 6.35.: Circular dichroism measurement of (**a**) dispersion ($h\nu = 100\,\text{eV}$), and (**b**) a Fermi surface map ($h\nu = 110\,\text{eV}$). (**c**) Circular dichroism at the Fermi level ($E_F \pm 5\,\text{meV}$) as a function of photon energy.

The sign of orbital angular momentum shows that the inversion symmetry breaking is the dominant energy scale, but it does not reveal its magnitude. As discussed in the context of the simple tight-binding models, the two $m_z = \pm 1$ states have to be degenerate at the $\overline{K}$ point in the absence of inversion symmetry breaking and spin orbit coupling. Therefore, the splitting between them at the $\overline{K}$ point can be used to estimate the inversion symmetry breaking energy scale. In Figure 6.36 I plot the band structure over a larger energy range than previously, down to 1.2 eV binding energy, coloured according to the out-of-plane spin (Figure 6.36a), and the orbital character of the surface Co $3d$ orbitals (Figure 6.36b). In addition to the bands crossing the Fermi level, another pair of spin-split states of the $m_z = \pm 1$ character is clearly resolvable. Because the system is in the strong inversion symmetry breaking limit, the energy scale of the splitting between those two pairs of states at the $\overline{K}$ point corresponds to the inversion symmetry breaking energy scale, and is found to be equal to $\sim 380\,\text{meV}$. This leads to the simplified energy scale diagram

for the surface states at the $\overline{K}$ point show in Figure 6.36c; similar diagrams are valid at other momentum points, with the appropriate quantisation axis governed by the momentum direction. Another place in the band structure where it is possible to estimate the inversion symmetry breaking energy scale is at the anti-crossing point of the states of different orbital character along the $\overline{\Gamma} - \overline{K}$ line. Although less well defined than the one at the $\overline{K}$ point, the splitting is about $\sim 230\,\mathrm{meV}$ here, still much larger than the spin-orbit coupling energy.

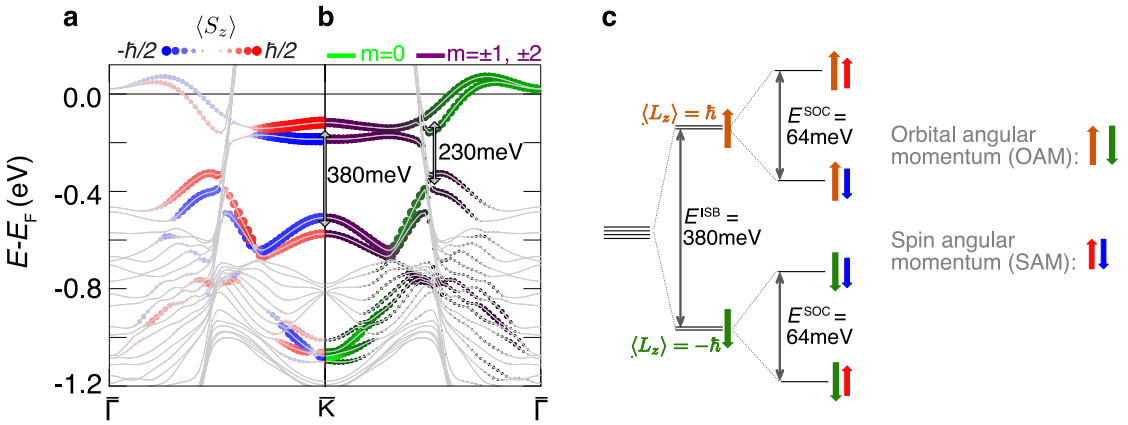

Figure 6.36.: The band structure of the CoO_2 layer of delafossite oxides, coloured according to (**a**) the out-of-plane spin projection, and (**b**) its orbital character. (**c**) An energy level diagram directly relevant for the surface states of $PtCoO_2$ at the $\overline{K}$ - point.

6.7.3. Kinetic inversion symmetry breaking

The inversion symmetry breaking energy scale we were able to deduce is truly large, more than four times the strength of the spin-orbit coupling of the Co $3d$ orbitals. Understanding its origin is the key to understanding the large spin-splitting. In the simple tight binding model the inversion symmetry breaking is essentially kinetic, i.e. the effective hopping Hamiltonian becomes asymmetric. This originates from the difference in the on-site energy of the two oxygens, which was also found in the density functional theory calculations of the partial density of states of the oxygen

p_z orbitals (Figure 6.29). To show that this remains relevant even when all of the orbitals are considered, I plot the layer-resolved total density of oxygen states for the first nine layers in Figure 6.37a. The DOS of the oxygens below the first CoO_2 layer (oxygen 3-9, grey in Figure 6.37a) are all very similar to each other, proving that they are not significantly affected by the surface. The DOS of the subsurface oxygen 2 (purple in Figure 6.37a) is somewhat, but not significantly, modified from the bulk-like one of the deeper oxygens. In contrast, the majority of the density of states of the surface oxygen (pink in Figure 6.37a) is shifted by $\sim 4\,\text{eV}$ towards the Fermi level. In the tight binding model this on-site energy difference caused the band crossing the Fermi level to hybridise strongly with the surface oxygen, and very weakly with the subsurface one. In Figure 6.37b I therefore plot the DFT band coloured according to the wave function weight of the surface (pink) and subsurface (purple) oxygen, proving that the hybridisation with the surface one is much stronger, as it is in the tight binding picture. The parallels drawn between the simple tight binding model and the density functional theory calculation reinforce the interpretation of the kinetic inversion symmetry breaking in the surface CoO_2 layer of delafossites.

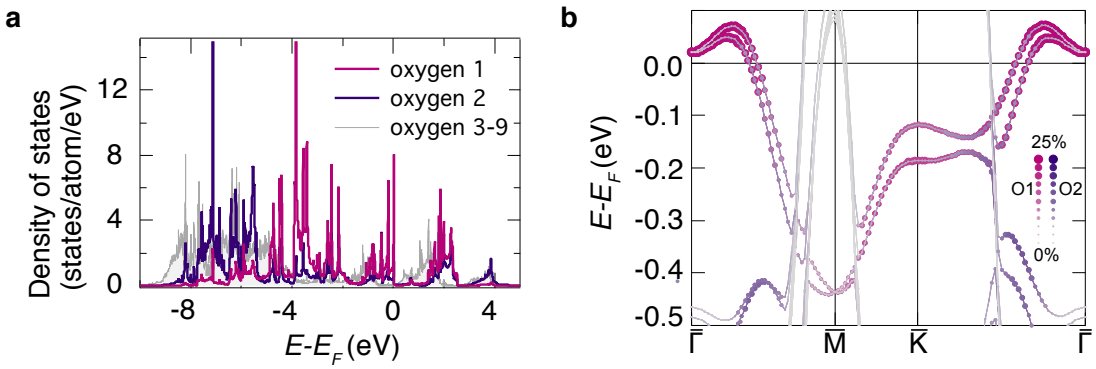

Figure 6.37.: (**a**) The density of states of the surface (pink), subsurface (purple), and deeper lying oxygens (grey). (**b**) The band structure of the CoO_2 layer of delafossite oxides, coloured according to the contribution of the surface (pink) and subsurface (purple) oxygen.

6.7.4. Confirmation: $PdRhO_2$

One of the features of the strong inversion-symmetry breaking limit is that the spin-splitting is limited by the spin-orbit coupling. In other words, if heavier atoms were used to increase the spin-orbit coupling, and the system remained in the strong ISB limit, the spin-splitting would grow proportionally to the spin-orbit coupling. We were able to test this prediction by measurements on a new compound, $PdRhO_2$. The atomic spin-orbit coupling of the $4d$ orbitals of rhodium in the $4d^6$ configuration is 175 meV [88], 2.5 times larger than that of Co, making it an ideal system in which to test if the spin-splitting indeed scales with the spin-orbit coupling.

The surface states on the transition metal oxide terminated surface of $PdRhO_2$ are qualitatively similar to those on $PdCoO_2$, as seen in dispersions measured along the $\overline{\Gamma} - \overline{M}$ and the $\overline{\Gamma} - \overline{K}$ directions, shown in Figure 6.38 (a, b).

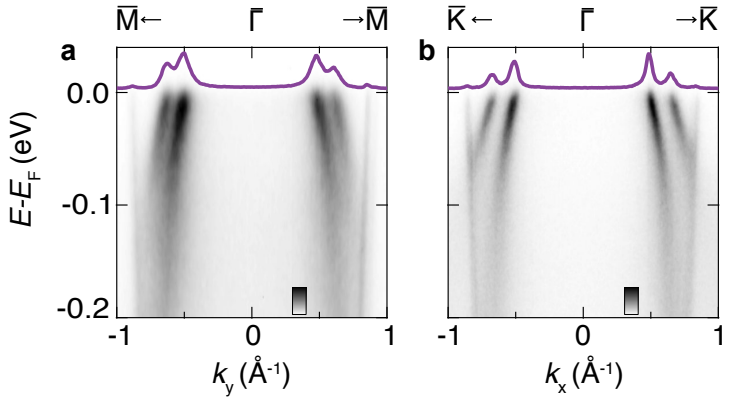

Figure 6.38.: Dispersion measured along (**a**) the $\overline{\Gamma} - \overline{M}$ and (**b**) the $\overline{\Gamma} - \overline{K}$ direction in $PdRhO_2$. The lines are the MDCs, averaged over $E_F \pm 5$ meV.

The Fermi momenta and velocities extracted from $PdRhO_2$ (Table 6.5) reveal that the quasiparticle masses are lower than in the cobaltates, reflecting the larger bandwidth of the Rh $4d$ bands compared to the Co $3d$ bands[6]. In spite of this, the momentum splitting at the Fermi level is higher, reaching $\Delta k_F = (0.16 \pm 0.01)$ Å^{-1} along the $\overline{\Gamma} - \overline{K}$ direction. This is a result of a strongly enhanced energetic splitting, which is as large as 150 meV at the $\overline{K}$ - point (Figure 6.39(c, d)). It is indeed on the order of the full atomic spin-orbit coupling strength of Rh, and to the best of

[6]See section D.3 for a comparison of the numerical values extracted from all the compounds.

my knowledge by far the largest spin splitting observed in an oxide to date. It is 2.5 times larger than the energetic splitting in $PdCoO_2$, reflecting the ratio of their atomic spin-orbit coupling energies, and confirming that the transition metal oxide surfaces of delafossites really are in the strong inversion symmetry breaking limit.

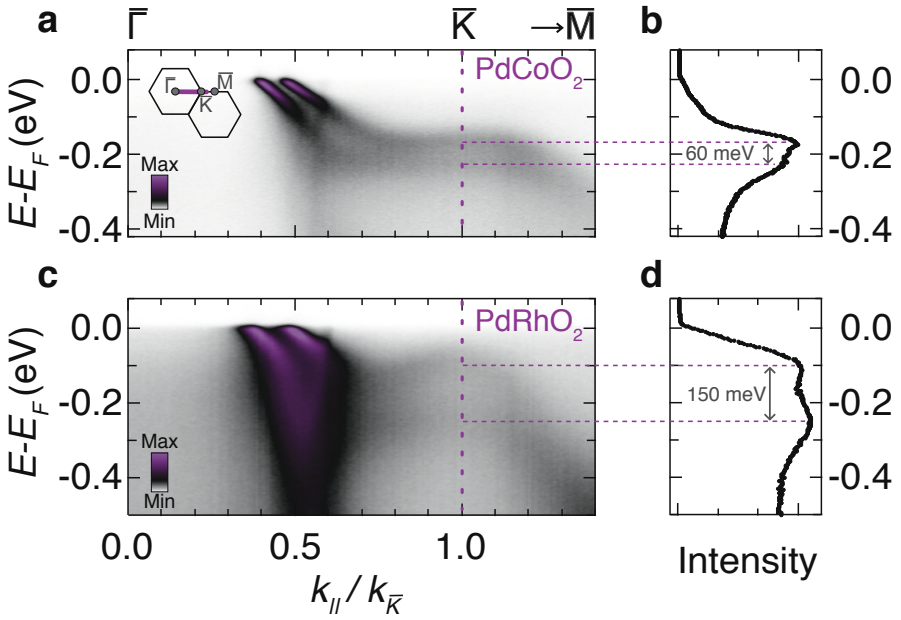

Figure 6.39.: Spin-split surface states of (**a**) $PdCoO_2$ and (**c**) $PdRhO_2$ measured along the $\overline{\Gamma}-\overline{K}$ direction. The inset in a shows the first two Brillouin zones, with the purple line indicating the direction along which the measurements were taken. $k_{\|}$ is the value of in-plane crystal momentum along this direction and $k_{\overline{K}}$ the momentum at the $\overline{K}$ point. Energy distribution curves (EDCs) for for $k/k_{\overline{K}} = 1 \pm 0.05$ are shown in (**b**) and (**d**) for $PdCoO_2$ and $PdRhO_2$, respectively.

		inner	outer
$\overline{\Gamma}-\overline{K}$	$k_F\left(\text{Å}^{-1}\right)$	0.49 ± 0.02	0.65 ± 0.02
	$v_F\left(\text{eVÅ}\right)$	0.64 ± 0.03	0.47 ± 0.03
	m/m_e	6 ± 1	11 ± 1
$\overline{\Gamma}-\overline{M}$	$k_F\left(\text{Å}^{-1}\right)$	0.48 ± 0.02	0.61 ± 0.02
	$v_F\left(\text{eVÅ}\right)$	0.70 ± 0.05	0.70 ± 0.05
	m/m_e	5 ± 1	7 ± 1

Table 6.5.: The Fermi momenta, velocities and effective masses of the two surface state bands in $PdRhO_2$. The uncertainties reflect the measurement and fitting precision.

6.8. Discussion

The above comparison of simple tight binding models, density functional theory calculations and experiments lead to the understanding of the large spin-splitting observed in delafossite oxides, but also to ideas that cast a new light on known materials, as well as suggesting routes for material design.

Maximising the inversion symmetry breaking energy scale is as important for large spin-splitting as is maximising the spin-orbit coupling. The critical new insight brought here is that the inversion symmetry breaking energy scale need not be a weak perturbation of a dominant symmetric kinetic Hamiltonian, such as is the often considered electric dipole term [110, 111]. Rather, the kinetic Hamiltonian itself can become asymmetric. The key for making this asymmetry a large fraction of the bandwidth is a structure which forces the hopping to be dominantly out-of-plane. Indeed, it is not directly the difference in on-site energies of the two oxygens that governs the relevant inversion symmetry breaking, but the fact that the Co electrons need to hop through them. To make this point completely transparent, in Figure 6.40 I compare the influence of surface on-site energy shifts on the edge-sharing transition metal oxide layer found in delafossites with that on its corner-sharing counterpart

found in ⟨001⟩ perovskites. In both cases the breaking of covalent bonds at the surface can lead to an on-site energy shift of the surface oxygen (O1) with respect to subsurface oxygens. However, the influence on the spin-splitting is very different. I use the same tight binding parameters for the two structures (as quoted in column II of Table 6.4), and in particular the same on-site energy shift, to calculate the band structure for a single transition metal oxide layer. It is clear that, despite the same on-site energy shift at the surface, there is negligible effect on the band structure of the corner-sharing layer. This is because the dominant hopping path between the transition metal ions is via the planar oxygens, and so the relevant electrons do not feel the surface symmetry breaking strongly. In contrast, the hopping between transition metal ions in delafossites is via either the surface or subsurface oxygen layers, and so the effect of a pure on-site energy shift of the surface layer is already sufficient to drive a large orbital angular momentum in the undistorted structure.

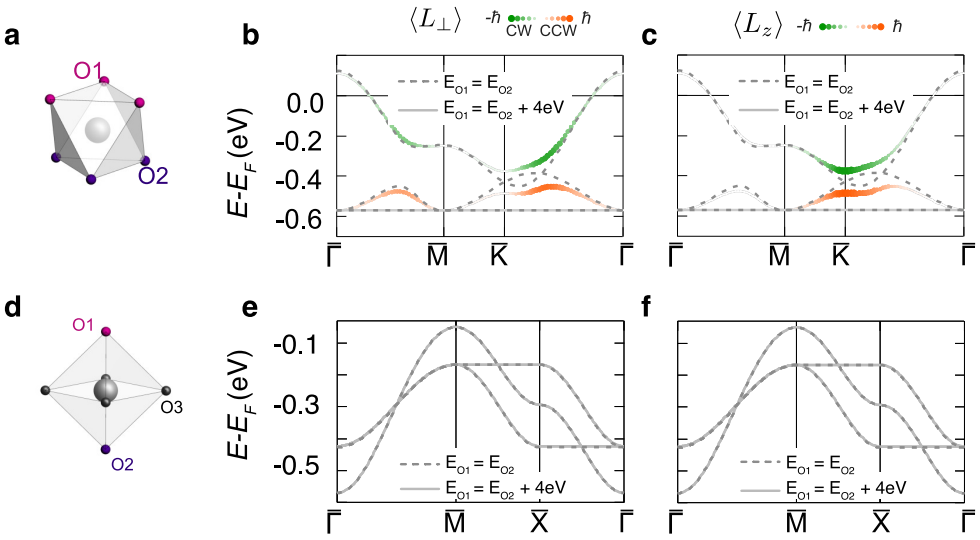

Figure 6.40.: A structural building block of (**a**) a delafossite and (**d**) a perovskite layer. The tight-binding band structure of the delafossite layer (**b**, **c**) and the perovskite layer (**e**, **f**), coloured according to the in-plane chiral (**b**, **e**) and the out-of-plane (**c**, **f**) orbital angular momentum.

6.8.1. Insights about known systems

Understanding the relevance of the two energy scales motivates revisiting the systems known to support spin-splitting, both to identify the limit they are in, and to understand the relevant mechanism of symmetry breaking. In what follows I discuss a few famous examples of spin-split systems. The list is by no means comprehensive, but it illustrates how may different materials can be understood within the same framework.

(001) surfaces and interfaces of perovskites

$SrTiO_3$ and $KTaO_3$ are both perovskite oxides whose bulk is insulating, but which can support two-dimensional electron gases (2 DEGs) at their (001) surfaces. The electronic structure of the 2 DEGs in the two materials is very similar, and consists of multiple subbands derived from the d orbitals of the transition metal (Ti, Ta), either of xy, or mixed yz and zx character [39, 112]. At the points where the bands of different orbital character cross, small hybridisation gaps open, and spin-splitting develops. In $SrTiO_3$ the orbital angular momentum points in the same direction on the two spin-split bands [39, 113], while in $KTaO_3$ it points in different directions [113], showing that $SrTiO_3$ and $KTaO_3$ are in the strong ISB and weak ISB limit, respectively. This is also confirmed by the relative size of the spin-splitting and the spin-orbit coupling in the two materials: in $SrTiO_3$ both the maximum spin-splitting and the spin-orbit coupling are calculated to be $\sim 20\,\mathrm{meV}$, while in $KTaO_3$ the calculated spin-splitting is $\sim 28\,\mathrm{meV}$, even though the atomic spin-orbit coupling of Ta is as large as $300\,\mathrm{meV}$ [113]. Very similar band structure is also found on the $LaAlO_3/SrTiO_3$ interface, with a splitting of $\sim 18\,\mathrm{meV}$ indicating this system is also in the strong inversion symmetry breaking limit, with the spin-splitting limited by the Ti spin-orbit coupling [114].

Some Bi-based systems

Many of the systems which exhibit the largest spin-splitting known contain bismuth, because the atomic spin-orbit coupling of Bi $6p$ orbitals is as large as $1500\,\mathrm{meV}$. The large spin-orbit coupling however means that those systems tend to be in the weak inversion symmetry breaking limit, and the spin-splitting is typically much weaker than the atomic-spin orbit coupling.

For example, in the so-called giant Rashba semiconductor BiTeI the largest energetic spin-splitting found in calculations is 400 meV, while the splitting at the Fermi level is ~ 300 meV, significantly smaller than the atomic spin-orbit coupling [90, 109, 115, 116]. The weak ISB limit is also confirmed by the direction of orbital angular momentum, which is locked opposite to spin [109, 117]. Although the splitting is limited by the inversion symmetry breaking energy scale, it is still large in absolute terms. In this case the symmetry breaking is not a surface effect, but rather reflects the lack of inversion symmetry of the crystal structure; specifically, Te and I layers are found on either side of a Bi layer. Therefore, microscopically the inversion symmetry breaking term could again be thought of as arising due to different hybridisation with layers above and below the one containing atoms with relevant spin-orbit coupling.

Even larger spin-splitting is found in Bi-containing surface alloys, in particular the Bi/Ag(111) surface alloy, where splitting as large as ~ 1 eV was observed [91, 118]. Again, splitting is smaller than the atomic spin-orbit coupling, and the direction of orbital angular momentum confirms the weak inversion symmetry breaking limit [119], but the absolute value is very large, indicating a large inversion symmetry breaking energy scale. This can be understood as a consequence of the structure of the surface alloy, in which the Bi atoms are displaced from the Ag plane. The inversion symmetry breaking is therefore again a consequence of asymmetric hopping paths between the atoms with strong spin orbit coupling [120]; here the asymmetry is made extreme, because to first order the hopping between bismuth atoms can proceed only through silver atoms, all of which are below bismuth.

Noble metal surfaces

A particularly interesting example of Rashba splitting is seen at the (111) surfaces of noble metals. The (111) surface of gold is a prototypical Rashba system [93], which motivated construction of the Petersen-Hedegård model to describe the spin-splitting [87]. Although this model was very insightful, first principles calculations later showed that it is actually a small contribution of $5d$ orbitals to the dominantly p-orbital state that is responsible for the splitting [121, 122]. The maximum energetic splitting observed and calculated at the (111) surfaces of gold is ~ 100 meV, while the atomic spin-orbit coupling of the $5d$ orbitals of gold is 608 meV. Nonetheless,

a circular dichroism measurement and a calculation of orbital angular momentum confirm that the system is in the strong inversion symmetry breaking limit [121, 123]. The size of the splitting is therefore limited by the spin-orbit coupling of the $5d$ orbitals, normalised by the $5d$ orbital content. This can be nicely seen by comparing the spin-splitting of the (111) surface of gold and copper [89]; the d orbital contribution to the surface states is similar in the two materials, so the ratio of the splitting sizes reflects the ratio of the atomic spin-orbit coupling of the relevant d orbitals. On the other hand, the d contribution to the surface state on the (111) surface of silver is negligible, and consequently so is the spin-splitting [121, 122].

6.8.2. Outlook

The largest influence the insights brought by the analysis of spin-splitting on delafossite oxides could have is to offer design principles for new materials. A promising material for achieving large spin splitting is one in which the hopping paths go out of plane, and are therefore significantly perturbed by creation of a surface. A spin-splitting on the order of the spin-orbit coupling energy scale can then be expected; if the absolute size of the atomic spin-orbit coupling is also large, so will be the spin-splitting. More generally, the analysis presented here points to the importance of energy scales associated with symmetry breaking. Although the breaking of symmetry is strictly speaking binary, i.e. a symmetry is either observed or it is not, the influence it can have on any physical system strongly depends on the energy scale associated with it. This is relevant in all cases where symmetry arguments are used to infer information on the allowed states, and possible properties of materials.

7. Conclusions and Outlook

In this thesis I show the results of our angle resolved photoemission measurements on delafossite metals, and the conclusions were able to draw from these experiments. We were initially motivated by the extraordinarily high conductivity of delafossites, and wanted to study their bulk electronic structure. In both $PtCoO_2$ and $PdCoO_2$ we observed fast bands crossing the Fermi level and forming hexagonal Fermi surfaces. However, the two most relevant novel physical insights arose from unexpected observations, as is often the case in science. We identified the Kondo-like coupling of itinerant and Mott-insulating layers as a cause of the signal observed in the antiferromagnetic delafossite metal $PdCrO_2$, and were able to show that this demonstrates that ARPES can be sensitive to spin-spin correlations. Furthermore, I show how the unusually large spin-splitting we observed on the transition-metal terminated surfaces of delafossites arises as a consequence of the structure of the transition metal oxide layers. These conclusions specific to the individual effects are discussed in detail at the ends of relevant chapters. Here I would like to mention a few general insights I have reached during the course of the research presented in the thesis.

Firstly, in every experiment it is important to understand how the measured signal arises, as well as to be aware of the limits of that understanding. While this may seem like a trivial statement, it is surprisingly easy to convince oneself that an observed effect is explicable in terms of known phenomena, and therefore miss something entirely new. This is especially true whenever we have an idea of what we are looking for, as we usually do, and therefore do not pay enough attention to other observed effects. Of course, I do not know how to avoid this in a general case. An approach I have taken in the two examples discussed in the thesis is to try to model the observed behaviour, starting from the assumed explanation, and simplifying the model as much as possible. If this approach captures the essential physics, the assumed explanation is probably correct. If it does not, the way in which it fails can be very informative, and motivate more complex models and theories. This also

emphasises the importance of discussion and collaboration between experimentalists and theorists, which contributed greatly to our understanding of the investigated effects.

Furthermore, understanding reached in the course of research of one specific phenomenon arising in one material can be general, and applicable to other systems. Every experimentally observed phenomenon is specific to the system under investigation; its generality often cannot be appreciated before the physics underlying the phenomenon is understood. Once it is, other systems in which the same physics plays a role may be recognised. To mention the two examples from the thesis, we wanted to understand why is the spin-splitting in delafossites so large and what causes the reconstructed signal in $PdCrO_2$. We now have the answers to both of these specific questions, but we also know what ingredients are necessary to design a system with a huge spin-splitting, and have an idea of how to probe magnetism in atomically-thin samples. It is too early to say if these insights will result in new independent experiments and material design, but it is possible that they will; if so, I would be delighted!

For me personally the most exciting prospect is not benefiting from these effects we were able to understand, but rather finding more such unexpected physics. Looking back at the Table 1.2 of the Introduction, it is clear that many delafossites have been synthesised to date. Some of them have been studied in detail due to their magnetic or semiconducting properties, but many have not. What is more, the surface states in the metallic delafossite oxides point to a rich variety of physical phenomena that can be found at polar surfaces. It is likely that many of the other delafossites host surface states, which to the best of my knowledge have not been studied to date. Each of these materials can be thought of as hosting three different electronic systems, leading to a staggering number of different electronic states that can be obtained through cleaving the delafossites listed in Table 1.2, and indicating a potentially fruitful field of future research.

A. The out-of-plane spectrum

Although the out-of-plane momentum, k_z, cannot be determined from the quantities directly measured in a photoemission experiment, some conclusions about the out-of-plane spectrum can be drawn from photon energy dependent measurements. To determine the measured k_z, however, an assumption has to be made about the final state of the photoexcited electrons. A commonly used model of the final state is the 'free electron model', in which the final state is approximated by a free-electron like parabola, with a material-dependent offset E_0:

$$E_f = \frac{1}{2m}\left(\vec{k} + \vec{G}\right)^2 - |E_0|\,, \tag{A.1}$$

where $|E_0| = V_0 - W$. V_0 is the so-called inner potential, which corresponds to the energy of the bottom of the valence band referenced to the vacuum level. It can be determined in comparison with calculations, but is usually estimated from the periodicity of the band features in experiments. Let us consider photoemission from an initial state of known in-plane momentum $k_\parallel$ into the free-electron like final state, as illustrated in Figure A.1 for two cases: if the binding energy of the initial state does not depend on the out-of-plane momentum k_z (blue line in Figure A.1a), and if it does (green line in Figure A.1b). The energy difference between the initial and the final state is equal to the photon energy used in the experiment, shown by pink and purple arrows in Figures A.1(a, b). As evident in the figures, the value of k_z that is probed in the experiment depends on the choice of the photon energy, and the k_z dispersion of the initial state. Crucially, if the initial state does not disperse along k_z, all photon energies probe the same *binding* energy. In contrast, if the initial state does disperse in the out-of-plane direction, the measured binding energy depends on the photon energy used. This qualitative statement does not depend on any assumptions about the final state, and can therefore be used to gain minimal information on the dimensionality of the electronic structure. However, to

infer the value of k_z from the measured quantities, and therefore the out-of-plane quasiparticle dispersion, an assumption about the final state needs to be made. In the free electron final state model employed here k_z is given by [33] :

$$\hbar k_z = \sqrt{2m\left(E_K \cos^2(\varphi) + V_0\right)}. \tag{A.2}$$

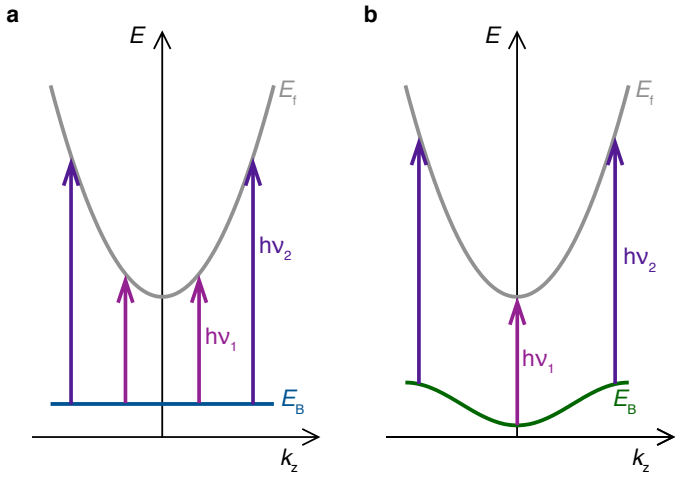

Figure A.1.: Schematic of determination of out-of-plane spectrum via photon energy dependent measurements, if the initial state exhibits (**a**) no k_z dispersion, and (**b**) some k_z dispersion.

As mentioned in the Section 2.1, ARPES is not an ideal probe of the out-of-plane dispersions for a number of reasons: an assumption about the final state needs to be made, the out-of-plane momentum is not conserved as the electron leaves the solid, and each measurement probes a range of out-of-plane momenta $\Delta k_z \sim 1/l_{mfp}$. All of these issues can be addressed by using high photon energies in the soft x-ray range: the free-electron like final state is a better approximation, the probing depth is larger (Figure 2.2), and so is the momentum, making the momentum loss at the surface less relevant. However, the use of higher photon energies reduces the in-plane momentum resolution, and the signal is typically weaker due to a smaller cross-section for x-ray photoemission.

B. Pd - terminated surface states

As discussed in the Introduction (Section 1.2.1), and shown in Section 2.6.5, both the Pd - terminated surface and the CoO_2 - terminated surface of $PdCoO_2$support surface states. The states arising on the CoO_2 - terminated surface are the topic of Chapter 6, while I briefly discuss the states on the Pd-terminated surface here.

The best-resolved Pd-surface states we observed are on patches of mixed termination, like the one shown in Figure 2.20e. In Figure B.1a I therefore show a high-resolution spectrum measured on one such surface. The bulk states, CoO_2-surface states (S-CoO_2) and the Pd-surface states (S-Pd) are all marked in Figure B.1a; in the following I discuss only the latter. There are two electron-like pockets around the $\overline{\Gamma}$ point. Additionally, a band dispersing parallel to the bulk band, and a flat band in the vicinity of the $\overline{K}$ point are all observed. If the total charge contained in these surface bands is calculated assuming spin - degeneracy, an unphysically high surface carrier density is found. In contrast, if we treat them as spin-polarised a surface charge density of 0.55 ± 0.03 electrons/unit cell is obtained, in good agreement with the additional 0.5 electrons per unit cell that would be expected from the polar surface charge. Our measurements therefore strongly suggest that the surface bands are spin-polarised, as was already proposed by Kim at al. [9] based on their DFT calculations. This interpretation is reinforced by the comparison of the measurements with our DFT band structures coloured according to the spin: in Figure B.1b the blue and red colour correspond to the spin majority and minority character projected onto the surface layer. Two pairs of exchange-split bands are seen in the calculation, labelled α and β , and γ and δ, for the two pairs. Both pairs can be identified in the experiment: the α and β bands are the flat band in the vicinity of the $\overline{K}$ - point and the band dispersing parallel to the bulk band, respectively. The γ and δ bands are the two electron-like bands seen at the zone centre in the measurements. The calculation also predicts a hole-like band crossing the Fermi level at the $\overline{M}$ - point. Experimentally, this band is found to be fully

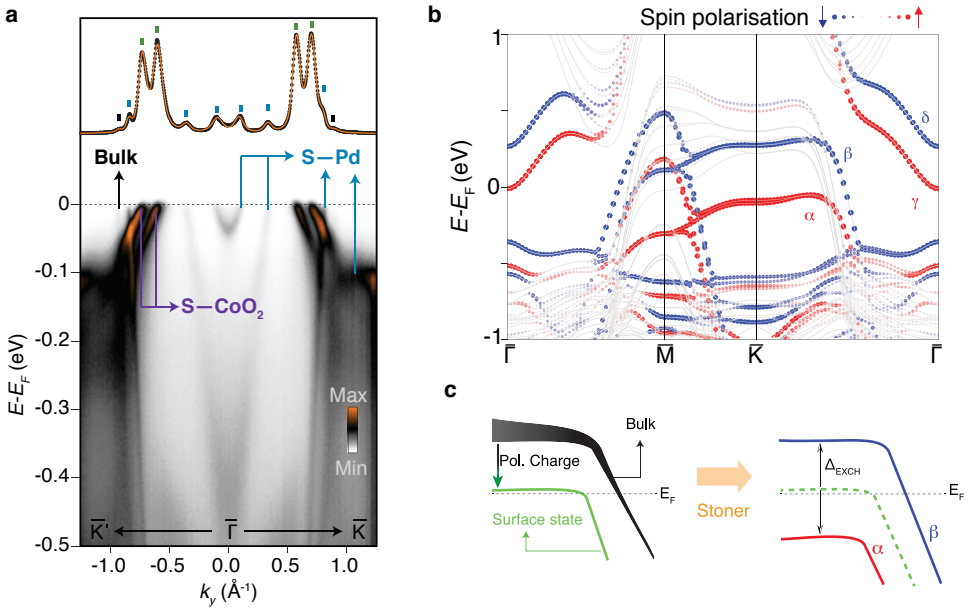

Figure B.1.: (**a**) The measured electronic structure, showing contributions from both surface terminations. (**b**) The calculated electronic structure of a Pd - terminated surface, coloured according to the spin polarisation of the top Pd layer. (**c**) Schematic showing how does the surface ferromagnetism arise. The calculations were done by Helge Rosner. Figure panels courtesy of Federico Mazzola.

occupied (Figure 2c of Ref. [10], not shown here). While it is possible to relate the bands predicted by the calculations to the experimental ones, it is interesting to note that their relative positions and occupations are not correctly captured by the calculation. This is often the case when the electronic structure of polar surfaces is calculated, and will be discussed in more detail in the context of the CoO_2- surface states in Section 6.2.

The origin of the surface ferromagnetism can be deduced by inspecting the influence of the polar charge on the bulk band structure. The bulk band crossing the Fermi level is steep at the Fermi level, but becomes flat above it, as shown schematically in Figure B.1c, and also evident in the DFT band structure in Figure 1.9c. The effective electron-doping at the Pd-surface discussed in the Introduction (Section 1.2.1) leads to a surface copy of the bulk band at a lower binding energy, shown in green on the schematic in Figure B.1c. The flat band is pushed sufficiently close to the Fermi level to trigger a Stoner transition, therefore exchange-splitting

into a pair of spin-polarised α and β bands, as observed in both our experiment and the calculations. The γ and δ bands, as well as the hole-like bands at $\overline{M}$, inherit a similar exchange splitting.

Consistent with the findings of Sobota et al., we have also observed surface states on $PdCrO_2$. In a comparative analysis we have shown that they are quantitatively, as well as qualitatively, similar to those in $PdCoO_2$, allowing us to identify the exchange-split pairs of bands in $PdCrO_2$. This is particularly exciting, as it means that the $PdCrO_2$, which is antiferromagnetic in the bulk, can host surface ferromagnetism.

C. Fermi velocity determination

As discussed in Section 2.5 in the context of the simulated spectral functions, it is important to carefully choose the fitting range when determining the Fermi velocity. Here I show how this was done for the bulk states in $PtCoO_2$ and $PdCoO_2$, as well as for surface states on the CoO_2 terminated surfaces of $PtCoO_2$.

C.1. Bulk states

The first step needed to determine the Fermi velocity is to extract the momenta as a function of binding energy by fitting Lorentzian peaks to momentum distribution curves. In Figure C.1a I show the absolute value of the momenta extracted from the data shown in Figure 4.5(a, b) for $PtCoO_2$ and $PdCoO_2$, respectively. The squares and circles represent the data extracted from the $k < 0$ and $k > 0$ sides of the dispersion, respectively. In an ideal measurement the absolute value of momentum would be the same for both sides of the dispersion at all binding energies. Indeed, the agreement is good in the data shown in Figure C.1a, but there are small observable deviations, offering a natural way to estimate the size of the systematic errors in the experiment.

In order to determine the Fermi velocity a linear fit needs to be performed in the vicinity of the Fermi level. In Figure C.1b I show the Fermi velocity obtained from such a fit for a variable fitting range; the fit is always performed between the Fermi level and the binding energy indicated on the x - axis. A few features are prominent. First of all, it is clear that the Fermi velocity in $PtCoO_2$ is larger than that in $PdCoO_2$, and that this statement does not depend at all on the fitting range chosen. However, the value of the extracted velocities does depend on the fitting range. If the range is smaller than $\sim 100\,\mathrm{meV}$, the extracted velocity depends strongly and non-monotonically on the fitting range both for $PtCoO_2$ and $PdCoO_2$. The fits are overly sensitive to the experimental noise, and therefore not reliable. Even when

the noise is not a limiting factor, the fits from the two sides of the dispersions do not coincide, reflecting systematic measurement errors, possibly due to small sample misalignment. A choice then needs to be made about the most appropriate fitting range, and the error bars associated with the extracted Fermi velocity need to be large enough to encompass the values that would be obtained by fitting to either positive or negative momenta. Ideally the smallest range in which the fit is stable should be chosen. In the cases shown here I averaged the Fermi velocity that would be obtained by fitting ranges between $-0.25\,\mathrm{meV}$ and $-0.15\,\mathrm{meV}$ (indicated by the length of horizontal lines in Figure C.1b), leading to Fermi velocity estimates of $5.6 \pm 0.3\,\mathrm{eV\AA}$ and $4.2 \pm 0.2\,\mathrm{eV\AA}$, for $PtCoO_2$ and $PdCoO_2$ respectively. The mean values and errors are marked by full and dashed lines in Figure C.1b, respectively. In Figure C.1c I show the data between 250 meV and the Fermi level together with linearised dispersions assuming the extracted Fermi velocities, showing that the fits are indeed good.

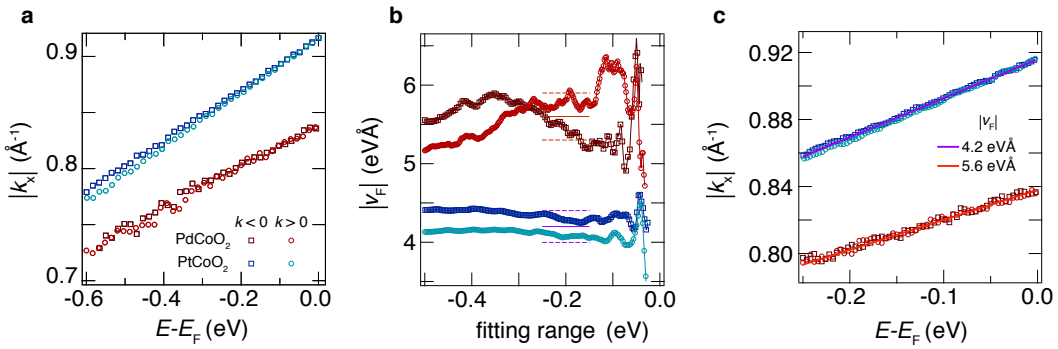

Figure C.1.: (**a**) Absolute value of momentum as a function of binding energy, extracted from the data shown in Figure 4.5(a, b) for $PtCoO_2$ and $PdCoO_2$, respectively. (**b**) The fitted Fermi velocity as a function of the fitting range. The symbols have the same meaning as in (a). The length of the horizontal lines indicates the range used to determine the Fermi velocity. The full and dashed lines indicate the mean value of the velocities, and the errors associated with them, respectively. (**c**) The absolute value of momentum as a function of binding energy, together with the linearised bands assuming the extracted Fermi velocities indicated in (b).

C.2. Surface states

Determining the Fermi velocity of the surface state bands, discussed in Chapter 6, is additionally complicated by their slight curving away from the linear dispersion in the immediate vicinity ($\sim 10\,\mathrm{meV}$) of the Fermi level. As discussed in Section 6.1.1, this apparent change of slope is likely not intrinsic to the surface electronic structure, but an artefact both of Coloumb interactions between the outgoing electrons, known as the space charge effect [55], and the finite measurement resolution. This change of slope is also visible in Figure C.2a, in which I show the absolute value of momentum as a function of binding energy of both the inner and outer band, extracted from the data shown in Figure 6.1b, for a measurement along the $\overline{\Gamma}-\overline{K}$ direction in $PtCoO_2$.

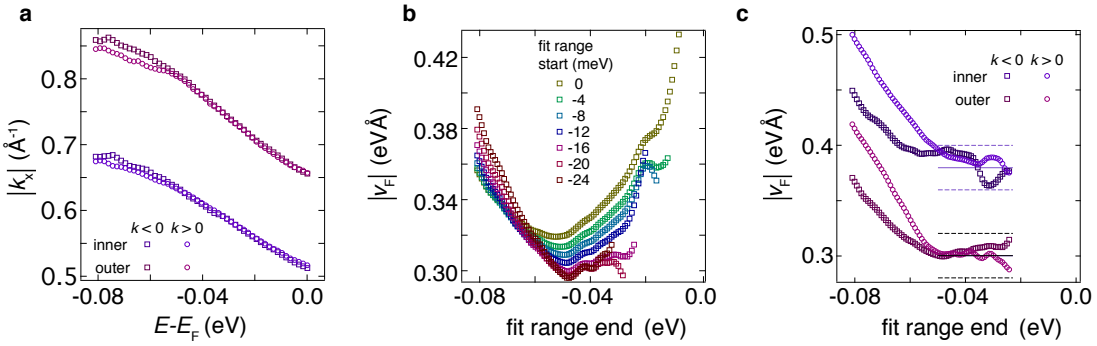

Figure C.2.: (**a**) Absolute value of momentum as a function of binding energy, extracted from the data shown in Figure 6.1b, taken along the $\overline{\Gamma}-\overline{K}$ direction in $PtCoO_2$. (**b**) The extracted Fermi velocity of the outer band for $k<0$, fitted from the data shown in (a), as a function of the last point of the fitting range, for a range of first points of the fitting range. (**c**) The extracted Fermi velocity of the four bands shown in (a), for fits performed between $-16\,\mathrm{meV}$ and the fitting range indicated on the x axis. The length of the horizontal lines indicates the range used to determine the Fermi velocity. The full and dashed lines indicate the mean value of the velocities, and the errors associated with them, respectively.

The extracted Fermi velocity therefore depends both on the first and the last point in the fitting range. To see this explicitly, in Figure C.2b I plot the extracted Fermi velocity as a function of the last point included in the fit, for various choices of the first point. Clearly the fit depends quite strongly on the first point, if the first point is closer to the Fermi level than $\sim 16\,\mathrm{meV}$. Therefore, to determine the Fermi

velocity I performed the linear fits between $-16\,\mathrm{meV}$ and a variable end point, for the inner and outer band for both positive and negative momenta (Figure 6.1c). The fits performed for both signs of momentum are in good agreement, and the difference in velocity between the two directions is larger than any errors associated with the fits. The Fermi velocities are found to be $0.38 \pm 0.02\,\mathrm{eV\AA}$ and $0.30 \pm 0.02\,\mathrm{eV\AA}$ for the inner and outer band, respectively. The final values quoted in Table 6.1 are obtained by averaging the results of such fits performed on multiple measurements on three different samples, the data from which are shown in Figure D.2. Equivalent fits were performed for the data extracted from measurements on $PdCoO_2$ (Figure D.3), leading to the extracted values listed in Table D.1.

D. Additional data on the Rashba-like surface states

In this Appendix I show the data from $PdCoO_2$ from measurements similar to those on $PtCoO_2$ which are presented in Chapter 6. I did not put them in the main body of the thesis to avoid repetition. The relevant values extracted from the $PdCoO_2$ data are shown in Tables D.1 and D.2.

D.1. Dispersions in $PdCoO_2$ and $PtCoO_2$

In this section I show the results of the fits to the dispersions measured in $PdCoO_2$, similar to the ones shown in Figure 6.2 for $PtCoO_2$ (Figure 6.2), as well as the parameter values extracted from them (Table D.1). The data from the two compounds are qualitatively very similar, while small quantitative differences are summarised in Section D.3. I also show dispersions from all the samples which were analysed to obtain the averaged values of Fermi velocities and momenta for both compounds (Figures D.2 and D.3).

		inner	outer
$\overline{\Gamma} - \overline{K}$	$k_F \left(\text{Å}^{-1}\right)$	0.55 ± 0.02	0.67 ± 0.02
	$v_F \left(\text{eVÅ}\right)$	0.46 ± 0.02	0.32 ± 0.02
	m/m_e	9.0 ± 0.4	15.8 ± 0.7
$\overline{\Gamma} - \overline{M}$	$k_F \left(\text{Å}^{-1}\right)$	0.54 ± 0.02	0.63 ± 0.02
	$v_F \left(\text{eVÅ}\right)$	0.52 ± 0.03	0.48 ± 0.03
	m/m_e	7.9 ± 0.5	10.1 ± 0.8

Table D.1.: The Fermi momenta, velocities and effective masses of the two surface state bands in $PdCoO_2$, averaged over three samples. The uncertainties reflect both the measurement and fitting precision, as well as sample-to-sample variation.

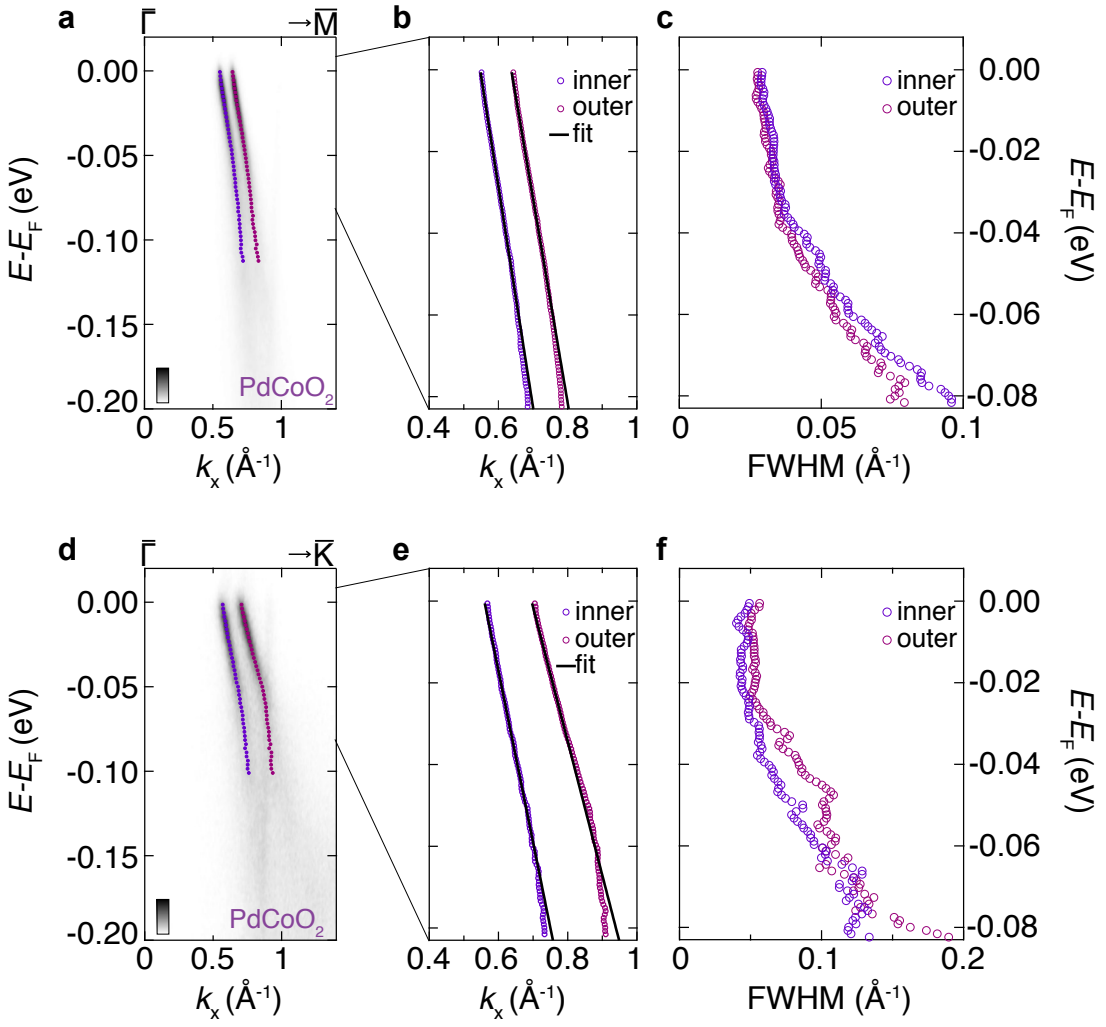

Figure D.1.: (**a**, **d**) Dispersion measured along the $\overline{\Gamma} - \overline{K}$ and the $\overline{\Gamma} - \overline{M}$ directions in $PdCoO_2$ (110 eV, *p*-polarised light), respectively. The dots in (**a**, **b**, **d**, **e**) are the peak positions of Lorentzian fits to extracted MDCs. The lines in (**b**, **e**) are linearised bands, defined by fitted band slopes and Fermi momenta of the relevant dispersion. (**c**, **f**) The full width at half maximum of Lorentzian fits to the MDCs as a function of binding energy.

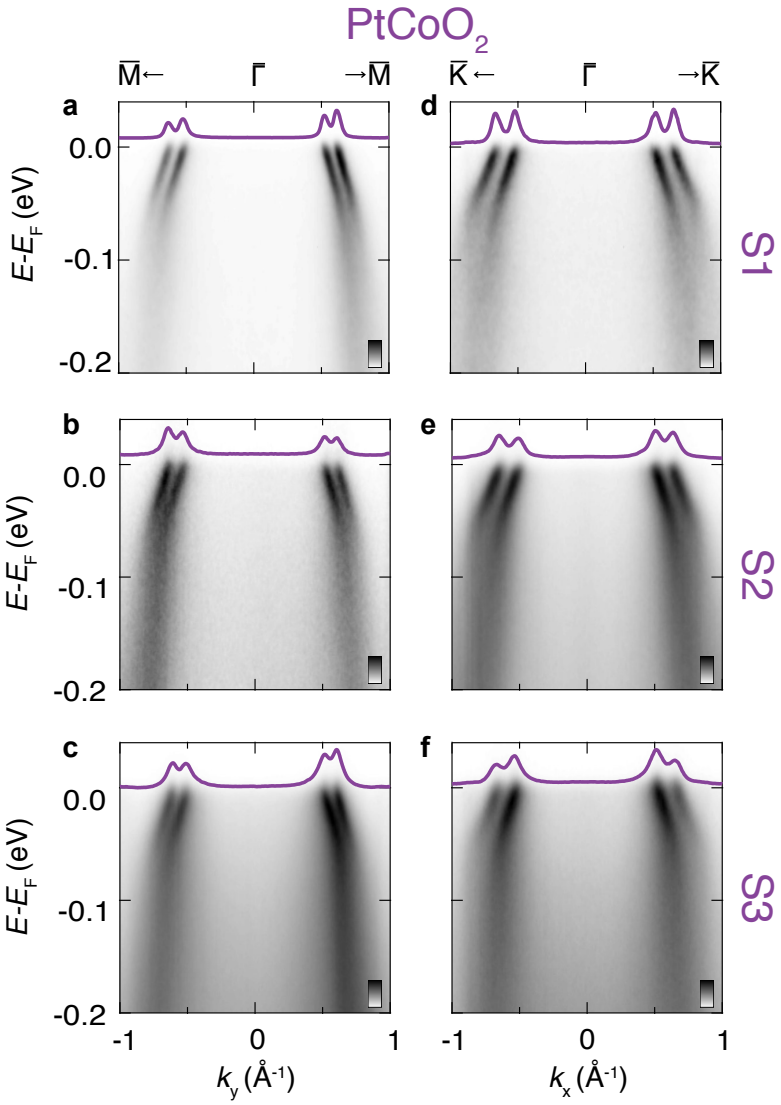

Figure D.2.: Dispersion measured along (**a**-**c**) the $\overline{\Gamma}-\overline{M}$ and (**d**-**f**) the $\overline{\Gamma}-\overline{K}$ direction in $PtCoO_2$ measured on three different samples, as indicated in the plot. The lines are the MDCs, averaged over $E_F \pm 5\,\mathrm{meV}$.

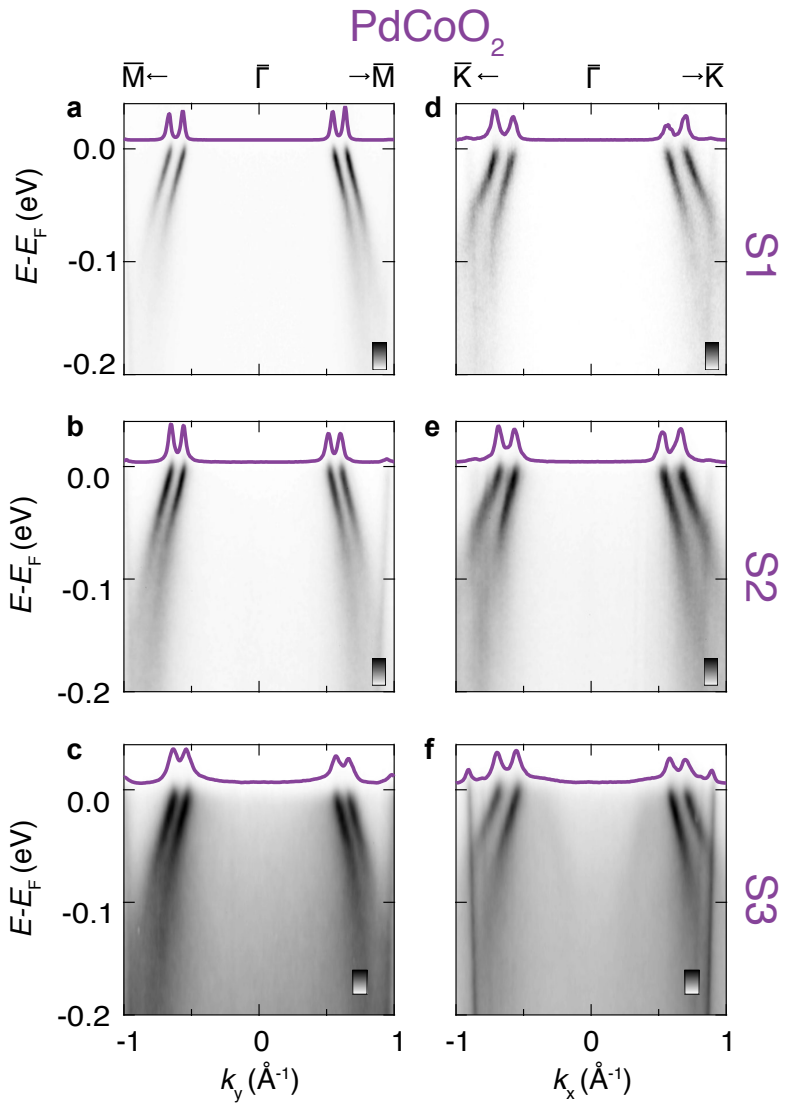

Figure D.3.: Dispersion measured along (**a**-**c**) the $\overline{\Gamma}-\overline{M}$ and (**d**-**f**) the $\overline{\Gamma}-\overline{K}$ direction in $PdCoO_2$ measured on three different samples, as indicated in the plot. The lines are the MDCs, averaged over $E_F \pm 5\,\mathrm{meV}$.

D.2. Fermi surface of $PdCoO_2$

In this section I show the fits to the surface state Fermi surfaces of $PdCoO_2$, similar to the ones shown for $PtCoO_2$ in Figure 6.3. The Fermi surface was fitted to a periodic function of the form:

$$k_F(\varphi) = k_0 + k_{6,0}\cos(6\varphi) + k_{12,0}\cos(12\varphi)\,. \tag{D.1}$$

The fit parameters are listed in Table D.2.

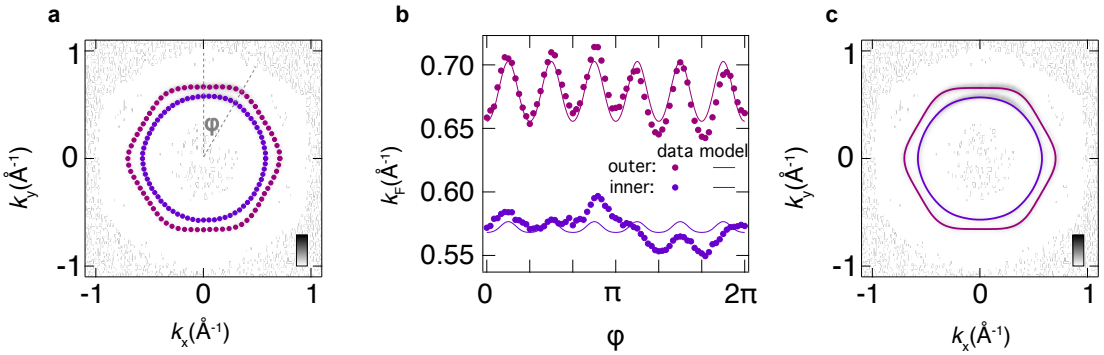

Figure D.4.: **(a)** Measured Fermi surface of $PdCoO_2$, with dots representing the Fermi momenta extracted by radially fitting MDCs. **(b)** Extracted momenta (dots) as a function of angle φ around the Fermi surface, with a sinusoidal fit (lines) describing the Fermi surface shape (Equation D.1). **(c)** The same fit as in **b** (lines), superimposed on measured data to demonstrate good agreement.

	inner	outer
k_0	0.5717 ± 0.0005	0.6777 ± 0.0005
$k_{6,0}$	-0.004 ± 0.001	-0.024 ± 0.001
$k_{12,0}$	0.000 ± 0.0008	0.0014 ± 0.0009

Table D.2.: Parameters of fits of a periodic function (Equation D.1) to the inner and outer surface state Fermi surfaces of $PdCoO_2$. An example of such a fit is shown in D.4(b, c).

D.3. Compound comparison

	$PtCoO_2$	$PdCoO_2$	$PdRhO_2$
$m_1/\ m_e$ [Γ-M]	9.6 ± 0.5	7.9 ± 0.5	5 ± 1
$m_2/\ m_e$ [Γ-M]	11.5 ± 0.8	10.1 ± 0.8	7 ± 1
$m_1/\ m_e$ [Γ-K]	9.5 ± 0.5	9.0 ± 0.4	6 ± 1
$m_2/\ m_e$ [Γ-K]	15 ± 1	15.7 ± 0.7	11 ± 1
$\Delta k_F/$ Å^{-1} [Γ-M]	0.11 ± 0.01	0.09 ± 0.01	0.13 ± 0.01
$\Delta k_F/$ Å^{-1} [Γ-K]	0.13 ± 0.01	0.12 ± 0.01	0.16 ± 0.01
$\Delta E/$ meV [K]	60	60	150

Table D.3.: Quasiparticle masses, m_i, of the inner ($i = 1$) and outer ($i = 2$) surface bands, and spin splitting at the Fermi level, Δk_F, along the high symmetry directions. These are very similar for $PtCoO_2$ and $PdCoO_2$. Despite the lower masses for $PdRhO_2$, Δk_F is larger, a consequence of the larger energetic splitting ΔE.

E. Basis transformations

In Chapter 6 I construct multiple tight-binding models using the Slater-Koster method (Section 3.1), with both p and d orbitals as bases. While the kinetic part of the Hamiltonian is the easiest to calculate in the cubic basis, the orbital angular momentum and spin-orbit coupling Hamiltonians are usually expressed in the spherical basis. What is more, the crystal field Hamiltonian necessary to account for the crystal field on the Co site in the delafossite structure is diagonal in the trigonal basis. It is therefore necessary to transform the operators between different bases. This is straightforward to do, if the transformation of the basis vectors is known: if the transformation which transforms the basis vectors of the basis x into the basis vectors of the basis y is labelled $B_{x\to y}$, the coordinate transformation between the two bases is given by $T_{x\to y} = \left(B^{-1}_{x\to y}\right)^T$. The representations of an operator O in the two bases are related by $O_y = T_{x\to y} O_x T^{-1}_{x\to y}$. In this Appendix I will explicitly list the basis transformations I used in the tight binding models, labelling the spherical, cubic and trigonal bases with letters s, c and t, respectively.

E.1. p - orbitals

The basis transformation between the cubic $\{p_y, p_z, p_x\}$ and the spherical $\{p_{-1}, p_0, p_1\}$ basis of p orbitals with z as a quantisation axis is given by:

$$B_{s\to c} = \begin{pmatrix} \frac{\imath}{\sqrt{2}} & 0 & \frac{\imath}{\sqrt{2}} \\ 0 & 1 & 0 \\ \frac{1}{\sqrt{2}} & 0 & -\frac{1}{\sqrt{2}} \end{pmatrix}$$

E.2. d - orbitals

The basis transformation between the cubic $\{d_{xy}, d_{yz}, d_{3z^2-r^2}, d_{xz}, d_{x^2-y^2}\}$ and the spherical $\{d_{-2}, d_{-1}, d_0, d_1, d_2\}$ basis of d orbitals with z as a quantisation axis is given by:

$$B_{s\to c} = \begin{pmatrix} \frac{\imath}{\sqrt{2}} & 0 & 0 & 0 & -\frac{\imath}{\sqrt{2}} \\ 0 & \frac{\imath}{\sqrt{2}} & 0 & \frac{\imath}{\sqrt{2}} & 0 \\ 0 & 0 & 1 & 0 & 0 \\ 0 & \frac{1}{\sqrt{2}} & 0 & -\frac{1}{\sqrt{2}} & 0 \\ \frac{1}{\sqrt{2}} & 0 & 0 & 0 & \frac{1}{\sqrt{2}} \end{pmatrix}. \tag{E.1}$$

The basis transformation between the trigonal $\{u^+, u^-, x^0, x^1, x^2\}$ and the spherical $\{d_{-2}, d_{-1}, d_0, d_1, d_2\}$ basis of d orbitals with z as a quantisation axis is given by:

$$B_{s\to t} = \begin{pmatrix} \frac{1}{\sqrt{3}} & 0 & 0 & -\sqrt{\frac{2}{3}} & 0 \\ 0 & \sqrt{\frac{2}{3}} & 0 & 0 & \frac{1}{\sqrt{3}} \\ 0 & 0 & 1 & 0 & 0 \\ 0 & -\frac{1}{\sqrt{3}} & 0 & 0 & \sqrt{\frac{2}{3}} \\ \sqrt{\frac{2}{3}} & 0 & 0 & \frac{1}{\sqrt{3}} & 0 \end{pmatrix}. \tag{E.2}$$

F. Co-O hybridisation

The inversion symmetry breaking Hamiltonian by definition introduces an energy difference between wave functions of different symmetry: the wavefunctions whose weights are dominantly above or below a certain plane will have a different energy. Which one of them has a lower energy depends on the type of inversion symmetry breaking. In the specific case of inversion symmetry breaking caused by the difference in on-site energy of surface and sub-surface oxygen, relevant for delafossites, this can be deduced by considering the hybridisation between Co and O orbitals, which I show schematically in Figure F.1 for states at the $\overline{K}$ point, chosen for the simplicity of the band structure at that momentum. In the symmetric environment the two degenerate oxygen states, derived from the p_z orbitals of the two oxygens, hybridise with the three degenerate t_{2g} orbitals of a Co ion. At the $\overline{K}$ point the a_{1g} state is not affected by this hybridisation, as evident from the fact it is not dispersive and its energy is not changed from its initial on-site value of $-0.57\,\mathrm{eV}$ (green line at the $\overline{K}$ point in Figure 6.28a); in Figure F.1 I therefore show only the e_g^π states. Once hybridisation is allowed, the energy of the dominantly oxygen states is decreased, and that of dominantly Co states increased, by t_{pd}^2/Δ , where t_{pd} is the off-diagonal matrix element connecting the p and $d$orbitals, and Δ their unperturbed energy difference (Figure F.1a). The value of effective t_{pd}^2/Δ at this point can be directly extracted as the difference in energy between the $m = 0$ state and the e_g^π states in Figure 6.28a, and is found to be equal to 140 meV. The admixture of the oxygen in the dominantly Co states, and vice versa, is given by $(t_{pd}/\Delta)^2 \sim 4\%$. A similar scenario takes place when the on-site energies of the two oxygens are made different, however now the d orbital wave function whose weight is above the Co plane, labeled $|up\rangle$ hybridises with O1, and the one whose weight is below ($|down\rangle$) hybridise with O2 (Figure F.1b). As the on-site energy difference between O1 and Co (Δ_1) is smaller than that between O2 and Co (Δ_2), the hybridisation of the $|up\rangle$ state with O1 is stronger than that of the $|down\rangle$ state with O2; consequently its

energy is increased *more* from the unperturbed value than that of the dominantly $|down\rangle$ state. The wave function weight of the higher energy state, corresponding to the band crossing the Fermi level in this model, is therefore pushed towards the top oxygen. It also has a higher oxygen content, 7% at the $\overline{K}$ point for the parameters used here, to be compared with 1% for the $|down\rangle$ state.

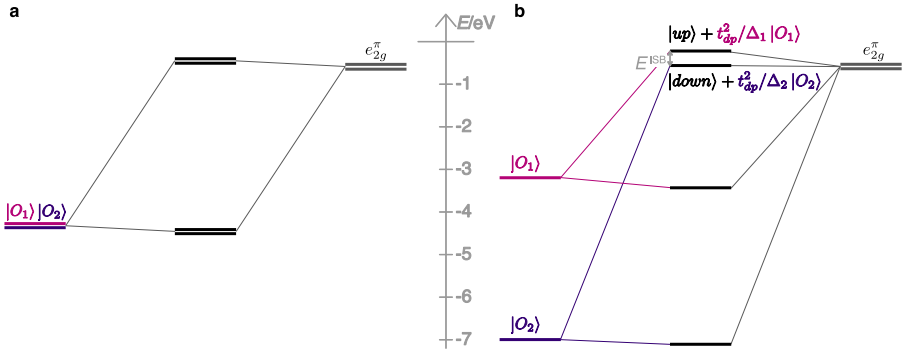

Figure F.1.: A schematic representation of the hybridisation between the p orbitals of two oxygens with the ${e_{2g}}^{\pi}$ orbitals of Co at the $\overline{K}$ point, if (**a**) the two oxygens are equivalent and (**b**) the on-site energies of the two oxygens are different. The energies of all the states correspond to the ones in the simple tight-binding model (Table 6.4).

Bibliography

[1] R. D. Shannon, D. B. Rogers, and C. T. Prewitt. Chemistry of noble metal oxides. I. Syntheses and properties of ABO_2 delafossite compounds. *Inorganic Chemistry*, **10**(4):713–718, (1971).

[2] R. D. Shannon, C. T. Prewitt, and D. B. Rogers. Chemistry of noble metal oxides. II. Crystal structures of platinum cobalt dioxide, palladium cobalt dioxide, coppper iron dioxide, and silver iron dioxide. *Inorganic Chemistry*, **10**(4):719–723, (1971).

[3] R. D. Shannon, D. B. Rogers, C. T. Prewitt, and J. L. Gillson. Chemistry of noble metal oxides. III. Electrical transport properties and crystal chemistry of ABO_2 compounds with the delafossite structure. *Inorganic Chemistry*, **10**(4):723–727, (1971).

[4] A. P. Mackenzie. The properties of ultrapure delafossite metals. *Reports on Progress in Physics*, **80**(3):032501, (2017).

[5] P. Kushwaha, V. Sunko, P. J. W. Moll, L. Bawden, J. M. Riley, N. Nandi, H. Rosner, M. P. Schmidt, F. Arnold, E. Hassinger, T. K. Kim, M. Hoesch, A. P. Mackenzie, and P. D. C. King. Nearly free electrons in a $5d$ delafossite oxide metal. *Science Advances*, **1**(9):e1500692, (2015).

[6] H. Usui, M. Ochi, S. Kitamura, T. Oka, D. Ogura, H. Rosner, M. W. Haverkort, V. Sunko, P. D. C. King, A. P. Mackenzie, and K. Kuroki. Hidden kagome-lattice picture and origin of high conductivity in delafossite $PtCoO_2$. *Physical Review Materials*, **3**(4):045002, (2019).

[7] H.-J. Noh, J. Jeong, B. Chang, D. Jeong, H. S. Moon, E.-J. Cho, J. M. Ok, J. S. Kim, K. Kim, B. I. Min, H.-K. Lee, J.-Y. Kim, B.-G. Park, H.-D. Kim, and S. Lee. Direct observation of localized spin antiferromagnetic transition

in $PdCrO_2$ by angle-resolved photoemission spectroscopy. *Scientific reports*, **4**:3680–3680, (2014).

[8] V. Sunko, F. Mazzola, S. Kitamura, S. Khim, P. Kushwaha, O. J. Clark, M. Watson, I. Marković, D. Biswas, L. Pourovskii, T. K. Kim, T.-L. Lee, P. K. Thakur, H. Rosner, A. Georges, R. Moessner, T. Oka, A. P. Mackenzie, and P. D. C. King. Probing spin correlations using angle resolved photoemission in a coupled metallic/Mott insulator system. *arXiv:1809.08972*, (2018).

[9] K. Kim, H. C. Choi, and B. I. Min. Fermi surface and surface electronic structure of delafossite $PdCoO_2$. *Physical Review B - Condensed Matter and Materials Physics*, **80**(June):1–4, (2009).

[10] F. Mazzola, V. Sunko, S. Khim, H. Rosner, P. Kushwaha, O. J. Clark, L. Bawden, I. Marković, Timur K. Kim, M. Hoesch, A. P. Mackenzie, and P. D. C. King. Itinerant ferromagnetism of the Pd-terminated polar surface of $PdCoO_2$. *Proceedings of the National Academy of Sciences*, **115**(51):12956–12960, (2018).

[11] V. Sunko, H. Rosner, P. Kushwaha, S. Khim, F. Mazzola, L. Bawden, O. J. Clark, J. M. Riley, D. Kasinathan, M. W. Haverkort, T. K. Kim, M. Hoesch, J. Fujii, I. Vobornik, A. P. Mackenzie, and P. D. C. King. Maximal Rashba-like spin splitting via kinetic-energy-coupled inversion-symmetry breaking. *Nature*, **549**(7673):492–496, (2017).

[12] H.-J. Noh, J. Jeong, J. Jeong, E.-J. Cho, S. Kim, K. Kim, B. Min, and H.-D. Kim. Anisotropic Electric Conductivity of Delafossite $PdCoO_2$ Studied by Angle-Resolved Photoemission Spectroscopy. *Physical Review Letters*, **102**(25):256404, (2009).

[13] G. Bergerhoff and I. D. Brown. *Crystallographic Databases*. International Union of Crystallography, Chester, (1987).

[14] N. Nandi, T. Scaffidi, P. Kushwaha, S. Khim, M. E. Barber, V. Sunko, F. Mazzola, P. D. C. King, H. Rosner, P. J. W. Moll, M. König, J. E. Moore, S. Hartnoll, and A. P. Mackenzie. Unconventional magneto-transport in ultrapure $PdCoO_2$ and $PtCoO_2$. *npj Quantum Materials*, **3**(1):66, (2018).

[15] P. J. W. Moll, P. Kushwaha, N. Nandi, B. Schmidt, and A. P. Mackenzie. Evidence for hydrodynamic electron flow in $PdCoO_2$. *Science*, **351**(6277):1061–1064, (2016).

[16] M. D. Bachmann, A. L. Sharpe, A. W. Barnard, C. Putzke, M. König, S. Khim, D. Goldhaber-Gordon, A. P. Mackenzie, and P. J. W. Moll. Supergeometric electron focusing on the hexagonal Fermi surface of $PdCoO_2$. *arXiv:1902.03769*, (2019).

[17] C. W. Hicks, A. S. Gibbs, A. P. Mackenzie, H. Takatsu, Y. Maeno, and E. A. Yelland. Quantum oscillations and high carrier mobility in the delafossite $PdCoO_2$. *Physical Review Letters*, **109**(0):116401, (2012).

[18] P. Kushwaha, H. Borrmann, S. Khim, H. Rosner, P. J. W. Moll, D. A. Sokolov, V. Sunko, Yu. Grin, and A. P. Mackenzie. Single Crystal Growth, Structure, and Electronic Properties of Metallic Delafossite $PdRhO_2$. *Crystal Growth & Design*, **17**(8):4144–4150, (2017).

[19] F. Arnold, M. Naumann, S. Khim, H. Rosner, V. Sunko, F. Mazzola, P. D. C. King, A. P. Mackenzie, and E. Hassinger. Quasi-two-dimensional Fermi surface topography of the delafossite $PdRhO_2$. *Physical Review B*, **96**(7):075163, (2017).

[20] D. Billington, D. Ernsting, T. E. Millichamp, C. Lester, S. B. Dugdale, D. Kersh, J. A. Duffy, S. R. Giblin, J. W. Taylor, P. Manuel, D. D. Khalyavin, and H. Takatsu. Magnetic frustration, short-range correlations and the role of the paramagnetic Fermi surface of $PdCrO_2$. *Scientific Reports*, **5**:12428, (2015).

[21] J.-P. Doumerc, A. Wichainchai, A. Ammar, M. Pouchard, and P. Hagenmuller. On magnetic properties of some oxides with delafossite-type structure. *Materials Research Bulletin*, **21**(6):745–752, (1986).

[22] H. Takatsu, H. Yoshizawa, and Y. Maeno. Comparative study of conductive delafossites with and without frustrated spins on a triangular lattice, $PdMO_2$ (M = Cr ; Co). *Journal of Physics: Conference Series*, **145**(1):012046, (2009).

[23] H. Takatsu, H. Yoshizawa, S. Yonezawa, and Y. Maeno. Critical behavior of the metallic triangular-lattice Heisenberg antiferromagnet $PdCrO_2$. *Physical Review B*, **79**(10):104424, (2009).

[24] M. Mekata, T. Sugino, A. Oohara, Y. Oohara, and H. Yoshizawa. Magnetic-Structure of Antiferromagnetic $PdCrO_2$ Possible Degenerate Helices on a Rhombohedral Lattice. *Physica B*, **213**:221–223, (1995).

[25] H. Takatsu, G. Nénert, H. Kadowaki, H. Yoshizawa, M. Enderle, S. Yonezawa, Y. Maeno, J. Kim, N. Tsuji, M. Takata, Y. Zhao, M. Green, and C. Broholm. Magnetic structure of the conductive triangular-lattice antiferromagnet $PdCrO_2$. *Physical Review B*, **89**(10):104408–104408, (2014).

[26] J. M. Ok, Y. J. Jo, Kyoo Kim, T. Shishidou, E. S. Choi, H.-J. Noh, T. Oguchi, B. I. Min, and J. S. Kim. Quantum Oscillations of the Metallic Triangular-Lattice Antiferromagnet $PdCrO_2$. *Physical Review Letters*, **111**(17):176405, (2013).

[27] C. W. Hicks, A. S. Gibbs, L. Zhao, P. Kushwaha, H. Borrmann, A. P. Mackenzie, H. Takatsu, S. Yonezawa, Y. Maeno, and E. A. Yelland. Quantum oscillations and magnetic reconstruction in the delafossite $PdCrO_2$. *Physical Review B*, **92**(1):014425, (2015).

[28] J. A. Sobota, K. Kim, H. Takatsu, M. Hashimoto, S.-K. Mo, Z. Hussain, T. Oguchi, T. Shishidou, Y. Maeno, B. I. Min, and Z.-X. Shen. Electronic structure of the metallic antiferromagnet $PdCrO_2$ measured by angle-resolved photoemission spectroscopy. *Physical Review B*, **88**(12):125109–125109, (2013).

[29] H. Lüth. *Solid Surfaces, Interfaces and Thin Films*. Graduate Texts in Physics. Springer International Publishing, Cham, (2015).

[30] S. Hufner. *Photoelectron Spectroscopy*. Advanced Texts in Physics. Springer Berlin Heidelberg, (2003).

[31] S. Hufner, editor. *Very high resolution photoelectron spectroscopy*. Lecture notes in physics. Springer, Berlin, (2007).

[32] A. Damascelli, Z. Hussain, and Z. X. Shen. Angle-resolved photoemission studies of the cuprate superconductors. *Reviews of Modern Physics*, **75**(April), (2003).

[33] A. Damascelli. Probing the Electronic Structure of Complex Systems by ARPES. *Physica Scripta*, **T109**:61, (2004).

[34] M. P. Seah and W. A. Dench. Quantitative electron spectroscopy of surfaces: A standard data base for electron inelastic mean free paths in solids. *Surface and Interface Analysis*, **1**(1):2–11, (1979).

[35] L. Hedin, J. Michiels, and J. Inglesfield. Transition from the adiabatic to the sudden limit in core-electron photoemission. *Physical Review B*, **58**(23):15565–15582, (1998).

[36] S. Moser. An experimentalist's guide to the matrix element in angle resolved photoemission. *Journal of Electron Spectroscopy and Related Phenomena*, **214**:29–52, (2017).

[37] D. I. Khomskii. *Basic Aspects of The Quantum Theory of Solids: Order and Elementary Excitations*. Cambridge University Press, Cambridge, (2010).

[38] G. Giuliani. *Quantum Theory of the Electron Liquid*. Cambridge University Press, Cambridge, 1st edition, (2008).

[39] P. D. C. King, S. McKeown Walker, A. Tamai, A. de la Torre, T. Eknapakul, P. Buaphet, S.-K. Mo, W. Meevasana, M. S. Bahramy, and F. Baumberger. Quasiparticle dynamics and spin - orbital texture of the $SrTiO_3$ two-dimensional electron gas. *Nature Communications*, **5**:3414–3414, (2014).

[40] F. Baumberger, N. J. C. Ingle, W. Meevasana, K. M. Shen, D. H. Lu, R. S. Perry, A. P. Mackenzie, Z. Hussain, D. J. Singh, and Z.-X. Shen. Fermi surface and quasiparticle excitations of Sr_2RhO_4. *Physical Review Letters*, **96**(24):246402–246402, (2006).

[41] N. J. C. Ingle, K. M. Shen, F. Baumberger, W. Meevasana, D. H. Lu, Z.-X. Shen, A. Damascelli, S. Nakatsuji, Z. Q. Mao, Y. Maeno, T. Kimura, and Y. Tokura. Quantitative analysis of Sr_2RuO_4 angle-resolved photoemission

spectra: Many-body interactions in a model Fermi liquid. *Physical Review B*, **72**(20):205114–205114, (2005).

[42] A.B. Migdal. Interaction between Electrons and Lattice Vibrations in a Normal Metal. *JETP*, **7**(6):996, (1958).

[43] G. Grimvall. The Electron-Phonon Interaction in Normal Metals. *Physica Scripta*, **14**(1-2):63, (1976).

[44] N. V. Smith, P. Thiry, and Y. Petroff. Photoemission linewidths and quasiparticle lifetimes. *Physical Review B*, **47**(23):15476–15481, (1993).

[45] M. S. Bahramy, O. J. Clark, B.-J. Yang, J. Feng, L. Bawden, J. M. Riley, I. Marković, F. Mazzola, V. Sunko, D. Biswas, S. P. Cooil, M. Jorge, J. W. Wells, M. Leandersson, T. Balasubramanian, J. Fujii, I. Vobornik, J. E. Rault, T. K. Kim, M. Hoesch, K. Okawa, M. Asakawa, T. Sasagawa, T. Eknapakul, W. Meevasana, and P. D. C. King. Ubiquitous formation of bulk Dirac cones and topological surface states from a single orbital manifold in transition-metal dichalcogenides. *Nature Materials*, **17**(1):21–28, (2018).

[46] L. Bawden, S. P. Cooil, F. Mazzola, J. M. Riley, L. J. Collins-McIntyre, V. Sunko, K. W. B. Hunvik, M. Leandersson, C. M. Polley, T. Balasubramanian, T. K. Kim, M. Hoesch, J. W. Wells, G. Balakrishnan, M. S. Bahramy, and P. D. C. King. Spin–valley locking in the normal state of a transition-metal dichalcogenide superconductor. *Nature Communications*, **7**:11711, (2016).

[47] O. J. Clark, M. J. Neat, K. Okawa, L. Bawden, I. Markovic, F. Mazzola, J. Feng, V. Sunko, J. M. Riley, W. Meevasana, J. Fujii, I. Vobornik, T. K. Kim, M. Hoesch, T. Sasagawa, P. Wahl, M. S. Bahramy, and P. D. C. King. Fermiology and Superconductivity of Topological Surface States in $PdTe_2$. *Physical Review Letters*, **120**(15):156401, (2018).

[48] O. J. Clark, F. Mazzola, J. Feng, V. Sunko, I. Marković, L. Bawden, T. K. Kim, P. D. C. King, and M. S. Bahramy. Dual quantum confinement and anisotropic spin splitting in the multivalley semimetal $PtSe_2$. *Physical Review B*, **99**(4):045438, (2019).

[49] M. D. Watson, O. J. Clark, F. Mazzola, I. Marković, V. Sunko, T. K. Kim, K. Rossnagel, and P. D. C. King. Orbital- and k_z-Selective Hybridization of Se 4p and Ti 3d States in the Charge Density Wave Phase of $TiSe_2$. *Physical Review Letters*, **122**(7):076404, (2019).

[50] V. Sunko, E. Abarca Morales, I. Marković, M. E. Barber, D. Milosavljević, F. Mazzola, D. A. Sokolov, N. Kikugawa, C. Cacho, P. Dudin, H. Rosner, C. W. Hicks, P. D. C. King, and A. P. Mackenzie. Direct Observation of a Uniaxial Stress-driven Lifshitz Transition in Sr_2RuO_4. *arXiv:1903.09581*, (2019).

[51] P. Willmott. *An Introduction to Synchrotron Radiation: Techniques and Applications*. Wiley, Chichester, West Sussex, UK, 1st edition, (2011).

[52] C. Schmitz-Antoniak. X-ray absorption spectroscopy on magnetic nanoscale systems for modern applications. *Reports on Progress in Physics*, **78**(6):062501, (2015).

[53] S. Mobilio, F. Boscherini, and C. Meneghini, editors. *Synchrotron Radiation: Basics, Methods and Applications*. Springer, Berlin Heidelberg, (2015).

[54] M. Hoesch, T. K. Kim, P. Dudin, H. Wang, S. Scott, P. Harris, S. Patel, M. Matthews, D. Hawkins, S. G. Alcock, T. Richter, J. J. Mudd, M. Basham, L. Pratt, P. Leicester, E. C. Longhi, A. Tamai, and F. Baumberger. A facility for the analysis of the electronic structures of solids and their surfaces by synchrotron radiation photoelectron spectroscopy. *Review of Scientific Instruments*, **88**(1):013106, (2017).

[55] X. J. Zhou, B. Wannberg, W. L. Yang, V. Brouet, Z. Sun, J. F. Douglas, D. Dessau, Z. Hussain, and Z. X. Shen. Space charge effect and mirror charge effect in photoemission spectroscopy. *Journal of Electron Spectroscopy and Related Phenomena*, **142**(1):27–38, (2005).

[56] D. Hoffman, B. Singh, and J. H. Thomas III, editors. *Handbook of Vacuum Science and Technology*. Elsevier, (1997).

[57] A. Thompson, editor. *X-ray booklet data*. Lawrence Berkley National Laboratory, Berkley, 3rd edition, (2009).

[58] T. Okuda, Y. Takeichi, Y. Maeda, A. Harasawa, I. Matsuda, T. Kinoshita, and A. Kakizaki. A new spin-polarized photoemission spectrometer with very high efficiency and energy resolution. *Review of Scientific Instruments*, **79**(12):123117, (2008).

[59] T. Okuda, K. Miyamaoto, K. Miyahara, K. Kuroda, A. Kimura, H. Namatame, and M. Taniguchi. Efficient spin resolved spectroscopy observation machine at Hiroshima Synchrotron Radiation Center. *Review of Scientific Instruments*, **82**(10):103302, (2011).

[60] T. Okuda, K. Miyamoto, A. Kimura, H. Namatame, and M. Taniguchi. A double VLEED spin detector for high-resolution three dimensional spin vectorial analysis of anisotropic Rashba spin splitting. *Journal of Electron Spectroscopy and Related Phenomena*, **201**:23–29, (2015).

[61] C. Bigi, P. K. Das, D. Benedetti, F. Salvador, D. Krizmancic, R. Sergo, A. Martin, G. Panaccione, G. Rossi, J. Fujii, and I. Vobornik. Very efficient spin polarization analysis (VESPA): new exchange scattering-based setup for spin-resolved ARPES at APE-NFFA beamline at Elettra. *Journal of Synchrotron Radiation*, **24**(4):750–756, (2017).

[62] M. Hoesch, M. Muntwiler, V. N. Petrov, M. Hengsberger, L. Patthey, M. Shi, M. Falub, T. Greber, and J. Osterwalder. Spin structure of the Shockley surface state on Au(111). *Phys. Rev. B*, **69**(24):241401, (2004).

[63] J. C. Slater and G. F. Koster. Simplified LCAO Method for the Periodic Potential Problem. *Physical Review*, **94**(6):1498–1524, (1954).

[64] P. W. Atkins and R. Friedman. *Molecular quantum mechanics*. Oxford University Press, New York, 4th edition, (2005).

[65] P. Hohenberg and W. Kohn. Inhomogeneous Electron Gas. *Physical Review*, **136**(3B):B864–B871, (1964).

[66] W. Kohn and L. J. Sham. Self-Consistent Equations Including Exchange and Correlation Effects. *Physical Review*, **140**(4A):A1133–A1138, (1965).

[67] K. Lejaeghere, G. Bihlmayer, T. Björkman, P. Blaha, S. Blügel, V. Blum, D. Caliste, I. E. Castelli, S. J. Clark, A. D. Corso, S. de Gironcoli, T. Deutsch, J. K. Dewhurst, I. di Marco, C. Draxl, M. Dułak, O. Eriksson, J. A. Flores-Livas, K. F. Garrity, L. Genovese, P. Giannozzi, M. Giantomassi, S. Goedecker, X. Gonze, O. Grånäs, E. K. U. Gross, A. Gulans, F. Gygi, D. R. Hamann, P. J. Hasnip, N. A. W. Holzwarth, D. Iuşan, D. B. Jochym, F. Jollet, D. Jones, G. Kresse, K. Koepernik, E. Küçükbenli, Y. O. Kvashnin, I. L. M. Locht, S. Lubeck, M. Marsman, N. Marzari, U. Nitzsche, L. Nordström, T. Ozaki, L. Paulatto, C. J. Pickard, W. Poelmans, M. I. J. Probert, K. Refson, M. Richter, G.-M. Rignanese, S. Saha, M. Scheffler, M. Schlipf, K. Schwarz, S. Sharma, F. Tavazza, P. Thunström, A. Tkatchenko, M. Torrent, D. Vanderbilt, M. J. van Setten, V. van Speybroeck, J. M. Wills, J. R. Yates, G.-X. Zhang, and S. Cottenier. Reproducibility in density functional theory calculations of solids. *Science*, **351**(6280):aad3000, (2016).

[68] K. Koepernik and H. Eschrig. Full-potential nonorthogonal local-orbital minimum-basis band-structure scheme. *Physical Review B*, **59**(3):1743–1757, (1999).

[69] I. Opahle, K. Koepernik, and H. Eschrig. Full-potential band-structure calculation of iron pyrite. *Physical Review B*, **60**(20):14035–14041, (1999).

[70] J. P. Perdew, K. Burke, and M. Ernzerhof. Generalized Gradient Approximation Made Simple. *Physical Review Letters*, **77**(18):3865–3868, (1996).

[71] N. Marzari, A. A. Mostofi, J. R. Yates, I. Souza, and D. Vanderbilt. Maximally localized Wannier functions: Theory and applications. *Reviews of Modern Physics*, **84**(4):1419–1475, (2012).

[72] M. W. Haverkort, M. Zwierzycki, and O. K. Andersen. Multiplet ligand-field theory using Wannier orbitals. *Physical Review B*, **85**(16):165113, (2012).

[73] H.-J. Noh, J. Jeong, J. Jeong, H. Sung, K. J. Park, J.-Y. Kim, H.-D. Kim, S. B. Kim, K. Kim, and B. I. Min. Orbital character of the conduction band of delafossite $PdCoO_2$ studied by polarization-dependent soft x-ray absorption spectroscopy. *Physical Review B*, **80**(7):073104–073104, (2009).

[74] C. Bergemann, A. P. Mackenzie, S. R. Julian, D. Forsythe, and E. Ohmichi. Quasi-two-dimensional Fermi liquid properties of the unconventional superconductor Sr_2RuO_4. *Advances in Physics*, **52**(7):639–725, (2003).

[75] H. Takatsu, S. Yonezawa, S. Mouri, S. Nakatsuji, K. Tanaka, and Y. Maeno. Roles of High-Frequency Optical Phonons in the Physical Properties of the Conductive Delafossite $PdCoO_2$. *Journal of the Physical Society of Japan*, **76**(10):104701, (2007).

[76] B. A. McDougall, T. Balasubramanian, and E. Jensen. Phonon contribution to quasiparticle lifetimes in Cu measured by angle-resolved photoemission. *Physical Review B*, **51**(19):13891–13894, (1995).

[77] C. Kittel. *Introduction to Solid State Physics*. Wiley, 7th edition, (2007).

[78] J. Voit, L. Perfetti, F. Zwick, H. Berger, G. Margaritondo, G. Grüner, H. Höchst, and M. Grioni. Electronic Structure of Solids with Competing Periodic Potentials. *Science*, **290**(5491):501–503, (2000).

[79] D. Shoenberg. *Magnetic Oscillations in Metals*. Cambridge University Press, Cambridge, 1st edition, (2009).

[80] E. Sasioglu, I. Galanakis, C. Friedrich, and S. Blügel. Ab initio calculation of the effective on-site Coulomb interaction parameters for half-metallic magnets. *Physical Review B*, **88**(13):134402, (2013).

[81] F. Lechermann. Hidden Mott insulator in metallic $PdCrO_2$. *Physical Review Materials*, **2**(8):085004, (2018).

[82] Q. Si. Quantum criticality and global phase diagram of magnetic heavy fermions. *Physica Status Solidi (b)*, **247**(3):476–484, (2010).

[83] H. v Löhneysen, A. Rosch, M. Vojta, and P. Wölfle. Fermi-liquid instabilities at magnetic quantum phase transitions. *Reviews of Modern Physics*, **79**(3):1015–1075, (2007).

[84] J. J. Yeh and I. Lindau. Atomic subshell photoionization cross sections and asymmetry parameters: $1 < Z < 103$. *Atomic Data and Nuclear Data Tables*, **32**(1):1–155, (1985).

[85] E. Rotenberg and A. Bostwick. Superlattice effects in graphene on SiC(0001) and Ir(111) probed by ARPES. *Synthetic Metals*, **210**:85–94, (2015).

[86] K. S. Burch, D. Mandrus, and J. G. Park. Magnetism in two-dimensional van der Waals materials. *Nature*, **563**(7729):47, (2018).

[87] L. Petersen and P. Hedegård. A simple tight-binding model of spin-orbit splitting of *sp*-derived surface states. *Surface Science*, **459**(1-2):49–56, (2000).

[88] M. W. Haverkort. *Spin and orbital degrees of freedom in transition metal oxides and oxide thin films studied by soft x-ray absorption spectroscopy.* PhD thesis, University of Cologne, (2005).

[89] A. Tamai, W. Meevasana, P. D. C. King, C. W. Nicholson, A. de la Torre, E. Rozbicki, and F. Baumberger. Spin-orbit splitting of the Shockley surface state on Cu(111). *Physical Review B*, **87**(7):075113, (2013).

[90] K. Ishizaka, M. S. Bahramy, H. Murakawa, M. Sakano, T. Shimojima, T. Sonobe, K. Koizumi, S. Shin, H. Miyahara, A. Kimura, K. Miyamoto, T. Okuda, H. Namatame, M. Taniguchi, R. Arita, N. Nagaosa, K. Kobayashi, Y. Murakami, R. Kumai, Y. Kaneko, Y. Onose, and Y. Tokura. Giant Rashba-type spin splitting in bulk BiTeI. *Nature Materials*, **10**(7):521–526, (2011).

[91] C. R. Ast, J. Henk, A. Ernst, L. Moreschini, M. C. Falub, Daniela Pacile, Patrick Bruno, Klaus Kern, and Marco Grioni. Giant Spin Splitting through Surface Alloying. *Physical Review Letters*, **98**(18):186807, (2007).

[92] H. Iwasawa, Y. Yoshida, I. Hase, K. Shimada, H. Namatame, M. Taniguchi, and Y. Aiura. True bosonic coupling strength in strongly correlated superconductors. *Scientific Reports*, **3**, (2013).

[93] S. LaShell, B. A. McDougall, and E. Jensen. Spin Splitting of an Au(111) Surface State Band Observed with Angle Resolved Photoelectron Spectroscopy. *Physical Review Letters*, **77**(16):3419–3422, (1996).

[94] J. J. Sakurai. *Modern Quantum Mechanics.* Addison Wesley, Reading, Mass, revised edition, (1993).

[95] J. D. Jackson. *Classical Electrodynamics Third Edition*. Wiley, New York, 3rd edition, (1998).

[96] E. U. Condon and G. H. Shortley. *The Theory of Atomic Spectra*. Cambridge University Press, Cambridge, (1935).

[97] L. D. Landau and L. M. Lifshitz. *Quantum Mechanics: Non-Relativistic Theory*. Butterworth-Heinemann, Singapore, 3rd edition, (1981).

[98] K. V. Shanavas, Z. S. Popović, and S. Satpathy. Theoretical model for Rashba spin-orbit interaction in d electrons. *Physical Review B*, **90**(16):165108, (2014).

[99] F. Herman and S. Skillman. *Atomic structure calculations*. Prentice-Hall, Englewood Cliffs, N.J., (1963).

[100] T. Kosugi, T. Miyake, and S. Ishibashi. Slab Thickness Dependence of Rashba Splitting on Au(111) Surface: First-Principles and Model Analyses. *Journal of the Physical Society of Japan*, **80**(7):074713, (2011).

[101] S. R. Park, C. H. Kim, J. Yu, J. H. Han, and C. Kim. Orbital-Angular-Momentum Based Origin of Rashba-Type Surface Band Splitting. *Physical Review Letters*, **107**(15), (2011).

[102] S. R. Park and C. Kim. Microscopic mechanism for the Rashba spin-band splitting: Perspective from formation of local orbital angular momentum. *Journal of Electron Spectroscopy and Related Phenomena*, **201**:6–17, (2015).

[103] B. Kim, P. Kim, W. Jung, Y. Kim, Y. Koh, W. Kyung, J. Park, M. Matsunami, S.-I. Kimura, J. S. Kim, J. H. Han, and C. Kim. Microscopic mechanism for asymmetric charge distribution in Rashba-type surface states and the origin of the energy splitting scale. *Physical Review B*, **88**(20):205408, (2013).

[104] S. Sugano, Y. Tanabe, and H. Kamimura. *Multiplets of transition-metal ions in crystals*. Academic Press, New York, London, (1970).

[105] W. B. Wu, D. J. Huang, J. Okamoto, A. Tanaka, H.-J. Lin, F. C. Chou, A. Fujimori, and C. T. Chen. Orbital Symmetry and Electron Correlation in Na_xCoO_2. *Physical Review Letters*, **94**(14):146402, (2005).

[106] W. Koshibae and S. Maekawa. Electronic state of a CoO_2 layer with hexagonal structure: a kagome lattice structure in a triangular lattice. *Physical Review Letters*, **91**(25):257003, (2003).

[107] S. R. Park, J. Han, C. Kim, Y. Y. Koh, C. Kim, H. Lee, H. J. Choi, J. H. Han, K. D. Lee, N. J. Hur, M. Arita, K. Shimada, H. Namatame, and M. Taniguchi. Chiral Orbital-Angular Momentum in the Surface States of Bi_2Se_3. *Physical Review Letters*, **108**(4), (2012).

[108] J.-H. Park, C. H. Kim, J. W. Rhim, and J. H. Han. Orbital Rashba effect and its detection by circular dichroism angle-resolved photoemission spectroscopy. *Physical Review B*, **85**(19):195401, (2012).

[109] L. Bawden, J. M. Riley, C. H. Kim, R. Sankar, E. J. Monkman, D. E. Shai, H. I. Wei, E. B. Lochocki, J. W. Wells, W. Meevasana, T. K. Kim, M. Hoesch, Y. Ohtsubo, P. Le Fevre, C. J. Fennie, K. M. Shen, F. Chou, and P. D. C. King. Hierarchical spin-orbital polarization of a giant Rashba system. *Science Advances*, **1**(8):e1500495, (2015).

[110] J. Hong, J.-W. Rhim, C. Kim, S. Ryong Park, and J. Hoon Shim. Quantitative analysis on electric dipole energy in Rashba band splitting. *Scientific Reports*, **5**:13488, (2015).

[111] G. Khalsa, B. Lee, and A. H. MacDonald. Theory of t_{2g} electron-gas Rashba interactions. *Physical Review B*, **88**(4):041302, (2013).

[112] P. D. C. King, R. H. He, T. Eknapakul, P. Buaphet, S.-K. Mo, Y. Kaneko, S. Harashima, Y. Hikita, M. S. Bahramy, C. Bell, Z. Hussain, Y. Tokura, Z.-X. Shen, H. Y. Hwang, F. Baumberger, and W. Meevasana. Subband Structure of a Two-Dimensional Electron Gas Formed at the Polar Surface of the Strong Spin-Orbit Perovskite $KTaO_3$. *Physical Review Letters*, **108**(11):117602, (2012).

[113] P. Kim, K. T. Kang, G. Go, and J. H. Han. Nature of orbital and spin Rashba coupling in the surface bands of $SrTiO_3$ and $KTaO_3$. *Physical Review B*, **90**:205423, (2014).

[114] Z. Zhong, A. Toth, and K. Held. Theory of spin-orbit coupling at $LaAlO_3/SrTiO_3$ interfaces and $SrTiO_3$ surfaces. *Physical Review B*, **87**(16):161102, (2013).

[115] M. S. Bahramy, R. Arita, and N. Nagaosa. Origin of giant bulk Rashba splitting: Application to BiTeI. *Physical Review B*, **84**(4):041202, (2011).

[116] H. Maass, H. Bentmann, C. Seibel, C. Tusche, S. V. Eremeev, T. R. F. Peixoto, O. E. Tereshchenko, K. A. Kokh, E. V. Chulkov, J. Kirschner, and F. Reinert. Spin-texture inversion in the giant Rashba semiconductor BiTeI. *Nature Communications*, **7**:11621, (2016).

[117] L. Bawden. *A spin- and angle-resolved photoemission study of coupled spin-orbital textures driven by global and local inversion symmetry breaking.* Thesis, University of St Andrews, (2017).

[118] G. Bihlmayer, S. Blügel, and E. V. Chulkov. Enhanced Rashba spin-orbit splitting in Bi/Ag(111) and Pb/Ag(111) surface alloys from first principles. *Physical Review B*, **75**(19):195414, (2007).

[119] J. Hong, J. W. Rhim, I. Song, C. Kim, S. R. Park, and J. H. Shim. Giant Rashba-type spin splitting through spin-dependent interatomic-hopping. *arXiv:1709.04087*, (2017).

[120] G. Bian, X. Wang, T. Miller, and T.-C. Chiang. Origin of giant Rashba spin splitting in Bi/Ag surface alloys. *Physical Review B*, **88**(8):085427, (2013).

[121] H. Lee and H. J. Choi. Role of *d* orbitals in the Rashba-type spin splitting for noble-metal surfaces. *Physical Review B*, **86**(4):045437, (2012).

[122] H. Ishida. Rashba spin splitting of Shockley surface states on semi-infinite crystals. *Physical Review B*, **90**(23):235422, (2014).

[123] B. Kim, C. H. Kim, P. Kim, W. Jung, Y. Kim, Y. Koh, M. Arita, K. Shimada, H. Namatame, M. Taniguchi, J. Yu, and C. Kim. Spin and orbital angular momentum structure of Cu(111) and Au(111) surface states. *Physical Review B*, **85**(19):195402, (2012).